DOCTORAL SCHOOL
MEDITERRANEA UNIVERSITY OF REGGIO CALABRIA

DEPARTMENT OF INFORMATION ENGINEERING, INFRASTRUCTURES
AND SUSTAINABLE ENERGY
(DIIES)

PHD IN
INFORMATION ENGINEERING

S.S.D. ING-INF/02
XXVIII CYCLE

STUDY OF ELECTROMAGNETIC WAVES PROPAGATION FOR INNOVATIVE MICROWAVE DIAGNOSTIC METHODS AND HEATING SCHEMES IN MAGNETIZED PLASMAS

CANDIDATE
Giuseppe TORRISI

ADVISOR
Prof. Tommaso ISERNIA

CO-ADVISORS
Dr. David MASCALI
Ing. Luigi CELONA

COORDINATOR
Prof. Claudio DE CAPUA

REGGIO CALABRIA, FEBRUARY 2016

GIUSEPPE TORRISI

STUDY OF ELECTROMAGNETIC WAVES PROPAGATION FOR INNOVATIVE MICROWAVE DIAGNOSTIC METHODS AND HEATING SCHEMES IN MAGNETIZED PLASMAS

Contents

List of Figures

Introduction

History and Motivation

The work presented in this PhD thesis has been carried out in the framework of the interaction between electromagnetic waves and dispersive anisotropic magnetized plasmas in electron cyclotron resonance and microwave ion sources [1]. The generation and heating of plasmas by means of microwaves is a widely-used method for high-temperature ion source and fusion plasmas [2] as well as for low temperature plasmas.

Interest in high frequency electromagnetic waves propagation in ionized gases was first motivated by ionospheric and astrophysical observations. Since about 1950, the efforts to understand the properties of plasma waves has been greatly boosted by the needs for supplementary heating in fusion-oriented plasmas, or by the needs to use the microwave propagation in plasma as a non-perturbative diagnostic tool, and it has developed into an essential part of plasma physics. The use of plasmas in various areas of scientific research has been growing in recent years. Since 1970, moreover, their contribution has been crucial in the field of accelerator physics, and consequently contributed to the impulse that this gave to Nuclear and Particle Physics in the last thirty years. The *Electron Cyclotron Resonance Ion Sources (ECRIS) and the Microwave Discharge Ion Sources (MDIS) are currently the best devices worldwide able to feed effectively high energy accelerators* such as Linacs, Cyclotrons, Synchrotrons or Colliders.

ECRIS are now among the best candidates to support the growing request of intense beams of multicharged ions coming from both fundamental science (nuclear and particle Physics, especially [3]) and applied research (neutrons spallation sources [4], subcritical nuclear reactors [5], hadrotherapy facilities [6], material treatments, ion implantation). Inside an ECRIS machine [7], a dense and hot plasma, made of multicharged ions immersed in a dense cloud of energetic electrons, is confined by multi-Tesla magnetic fields and resonantly heated by some kWs of microwave power in the 2.45-28 GHz frequency range, absorbed during the interaction with a low pressure gas

(10^{-6} - 10^{-3} mbar). In presence of the magnetostatic field, the electromagnetic wave absorption is particularly efficient at the so-called *"Electron Cyclotron Resonance"* frequency which gives the name to these devices. When part of the ion content is extracted from the high density and high temperature plasma ($n_e \sim 10^{10}$ - 10^{12} cm^{-3}, $T_e \sim$ 0.1 - 100 keV), to supply the ion beam for the accelerator machines, most of the parameters of the extracted beam, such as the intensity, the emittance and the shape in the real space depend in a decisive way on the characteristics of the plasma from which the beam is extracted.

The further development of microwave ECR-heated ion sources is however intrinsically limited by physical properties of the plasmas. The electromagnetic wave can travel in a plasma only if $\omega_{RF} > \omega_{pe}$, i.e. the operative frequency is greater than the plasma frequency: this implies that the electromagnetic energy can not be transferred to the plasma electrons over a certain density threshold, named cutoff density. At the cutoff the wave becomes evanescent, making inaccessible the ECR layer and, normally, in plasmas sustained by microwaves, *the density increases with microwave power but it stabilizes below a limit value situated just slightly below the critical density.*

In the ion sources field, this topic is of fundamental importance, because the extracted currents are directly proportional to the plasma density ($i_{ext} \propto n_e$): the presence of the cutoff limitation, therefore, limits the performance of the sources.

Up to now, the ECRIS development path has been traced – since the years of general scaling laws [1] definition (1980–1995) – on the philosophy of magnetic field and microwave source frequency and power boosting. This trend is now deemed of approaching saturation due to technological constraints.

In the last years, together with the trend to increase the microwave frequency, new techniques have been evaluated in order to improve the performances of the existing ECRIS or of those under development. The possibility to tune the frequency of the microwave power is a promising aspect for suchlike improvement. Several experiments confirming this assumption have been carried out in the last years and interesting interpretations of the results of this so called *frequency tuning effect* have been proposed. Another technique successfully used to enhance the ion beam current and the production of highly charged ions is called *double frequency heating* and consists in the multiple injection of two electromagnetic waves at different frequencies into the ion source. These techniques are based on the different electromagnetic field patterns which can be excited inside an ECRIS plasma chamber (that is a microwave resonant cavity) and on the improvement of the microwave coupling between the electromagnetic waves and the confined plasma. However, even if these techniques provided interesting results, a better understanding of the *microwave coupling between waves and cavity filled with plasma is mandatory. The modeling of waves in magne-*

tized anisotropic plasma for microwave heating and diagnostic is the main argument developed in this PhD thesis. It well fits also for fusion research on microwave-plasma interaction and with a large range of industrial applications such as plasma sources for generation of radicals (e.g. atomic oxygen), plasma etching, plasma-enhanced chemical vapor deposition (PECVD), surface treatment (nitruration, cleaning etc.).

Also in the field of magnetic confinement controlled nuclear fusion reactor in fact, the cutoff limitation discussed above has a crucial importance since it limits the satisfaction of the Lawson criterion [8–10]. However, there is a wave which can propagate in plasmas without upper density limit. It is the electrostatic "Electron Bernstein wave" (EBW) [11] that has been already investigated and exploited for different fusion-relevant experiments [12]. The EBW has no cutoff limit but its nature does not allow propagation outside of the plasma [13]. How to obtain this wave/mode inside the plasma of an ion source, through the conversion [14] from other externally launched electromagnetic waves/modes, is a relevant topic of the present thesis, and it was studied through numerical codes and dedicated experiments.

For these reasons, this research work has been carried out with the aim to investigate the microwave coupling to the plasma, to analyze and design new techniques to improve the performances of the ECRISs [15] and new microwave diagnostic techniques putting us on a road that takes beyond what achieved so far, i. e. towards a **"microwave-absorption oriented"** design of future ion sources.

Overview and main results of this thesis

This thesis focuses on several aspects of elecromagnetic waves in magnetized plasma, the common subject being the development of a full-wave simulation code based of Finite Element Methods (FEM), that in future it could be used in support of experiments carried out on ECRIS and microwave-heated plasma: *direct solution of the wave equation considering full-wave effects and realistic geometries, together with a 3D kinetic code for particles dynamics was used to calculate the electron distribution function in a self-consistent way.*

The studies we performed during the PhD course, have shown the importance of a complete modeling of electromagnetic waves propagation in plasma. The results of the simulations allowed to interpret and explain the experimental results, and, on the other hand, to implement techniques and systems capable of improving the absorption of electromagnetic power by the plasma contained within the resonant cavity of the ion source. The general efforts paid in wave-to-plasma interaction modeling were very useful for the development at INFN-LNS of a multipurpose *microwave-based interferometer* for non-invasive measurement of the plasma density in plasma-based

ion sources. This tool, completely designed, manufactured and tested, is an important part of this PhD thesis with potential applications in the field of laser generated plasmas for ion acceleration. The thesis work has hugely benefited of the multidisciplinarity, exploiting and inheriting techniques well known in other applications such as microwave radar which have been readapted for the particular scenario.

The electron density measurement, carried out by means of the microwave interferometer, represents the first measurement of electron density in ion sources with this method, it is absolutely relevant by a scientific point of view, and it will provide a non-invasive diagnostic and a fruitful strategy supporting the design and construction of new ion sources or for optimizing the performances of the existing ones.

The 3D full-wave code developed to study the microwave behaviour in the ECRIS plasma geometry, allowed to design a new antenna to heat by Electron Bernstein Waves, an ECRIS-like plasma trap, called Flexible Plasma Trap (FPT). The microwave launcher may be used to heat the plasma by launching an electromagnetic wave that (mode) converts and damps as an EBW. A proper O-X-B scenario has been simulated and chosen to run the experiments.

Thesis outline

The subjects up to now described were organized in six different chapters:

In the Chapter 1 an overview of the **microwave-generated plasma ion sources** is given, with the main peculiarities of the microwave discharge and ECRIS.

Chapter 2 presents the theory of **wave propagation in magnetized plasma**, including a brief discussion of the effect of cavity in case of a plasma confined in a resonant cavity. This chapter aims to provide the theoretical basis of the numerical model developed in this thesis and presented hereinafter in Chapter 4, providing the necessary references.

In the Chapter 3 some methodologies of **plasma diagnostics** will be presented with particular attention to the **microwave interferometry**. A brief survey of other plasma diagnostic techniques besides of microwave was also given. The remaining chapters were focused on the numerical and experimental results.

Chapter 4 describes the modeling of the electromagnetic field in the anisotropic inhomogeneous magnetized plasma of ECR Ion Sources. Therefore, **numerical solution of Vlasov equation via particle in-cell (PIC)-based strategy kinetic codes coupled to full wave FEM solver**, has been developed: it represents a very important tool to investigate wave-plasma interaction, electron-ion confinement and ion beam formation. **The full wave calculations show the possibility of the electromagnetic mode conversion also in the ECRIS plasma**.

Chapter 5 is devoted to extensive description of the **microwave diagnostic experiment**. The strategies of design and sizing of the microwave interferometer instrument are described, up – finally – to the development of a calibration procedure and experimental tests carried out through a special technique of **"frequency sweep"**.

Chapter 6 is devoted to the numerical and experimental study of **alternative plasma heating mechanisms** for ECRIS: a series of numerical simulation have been carried out and a possible injection scheme designed. The chapter shows the experimental data collected in terms of electromagnetic characterization on a new **"microwave launcher"**, ready to be installed on a new ECRIS-like device, the Flexible Plasma Trap (FPT), recently installed at LNS, for the production of overdense plasma through possible alternative mechanism of plasma excitation.

Finally, the chapter devoted to conclusion remarks. Particularly important are the perspectives opened by a more powerful handling of the RF energy deposition into the plasma, including the diagnostics for monitoring what's going on into the plasma itself, in terms of density and electron energy distribution function.

1

Microwave-generated plasma Ion Sources

1.1 Introduction

An ion source represents the first stage of an accelerator. It generates and contains the plasma from which ions are extracted. In the XX century several types of ion sources have been developed, each one characterized by a different manner to generate and maintain the plasma. Ion sources are different for electron temperatures and densities and for plasma lifetime. These properties have consequences on the ion beam.

Generally, plasmas are created by means of electrical discharges under vacuum, by means of electron beams passing through the neutral gases or by means of electromagnetic waves interacting with gases or vapours, in presence of a well shaped magnetic field.

Ion sources based on this last method usually produce plasmas by means of the Electron Cyclotron Resonance or by means of the so-called off-resonance discharge. They are frequently used in modern accelerator facilities, as they enable to reach larger charge states and extracted. In the forthcoming chapter a description of the main microwave-based ion sources will be given. Particular attention will be paid to the Electron Cyclotron ion sources and Microwave discharge Ion sources, the equipment on which a large part of the experimental measurements have been carried out bu LNS group.

Electron cyclotron resonance ion sources (ECRISs) are delivering beams of singly or multiply charged ions for a wide range of applications in many laboratories. In particular, such devices are well suited for the productions of highly charged ions (HCIs) which are a key point for the new acceleration facilities (e.g., FAIR, RIA, HRIBF, etc.) which will require mA level of HCI. In order to get such high currents, the recent progress of ECRIS performances has been mainly linked to the improvement of the plasma magnetic confinement time τ_i within the source chamber and to the frequency increase for the feeding microwaves which, under proper conditions, take to higher plasma densities n_e [16].

The product $n_e\tau_i$ is called **quality factor** for ion sources and, together with the electron temperature, determines the performances of the ion source. This means that it is possible to improve the performances of an existing source by opportunely increasing these three fundamental parameters. In figure 1.1 the function $n_e\tau_i = f(t_{opt})$ together with the main ions obtainable in such conditions is shown.
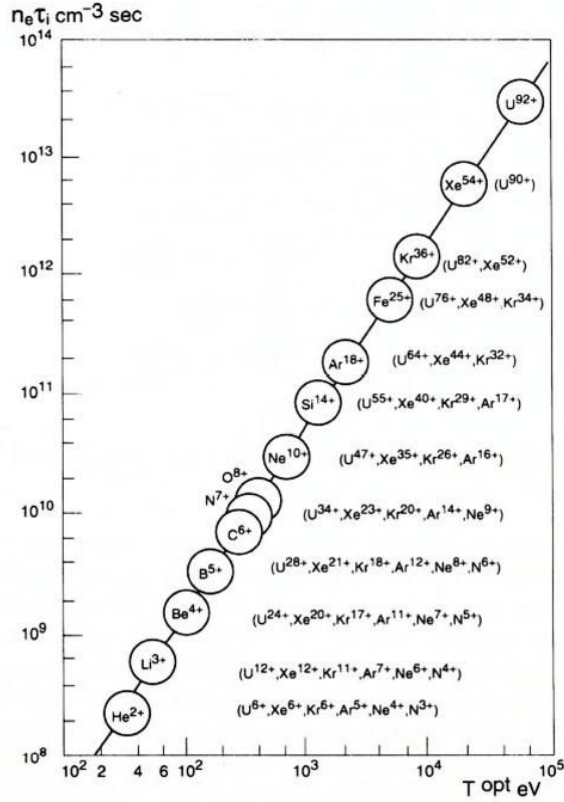
Fig. 1.1. Golovanivskys diagram, which shows the criteria for the production of highly charged ions. The ions enclosed by circles are completely stripped; some combinations of electron temperature, electron density and ion confinement time allow to produce completely stripped ions; inside brackets uncompletely stripped ions are shown: they can be produced with the corresponding plasma parameter of ions enclosed in circles.

The increase of the quality factor and of the electron temperature through the development of new plasma heating methodic represents the main frontier of the research and one of the main goals of the PhD activity.

Nowadays, if compared to other kind of sources, the ECRIS give the best compromise between charge state, extracted current and emittance. Since the beginning of 90s, when ECRIS started to be operative, the increase of performances has been done by means of a "brute force" approach through the control of the power and of

the frequency ω_{RF} of the electromagnetic injected in the source. This approach has been summarized by the *Geller's scaling laws*:

$$I_{extr} \propto \frac{\omega_{RF}^2}{M} \qquad \langle q \rangle \propto \log \omega_{RF}^{3.5} \qquad (1.1)$$

where M is the atomic mass number, which have traced the road, for more than 20 years, for the development of ECRIS; indeed for a couple of decades people spoke about a "standard model of ECRIS".

The trend followed until now, has been increasing frequency and magnetic field leading to rising cost of the technology and safety problems for the magnet's cryostat because of the hot electrons growth: frequency and magnetic field scaling are close to saturation. Apart from this main road, different techniques are also used to enhance the production of HCI, such as the usage of secondary emission materials, the wall coatings, the installation of bias disk, or the gas mixing to mention the most important ones [17].

Moreover, in the past decade, some experiments involving new feeding approaches permitted to increase the performances of the conventional ECR ion sources with *B-minimum* magnetic field structure by feeding them with electromagnetic waves having large spectral content or obtained by the superimposition of a discrete set of microwaves at different frequencies [18]-[19].

Even if these experiments provided interesting results, they have not given an explanation or a methodology to better understand the coupling mechanism between feeding waveguide and cavity filled with plasma and the energy transfer between the electromagnetic field in the source plasma chamber and the plasma therein confined. The increase of knowledge in terms of microwave coupling to ECRIS plasma and therefore the optimization of the ECR power transfer processes may allow to design ion sources with higher performances. Further improvements of ECRIS output currents and average charge state require a deep understanding of electron and ion dynamics in the plasma and of the impact of electromagnetic structure on electrons density distribution: theoretical investigations, in order to find a reasonable and adequate modelling for these mechanisms and to predict their possible improvement, can lead to design a future innovative ECR ion source.

During the past years, dedicated experiments at INFN-LNS have aimed to investigate these topics and, at the same time, some theoretical studies have been undertaken to describe them in details [20].

The microwave coupling between the electromagnetic wave and the plasma determines the efficient transfer of the energy from the microwaves to the plasma electrons inside the ECRIS. The plasma chamber, on the other hand, can be considered as a resonant cavity for the electromagnetic waves and, when the magnetized plasma is

created, the electrical permittivity of the medium filling the chamber is not longer homogeneous and not longer electrically isotropous. A detailed investigation have been carried out to demonstrate that the performances of the ECR ion sources depend on the electromagnetic field configuration excited inside the plasma chamber and on the coupling mechanism used to provide the microwaves to the plasma. In the following the differents approachs used over the years are presented together with the possible alternative heating schemes.

1.2 ECR-based ion sources

ECR-based ions sources generate a plasma by means of the absorption of E.M waves in the microwaves range. ECR ions sources maximize the quality parameter $n_e \tau_i$. Equations

$$< q > \propto n_e \tau_i \tag{1.2}$$

and

$$I_{extr} \propto \frac{n_e}{\tau_i} \tag{1.3}$$

show how the confinement time is a fundamental parameter to determine the characteristics of the extracted beams. A high confinement time leads to the production of relatively low current of highly charged ion beams, while a low confinement time determines high currents of low charged ions (generally 1^+ ionized). ECRIS can be included in the first category, whereas the MDIS belong to the second one. For sake of simplicity, the main differences between ECRIS and MDIS can be depicted as in figure 1.2.
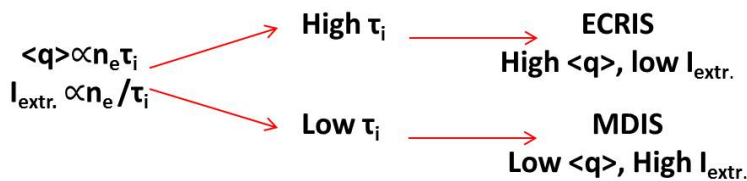
Fig. 1.2. A sketch of ECRIS and MDIS comparison

1.2.1 ECRIS scheme

ECRIS were first proposed by R.Geller in 1965 [21]. In 1971 the first operational ECRIS, called MAFIOS, was completed. The long ion confinement time is obtained by means of a "B-minimum" structure. The Electron Cyclotron Resonance ensures

a resonant absorption of electromagnetic energy by the plasma electrons. At the beginning of the discharge process few free electrons, spiralizing around the magnetic field lines, are accelerated by the electric field of the injected microwaves. In a time of several hundreds of μs the discharge develops with an avalanche of ionization events. Then a plasma in a stationary state is established. The electron-atom collisions allow to obtain multiply-charged ions, and very high charge states can be reached because of quite long confinement times ($\gg 10^{-3} - 10^{-2}$ sec).

The B minimum magnetic configuration is generated by means of two or three solenoids producing an axis-symmetric simple mirror structure, while an hexapole generates a field which increases from the center of the plasma chamber to the walls. Electrons are heated by means of ECR in the region of the chamber where $B = B_{ECR} = qB/m$ which is an iso-B surface with egg-shaped structure. Figure 1.3 shows the typical B-*minimum trap* [15], whereas in figure 1.4 a simulation of the electron dynamic within the B minimum trap is shown. From the two images it comes out that the largest part of particles is well confined inside the egg-shaped resonant surface. This effect, not adequately investigated in the past, has been recently focused by the INFN-LNS group; it is based on the additional confinement provided by the resonant acceleration of cold electrons crossing for the first the resonance layer. In [22] the reason of the electrons fluxes concentration in the axis region is given. According to this model, the plasma separates in two well distinguishable regions called "plasmoid" (inside the ECR surface) and "halo" (outside the ECR surface) as confirmed by the full-wave-PIC integrated code described in chapter 4.
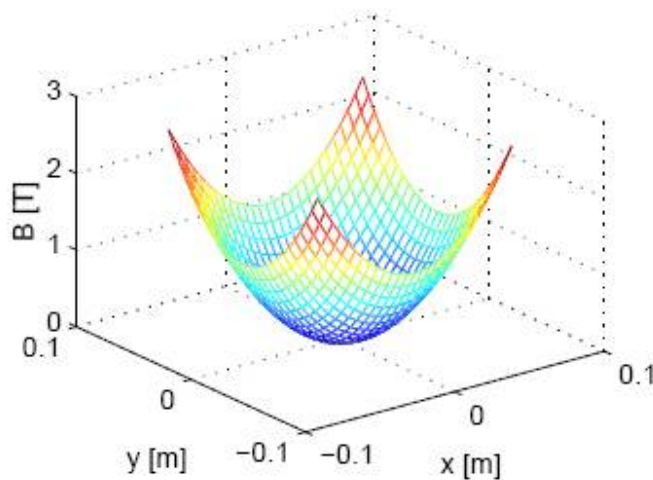
Fig. 1.3. B-minimum field structure in an ECRIS. The magnetic field is given by the sum of the field generated by two solenoids (simple mirror) and of the field generated by an hexapole.
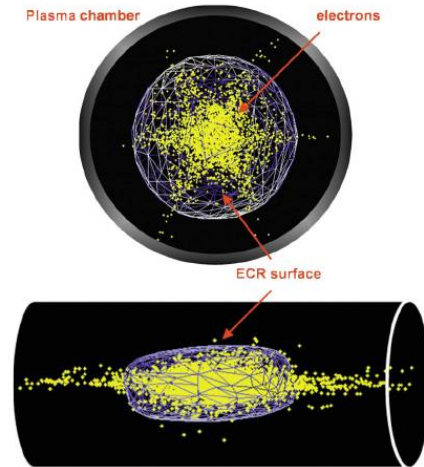
Fig. 1.4. Simulated electrons inside the SERSE plasma chamber together with the egg-shaped ECR surface.

The constituents of an ECRIS can be summarized as it follows:

- resonant cavity: a vacuum metallic chamber containing the plasma, which acts as a resonant cavity for the microwaves necessary so that we can have resonance ECR. It is insulated from the magnetic system and usually positively charged to allow the extraction of the ions;
- system of magnets for the magnetic confinement of the plasma: formed by two or more solenoids which generate a Simple Mirror type field for axial confinement and by a multipole magnet (usually a hexapole) to improve the radial confinement;
- gas injection system and microwaves injection.

  The microwave injection system consists of one or more waveguides with the corresponding ports located in the injection flange of the plasma chamber. As an example, Fig. 1.5 shows the injection flange with the location of the microwave ports for the SERSE source.

  The insulation of the chamber is ensured by a DC break placed in proximity to the injection flange. When two waveguide ports are present, the two injection ports are often perpendicular to each other to provide polarization diversity. The *microwave generators* are usually of two types: *klystron generators* and *Travelling Wave Tube (TWT) amplifiers*. For third-generation sources the gyrotron-based generators are used, with frequencies of 28 GHz or higher.

- Extraction of the ion beams with different charge states in the plasma. Appropriate generators or amplifiers (magnetron, TWT) provide microwaves, whose frequencies span from about 2 GHz to about 30 GHz, delivered to plasma through circular or rectangular waveguides.
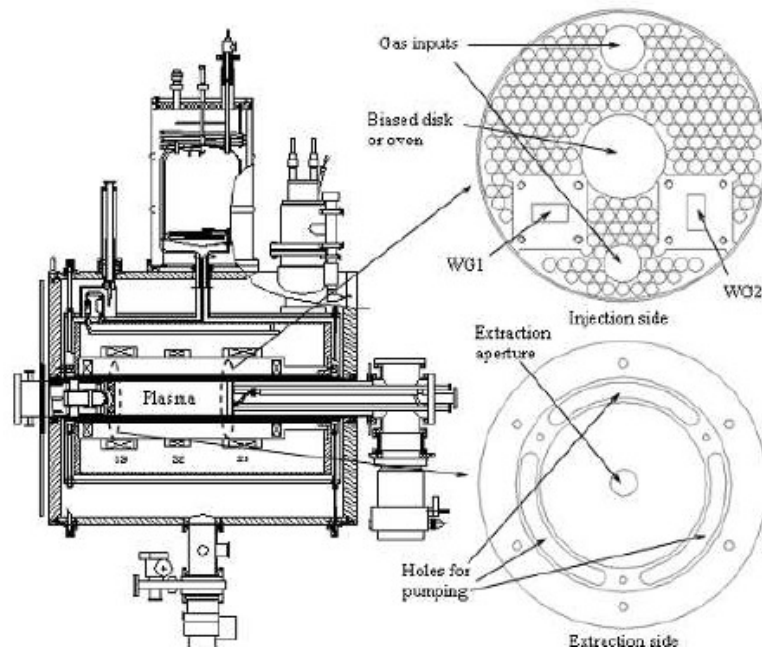
Fig. 1.5. Detail of the injection flange of the SERSE source with the two microwave ports and a sketch of the microwave generators–plasma chamber connections via waveguides.
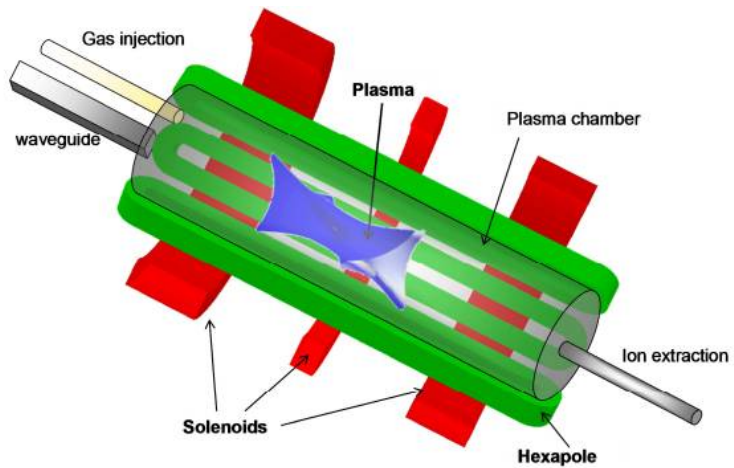
Fig. 1.6. The main ECRIS devices (magnets, microwave injection, gas injection, ion extraction, plasma chamber) together with the six-cusp plasma generated in the central region of the plasma chamber.

1.2.2 MDIS scheme

The MDIS were first developed at the beginning of nineties for the production of high currents of proton beams and light ions. Their principal characteristic is the absence of a confining magnetic field. On the contrary, the magnetic field is about flat within the plasma chamber. The shape of the magnetic field is designed in order to allow that the injected microwaves match ECR conditions at the injection and extraction points. In the central region of the plasma chamber, the field is about flat and off-resonance, i.e. $B > B_{ECR}$, according to figure 1.7 showing the magnetic configuration of the first MDIS. Through the years the magnetic field profile in the extraction region was designed to be about zero, in order to decrease the beam emittance, which is proportional to the field at extraction.
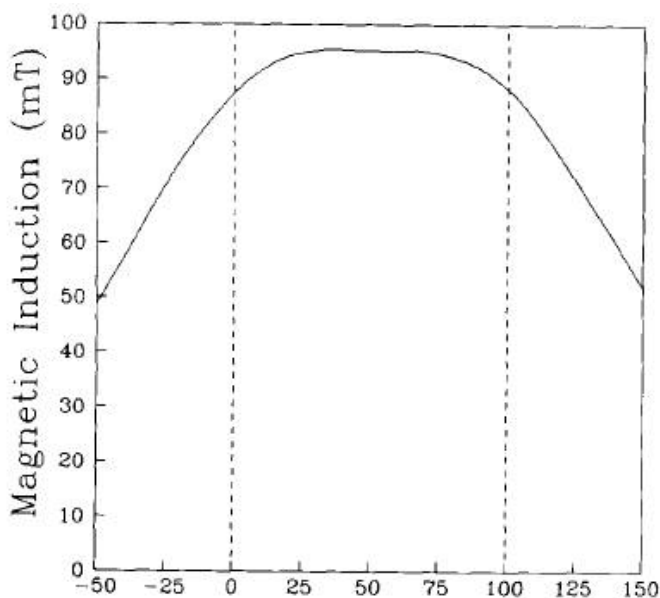
Fig. 1.7. Magnetic field profile of the MDIS designed by Taylor and Willis in 1991. The dashed vertical lines define the axial extent of the plasma chamber. Nowadays the magnetic field is designed to be zero in extraction region, in order to decrease the beam emittance, proportional to the field at extraction.

A large part of the MDIS operates at 2.45 GHz, with a off-resonance magnetic field of 0.1 T in the center of the plasma chamber. Several measurement carried out during the last decades (and reported also in this thesis) demonstrate that **slightly overdense plasmas can be generated in MDIS** [1], which are not expected by the standard theory of E.M absorption. In particular, Sakudo in ref. [23] demonstrated that the higher plasma density is obtainable when $B_{ECR} < B < 1.3B_{ECR}$.

A large part of the simulations present in this thesis have been carried out in a MDIS magnetic configuration. In particular, we have studied the performances of our source

in an under-resonance magnetic configuration, ($\omega > \omega_c$, Y<1). Also in these conditions ECR is not possible, but the eventual presence of the UHR can enable the generation and propagation of EBW, which then can be absorbed at the cyclotron harmonics, generating an overdense plasma. The absorption of the electrostatic waves is really more effective than the usual off-resonance heating. In particular this heating method increases significantly both electron density and temperature, and therefore the energy content of plasma $n_e\tau_e$. This new plasma heating approach, once adequately studied, can therefore represent a step forward in the field of MDIS (and in general, of all ECR-based ion sources) because it can allow to generate high current of multi-charged light ions by means of a simple and inexpensive device (with respect to other ion sources) like MDIS.

1.3 The ECR standard model

Up to now the so-called "ECRIS Standard Model" has been for most of one decade the road map followed by ECRIS designers. The main rules were confirmed by experiments performed at MSU-NSCL in 1993-94 and in 1995 and they can be summarized as it follows [24]:

- the radial magnetic field value at the plasma chamber wall must be $B_{rad} \geq 2B_{ECR}$;
- the axial magnetic field value at injection must be $B_{inj} \simeq 3B_{ECR}$ or more;
- the axial magnetic field value at extraction must be about $B_{ext} \simeq B_{rad}$;
- the axial magnetic field value at minimum must be in the range $0.30 < \frac{B_{min}}{B_{rad}} < 0.45$.
- the optimum power increases with the volume of the plasma and with the square of the frequency.

Up to now almost all operaring ECRIS obey to the Standard Model: the extracted current increases as the microwave frequency increases, but only the increase of mirror ratio can exploit the performances, making effective the increase of electron density with frequency. Then according to the Standard Model the ECRIS development is strictly linked to the improvements of superconducting magnets and of the microwave generators technology. Different authors studied the RF coupling to the plasma in terms of the maximum power rate per unit volume and of its relationship with the beam intensity produced by different ECR ion sources [25], but this description is not satisfactory. The cavity design and the microwaves injection geometry are of primary importance for a high RF energy transmission to the plasma chamber. Note that the problem of the wave energy transmission into the plasma must be divided into two parts: the first is connected to the microwave generator-waveguide-plasma chamber coupling, while the second one regards the wave-plasma interaction. Both aspects play

a notable role for future improvements of ECRIS performances. Many experiments have been carried out to verify the possibility to improve the plasma heating outside the framework traced by the Standard Model. Principally they follow three different roadmaps: a first series of experiments has been devoted to the study of the variation of ECRIS performances with slight variations of the microwave frequency. The second one regards the possibility to operate with more than one frequency for plasma heating (usually two) or by using broad microwave spectra. The third method actually is a mix of the previous ones: two or more frequencies are used for plasma heating, but at least one is provided by a broadband microwave generator (like a TWT), which allow to combine the effects of frequency tuning and of multi-frequency heating.

Just to make a summary, in Fig. 1.8 a conceptual scheme with three possible profiles of B-field for each source type is reported.

1.4 Frequency Tuning Effect (FTE)

Many experiments in the last years have shown that significant improvements of ECRIS performances (both in terms of total extracted current and highly charged ions production) are obtainable by slightly varying the microwave frequency in the case of Single Frequency Heating (SFH), that is defined as a "frequency tuning" effect. It was known that a large increase of the frequency ($\sim$GHz) increases the electron density and improves the ECRIS performances because of the increase of the cutoff density, but Since 2001 several experiments have demonstrated that even slight variations of the pumping wave frequency ($\sim$ MHz) may lead to strong variation of the extracted current. The first evidence was given by the different performances observed for the SERSE and CAESAR ion sources when fed by a klystron based or a travelling-wave-tube (TWT) based generator, [26], [27] either at 14 and 18 GHz. Other interesting results came from experiments performed at GSI[1] and at JYFL[2]. In the frequency tuning, the microwave frequency is varied in order to select the efficient heating mode inside the plasma chamber of ECRIS. In the experiments ,the input frequency for the klystron was swept from 14.05 to 14.13 GHz in 100 s with Rohde & Schwartz signal generator. This bandwidth was found adequate to maintain the constant output power over the whole frequency sweep using the automatic level control feature of the klystron.

---

[1] The GSI Helmholtz Centre for Heavy Ion Research (German: GSI Helmholtzzentrum fr Schwerionenforschung) research center in the Arheilgen suburb of Darmstadt, Germany.

[2] Accelerator Laboratory, Department of Physics. University of Jyvskyl , Finland.
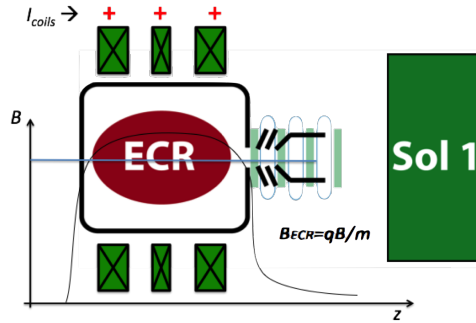
(a) Flat-B field MDIS for protons
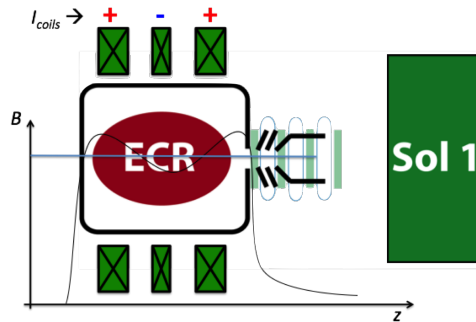
(b) Central "dip" for multiply charged ions
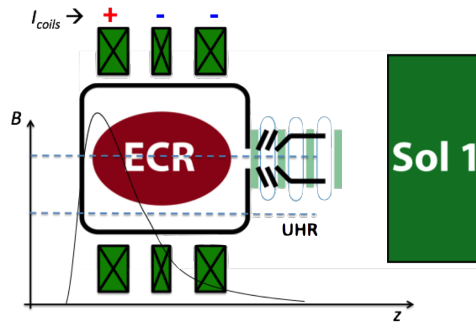
(c) Magnetic "beach" for Overdense plasma

Fig. 1.8. B-field profiles

1.4.1 Effect on beam structure and emittance

Figure 1.9 shows three beam viewer pictures. The beam structure varies strongly with the microwave frequency as an indication of the plasma-wave coupling changing during the scan. However, no unequivocal explanation concerning the origin of beam structure variations can be given: they could originate from the changes in the plasma in electron ion dynamics due to electromagnetic field variations and/or in the beam line due to changes in ion beam intensity and space charge. The explanation of the data presented above is based on the assumption that the frequency tuning changes the electromagnetic field distribution inside the resonator in terms of its distribution over the resonance surface, i.e. where the wave-electron energy transfer takes place.

This assumption requires that, even in case of plasma filling the cavity, the resonant modes persist, i.e. the formation of standing waves is still possible.
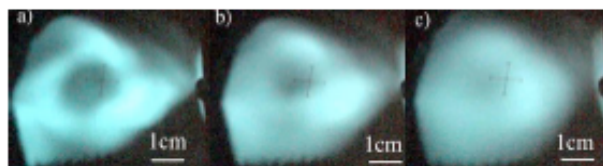
Fig. 1.9. The structure of the Ar^{9+} ion beam with different plasma heating frequencies: (a) 14.050 GHz, (b) 14.090 GHz, and (c) 14.108 GHz.
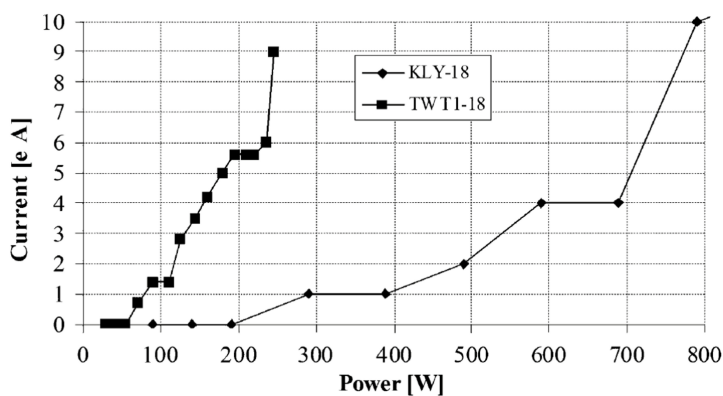
Fig. 1.10. Comparison between trends of O^{8+} at 18 GHz for a klystron (up to 800 W) and a TWT.

Figure 1.10 shows that a remarkable increase in the production of O^{8+} can be obtained by using the TWT instead of klystrons. In particular, the current of O^{8+} obtained with the TWT at 240 W is obtained by the klystron at 800 W, i.e. a power three times higher. It is important to underline that the two generators operated at two different but close frequencies. In particular, the klystron was operating at 18.0 GHz, while the TWT was at 17.9 GHz (both the amplifiers were fed by dielectric resonator-type oscillators). Such difference of performance was initially explained as a greater frequency dispersion of the TWT, but a series of measurements carried out with the two microwave generators, by means of a spectrum analyser, pointed out that the spectrum of the emitted radiation of a TWT is similar to that of the klystron. So the only difference between the two generators is the output frequency, with the further possibility for the TWT to vary the emitted frequency, thus optimizing the source performance.

The experimental set-ups used for the confirmation of the frequency tuning effect were the SUPERNANOGAN ion source of CNAO, Pavia, and the CAPRICE source at GSI, Darmstadt, which demonstrated that the frequency tuning strongly affects also the ion beam formation. Figure 1.11 shows the current for C^{4+} obtained with the SUPERNANOGAN ion source in 2005 versus the microwave frequency, keeping the power and all the other source parameters unchanged. The figure 1.11 features strong fluctuations of the extracted current in a frequency span of about 90 MHz.
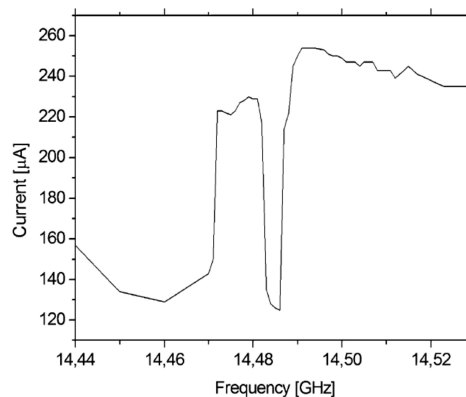
Fig. 1.11. Trend of the analysed C^{4+} current for the SUPERNANOGAN ECR ion source versus the RF frequency.

The frequency was changed in the range 14.44 to 14.53 GHz with a step of 1 MHz and it was observed that changes of a few MHz changed the C^{4+} current even by 70%. Further experiments including the final validation of the frequency tuning effect were carried out with the SUPERNANOGAN source of CNAO. It permitted an increase by 30% in its performance for C^{4+} and by 50% for H^{3+} (these ions are particularly requested for medical applications), and an additional increase of reliability and availability figures was registered.

Interesting results come from the GSI experiment carried out in 2007. On that occasion, as stated before, the frequency tuning was demonstrated to strongly affect also the beam shape, along with the extracted current for each charge state. As an example, Fig. 1.12 reports the shape evolution of a helium beam recorded on a viewer. The two helium charge states can be observed as well as the aberrations introduced by the hexapole. Furthermore, Fig. 1.12 evidently shows that the beam intensity distribution is inhomogeneous and that this distribution changes with the microwave frequency, while keeping all the other parameters constant.

Measurements of the S_{11} scattering parameter were carried out in parallel. The S_{11} parameter is the reflection coefficient, and the measurements have shown that, for some frequencies, the amount of reflected power increases, thus demonstrating that
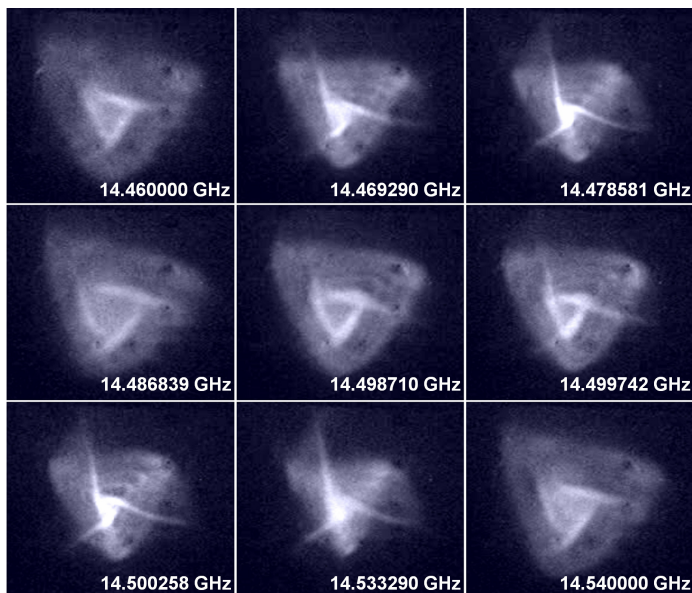
Fig. 1.12. Variation of the extracted beam shape for different microwave frequencies.

some resonances are present inside the cavity with or without plasma. In addition, variation in the extracted power versus frequency occurs also in the case of operating points with similar reflection coefficient.

Thus the excitation of near modes, even with distances of a few MHz, strongly changes not only the maximum field over the surface, but also the distribution of the zones of minima and maxima.

Simulations carried out considering different modes have demonstrated that some of them are able to heat the electrons up to energies much higher than others (even ten times higher).

1.5 Two frequency heating

The Two Frequency Heating (TFH) has been demonstrated to be a powerful method. For example, in the case for ^{238}U [28], it increased the production of higher charge states (from 35^+ to 39^+) by a factor of 2–4 and shifted the peak charge state from 33^+ to 36^+. Unfortunately, neither the relationship between the two frequencies nor the respective power was unequivocally determined. In fact, any source features a different set of parameters and the optimization is done empirically, just by looking to the maximization of beam current.

Several qualitative explanations have been given about this phenomenon, all related to the increase of the average electron temperature T_e and the ionization rate by assuming that the crossing of two resonance surfaces helps the electron to gain more energy. This simple picture does not explain the reason for the relevant changes

in the Charge State Distribution (CSD) for different pairs of frequencies (even for the case of minor changes, let us say a few MHz over 14 or 18 GHz), which can be explained by the frequency tuning effect. It is important to underline that, even in the case of TFH applied to many existing sources, a TWT is often used, the other being a klystron-based generator. The choice of TWT allows experimentalists to vary the second frequency slightly. As an example, a strong variation of ECRIS performance has been observed in TFH operations [29]. Thus, the TFH is an effective method to increase the extracted current from ECRIS, but it can be fully exploited only by means of frequency tuning. Experimental results demonstrate the advantages of TFH operations, for highly charged ion production when the chosen frequency has the right electromagnetic field distribution in the plasma chamber. Moreover, the closer frequencies are the best choice.

To explain TFH on the basis of the fundamental processes occurring during the electron–wave interaction, numerical simulations based on a pure Monte Carlo approach were developed. To be adequately modelled, the TFH effects can be depicted in the following way:

1. We double the resonance zone width, so that electrons that do not gain energy during the first crossing may have another possibility to be heated by the second one. Figure 1.13 shows the locations of these two resonance regions inside the plasma chamber calculated for the initial set-up of our simulations.

2. Preliminary simulations have shown a significant role played by the ECR interaction in recovering electrons otherwise contained in the magnetic loss cones. This effect (a deterministic plug-in of cold electrons) is currently deemed to play the main role in confining most of the plasma inside the volume embedded by the resonance surface. Adding a second resonance, electrons that have not been plugged by the first wave can be recovered by means of the second one, with a further increase of the plasma confinement.

The first evidence that significant improvements can be obtained by varying the frequency of the microwaves was given by the different performance observed for the SERSE and CAESAR ion sources when fed by a klystron-based or a TWT-based generator [20, 30] at either 14 or 18 GHz. Similar results came from experiments performed at ORNL and at JYFL [18].

1.6 Alternative heating methods: the Electron Bernstein Waves (EBW)

ECR devices are density limited, because the electromagnetic waves cannot propagate over a certain density, called cut-off density. As it will be explained in chapter 2, an
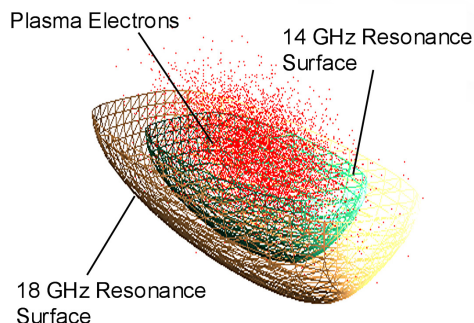
Fig. 1.13. Section of the two resonance surfaces showing the position of the plasma electrons.

alternative to the classical ECR interaction is the electrostatic wave heating, driven by Bernstein waves.
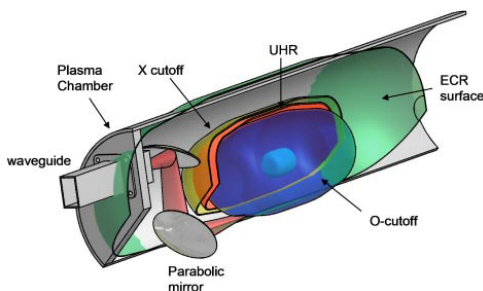
Fig. 1.14. A possible design for the microwave injection system producing the O-X-B conversion. Two parabolic mirrors are used to bring a focused microwave beam in the optimal region of the O cutoff layer.

In big-size fusion reactors it was shown that the OXB mode conversion may be optimized by changing the O-mode insertion angle with respect to the external magnetic field direction: in this case the O mode is completely converted into a slow X mode, which under certain conditions is in turn coverted to BWs in the Upper Hybrid Resonance layer [31].

The generated Bernstein waves travel inside the plasma until they are absorbed at the ECR or at the higher-order cyclotron harmonics. A possible design for the microwave injection system producing the O-X-B conversion is shown in Fig. 1.14. It is based on a "quasi-optical" approach resembling the ones developed for big-size fusion reactors. The thesis will be – see Chapter 6 – focused on the design and implementation of an OXB launcher optimized and made suitable for ECRIS. In Fig. 1.14, first, an O-wave is launched from the outside with an oblique angle of incidence obtained with a proper orientation of the parabolic mirrors. For an optimal launch angle, it is possible to obtain a correlated optimal parallel refractive index and then

a coincidence of the O-mode and the X-mode at the critical plasma density (cut-off). This means that both modes have the same phase and group velocities and the power is transferred without reflections. Once the X-waves are generated, they propagate towards the upper hybrid resonance (UHR). Here the X mode coincides with the electron Bernstein mode. In the linear description the X-waves are completely converted into EBWs. This process is called the X-B conversion. It should be noted that the OXB-process can only take place if the plasma density is above the O-wave cut-off density.

The OXB plasma heating and current drive with BW in an overdense plasma was demonstrated in the Stellarator WEGA, operating at Max Planck Institute for Plasma Physics of Greifswald, Germany. [32]. The heating of plasma by means of EBW at particular frequencies enabled to reach densities much larger than the cutoff ones. Evidences of EBW generation and absorption together with X-ray emissions due to high energy electrons are shown in ray tracing simulation and CCD photos in [33].

A plasma reactor operating at the INFN-LNS, Catania, has been used as a test-bench for the investigation of innovative mechanisms of plasma ignition based on electrostatic waves (ES-W), obtained via the inner plasma EM-to-ES wave conversion. Evidences of Bernstein wave (BW) generation are shown in [34]. Futhers results and discussion can be found in [33]. The results are interpreted through the Bernstein wave heating theory and are very promising for future high intensity multicharged ion sources. They can, therefore, be based on the results described here, by employing a simplified magnetic configuration with respect to typical B-minimum ECR ion sources. These results were the basis for the steps forward made in the present work, which in Chapter 6 will describe the design of a microwave launcher with an optimum angle of incidence to obtain EBW on a plasma trap testbench operating at the INFN–LNS, to study overdense plasma mechanism.

2

Waves in plasma

This thesis is written mainly in the context of the Ion Sources plasmas, which are characteristically *hot* (implying a high degree of ionization and low interparticle collision rate) and *small* (relative to wavelength of electromagnetic wave with respect to the typical dimension of the system). However, most of the material present in this work is relevant also in the field of fusion plasma reactors, magnetohydrodynamic power generation, space vehicle propulsion and communication, ionospheric radio propagation, microwave devices, classical gas discharges, and radioastronomy.

Wave propagation in plasmas is treated in various form of different depths in numerous plasma physics textbooks as, for example [2, 35]. In particular, an excellent monographs on plasma waves is given in [36–38]. We limit the general treatment, at first to the case of unbounded plasma. We have limited the detailed discussions to "high frequency" techniques that use waves at frequencies of the order of the electron plasma frequency ($\omega_{RF} \sim \omega_p$). Since we are interested only in the propagation of waves at high frequencies, only the response of the plasma electrons is considered, while the ions due to their higher inertia are assumed unaffected, staying fixed.

After that, the conditions are evaluated under which the description is applicable to bounded and inhomogeneous laboratory plasmas as well.

High frequency waves in magnetized plasmas can be classified into two broad classes with rather different characteristics, namely those with frequencies comparable tho the electron cyclotron and plasma frequencies, which depend only on the electron dynamics with the ions providing in first approximation only an immobile neutralizing background, and those with lower frequencies for which the ion dynamics is essential. All waves of the first class have a **phase velocity much greater than the electron thermal velocity**; in particular, at very high frequency, the phase velocity approaches and overcomes the speed of light. On the other hand, the phase velocity of low frequency plasma waves is often much smaller than the speed of light in vacuum. Hereinafter we will discuss only the first condition because ECRIS and MDIS operative frequencies range between 2.45 GHz and some tens of GHz. At so high

frequency ions are unsensitive to the electric field because of their high inertia, and their contribution in wave propagation can be neglected. In particular, in this thesis we consider the theory of electromagnetic wave propagation in a *Lorentz* plasma. A Lorentz plasma denotes a simplified plasma model in which it is assumed that the **electrons interact each other only through collective spacecharge forces**, and that the **heavy ions and neutral molecules are at rest**. In effect, the ions and neutrals are regarded as a continous stationary fluid through which the electrons move with viscous friction. In addition, we use the semplified analysys that infers the properties of the plasma medium from the motion of individual representative particles.

2.1 Introduction

A real life plasma is a very complicate phenomenon. Viewed as a medium for the propagation of electromagnetic waves, a ***plasma in a magnetic field is refractive, lossy, dispersive, resonant, anosotropic, non-reciprocal, nonlinear, and inhomogeneous***. We begin by accepting as many semplifications as possible and introduce refinements to the elementary treatment when it is useful. The theoretical description of high frequency waves in plasma requires "only" classical physics, i.e. Newtonian mechanics, Maxwell's equation, and classical statistics.

This chapter wants to give a description of the propagation of electromagnetic waves in magnetized waves at a level necessary for the envisaged frame: first, the understanding of the physics basis fot the modeling developed in chapter 4; second, to provide the necessary basis for the design and application of millimiter-wave-based interferometry techinique described in chapter 5. Additionally difficulties arises when considering also thermal motions of the electrons in the frame of hot-plasma description. As shown later, however, most diagnostic applications can be sufficiently accurate within the cold-plasma approximation, thus strongly reducing the mathematical complexity.

Definition of the most important parameters

A plasma is a partially ionized gas of charged particles, which consists of "free" positive and negative charge carriers, in which the potential energy of a particle due to its nearest neighbor force is much smaller than its kinetic energy.

A ionized gas can be defined a plasma only if its characteristic dimension L is much larger than **Debye length**, i.e. $L \gg \Lambda_D$. The Debye length represents the

scalelength over which mobile charge carriers (e.g. electrons) screen out electric fields in ionized gas:

$$\Lambda_D = \sqrt{\frac{\epsilon_0 T_e}{n_e e^2}} \tag{2.1}$$

As a consequence of the screening of the electric fields, for scalelengths larger than Debye length, the plasma is quasi-neutral, i.e. the average ion charge density $< q > n_i$ is equal to the average electron charge density n_e. A plasma has a strong tendency to mantain this macroscopic charge neutrality. The **plasma frequency**

$$\omega_{pe} = \left(\frac{n_e e^2}{m_e \epsilon_0}\right) = 56.41 n_e^{1/2}, \quad f_{pe} = 8.97 n_e^{1/2} \quad \text{Hz} \tag{2.2}$$

is the frequency of the oscillations arising when charge neutrality is locally disturbed. ω_{pe} and Λ_D are related each other by:

$$\Lambda_D = \frac{v_{th}}{\sqrt{2}\omega_{pe}} \tag{2.3}$$

where

$$v_{th} = \left(\frac{2T_e}{m_e}\right)^{1/2} \tag{2.4}$$

is the electron thermal speed. Waves are considered with wavelengths λ much larger than the plasma Debye lenght Λ_D.

Most laboratory plasmas, such as MDIS and ECRIS plasmas, are immersed in static magnetic field. The gyration motion of charged particles introduces an addditional characteristic frequency and length, namely the cyclotron frequency and the **"thermal" Larmor radius**:

$$\omega_c = \frac{eB}{m_e}, \quad \rho_{th} = \frac{v_{th}}{\omega_c} \tag{2.5}$$

The fundamental parameters characterizing the plasmas generated in an Electron Cyclotron Resonance Ion Source are the **electron density** n_e (measured in cm^{-3} or m^{-3}), the **temperature** T of each species (usually measured in eV or keV), the ion **confinement time** τ_c and the external magnetic field B.

All the main characteristics of the plasma and of the extracted beam depend on these four parameters. The plasma response to high frequency waves depends sensitively on the ratio of the wave frequency to the plasma and cyclotron frequencies. It is therefore useful to note that in magnetically confined ECRIS plasmas, the plasma frequency and the cyclotron frequencies are typically of the same order of magnitude.

2.2 Propagation and absorption of electromagnetic waves in magnetized plasmas

Discussion of Cold-Plasma Dispersion Relations

For this treatment, **we will regard the plasma as a cold inhomogeneus anisotropic linear magnetofluid with an associated dielectric tensor permettivity**. We then derived a wave equation using Maxwell's Equations, assuming a harmonic solution to obtain a dispersion relation that describes all possible propagating wave modes consistent with our assumptions.

A complete analysis of the waves propagation in a magnetized plasma should take into account the effects of the wave on the different plasma particles. Wave and particles dynamics are in facts reciprocally influenced. If the thermal velocity of the particle is low with respect to the wave's phase velocity, i.e. $v_{th} \ll v_\phi$, v_{th} can be neglected. This approximation is called "cold plasma approximation": the electromagnetic waves propagate in the plasma with phase velocity of $10^7 - 10^8 m/s$, values much higher than the particles thermal velocity $(10^3 - 10^5 m/s)$, except for the restricted regions where the waves exhibit resonances; therefore, the cold plasma model is a useful approximation to determine the dispersion relation of the electromagnetic wave in a magnetized plasma.

Although the absorption is a kinetic effect that can only be determined by considering the behaviour of the plasma on a microscopic scale, the propagation properties are not strongly affected and can be mainly described in the frame of the cold plasma dispersion relation. In the following only the propagating electric field on electromagnetic wave will be considered. The module of magnetic force due to the influence of the magnetic field of the wave, in facts, is [39]:

$$F_m = \frac{v}{c}\sqrt{\epsilon_r}qE \tag{2.6}$$

Thus, for particles velocity $v << c$ the magnetic field of the wave can be neglected. This approximation is totally valid in the case of MDIS, whereas in ECRIS only a little part of hot electrons can reach relativistic energies, then being influenced by the magnetic field of the wave. For the scope of this section the magnetic effect can be neglected.

Electromagnetic waves in a cold-unmagnetized plasma

Derivation within Fluid Description

The cold-plasma dispersion relation can easily be obtained within the fluid plasma model in which all particle move coherently with velocity $\mathbf{v}$, and no individual thermal motions are taken into account. *When a magnetostatic field $\mathbf{B_0}$ is applied to a plasma, the plasma becomes electrically anisotropic for the electromagnetic waves*; that is the magnetic permeability remains that of the vacuum case μ_0, while the dielectric constant becomes a tensorial quantity $\bar{\bar{\epsilon}}$. In order to demonstrate this, we start writing the equation of motion for an electron under the effect of a monochoromatic electromagnetic field (negleting its magnetic field part) and a magnetostatic field $\mathbf{B_0}$:

$$m_e \frac{\partial \mathbf{v}}{\partial t} = q\mathbf{E} - m_e \mathbf{v}\omega_{eff} + q\mathbf{v} \times \mathbf{B_0} \tag{2.7}$$

Nonmagnetized plasma, $\mathbf{B_0} = 0$

In absence of a magnetic field, plasma is an isotropic medium. This means that the constitutive parameters assume the simple form of multiplicative constants. The fluid equation, in absence of magnetic field and in the cold plasma approximation is:

$$\frac{\partial \mathbf{v}}{\partial t} = q\mathbf{E} \tag{2.8}$$

Assuming that both electric field and velocity are varying in time as $e^{i\omega t}$, following the direction of the electric field, it can be easily shown that the dielectric constant is [39]:

$$\epsilon = \epsilon_0 \left(1 - \frac{\omega_p^2}{\omega^2}\right) \tag{2.9}$$

where ω_p is the plasma frequency and represents the natural oscillation frequency of an electron in a plasma (see section 2.1).

As ϵ is defined positive, from equation (2.9) it follows that:

$$\left(1 - \frac{\omega_p^2}{\omega^2}\right) \geq 0 \quad \rightarrow \quad \omega^2 > \omega_p^2 \tag{2.10}$$

this means that electromagnetic waves with frequencies lower than ω_p cannot propagate into the plasma. As a consequence in homogeneous and non magnetized plasmas the density cannot exceed the so called cutoff density given by:

$$n_{cutoff} = \frac{m\epsilon_0}{e^2}\omega^2 \tag{2.11}$$

An overdense (i.e. above the cutoff) plasma would totally reflect the incoming (feeding) wave, so that the plasma would automatically adjust its own density to

contemporary allow the maximum production with transparency for wave propagation. The cutoff density is consequently the main limitation of the plasmas generated by means of electromagnetic waves. Plasmas having a density larger than the cut-off density, i.e. $n_e > n_{cutoff}$, are usually named overdense. When this condition is not satisfied, i.e. $n_e < n_{cutoff}$, the plasma is named underdense. The dispersion relation for waves in unmagnetized plasma is [1]:

$$\omega^2 - \omega_p^2 = k^2 c^2 \tag{2.12}$$

For the dispersion relation $\mathbf{k}$ is imaginary whenever $\omega < \omega_p$, implying the total reflection of the incident radiation, as it has been deduced from equation (2.9).

The Dispersion Relation in Cold Magnetized Plasma

Since being tensorial the permittivity $\bar{\bar{\epsilon}}$, as the field propagation will depend on the direction of propagation of the wave with respect to the external magnetic field.

Let's assume, without losing in generality, $\mathbf{B}$ directed along the z axis, so that it can be written as $\mathbf{B} = B_0 \hat{z}$. It is possible to consider the plasma as a dielectric with internal current $\check{\mathbf{J}}$. In Maxwell's Equation it is necessary to express the plasma current density $\check{\mathbf{J}}$ in terms of the Electric field $\check{\mathbf{E}}$. This replacement makes use of a $\check{\mathbf{J}}$ as a displacement current in a dielectric medium and introduce a dielectric tensor.

As a consequence, by assuming harmonic fields with $e^{-i\omega t}$ dependence, Maxwell equations can be written as:

$$\boldsymbol{\nabla} \times \check{\mathbf{E}}(\mathbf{r}) = i\omega \check{\mathbf{B}}(\mathbf{r}) \tag{2.13}$$

$$\boldsymbol{\nabla} \times \check{\mathbf{H}}(\mathbf{r}) = -i\omega\epsilon_0 \check{\mathbf{E}}(\mathbf{r}) + \check{\mathbf{J}}(\mathbf{r}) = -i\omega\bar{\bar{\epsilon}} \cdot \check{\mathbf{E}} = -i\omega \check{\mathbf{D}}(\mathbf{r}) \tag{2.14}$$

$$\boldsymbol{\nabla} \cdot \check{\mathbf{D}}(\mathbf{r}) = \check{\rho}(\mathbf{r}) \tag{2.15}$$

$$\boldsymbol{\nabla} \cdot \check{\mathbf{B}}(\mathbf{r}) = 0 \tag{2.16}$$

if we use the constituive relations written in the following way:

$$\mathbf{J} = \bar{\bar{\sigma}}\mathbf{E} \tag{2.17}$$

$$\mathbf{D} = \frac{\mathbf{J}}{-i\omega} + \epsilon_0 \check{\mathbf{E}} = \left(\frac{\bar{\bar{\sigma}}}{-i\omega} + \epsilon_0\right)\check{\mathbf{E}} = \bar{\bar{\epsilon}}\check{\mathbf{E}} \tag{2.18}$$

$$\bar{\bar{\epsilon}} = \epsilon_0 \left(\bar{\bar{\mathbf{I}}} + \frac{i\bar{\bar{\sigma}}}{\omega\epsilon_0}\right) \tag{2.19}$$

then the effective dielectric constant of the plasma is the tensor $\bar{\bar{\epsilon}}$ and $\mathbf{J}$ represents electrons-field interaction in Maxwell's equation. Skipping mathematical derivations, [36] the **relation dispersion** $\epsilon(\omega,\mathbf{k})=0$ for electromagnetic waves in plasmas reads as:

$$\left(S \sin^2 \theta + P \cos^2 \theta\right) N^4 + \left(RL \sin^2 \theta + SP(1 + \cos^2 \theta)\right) N^2 + PRL = 0 \qquad (2.20)$$

where, for sake of simplicity, we defined $R = S + D$ and $L = S - D$. Equation (2.20) contains all the information about the propagation of the waves in "cold" magnetized plasma. It has two solutions:

$$N_{O,X}^2(\theta) = 1 - \frac{2X(1 - X)}{2(1 - X) - Y^2 \sin^2 \theta \pm \sqrt{Y^4 \sin^4 \theta + 4Y^2(1 - X)^2 \cos^2 \theta}} \qquad (2.21)$$

that is the Appleton-Hartree cold plasma dispersion relation. Hence for a given arbitrary direction, defined by θ, we have two waves characterized by different index of refraction. $N^o(\theta)$ is called **ordinary wave**, whereas $N^x(\theta)$ is named **extraordinary wave**. Here we have introduced two important parameters, X and Y, which will be very useful to simplify the mathematical notation:

$$X = \frac{\omega_p^2}{\omega^2} \propto n_e \qquad Y = \frac{\omega_c}{\omega} \propto B_0 \qquad (2.22)$$

X is the parametric electron density, proportional to n_e, whereas Y is the parametric magnetic field, proportional to B_0.

Ordinary and Extraordinary modes

Two fundamental electromagnetic modes can be distinguished [40], according to the wave polarization with respect to the orientation of the background magnetic field. The essential features of the propagation can be most easily understood by analysing two particular cases of propagation: parallel ($\mathbf{k} \parallel \mathbf{B}_0$) and perpendicular ($\mathbf{k} \perp \mathbf{B}_0$) to the background magnetic field direction. In this limit two different modes for each case can be discussed independently.

By means of equation (2.21) it is possible to determine the wave's propagation properties as a function of the angle θ, of the electron density n_e and of the magnetic field B_0.

Particularly important is to determine when the refractive index goes to zero (cutoff condition) or tends to infinite (resonance condition). The classification described above follows the scheme shown in Figs. 2.1 and 2.2.

The various ways in which electromagnetic waves can be injected into a column of magnetized plasma are shown in Fig. 2.3.

In Table 2.1, cutoffs and resonances of the waves propagating inside the plasma have been resumed. Furthermore, from Table 2.1 it can be seen that the R wave suffers the resonance reported before (i.e. the ECR resonance), as its index of refraction goes

Electromagnetic waves in plasmas

Possible EM to ES wave conversions
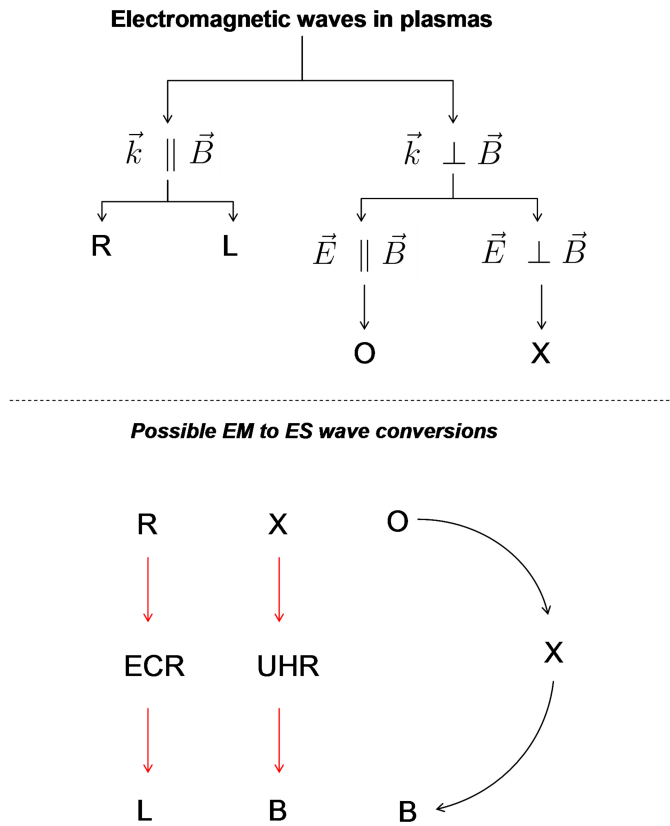
Fig. 2.1. Scheme of the wave propagation in anisotropic plasmas.
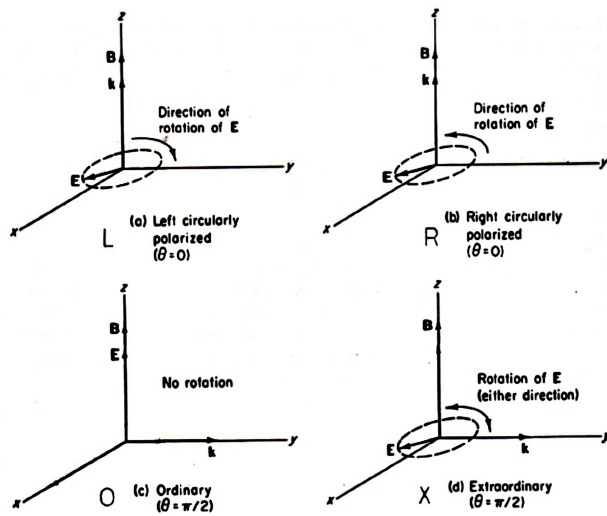
Fig. 2.2. Diagram showing the possible orientations of the electric field with respect to the magnetostatic field, and also the possible polarizations in waves propagating in magnetized plasmas.
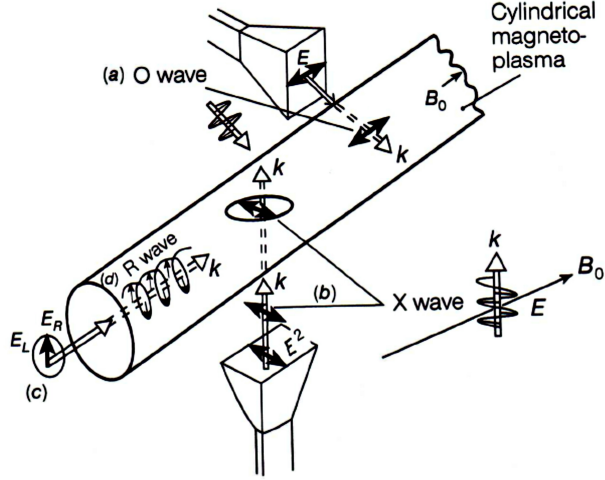
Fig. 2.3. Schematic representation of the possible ways to inject electromagnetic waves into a column of a magnetized plasma. The different modes can be excited, according to the location of the waveguide providing the electromagnetic field, and also according to the wave polarization inside the waveguide.

Table 2.1. Cutoffs and resonances of the waves propagating inside the plasma [2].

Vector orientation	Refractive index	Wave type
$\mathbf{B}_0 = 0$	$\omega^2 = \omega_p^2 + k^2 c^2$	Light waves
$\mathbf{k} \perp \mathbf{B}_0, \ \mathbf{E} \parallel \mathbf{B}_0$	$\dfrac{c^2 k^2}{\omega^2} = 1 - \dfrac{\omega_p^2}{\omega^2}$	O wave
$\mathbf{k} \perp \mathbf{B}_0, \ \mathbf{E} \perp \mathbf{B}_0$	$\dfrac{c^2 k^2}{\omega^2} = 1 - \dfrac{\omega_p^2}{\omega^2} \dfrac{\omega^2 - \omega_p^2}{\omega^2 - \omega_h^2}$	X wave
$\mathbf{k} \parallel \mathbf{B}_0$	$\dfrac{c^2 k^2}{\omega^2} = 1 - \dfrac{\omega_p^2/\omega^2}{1 - (\omega_c/\omega)}$	R wave
$\mathbf{k} \parallel \mathbf{B}_0$	$\dfrac{c^2 k^2}{\omega^2} = 1 - \dfrac{\omega_p^2/\omega^2}{1 + (\omega_c/\omega)}$	L wave

to infinity when $\omega \to \omega_c$. Also the X mode has a resonance, but at the upper hybrid frequency. Thus, inside a magnetized plasma, where an X mode is travelling, the so-called *upper hybrid resonance* (UHR) occurs if

$$\omega^2 = \omega_p^2 + \omega_c^2 = \omega_h^2. \tag{2.23}$$

The L wave does not suffer any resonance, as well as the O mode. Instead, they suffer a cutoff that can be determined by the equations reported in Table 2.1 when the index of refraction, i.e. $c^2 k^2/\omega^2$, goes to zero. A powerful method to visualize

the cutoffs and the resonances of the various modes is to plot them on a so-called Clemmow–Mullaly–Allis (CMA) diagram.[1] This diagram is reported in Fig. 2.4.

The CMA diagram can be viewed as a plot of ω_c/ω versus ω_p^2/ω^2, or equivalently a plot of the magnetic field versus the plasma density. For a given frequency ω, any experimental situation characterized by ω_c (i.e. the magnetic field) and by ω_p (i.e. the plasma density) is denoted by a point on the graph. The total plane is divided into several zones, and the boundaries of each zone are the cutoffs and the resonances mentioned above. For example, the upper hybrid resonance can be easily found in the graph. Considering an X wave propagating from a region with high magnetic field, inside a plasma with a fixed value of density (e.g. $\omega_p^2/\omega^2 = 0.7$), the value of the magnetic field where the UHR occurs can be easily determined on the graph.
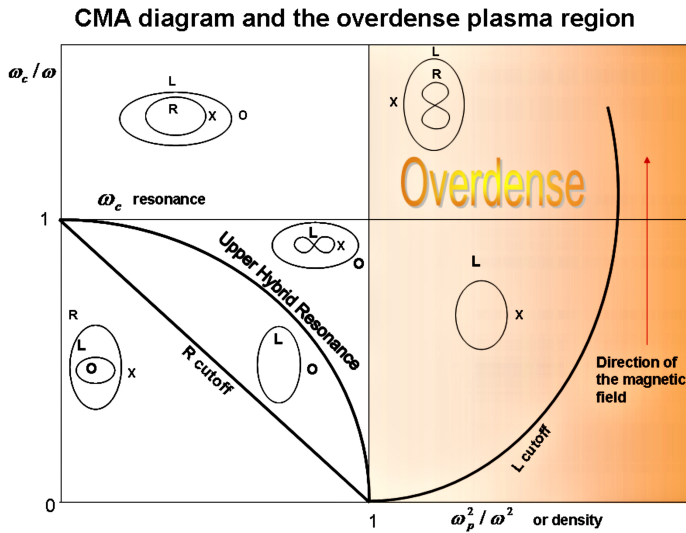
Fig. 2.4. A detailed view of the Clemmow–Mullaly–Allis diagram showing the region of the so-called overdense plasma, i.e. that region where the plasma density exceeds the cutoff of the ordinary (O) mode.

The vertical line at $\omega_p^2/\omega^2 = 1$ is the so-called O cutoff, and it corresponds to the cutoff density in an unmagnetized plasma. Above this value, the plasma will be called *overdense*, as shown in Fig. 2.4. The small diagrams in each region delimited by the cutoffs and the resonances (i.e. the ellipsoidal small diagrams) indicate not only which wave propagates, but also the qualitative variation of the phase velocity with the angle (considering that the magnetic field is directed along the vertical direction).

---

[1] The CMA diagram takes its name from the three authors who proposed the graphical representation of the many cutoffs and resonances of electromagnetic waves propagating in a cold plasma.

The ECR resonance

Because of their polarization, electric field of the R wave rotates in the same direction and versus of the gyrating electrons in a magnetic field. When the frequency of the injected microwave ω_{RF} matches the cyclotron frequency ω_c, then electrons see a constant field leading to resonant energy absorption. If the electrons gain enough energy, they are able to ionize the neutrals of the nascent plasma. It is really important to note that in a collisionless plasma, the ECR is the only physical mechanism allowing the direct energy transfer from electromagnetic wave to electrons. The mechanism of the resonant electron acceleration can be easily demonstrated by looking to the solution of the equation of motion (2.7) for an harmonic electromagnetic field in a magnetized plasma acting on a free electron:

$$\begin{cases} v_x = \dfrac{e}{m}\dfrac{-i\omega E_x + \omega_c E_{E_y}}{\omega_c^2 - \omega^2} \\[3mm] v_y = \dfrac{e}{m}\dfrac{-i\omega E_y + \omega_x E_x}{\omega_c^2 - \omega^2} \\[3mm] v_z = \dfrac{eE_z}{-im\omega} \end{cases} \tag{2.24}$$

Electron velocity and kinetic energy goes to infinity only when $\omega_c \to \omega$, that is the ECR. ECR heating, is actually the most powerful method to generate and sustain a plasma. In other plasma resonances, in facts, the electromagnetic energy is not directly transferred to electrons, but indeed to plasma oscillation modes that, only in a second time, can transfer their energy to electrons by means of collisions or non-linear effects.

2.3 "Cold" approximation in a "minimum–B" magnetic field configuration

The numerical approach to solve the 3D Maxwell-Lorentz system with the aim of investigating the interaction of the electromagnetic waves with the magnetized non-homogeneous plasma produced inside Electron Cyclotron Resonance Ion Sources, described in the Chapter 4, has to consider the actual magneto-static structure of an ECRIS (minimum-B configuration, $B_{x,y,z}$ components) that is not uniform nor axis-symmetric (see Figure 2.5). The dielectric tensor $\bar{\bar{\epsilon}}_r$ depends in a complex way from the magnetostatic field $B_0(r)$ and the local electron density $n_e(x,y,z)$, (details in chapter 4).

The mathematical formulation to derive $\bar{\bar{\epsilon}}_r$ is developed hereinafter, starting from the equation of motion for single particle is:
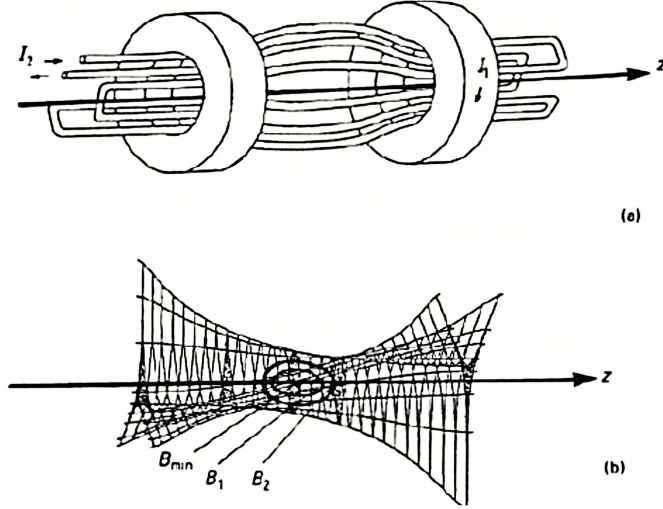
Fig. 2.5. Magnetic system (a) and magnetic field structure obtained by the superposition of the field produced by two solenoids and an hexapole (minimum-B field) (b).

$$m\frac{\partial \mathbf{v}}{\partial t} = q\left(\mathbf{E} + \mathbf{v} \times \mathbf{B_0}\right) - \omega_{\text{eff}} m\mathbf{v} \tag{2.25}$$

Assuming the electric field time-harmonic $\mathbf{E} = \mathbf{E_0}e^{-i\omega t}$, the stationary solution for the velocity willl be harmonic too $\mathbf{v} = \mathbf{v_0}e^{-i\omega t}$. Substituting it in eq. (2.25) we obtain:

$$m(-i\omega\check{\mathbf{v}}) = q\left(\check{\mathbf{E}} + \check{\mathbf{v}} \times \mathbf{B_0}\right) - \omega_{\text{eff}} m\check{\mathbf{v}} \tag{2.26}$$

$$(-i\omega + \omega_{\text{eff}})\check{\mathbf{v}} + \frac{q}{m}\mathbf{B_0} \times \check{\mathbf{v}} = \frac{q}{m}\check{\mathbf{E}} \tag{2.27}$$

Magnetic field $\mathbf{B_0}$ is a position dependent vector with 3 component:

$$\mathbf{B_0}(x,y,z) = B_{0x}(x,y,z)\hat{\mathbf{u}}_x + B_{0y}(x,y,z)\hat{\mathbf{u}}_y + B_{0z}(x,y,z)\hat{\mathbf{u}}_z \tag{2.28}$$

We have to compute the cross product $\mathbf{B_0} \times \check{\mathbf{v}} = (B_{0x}\hat{\mathbf{u}}_x + B_{0y}\hat{\mathbf{u}}_y + B_{0z}\hat{\mathbf{u}}_z) \times (v_x\hat{\mathbf{u}}_x + v_y\hat{\mathbf{u}}_y + v_z\hat{\mathbf{u}}_z)$

The matricial cross product reads as:

$$\mathbf{B_0} \times \check{\mathbf{v}} = [B_0]_\times \check{\mathbf{v}} = \begin{bmatrix} 0 & -B_{0z} & B_{0y} \\ B_{0z} & 0 & -B_{0x} \\ -B_{0y} & B_{0x} & 0 \end{bmatrix} \begin{bmatrix} v_x \\ v_y \\ v_z \end{bmatrix} \tag{2.29}$$

The equation (2.27) can be written mixing matrix and vectors with an abuse of notation:

$$(-i\omega + \omega_{\text{eff}})\check{\mathbf{v}} + \frac{q}{m}\begin{bmatrix} 0 & -B_{0z} & B_{0y} \\ B_{0z} & 0 & -B_{0x} \\ -B_{0y} & B_{0x} & 0 \end{bmatrix}\check{\mathbf{v}} = \frac{q}{m}\check{\mathbf{E}} \tag{2.30}$$

$$
\underbrace{\begin{bmatrix} -\mathrm{i}\omega + \omega_{\text{eff}} & -B_{0z}\frac{q}{m} & B_{0y}\frac{q}{m} \\ B_{0z}\frac{q}{m} & -\mathrm{i}\omega + \omega_{\text{eff}} & -B_{0x}\frac{q}{m} \\ -B_{0y}\frac{q}{m} & B_{0x}\frac{q}{m} & -\mathrm{i}\omega + \omega_{\text{eff}} \end{bmatrix}}_{\overline{\overline{\mathbf{T}}}} \begin{bmatrix} v_x \\ v_y \\ v_z \end{bmatrix} = \frac{q}{m} \begin{bmatrix} E_x \\ E_y \\ E_z \end{bmatrix} \tag{2.31}
$$

We place:

$$
\overline{\overline{\mathbf{T}}} = \begin{bmatrix} -\mathrm{i}\omega + \omega_{\text{eff}} & -B_{0z}\frac{q}{m} & B_{0y}\frac{q}{m} \\ B_{0z}\frac{q}{m} & -\mathrm{i}\omega + \omega_{\text{eff}} & -B_{0x}\frac{q}{m} \\ -B_{0y}\frac{q}{m} & B_{0x}\frac{q}{m} & -\mathrm{i}\omega + \omega_{\text{eff}} \end{bmatrix} \tag{2.32}
$$

to finally obtain a very compact form of equation (2.27) inmatrix format:

$$
\overline{\overline{\mathbf{T}}} \cdot \check{\mathbf{v}} = \frac{q\check{\mathbf{E}}}{m} \tag{2.33}
$$

which it can be easily inverted:

$$
\check{\mathbf{v}} = \frac{q}{m}\overline{\overline{\mathbf{T}}}^{-1} \cdot \check{\mathbf{E}} \tag{2.34}
$$

$$
\det(\overline{\overline{\mathbf{T}}}) = \Delta = (-\mathrm{i}\omega + \omega_{\text{eff}})[(-\mathrm{i}\omega + \omega_{\text{eff}})^2 + B_{0x}^2(\frac{q}{m})^2] + B_{0z}\frac{q}{m}[B_{0z}\frac{q}{m}(-\mathrm{i}\omega + \omega_{\text{eff}}) - B_{0x}B_{0y}(\frac{q}{m})^2]
$$
$$
+ B_{0y}\frac{q}{m}[B_{0y}\frac{q}{m}(-\mathrm{i}\omega + \omega_{\text{eff}}) + B_{0x}B_{0z}(\frac{q}{m})^2]
$$

$$\tag{2.35}$$

$$
\overline{\overline{\mathbf{T}}}^{-1} = \begin{bmatrix} \frac{(-\mathrm{i}\omega + \omega_{\text{eff}})^2 + B_{0x}^2(\frac{q}{m})^2}{\Delta} & \frac{B_{0z}\frac{q}{m}(-\mathrm{i}\omega + \omega_{\text{eff}}) + B_{0x}B_{0y}(\frac{q}{m})^2}{\Delta} & \frac{-B_{0y}\frac{q}{m}(-\mathrm{i}\omega + \omega_{\text{eff}}) + B_{0x}B_{0z}(\frac{q}{m})^2}{\Delta} \\ \frac{-B_{0z}\frac{q}{m}(-\mathrm{i}\omega + \omega_{\text{eff}}) + B_{0x}B_{0y}(\frac{q}{m})^2}{\Delta} & \frac{(-\mathrm{i}\omega + \omega_{\text{eff}})^2 + B_{0y}^2(\frac{q}{m})^2}{\Delta} & \frac{B_{0x}\frac{q}{m}(-\mathrm{i}\omega + \omega_{\text{eff}}) + B_{0y}B_{0z}(\frac{q}{m})^2}{\Delta} \\ \frac{B_{0y}\frac{q}{m}(-\mathrm{i}\omega + \omega_{\text{eff}}) + B_{0x}B_{0z}(\frac{q}{m})^2}{\Delta} & \frac{-B_{0x}\frac{q}{m}(-\mathrm{i}\omega + \omega_{\text{eff}}) + B_{0z}B_{0y}(\frac{q}{m})^2}{\Delta} & \frac{(-\mathrm{i}\omega + \omega_{\text{eff}})^2 + B_{0z}^2(\frac{q}{m})^2}{\Delta} \end{bmatrix} \tag{2.36}
$$

Using the inverted matrix $\overline{\overline{\mathbf{T}}}^{-1}$, it can be founded the solution $\mathbf{v}$ and the related current density $\mathbf{J}$ can be written:

$$
\check{\mathbf{J}} = n_0 q\check{\mathbf{v}} = \frac{n_0 q^2}{m}\overline{\overline{\mathbf{T}}}^{-1} \cdot \check{\mathbf{E}} = \epsilon_0 \omega_p^2 \overline{\overline{\mathbf{T}}}^{-1} \cdot \check{\mathbf{E}} \tag{2.37}
$$

Substituting the current density in Maxwell equation we obtain:

$$
\boldsymbol{\nabla} \times \check{\mathbf{H}} = -\mathrm{i}\omega\epsilon_0\check{\mathbf{E}} + \check{\mathbf{J}} = -\mathrm{i}\omega\epsilon_0\check{\mathbf{E}} + \epsilon_0\omega_p^2\overline{\overline{\mathbf{T}}}^{-1} \cdot \check{\mathbf{E}} = -\mathrm{i}\omega\epsilon_0 \underbrace{\left(\overline{\overline{\mathbf{I}}} - \frac{\omega_p^2\overline{\overline{\mathbf{T}}}^{-1}}{\mathrm{i}\omega} \right)}_{\overline{\overline{\epsilon}}_r} \cdot \check{\mathbf{E}} \tag{2.38}
$$

where we can place:

$$\bar{\bar{\epsilon}} = \epsilon_0 \bar{\bar{\epsilon}}_r = \epsilon_0 \left(\bar{\bar{\mathbf{I}}} + \frac{\mathrm{i}\bar{\bar{\sigma}}}{\omega \epsilon_0} \right) = \epsilon_0 \left(\bar{\bar{\mathbf{I}}} + \frac{\mathrm{i}\omega_p^2 \bar{\bar{\mathbf{T}}}^{-1}}{\omega} \right) =$$

$$\epsilon_0 \begin{bmatrix} 1 + \frac{\mathrm{i}\omega_p^2}{\omega} \frac{(-\mathrm{i}\omega+\omega_{\mathrm{eff}})^2 + B_{0x}^2 (\frac{q}{m})^2}{\Delta} & \frac{\mathrm{i}\omega_p^2}{\omega} \frac{B_{0z} \frac{q}{m}(-\mathrm{i}\omega+\omega_{\mathrm{eff}}) + B_{0x} B_{0y}(\frac{q}{m})^2}{\Delta} & \frac{\mathrm{i}\omega_p^2}{\omega} \frac{-B_{0y} \frac{q}{m}(-\mathrm{i}\omega+\omega_{\mathrm{eff}}) + B_{0x} B_{0z}(\frac{q}{m})^2}{\Delta} \\ \frac{\mathrm{i}\omega_p^2}{\omega} \frac{-B_{0z} \frac{q}{m}(-\mathrm{i}\omega+\omega_{\mathrm{eff}}) + B_{0x} B_{0y}(\frac{q}{m})^2}{\Delta} & 1 + \frac{\mathrm{i}\omega_p^2}{\omega} \frac{(-\mathrm{i}\omega+\omega_{\mathrm{eff}})^2 + B_{0y}^2 (\frac{q}{m})^2}{\Delta} & \frac{\mathrm{i}\omega_p^2}{\omega} \frac{B_{0x} \frac{q}{m}(-\mathrm{i}\omega+\omega_{\mathrm{eff}}) + B_{0y} B_{0z}(\frac{q}{m})^2}{\Delta} \\ \frac{\mathrm{i}\omega_p^2}{\omega} \frac{B_{0y} \frac{q}{m}(-\mathrm{i}\omega+\omega_{\mathrm{eff}}) + B_{0x} B_{0z}(\frac{q}{m})^2}{\Delta} & \frac{\mathrm{i}\omega_p^2}{\omega} \frac{-B_{0x} \frac{q}{m}(-\mathrm{i}\omega+\omega_{\mathrm{eff}}) + B_{0z} B_{0y}(\frac{q}{m})^2}{\Delta} & 1 + \frac{\mathrm{i}\omega_p^2}{\omega} \frac{(-\mathrm{i}\omega+\omega_{\mathrm{eff}})^2 + B_{0z}^2 (\frac{q}{m})^2}{\Delta} \end{bmatrix}$$

The complex tensor components represent, in general, losses in the medium. The anti-Hermitian part is of special importance for the calculation of the absorption of electromagnetic wave energy by the plasma.

In this case, we finally found the wave equation that it will be numerically solved in Chapter 4 :

$$\nabla \times \nabla \times \mathbf{E} = \omega^2 \epsilon_0 \mu \bar{\bar{\epsilon}} \cdot \mathbf{E} \tag{2.39}$$

assuming that $\mathbf{E}$ vay as $e^{[\mathrm{i}(\mathbf{k}\cdot\mathbf{r}-\omega t)]}$ it becomes:

$$\mathbf{k} \times \mathbf{k} \times \mathbf{E} + \omega^2 \mu \bar{\bar{\epsilon}} \mathbf{E} = 0 \tag{2.40}$$

2.4 Collisional absorption

In ECRIS, the collision frequency is low and the collisional effects can be neglected. In other types of ion sources, working at higher neutral pressure and lower electron temperature, like MDIS a new plasma heating mechanism must be taken into account, called **collisional absorption**. The issue of RF power absorption in plasmas is of paramount importance, implying the way the energy is released to the different electrons populations. The simplest model describing wave-to-plasma energy exchange assumes a frictional interaction among the plasma electrons. This assumption is valid for MDIS (low temperature – high density plasmas) but hardly applicable to ECRIS (high temperature plasmas), where electrons can be considered almost collisionless. Due to the complexity of the stochastic heating description in the frame of cold plasma approximation, we will limit the treatment to collisional damping, stating that only the terms in the imaginary part of the dielectric tensor are eventually affected by the stochastic effects. These do not change the form of the equations, but eventually only the damping/heating rates.

How it is evident, collisions play the role of a frictional term. From the equation of motion, it is then possible to write the dispersion relation in presence of collisions, which represents the generalization of equation (2.21):

$$N_{o,x}^2(\theta) = 1 - \frac{2X(1 + iZ - X)}{2(1 + iZ)(1 - X) - Y^2 \sin^2 \theta \pm \Gamma} \tag{2.41}$$

Γ being:

$$\sqrt{Y^4 \sin^4 \theta + 4Y^2(1 + iZ - X)^2 \cos^2 \theta} \qquad (2.42)$$

Where Z is:

$$Z = \frac{\omega_{eff}}{\omega} \qquad (2.43)$$

The imaginary term in equation (2.41) indicates the presence of an absorption term in the dispersion relation and it will be used in chapter 4 to model the microwave absorption by plasma electrons and, at the same time, to solve the singularity due to the resonance of the wave solution. To clarify this aspect, it is sufficient to remember that in a plasma the electric field is carried by the oscillating electrons. If electrons do not collide during oscillation, the wave is transmitted, but if a collision occurs, part of the wave energy is transferred to the medium, thus damping the wave. Collisions limit also the energies achievable in ECR heating: in facts for each collision occurring during acceleration, the electron loses part of its own energy. Hereinafter we will limit our consideration to slightly collisional plasmas, like the ones generated by MDIS and ECRIS sources (ν_{ee} lies between 10^5 and $10^6 Hz$) and then $Z = 1 \cdot 10^{-3} \div 1 \cdot 10^{-4}$.

2.5 Waves in warm plasma

This section aims to introduce *plasma spacecharge* waves of the "warm" plasma approximation. These "warm approximation" solutions waves are commonly referred as "plasma oscillations" [41]: they are longitudinal, analogous to sound waves in unionized gas, and, in presence of magnetic field or density gradient, may couple to electromagnetic waves, as simulation and experimental evaluation will show in the following chapters.

The preceding sections have assumed a cold plasma in which electron thermal motion could be neglected. In "cold" plasma approximation we neglect the effects which depend explicitely on electron temperature. Nevertheless it cannot be assumed that the electron thermal velocity is zero. Therefore the term **"temperate"** should be perhaps more appropriate than "cold". Even in a cold plasma, however, the electron velocity must be greater than the velocity increment produced by the electromagnetic field if the presence of the wave does not modify the distribution function significantly. In recognition of this lower bound on velocity, the term "temperate plasma" has been used [42]. In a sense, however, this is more an upper bound on the electric field than a lower bound on thermal velocity. In literature it is possible to find this approximation termed as "hot" which it is better to reserve for the relativistic case. We shall use the

term "warm" to designate the case in which the temperature is considered explicitly but for which non relativistic case is still appropiate.

In the following sections, the influence of the finite temperature on the plasma dielectric properties is evaluated also in order to validate the cold approximation done in the modeling treatment of chapter 4. Finite temperature corrections can be introduced to study the transition from the cold-plasma description to the one that considers temperature effects to first order [43].

The most realistic from the simplified models is kinetic theory, based on Vlasov's equation for a Collisionless Plasma for the particle distribution function $f(\mathbf{r}, \mathbf{p}, t)$,

$$\frac{\partial f}{\partial t} + \mathbf{v} \cdot \frac{\partial f}{\partial \mathbf{r}} + q(\mathbf{E} - \mathbf{v} \times \mathbf{B}) \cdot \frac{\partial f}{\partial \mathbf{p}} = 0 \tag{2.44}$$

which together with Maxwell's equation and the definitions for space charge and plasma current:

$$\rho = e \int d^3\mathbf{v}\, f(\mathbf{r}, \mathbf{p}, t)$$

$$\mathbf{J} = e \int d^3\mathbf{v}\, \mathbf{v} f(\mathbf{r}, \mathbf{p}, t)$$

form a complete set of equation describing collisionless plasmas.

Maxwell's equation yield:

$$\nabla \times \check{\mathbf{E}}(\mathbf{r}) = \mathrm{i}\omega \check{\mathbf{B}}(\mathbf{r}) \tag{2.45}$$

$$\nabla \times \check{\mathbf{H}}(\mathbf{r}) = -\mathrm{i}\omega\epsilon_0 \check{\mathbf{E}}(\mathbf{r}) + e \int d^3\mathbf{v}\, \mathbf{v} f(\mathbf{r}, \mathbf{p}, t) = -\mathrm{i}\omega \bar{\bar{\epsilon}} \cdot \check{\mathbf{E}} \tag{2.46}$$

$$\nabla \cdot \check{\mathbf{D}}(\mathbf{r}) = e \int d^3\mathbf{v}\, f(\mathbf{r}, \mathbf{p}, t) \tag{2.47}$$

$$\nabla \cdot \check{\mathbf{B}}(\mathbf{r}) = 0 \tag{2.48}$$

Let:

$f(\mathbf{r}, \mathbf{p}, t) = f_0(\mathbf{r}, \mathbf{p}) + f_1(\mathbf{r}, \mathbf{p}, t)$

$\mathbf{B} = \mathbf{B}_0 + \mathbf{B}_1$

$\mathbf{E} = \mathbf{E}_0 + \mathbf{E}_1 = \mathbf{E}_1$

f_1 is the perturbed distribution function, and f_0 the equilibrium distribution function, and $f_1, \mathbf{B}_1, \mathbf{E}_1$ are dependent of $e^{\mathrm{i}(\mathbf{k}\cdot\mathbf{r}-\omega t)}$.

Linearizing Vlasov equation and after a great deal of rather tedious analysis, Eqs. reduce to the following expression for the dielectric permettivity tensor:

$$\frac{\bar{\bar{\epsilon}}}{\epsilon_0} = \bar{\bar{\mathbf{I}}} + \frac{\omega_p^2}{\omega^2} \sum_{l=-\infty}^{\infty} \int \frac{d^3p \frac{1}{\gamma p} \frac{\partial f_0}{\partial p}}{\omega - k_{\parallel} v_{\parallel} - \frac{l\omega_c}{\gamma}} \begin{bmatrix} \frac{l^2}{b^2} J_l^2 p_{\perp}^2 & \mathrm{i}\frac{l}{b} J_l J_l' p_{\perp}^2 & \frac{l}{b} J_l^2 p_{\perp}^2 p_{\parallel} \\ -\mathrm{i}\frac{l}{b} J_l J_l' p_{\perp}^2 & (J_l')^2 p_{\perp}^2 & -\mathrm{i} J_l J_l' p_{\perp} p_{\parallel} \\ \frac{l}{b} J_l^2 p_{\perp}^2 p_{\parallel} & \mathrm{i} J_l J_l' p_{\perp} p_{\parallel} & (J_l')^2 p_{\parallel}^2 \end{bmatrix} \tag{2.49}$$

where f_0 is the equilibrium distribution function, $J_l(b)$ the Bessel function of order l and argument $b = \left(\dfrac{k_\perp p_\perp}{m_e \omega_g}\right)^2 = \left(\dfrac{k_\perp v_{T_\perp}}{\omega_g}\right)^2$.

When the plasma is bi-Maxwellian:

$$f_0(v_\perp, v_z) = n_e F_\perp(v_\perp) F_z(v_z)$$

$$F_\perp(v_\perp) = \frac{m}{2\pi\kappa T_\perp} e^{\left(-\frac{mv_\perp^2}{2\kappa T_\perp}\right)}$$

$$F_z(v_z) = \left(\frac{m}{2\pi\kappa T_z}\right)^{\frac{1}{2}} e^{\left(-\frac{m(v_z - V)}{2\kappa T_z}\right)}$$

The dielectric tensor is given by:

$$\frac{\overline{\overline{\epsilon}}}{\epsilon_0} = \overline{\overline{\mathbf{I}}} + \frac{\omega_p^2}{\omega^2}\left[\sum_{l=-\infty}^{+\infty}\left(\xi_0 Z(\xi_l) - \left(1 - \frac{1}{\lambda_T}\right)(1 + \xi_l Z(\xi_l))\right)e^{-b}\overline{\overline{\mathbf{X}}}_l + 2\eta_0^2\lambda_T\overline{\overline{\mathbf{L}}}\right] \quad (2.50)$$

where:

$$\overline{\overline{\mathbf{X}}}_l = \begin{bmatrix} \frac{l^2}{b}I_l & il(I_l' - I_l) & -(2\lambda_T)^{\frac{1}{2}}\eta_l\frac{l}{\alpha}I_l \\ -il(I_l' - I_l) & (\frac{l^2}{b} + 2b)I_l - 2bI_l' & i(2\lambda_T)^{\frac{1}{2}}\eta_l\alpha(I_l' - I_l) \\ -(2\lambda_T)^{\frac{1}{2}}\eta_l\frac{l}{\alpha}I_l & -i(2\lambda_T)^{\frac{1}{2}}\eta_l\alpha(I_l' - I_l) & (2\lambda_T)\eta_l^2 I_l \end{bmatrix} \quad (2.51)$$

$$Z(\xi) = \frac{1}{\sqrt{\pi}}\int_{-\infty}^{+\infty}\frac{e^{-\beta^2}}{\beta - \xi}d\beta \quad \text{is the plasma dispersion function}$$

$I_l(b)$ is the l_{th} modified Bessel function and the remaining parameters are:

$$\eta_l = \frac{\omega_{RF} + l\omega_g}{\sqrt{2}k_z v_{T_z}}, \qquad \xi_n = \frac{\omega - k_z V + l\omega_g}{\sqrt{2}k_z v_{T_z}},$$

$$\lambda_T = \frac{T_z}{T_\perp}, \qquad b = \left(\frac{k_\perp v_{T_\perp}}{\omega_g}\right)^2, \qquad \alpha = \frac{k_\perp v_{T_\perp}}{\omega_g},$$

$$v_{T_z}^2 = \frac{\kappa T_z}{m}, \qquad v_{T_\perp}^2 = \frac{\kappa T_\perp}{m}$$

The component of $\overline{\overline{\mathbf{L}}}$ matrix are zero except $L_{zz}=1$.

If we consider an isotropic Maxwellian plasma $(T_z = T_\perp)$ for which the solutions are well known and zero order electron drift velocity $V=0$ and $f_0 = n_e\left(\dfrac{m}{2\pi\kappa T}\right)^{\frac{3}{2}}e^{(-\frac{mv^2}{\kappa T})}$, the dielectric tensor reduces to:

$$\frac{\overline{\overline{\epsilon}}}{\epsilon_0} = \overline{\overline{\mathbf{I}}} + \frac{\omega_p^2}{\omega_{RF}^2}\left[\sum_{l=-\infty}^{+\infty}\xi_0 Z(\xi_l)e^{-b}\overline{\overline{\mathbf{X}}}_l + 2\xi_0^2\overline{\overline{\mathbf{L}}}\right] \quad (2.52)$$

The dielectric tensor at ECR Heating (or Damping) Rates

We only consider the fundamental electron cyclotron resonance, since the higher order resonances are typically at magnetic fields strengths smaller than minimum field in the ECRIS.

So we study plasma heating at ω_c but not at the harmonics of this frequency, so that the limit of zero Larmor radius ρ_{ω_g} is considered.

In the case of taking first order in the temperature from hot plasma Dispersion Relation $b = (k_\perp \rho_{\omega_g})^2 \ll 1$, ($\rho_{\omega_g} = \frac{v_{T_\perp}}{\omega_g}$ is Larmor radius), it is possible to expand $e^{-b}\overline{\overline{\mathbf{X}}}_l$ by b and including only terms up to the first harmonic.

The dielectric tensor ϵ_{ij} components for $\omega_{RF} \gg \omega_{pi}, \omega_{g_i}$ (considering only electrons), $\omega_{RF} \sim \omega_g$ and for large argument expansion of $Z(\xi_l)$ for $l \neq -1$ is:

$$\epsilon_{xx} = \epsilon_{yy} = 1 + \frac{\omega_p^2}{\omega_{RF}^2}\left(\frac{\omega_{RF}}{\sqrt{2}k_z v_{T_z}}\right)\frac{1}{2}Z\left(\frac{\omega_{RF} - \omega_g}{\sqrt{2}k_z v_{T_z}}\right) - \frac{\omega_p^2}{2\omega_{RF}(\omega_{RF} + \omega_g)}$$

$$\epsilon_{zz} = 1 - \frac{\omega_p^2}{\omega_{RF}^2} + \left(\frac{k_\perp c}{\omega_{RF}}\right)^2\left(\frac{\omega_p}{\omega_g}\right)^2\left(\frac{v_T}{c}\right)^2\left(\frac{\omega_{RF}}{\sqrt{2}k_z v_{T_z}}\right)\left(\frac{\omega_{RF} - \omega_g}{\sqrt{2}k_z v_{T_z}}\right)\left[1 + \left(\frac{\omega_{RF} - \omega_g}{\sqrt{2}k_z v_{T_z}}\right)Z\left(\frac{\omega_{RF} - \omega_g}{\sqrt{2}k_z v_{T_z}}\right)\right]$$

$$\epsilon_{xy} = -\epsilon_{yx} = -\mathrm{i}\frac{\omega_p^2}{\omega_{RF}^2}\left(\frac{\omega_{RF}}{\sqrt{2}k_z v_{T_z}}\right)\frac{1}{2}Z\left(\frac{\omega_{RF} - \omega_g}{\sqrt{2}k_z v_{T_z}}\right) - \mathrm{i}\frac{\omega_p^2}{2\omega_{RF}(\omega_{RF} + \omega_g)}$$

$$\epsilon_{xz} = \epsilon_{zx} = \left(\frac{k_\perp c}{\omega_{RF}}\right)\frac{1}{\sqrt{2}}\frac{\omega_p^2}{\omega_{RF}^2}\left(\frac{\omega_p}{\omega_g}\right)\left(\frac{v_T}{c}\right)\left(\frac{\omega_{RF}}{\sqrt{2}k_z v_{T_z}}\right)\left[1 + \left(\frac{\omega_{RF} - \omega_g}{\sqrt{2}k_z v_{T_z}}\right)Z\left(\frac{\omega_{RF} - \omega_g}{\sqrt{2}k_z v_{T_z}}\right)\right]$$

$$\epsilon_{yz} = -\epsilon_{zy} = \mathrm{i}\left(\frac{k_\perp c}{\omega_{RF}}\right)\frac{1}{\sqrt{2}}\frac{\omega_p^2}{\omega_{RF}^2}\left(\frac{\omega_p}{\omega_g}\right)\left(\frac{v_T}{c}\right)\left(\frac{\omega_{RF}}{\sqrt{2}k_z v_{T_z}}\right)\left[1 + \left(\frac{\omega_{RF} - \omega_g}{\sqrt{2}k_z v_{T_z}}\right)Z\left(\frac{\omega_{RF} - \omega_g}{\sqrt{2}k_z v_{T_z}}\right)\right]$$

When T $\to$ 0, that is, $\xi_{-1} \to \pm\infty, b \to 0$, the dielectric tensor of hot plasma is reduced to the dielectric tensor of cold plasma.

At ECR region where $\omega_{RF} = \omega_g$

$$\epsilon_{xx_{ECR}} = \epsilon_{yy_{ECR}} = 1 + \frac{\omega_p^2}{\omega_{RF}}\left(\frac{1}{\sqrt{2}k_z v_{T_z}}\right)\frac{1}{2}\mathrm{i}\sqrt{\pi}$$

$$\epsilon_{zz_{ECR}} = 1 - \frac{\omega_p^2}{\omega_{RF}^2}$$

$$\epsilon_{xy_{ECR}} = -\epsilon_{yx_{ECR}} = -\frac{\omega_p^2}{\omega_{RF}}\left(\frac{1}{\sqrt{2}k_z v_{T_z}}\right)\frac{\sqrt{\pi}}{2}$$

$$\epsilon_{xz_{ECR}} = \epsilon_{zx_{ECR}} = \frac{1}{2}\frac{k_\perp}{k_z}\frac{\omega_p^2}{\omega_{RF}^2}$$

$$\epsilon_{yz_{ECR}} = -\epsilon_{zy_{ECR}} = \mathrm{i}\frac{1}{2}\frac{k_\perp}{k_z}\frac{\omega_p^2}{\omega_{RF}^2}$$

Despite the fact that the cold plasma approximation provides already a reasonable description of the plasma dielectric properties, the explicit inclusion of the thermal effects gives the possibility to quantify its accuracy.

Inspection of equations of hot dielectric tensor components [43] shows that the parameter b enters explicitely and as argument of the Bessel functions. As an example, expanding the hot dielectric tensor element ϵ_{xx}, considering only terms n= $0, \pm 1, \pm 2$, making use of the small argument approximation of the Bessel function $I_n(b) = I_{-n}(b) \sim (1/n!)(b/2)^n$, and approximating $e^{-b} \sim 1 - b$, we get:

$$
\begin{aligned}
\epsilon_{xx} &= 1 - \frac{\omega_p^2}{\omega_{RF}^2} \sum_{l=-\infty}^{+\infty} \frac{n^2}{b} e^{-b} I_n(b)(-\xi_0 Z(\xi_l)) \\
&\approx 1 - \frac{\omega_p^2}{\omega_{RF}^2} \left[\frac{1}{2}(-\xi_0 Z(\xi_{-1}) - \xi_0 Z(\xi_1)) + \frac{1}{2}b(-\xi_0 Z(\xi_{-2}) - \xi_0 Z(\xi_2)) \right] (1 - b)
\end{aligned}
$$

$$(2.53)$$

and neglecting terms proportional to b^2, the result is:

$$
\begin{aligned}
\epsilon_{xx} &= 1 - \frac{\omega_p^2}{\omega_{RF}^2} \left[\frac{1}{2}(-\xi_0 Z(\xi_{-1}) - \xi_0 Z(\xi_1)) \right] \\
&- \frac{1}{2}N^2 \frac{\omega_p^2}{\omega_c^2} \frac{v_{th}^2}{c^2} \left[\frac{1}{2}(-\xi_0 Z(\xi_{-1}) - \xi_0 Z(\xi_1)) - \frac{1}{2}(-\xi_0 Z(\xi_{-2}) - \xi_0 Z(\xi_2)) \right]
\end{aligned}
$$

$$(2.54)$$

$$
\epsilon_{xx} = S^{FLR} - N^2 \sigma^{FLR}
$$

$$(2.55)$$

In the cold-plasma limit the term S^{FLR} remains finite, approaching the cold term S, while the correction function σ^{FLR} vanishes, as it proportional to v_{th}^2. The order of magnitude of this function is governed by the factor $(v_{th}/c)^2 = (m_{e0}v_{th}^2/m_{e0}c^2)$, which is, with $m_{e0}c^2 = 511$ keV even for hot fusion/ECRIS plasma at $k_B T_e = 10 - 20$ keV, only in the order of some 10^{-2}. As exemplified here for the hot tensor element ϵ_{xx}, all others can be treated in the same way. As with S^{FLR}, the other terms all have the same factor as discussed, with σ^{FLR} giving the order of magnitude of the correction terms. **In summary, lowest order finite temperature corrections are of the order of a small percentage at maximum. The estimates, on the other hand, show more quantitavely that the cold-plasma approximation already provides a good description of wave propagation even in hot plasmas.** Also in the plasma modeling for microwave diagnostic purpose described in Chapter 5, it has been used with very good agreement between experimental measurements and analytical cold plasma model.

2.5.1 Spatially dispersive medium

Finite-temperature effects introduce the so-called *spatial dispersion*, i. e. the generalized dielectric tensor $\epsilon_{ij}(\omega, \mathbf{k})$ depends on the wave vector $\mathbf{k}$. This means that the electric induction $\mathbf{D}$ at a given spatial point depends not only on the electric field $\mathbf{E}$ at the same point (the local medium response) but also on the electric field in the surrounding areas (nonlocal response). Fourier transform of $\epsilon_{ij}(\omega, \mathbf{k})$ offers a powerful tool to describe nonlocal behavior in wavenumber domain:

$$D_i(\omega, \mathbf{k}) = \epsilon_{ij}(\omega, \mathbf{k})E_j(\omega, \mathbf{k}) \qquad (2.56)$$

Inverting (2.56) we can express the relation in real space domain in the form of convolution:

$$D_i(\mathbf{r}, t) = \int_{-\infty}^{t} \int d\mathbf{r}' \, \epsilon_{ij}(t - t', \mathbf{r} - \mathbf{r}')E_j(\mathbf{r}', t')$$

In this case it is an expedient to expand the electromagnetic field in a Fourier integral, i. e. to express it as the sum of plane monochromatic wave waves of the type $e^{-i\omega t + i\mathbf{k}\cdot\mathbf{r}}$[44].

$$\epsilon_{ij}(\omega, \mathbf{k}) = \int_{-\infty}^{t} dt \int d\mathbf{r} e^{(-i\omega t + i\mathbf{k}\cdot\mathbf{r})} \epsilon_{ij}(t, \mathbf{r})$$

$$\epsilon_{ij}(\mathbf{r}, t) = \frac{1}{(2\pi)^4} \int d^3k \int d\omega e^{(-i\omega t + i\mathbf{k}\cdot\mathbf{r})} \epsilon_{ij}(\omega, \mathbf{k})$$

2.5.2 Modal conversion and EBW "quasi-static" field

As the pumping wave must reach the resonant region where the electron cyclotron resonance takes place, the density along the trajectory of the wave must not exceed the cutoff density value. Cutoff density is different for different modes propagating in the plasma. However, there is a mode, which has no upper density limit. It is the electrostatic[2][45] Electron Bernstein wave (EBW, EB-mode, B-mode). The EBW has no cutoff limit but its nature does not allow propagation outside of the plasma. To obtain this mode inside of the plasma the conversion from other externally launched modes is needed. For ECR heating in toroidal devices Ordinary-mode[3] (O-mode) or Extraordinary-mode [4] (X-mode) is externally launched to the plasma from high or low field side of the torus. Both modes have a cutoff limit for propagation. However, Slow Extraordinary mode (SX-mode) may be converted to EB-mode if it reaches the Upper Hybrid Resonance (UHR) layer. O-mode launched from low field side may be

---

[2] $\mathbf{E}$ field is directed parallel to k vector
[3] The E-field of this mode is directed parallel to the external magnetic field
[4] The E-field component in the perpendicular direction to the external magnetic field

coupled to the SX-mode in the region of the O-mode cutoff layer, and then the SX-mode is coupled to the B-mode. This process called OXB mode conversion, and was described in 1973 by Preinhaelter and Kopecky [14]. In their fundamental work, it was shown that the OXB mode conversion might be optimized in terms of O-mode insertion angle with respect to the external magnetic field direction. This optimization leads to interconnection of O and SX-cutoff layers. Under these conditions, O-mode is completely converted into SX-mode, which then completely converts to EB-mode in the UHR layer.

Another possibility of producing an EB mode inside the plasma is the launching of an SX-mode from high field side of the torus. In this case, the SX-mode may reach the UHR layer directly if it does not encounter the L-cutoff[5] barrier. This scheme is called SX-B conversion. Additionally, FX-mode, launched from low field side, may tunnel from the FX[6] into SX-mode through evanescent region, which is bordered by R-cutoff and UHR. SXmode, reflected from L-cutoff, reached the UHR layer where it is converted to EBW. This process is called FX-SX-B mode conversion. To obtain desirable SX-FX tunneling efficiency the density steepness in the region of the R-cutoff and the UHR layer should be high enough to minimize the region size inaccessible for X-mode [46].

EBW are absorbed at the harmonics of ω_c, which means that in a ion source like ECRIS or MDIS, EBW absorption is possible for the same can occur at the harmonics of the resonance magnetic field B_{ECR}. Hereinafter we will define ω_c as fundamental harmonic, $\omega = \omega_c/2$ will be the first harmonic, $\omega = \omega_c/3$ will be the second harmonic and so on.

Property of EBW is an important step forward with respect to the electromagnetic waves, which are reflected at the cutoff frequency ω_p. EBW does not suffer this cutoff and could be able to sustain the plasma at electron density much larger than the ones obtainable by means of the usual ECR heating. At WEGA stellarator of Greifswald, for example, EBW heating has been used to reach densities up to $10 \ n_{cutoff}$ [8]. EBW heating thus, could be a valid alternative to the ECR heating.

The schemes to couple electromagnetic waves (X wave) to EBW have been largely studied for the application in fusion devices [12]. In ECRIS and MDIS devices it is difficult to inject a wave with a precise **k** wavenumber direction. Plasma chamber, in facts, is a resonator and practically allowe modes are approximated by a sum of plane waves. So it is very difficult to define which mechanism allowed extraordinary waves to reach UHR. If the UHR layer is enclosed by R and L cutoffs, the X wave can be reflected back and forth passing through the UHR. We are in the case where

---

[5] L-cutoff is the cutoff for the SX-mode

[6] FX- is the X-mode outside the R-cutoff layer SX is the X-mode beyond the UHR layer

the wavelength is comparable with the characteristic density scale length, or even the plasma size. In this case, ray tracing is not applicable and simulations can only be performed using the full wave calculations. Both simualtion and experimental tests of EBW launching in a ECRIS-like device have been treated in this thesis.

2.6 Remarks about wave propagation in plasmas

The theory of electromagnetic waves propagation in magnetized plasmas predicts that both ordinary and extraordinary wave are reflected above their respective cutoff density, (O cutoff for ordinary waves, L cutoff for the extraordinary). The experimental measurements confirm the theoretical results: in the case of the ECRIS were measured plasma density slightly higher than the cutoff wave O [47], the MDIS, thanks to the non-resonant absorption of the electromagnetic waves, can generate plasmas with density 2-3 times higher than the cut-off value [1]. However, in both cases, the cut-off density is a limiting value and it is clear that the only way to raise the electron density value is to increase the microwave frequency, so that the density cutoff occurs at higher values. The increased frequency RF also involves the increase in the magnetostatic field associated, according to the scheme shown in the following equation:

$$n_{cutoff} \propto \omega_{RF} = \omega_c \propto B_{ECR} \qquad (2.57)$$

Consequently, the increase in performance of the sources of new generation implicitly involves a continuous increase of the magnetic fields used. The latest generation of ECRIS in the design phase, for example, have being projected to operate at frequencies in the range 40-56 GHz and to make use of magnetic fields (generated by superconducting magnet materials) of the order of 7 T [48]. By looking to the results of ECR ion sources in the last thirty years, it is evident that such a rush cannot be continued "ad libitum". Moreover, the technological limits of the superconducting magnets and of microwave generators, as well as the increasing cost, suggest that the saturation point is approaching. The above discussion explains why in recent years the search for new technologies of plasma ignition has become a priority. One possible candidate to replace the heating electromagnetic waves is represented by the Electrostatic waves, and in particular by the Bernstein waves. These waves are not affected by any cutoff and can propagate and be absorbed in widely overdense plasmas (see Fig. 2.6).

Necessary condition for the EBW generation is the presence of the UHR resonance, which exists when $\omega_p < \omega_{RF}$ and $\omega_c < \omega_{RF}$ or, in terms of plasma parameters, $X < 1$ and $Y < 1$. UHR lies between the fundamental harmonic (B_{ECR}) and the first harmonic ($B_{ECR}/2$).
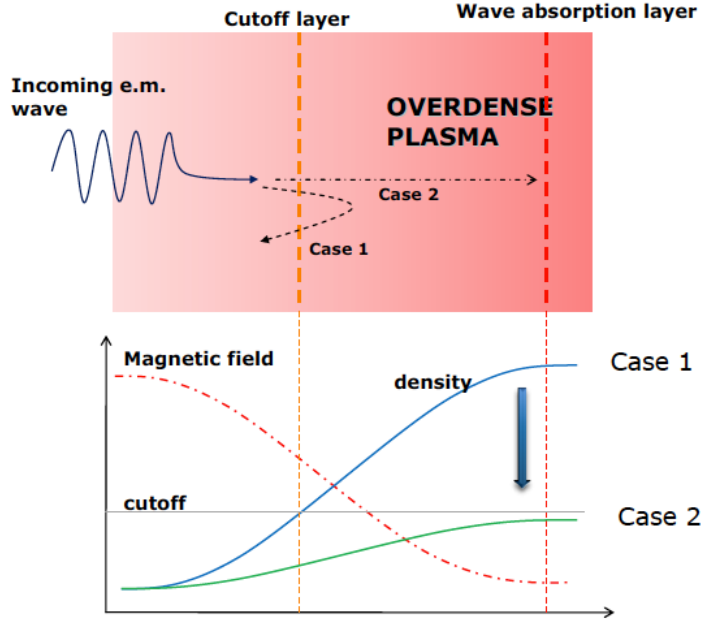
Fig. 2.6. Overdense plasma core is accessible by plasma (matter) waves excited by electromagnetic waves launched at the low density side

The generation and absorption of EBW can be demonstrated by means of 3 fundamental evidences:

1. *Appearance of sidebands in the spectrum of the pumping electromagnetic waves and of ion waves in the range of MHz;*
2. *Generation of large energy electrons (with respect to the usual energies in the source;*
3. *Achievement of densities much higher than the density cutoff;*

2.7 Inhomogenous and bounded plasmas

So far, the plasma has been assumed homogeneous and unbounded, without considering any gradients of the quantities determing the propagation of microwaves through the plasma, that is, electron density and temperature, and the static $\mathbf{B_0}$-field. The leading parameter in this context is the electron density entering via the plasma frequency of all components of the dielectric tensor, since the $\mathbf{B_0}$-field gradient is relatively small in fusion and ion sources devices and because the temperature has only a minor influence on the dispersion relation of ordinary and extraordinary modes even at fusion-relevant temperatures.

In the case where plasma parameters are varying slowly, that is with a scale length $L_n = n_e/\boldsymbol{\nabla} n_e$ much larger than the wavelenght of the probing wave, the formalism developed for homogeneuos plasma can be applied as well.

3

Plasma diagnostics

3.1 Plasma diagnostics in ECR Ion Sources

The improvement of Ion Sources is boosted by means of a deep knowledge of parameters characterizing the plasma, among these the most fundamental being the **density and temperature**. They, indeed, deeply influence the features of the extracted beam (for example in terms of current and emittance), of central importance in Nuclear Physics experiments with the beams accelerated by linear or circular machines.

In the last years, however, further developments have been limited due to the technological limit in the production of high magnetic fields. This technological impasse can be overcome only by means of a better understanding of **plasma physics**, that's the reason why many efforts have been devoted to plasma diagnostics. If one wants to understand what is the kind of interaction between the electromagnetic wave and the magnetized plasma, a direct inspection of the plasma is required.

Plasma diagnostics has been mainly driven by the great interest to economically produce energy from thermonuclear fusion. In this field, the research is mainly oriented to the development of stable magnetic confinement in order to allow nuclear fusion reactions occurring at a rate high enough to sustain a chain reaction. Also, from the diagnostics point of view, thermonuclear fusion is really challenging because of the high temperature required (10^8 K), which excludes the possibility to insert any kind of probes.

A short list of the main diagnostics tools is:

- *Magnetic measurements* which are measurements consisting in directly probing the magnetic field in various places inside and outside the plasma using coils and/or probes of various types;
- *Plasma particle flux measurements*, using probes directly in contact to the plasma;

- ***Plasma refractive index measurements***, based on the transmission of an electromagnetic wave of appropriate frequency through the plasma: an original tool falling in this category has been developed in Chapter 5);

- *Electromagnetic emission from free electrons*, based on the detection of the radiation emitted by the electrons through cyclotron (synchrotron emission), brehmsstrahlung and Cerenkov processes;

- *Electromagnetic emission from bound electrons*, based on the observation of the line radiation from atoms and ions that are not fully ionized;

- *Scattering of electromagnetic waves*, based on the scattering of the incident radiation by plasma particles;

- *Neutral atom diagnostics*, based on charge exchange reactions;

- *Fast ion and fusion products*, based on nuclear reactions.

The diagnostics systems to analyze these plasmas are based on the analysis of waves injected and transmitted through the plasma, or can be based on passive methods detecting the radiation emitted by particles in different processes. We can group all these arrangements of diagnostics in four cathegories: **transmission, scattering, reflection and emission of waves**.
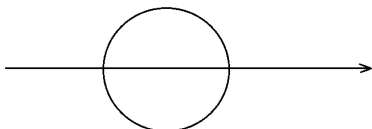
Fig. 3.1. Transmission
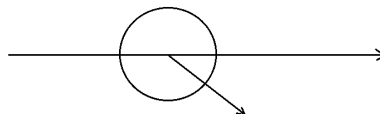
Fig. 3.2. Scattering
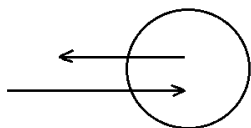
Fig. 3.3. Reflection
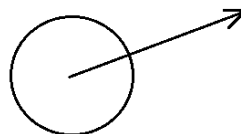
Fig. 3.4. Emission

In the transmission (Fig. 3.1), a **probing wave is launched in plasma and quantities like amplitude, frequency, phase wave vector and polarization state are measured**. In this arrangement one measures the change in phase and in the polarization state. The single *"chord"* (integration path) arrangements gives the line-integrated density information. To obtain local information, multiple chord are needed.

The arrangement of Fig. 3.2 allow scattering measurement: the electric field of the wave passing through the plasma interacts with individual plasma electrons becom-

ing themselves emitters of electromagnetic radiation. Also, since electrons have an intrinsic thermal motion, **the Doppler effect is observed with respect to the probing frequency. The width of the emission lines give the information about the velocity distribution of electrons**. Moreover, the scattering can be caused by a single electron, in this case we talk about *incoherent scattering* or by a collective motion of electron in the Debye cloud, in this case being referred to *coherent scattering*.

In the arrangement in Fig. 3.3 **the launched wave is back reflected when it reaches a cutoff layer where the refractive index approaches to zero**. By measuring the round trip phase delay with a radar-like arrangement, one can locate the position of the cutoff layer.

In the configuration in Fig. 3.4 the emission of plasma in a large range of the electromagnetic spectrum which extends from the gyration frequency of ions ($\sim$ kHz) to the tenths of megahertz in the region of X-rays is exploited. **The physical mechanisms involved are the brehmsstralung radiation and the characteristic emission of spectral lines**. The presence of impurities can be determined by the intensity of spectral lines and the width of the line carries information about the velocity distribution of particles. Passive and Active probing with waves and particles are briefly list in Table 3.1

Table 3.1. Standard diagnostic systems by dividing into active and passive system, either probing with waves or with particles.

Passive diagnostics	Active Diagnostics
Waves	**Waves**
Spectroscopy (IR, visible, UV, VUV, and X-ray)	Interferometry
Radiometry of electron cyclotron emission	Polarimetry
Bolometry of total radiation	Reflectometry
Thermography of wall surfaces	Scattering
Particles	**Particles**
CX neutral particle analysis	H-, He-, Li-beam, and emission after e$^-$ impact
Detection of fusion products	CX recombination spectroscopy

3.2 Plasma diagnostics at INFN-LNS

At INFN-LNS a wide set of disgnostics tools has been designed and developed in the recent past. The adopted methods span from intrusive (e. g. electrostatic probes) to non-intrusive (e. g. volumetric X-ray spectroscopy) tools (see Figure 3.5).
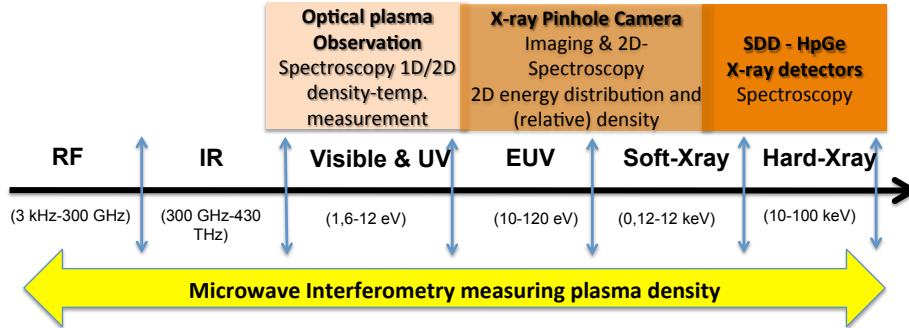
Fig. 3.5. Existing plasma diagnostic tools

Plasma is a radiation emitter in a wide range of the electromagnetic spectrum, spanning from the infrared to gammas; this feature permitted to implement several techniques, each of them specialized in a certain portion of the electromagnetic spectrum. **X-ray spectroscopy**, for example, allows to characterize the component of plasma able to emit X-rays (warm and hot population), through the analysis of the brehmsstrahlung spectrum. This technique gained relevant success also as a non invasive tool for cultural heritage.

During last years, at LNS, a diagnostic system based on the **X-ray imaging** (1-20 keV) has been developed, consisting in a pin hole camera [49, 50] based on a CCD detector. By means of this technique it was possible to determine the spatial distribution of the X emission and to better understand the mechanisms of wave-to-plasma interaction. In Figure 3.6, a general scheme of a X-ray pinhole camera along with a real setup used for the ATOMKI-Debrecen 14 GHz ECRIS is shown.

In order to characterize the so-called "plasma bulk", i.e. electrons which weakly interact with the electromagnetic wave, but have a leading role in the diffusion/confinement processes of plasma, a tool based on **optical spectroscopy** (1-10 eV) is being developed. It has been widely applied to study the cold electron population in ECR plasmas. At LNS, a spectrometer coupled to a high sensitivity CCD camera has been developed, able to measure at the same time the components of the optical spectrum and the spatial distribution.

Another diagnostic tool is the so-called **"Langmuir Probe"** (LP), designed to characterize the plasma through *resistivity curves* measurements. It is a metallic tip
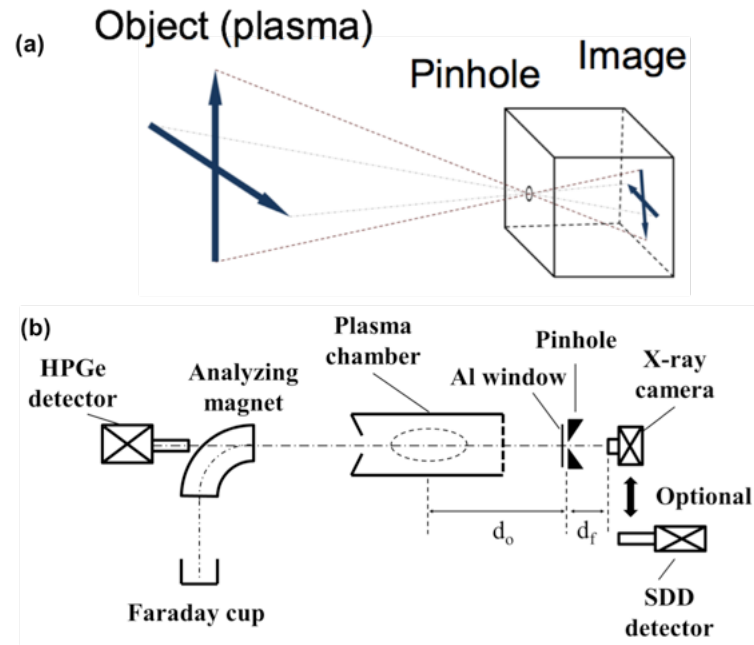
Fig. 3.6. General scheme of a X-ray pinhole camera (a) along with a real setup (b) used for the ATOMKI-Debrecen 14 GHz ECRIS

of tungsten or tantalium normally, that, once inserted inside the plasma, measures the I-V curve of the plasma bulk, which has a temperature of about 10-50 eV. The LPs can be used also as antennae to detect the electromagnetic waves emitted by the oscillation of the ionic component of plasma, known as *ionic waves*, which oscillate at the kHz frequency. The LPs are tools simple to be used; however, they are very invasive diagnostic tools, especially when used in plasma chambers of compact size, like those usually used for ion sources (see Fig. 3.7).
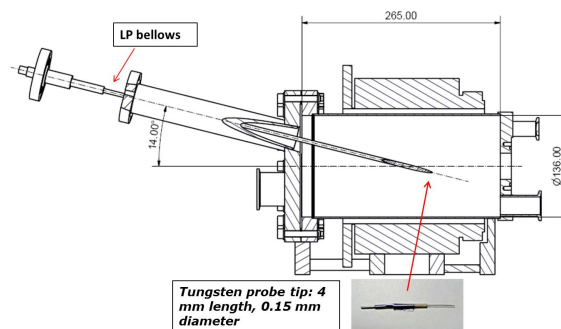
Fig. 3.7. Langmuiri Probe penetrating into the plasma chamber

Regarding the **non-invasive techniques** in Ion Sources, an important role is that of the **microwave interferometry**, already successfully tested for the controlled fusion plasmas inside nuclear reactors like Stellarator and Tokamak. This technique

has many difficulties of application in the case when, in contrast to the case of the big reactors for controlled thermonuclear fusion, the ratio between the wavelength of the radiation for the diagnostics λ and the dimensions of the plasma chamber L do not satisfy the condition $\lambda/L \ll 1$. Additional issues come from the mechanical constraints for the probing microwave injection apparatus, for example, areas already occupied by the extraction system, space occupied by the magnets used for the magnetic confinement and other areas occupied by other diagnostics systems.

The interpretation of the probing signal passed through the plasma, in this contest, requires the usage of filtering methodologies to remove the spurious components of the signal. However, microwave interferometry, since it is a non-invasive technique, allows a very reliable reconstruction of the density profile; this has to be done altogether with studies of modeling of plasma distribution. An innovative microwave interferometry-based experiment has been carried out during this PhD course and it is described in Chapter 5.

3.3 Microwave Diagnostics

Microwave diagnostics [51] are active and passive wave diagnostic systems. They operated in a range of frequencies wheree the refractive index of the magnetized plasma differs significantly from the vacuum value and/or where it shows largest variations with plasma parameters. The range depends on the electron density and on the $\mathbf{B_0}$-field, the first determing the plasma frequency and the second the electron cyclotron frequency ω_c. These system probe the plasma dielectric properties by measuring the wave phase (interferometry) and polarization changes (polarimetry) when passing the plasma and they also detect the cutoff layers by measuring time delays in radio detecteion and ranging RADAR-like schemes (reflectometry) In both cases, the plasma is probed without material contact.

3.3.1 Microwave interferometry

The term interferometry refers to the fact that in early experiments the phase shift was measured by means of interferometric arrangements, superimposing signal and reference waves, and by evaluating the change in the interference pattern when the plasma builds up. The microwave interferometry is a plasma density measurement technique based on the study of the passage of microwaves through a plasma. Microwave interferometry offers a less invasive and more precise measurement if compared to Langmuir probes, because electromagnetic waves modify far less the state of plasma than a Langmuir Probe does.

Interferometry is often used as a method to measure the refractive index of a medium

and is essentially based on a device, an interferometer, able to measure the coherent superposition of two ore more signals. In the simplest case, when the magnetic field is negligible, in equation (2.21), Y tends to zero ($Y \to 0$) and then, the refractive index becomes:

$$N^2 = 1 - X = 1 - \omega_p^2/\omega^2 \tag{3.1}$$

The refractive index, hence, doesn't depend on the direction of propagation of waves. In the case of magnetized plasma the study becomes much more complex. The intensity of the observed signal depends on weather the signals added in phase or out of phase.

In the general scheme, an interferometer is a device, where two or more electromagnetic waves can interfere by the coherent addition of the electric fields. Let us consider, for example, a two beams interferometer where two monochromatic fields $E_1 e^{i\omega t}$ and $E_2 e^{i(\omega t + \phi)}$ are superimposed with some phase ϕ between them. Then, the total field is given by:

$$E_t = (E_1 + E_2^{i\phi}) e^{i\omega t} \tag{3.2}$$

the power detected, for example, by a square-law RF detector is proportional to $|E_t|^2$, which may readily be shown to be:

$$|E_t|^2 = [E_1^2 + E_2^2]\left[1 + \frac{2E_1 E_2}{E_1^2 + E_2^2}\ \cos\ \phi\right] \tag{3.3}$$

So the output intensity (power) has a constant term plus a component varying as $\cos\phi$.

There are mainly three configurations of interferometer which are:

- The **Michaelson interferometer** (Fig. 3.8), which is a two-beam interferometer with a beamsplitter, two arms in which the beams travel in both directions and two outputs. Along the arm there can be free space optical path or, for example, waveguides. The principle is the same in all cases: phase difference arises in the case of change of the refractive index in one of the arms of the interferometer.
- The *Mach-Zehnder configuration* (Fig. 3.9) is also a two-beam interferometer but it differs from the Michaelson interferometer in having two arms in which the beams travel only in one direction. Again, the phase changes are caused by variation in the refractive index in one arm.

- The *Fabry-Perot interferometer* is a multiple -beam interferometer in which there are two beamsplitters and two composite output beams. Because it has multiple beams, the output is not a simple cosine as in the two-beam interferometers. This makes phase shift interpretation more difficult, so it is less often used for plasma refractive-index measurements.

The interferometer we are going to discuss in the present thesis is a Mach-Zehnder interferometer.
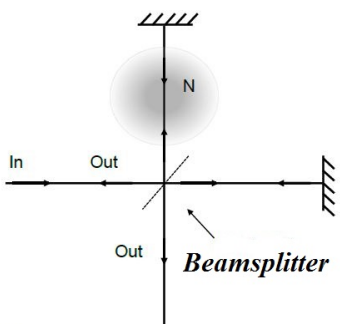
Fig. 3.8. *A schematic diagram of a Michaelson interferometer*
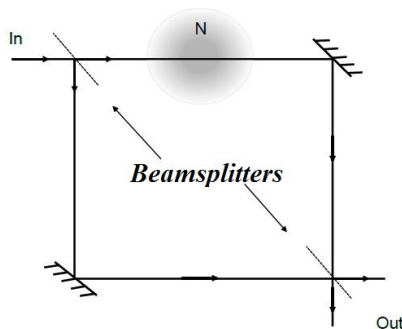
Fig. 3.9. *A schematic diagram of the Mach-Zehnder interferometer*

In this Mach-Zehnder interferometer, the beam is split in two directions: one beam goes straightforward through the medium, while the other one travels in vacuum and serves as a reference path, the two signals are eventually mixed at the output. If the two paths have the same length then the difference in the phases between the two signals is only due to the refractive index of the medium.
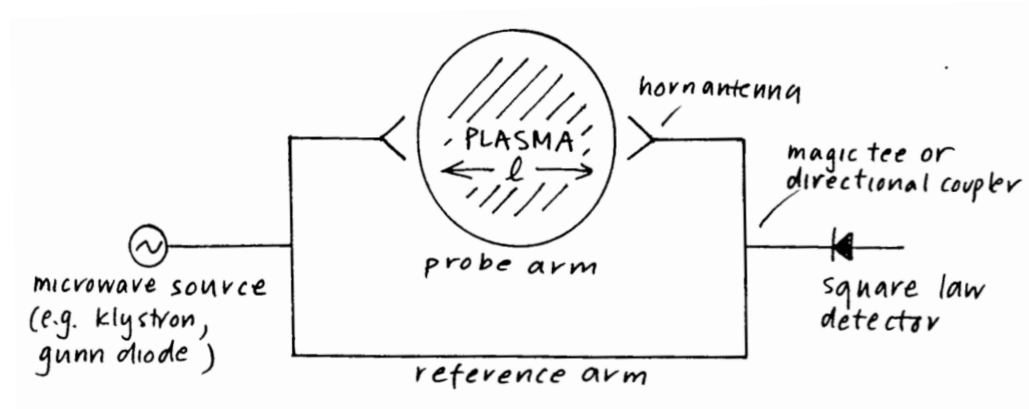
Fig. 3.10. microwave interferometer general scheme.

The net phase lag is given by:

$$\phi = \int N \frac{\omega}{c} \, dl \tag{3.4}$$

where ω is the frequency of the signal and N its refractive index; the integral is evaluated along the distance traveled inside the medium. Often, due to technical constraints, it is hard to have exactly two legs of the same length, then a part of phase shift is introduced by the extra path of the reference leg. The consequent phase shift then depends on weather, for example, the wave has traveled a path in vacuum or inside a waveguide.

The effects of the extra lengths can be removed by comparing the phase difference between the two arms with or without the plasma. The difference in these phases is then simply introduced into the plasma arm by the plasma itself, namely:

$$\Delta\phi = \int (k_{plasma} - k_0) dl = \int (N - 1) \frac{\omega}{c} \, dl \tag{3.5}$$

where we assume that in the absence of plasma $k_0 = \omega/c$, that is, the wave propagates effectively in vacuum. The measurement of the interferometer phase shift $\Delta\phi$ thus provides us a measure of the refractive index of the given mean along the line of the interferometer beam through the plasma. In an isotropic plasma the refractive index can be related to density:

$$N^2 = 1 - \frac{\omega_p^2}{\omega^2} = 1 - \frac{n_e}{n_c} \tag{3.6}$$

where n_c is the so called cut off density:

$$n_c = \frac{\omega^2 m \epsilon_0}{e^2} \tag{3.7}$$

For $n_e < n_c$ the interferometer gives a measure of electron density from:

$$\Delta\phi = \frac{\omega}{c} \int \left[\left(1 - \frac{n_e}{n_c}\right)^{1/2} - 1 \right] dl \tag{3.8}$$

Which is a form of average along the beam path. If the density exceeds the cutoff value, $n_e > n_c$, then N^2 becomes negative and N is a pure imaginary. This means that the wave is no longer propagating but it is evanescent, falling off exponentially with the distance.

If the plasma density is low enough, $n_e < n_c$, expressing (3.6) in Taylor expansion:

$$N \simeq 1 - \frac{1}{2} \frac{n_e}{n_c}$$

we can obtain:

$$\Delta\phi = \frac{-\omega}{2cn_c} \int_L n_e \, dl \tag{3.9}$$

The phase difference results proportional to the line integrated density and to the wavelength as it follows:

$$\omega \propto \lambda^{-1}, \qquad n_c \propto \lambda^{-2} \qquad \rightarrow \qquad \Delta\phi \propto \lambda$$

The design and experimetal tests on a Mach-Zender configuration microwave interferometer will be widely discussed in the chapter 5 of the present thesis.

3.3.2 Polarimetry

The study of the change of the polarization state of an electromagnetic wave that propagates through a magnetized plasma is an important diagnostic technique [52] that can be used to determine the electron density in plasma, provided that the distribution of the magnetic field is known [43]. For a high frequency radiation, as we explained in Chapter 2, a plasma subjected to a magnetic field, eorks such as a birefringent and optically active anisotropic medium. For propagation perpendicular to the $\mathbf{B_0}$-field the plasma is linear birefringent and exhibits the Cotton-Mouton effect $(N_0 \neq N_X)$, while for propagation parallel to the magnetic field it is optically active and circular birefringent $(N_R \neq N_L)$ and it features the Faraday effect (see Figure 3.11) [53].
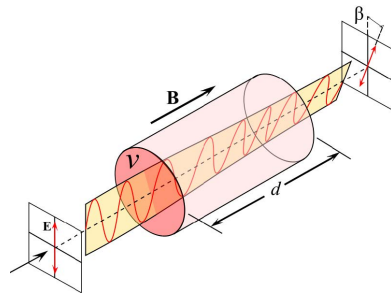
Fig. 3.11. Faraday effect: polarization plane rotation

In the first case the wave ellipticity changes, while in the second case there is a rotation of the ellipse of polarization (or plan, for linear polarization), with ellipticity constant. For propagation with arbitrary direction with respect to the magnetic field, in general a combination of the two effects is present, rather complicated to be treated . A further complication derives from the fact that the plasmas are not uniform, so the plasma density and the the magnetic field vector will vary with the position along

the path of the radiation. To carry on a polarimetric measurement, with good approximation, the variation of the polarization state has to be due only to the Faraday effect. If z is the wave propagation direction, the Faraday rotation angle, expressed in radians, is represented by this line integral along the line of sight of the probing linear polarized wave:

$$\alpha \propto \lambda^2 \int n_e(z) B_z(z) \, dz \tag{3.10}$$

If the B-field is known, the line-integrated of the density can be determined.

4

Modeling the electromagnetic field in anisotropic inhomogeneous plasma

———————————————————————— -

Introduction

Any further boost of both ion currents and average charge state from ECRIS requires a deep understanding of wave-to-plasma interaction. This issue represents an important field of research for plasma physics in general, being – in the most part of the cases – the wave-to–plasma interaction the chennel of energy deposition and/or current drive in magnetically confined plasmas.

A complete and accurate design of future ECRIS, cannot neglect the investigation of electromagnetic wave propagation in plasma with the aid of numerical and theoretical models.

With respect to the theory and modeling, the problem of electron-cyclotron heating may be divided into two different parts:

- The problem of the wave propagation and absorption (effect of the plasma on the wave);
- The problem of the evolution of the electron distribution function (wave effect on the plasma).

One usually treats each part of the problem separately, while a coupling of the two parts constitutes the core of a **self-consistent treatment**.

A coupled particle-wave propagation code could be very useful to investigate the effect of the plasma on wave propagation and the effect of wave on ion and the electron dynamics, beam formation and beam optical properties.

In order to describe electromagnetic wave propagation in plasmas there exist basically two different approaches. One is the geometrical optical approximation, where the wave is described as a ray, known as ray tracing, applicable only if the refractive index n changes only slowly over a distance x that is comparable to the wavelength of the incident wave, $\left| \frac{1}{n} \frac{dn}{dx} \ll n \right|$ and geometrical optics can be used to calculate the

wave trajectory. A ray tracing code cannot be applied here, since the geometrical optics assumption breaks down when the wavelength of the microwave is comparable to the size of the plasma as is the case for ECRIS.

The second approach is referred to as **full-wave solution**, since Maxwells equations are exactly solved. Full wave solution will take into account the influence of the merging of two different types of wave modes, along with tunneling, reflection, conversion and absorption.

This chapter will mainly deal with the full-wave code, which has been developed in the course of this thesis. It is applied to wave propagation and heating in ECRIS. Furthermore, the code has been successfully used to optimize OXB heating schemes for small scale ion sources devices.

We present a numerical approach to solve the 3D Maxwell-Lorentz system with the aim of investigating the interaction of the electromagnetic waves with the magnetized non-homogeneous plasma produced inside Electron Cyclotron Resonance Ion Sources [54, 55]. The full-wave solution is then coupled to an in Matlab developed kinetic code based on a PIC Particle-In-Cell strategy, solving the Newton-Lorentz equation of motion for plasma electrons [56]. Our model explains the experimentally observed frequency sensitivity and gives a relevant contribution to the challenging goal of predicting the electron/ion dynamics in ECR plasmas. The obtained results are very helpful to better understand the influence of the different parameters (especially RF frequency and power) on the ion beam formation mechanism. Finally preliminary results about the use of 1D Continuous Wavelet Transform to solve the "Spatial dispersion" that is involved in the modeling of "hot plasma approximation" will be shown [57].

4.1 State of the art in plasma modelling and existing numerical tools for waves in ECR and fusion plasmas

The propagation of waves in anisotropic media is relevant for many fields of optics and microwaves. Searching the solution of Maxwell's equations considering a metallic cylindrical cavity eventually completely or partially filled by an anisotropic material whose electric permittivity is described by a second order tensor, is a particularly difficult task. In electromagnetism only very few scenarios can be analitically solved. In the present case, the cavity has a non canonical form, and is filled by a non homogeneous anisotropic medium (magnetized plasma), therefore the numerical approach is mandatory. Such is the case of electron cyclotron resonance ion sources (ECRIS) [7] plasma chamber. Several experimental results show that electromagnetic waves coupling with the plasma load is crucial to optimally transfer energy to the electrons, then

to optimize plasma ionization and ion beam extraction [58–60]. However, for a better understanding of the physical processes involved in plasma and in beam formation process, it is crucial to consider tha actual geometry of ECRIS microwave injection in presence of a realistic plasma model. Up to now several studies make various approximations by considering the medium as an **equivalent dielectric load** [61] and by solving the wave equation in **Wentzel Kramers Brillouin** (WKB) approximation [62]. This latter approximation is questionable in particular regions of the plasma, where cut-offs and resonances break the slow varing assumptions of the media parameters $\left|\frac{\nabla \cdot \mathbf{k}}{k^2}\right| \ll 1$, and a fortiori it is not feasible in ECRIS configuration where plasma load and the chamber's electromagnetic properties are extremely variable even over fractions of a wavelegth. In these cases a **full wave solution** of Maxwell's equations is needed.

The LNS-INFN Catania's group developed a numerical code able to model the electron and ion dynamics in an ECR ion source using a Monte Carlo approach. This model allowed to explain for the first time the impact of the frequency tuning on the electron heating rapidity, on the plasma density distribution [59], and in turn on the shape, emittance and brightness of the output beam. Alternative models and numerical strategies have been attempted by other authors [63–66], that can be summarized in two groups: a) assuming a "zero-dimensional" model for calculating the charge state distribution in a parametric way, or b) considering a simplified magnetostatic scenario (only simple mirror configuration instead of minimum-B) for simulating the plasma dynamics via Fokker-Planck calculations based on a diffusion-like model for the RF heating [67]. Both these approaches do not include peculiarities of electromagnetic wave propagation into a dense, non-isotropic, non homogeneous plasma, that is indeed the condition holding in ECRIS-like systems. These properties are deemed to play a crucial role in frequency tuning effect, two frequency heating, etc.

Actually, the challenging goal of predicting the electron/ion dynamics in the ECR source in a self-consistent way requires to consider the fundamental aspect of the coupling between the electromagnetic wave and the plasma and it represents one of the achievements of this work

Other codes for wave in plasma modeling

Considerable efforts has been devoted to numerical modelling especially of Ion cyclotron and **electron cyclotron of Tokamak** fusion reactors plasmas to find the solution of Maxwelll equations in a hot plasma in **toroidal geometry**. Most solvers assume linear cold plasma dispersion for the real part of the wavenumber (describing the wave propagation) near and far from resonance, and the imaginary part, which describes cyclotron damping, is computed from the complex dispersion relation only

in the resonance area. Furthermore, the assumption of weak absorption is adopted, where the imaginary wavenumber is considered an order of magnitude smaller that the real part. Hereinafter they are listed and briefly described some of the most known full wave codes to model waves in plasma.

- **GENRAY** is a ray tracing code that allows for the simulation of waves in axisymmetric toroidal plasma through the use of the geometrical optics approximation. It use a 2-D profile for plasma density and 1D for temperature; it interfaces a Fokker Plank code CQL3D to self-consistently take into account the non-maxwellian distribution function. Being a ray-tracing, it is affected by the uncertainty related to the initial condition of the beam[68].

- **TORIC** uses a spectral decomposition along the poloidal and toroidal directions and finite elements along the radius of the torus. In Toric the wave field excitation is done by imposing a known wave field distribution a the boundary of simulations domain [69]

- **AORSA**: in addition to the toroidal spectral decomposition, AORSa uses a Cartesian spectral decomposition in the poloidal direction. It allows a Numerical Computation of Wave Plasma-Interactions in Multi-dimensional Systems. There are a 2-D and 3-D versions of AORSA. AORSA-2D provides a high-resolution, two-dimensional solutions for mode conversion and high harmonic fast wave heating in tokamak plasmas. AORSA-3D model provides fully three-dimensional solutions of the integral wave equation for ion cyclotron heating in three dimensional stellarator plasmas. By combining multiple periodic solutions for individual helical field periods, it is possible to obtain complete 3-D wave solutions valid over the entire volume of the stellarator for arbitrary antenna geometry [70].

- **GRILL, FELHS, ALOHA** tools essential to understand and thus controlling the interaction between antenna and plasma; they are often the starting point of other numerical calculation. Usually the EM field scattered by the antenna is assumed to be dissipated far away from the coupling region with plasma so that the coupling problem is treated as a problem of radiation in a semi-infinite medium and the propagation into the plama core is not calculated. The disadvantage is a restriction to slab geometries [71–73]

- **TOPICA code** [74] for ion cyclotron antennas is a boundary element code. TOPICA calculates the electric and magnetic currents on all surfaces of a 3D antenna, located in vacuum and radiating towards a 1D plasma. The knowledge of the magnetic currents on the aperture of the antenna and the knowledge of the surface impedance matrix at the plasma edge, is sufficient to calculate the radiated fields in the vacuum gap between the aperture and the plasma. The surface impedance

matrix relates the transverse electric and magnetic fields at the plasma edge, and is provided by the 1D plasma code FELICE [75].

- **3D ECRF STELEC** full wave code modelling for fundamental and second harmonics scenarios in tokamaks and ITER. The 3D STELEC code was used to numerically model the electron cyclotron and electron Bernstein wave heating in several tokamaks and ITER at the fundamental and second harmonic. Refraction and diffraction effects in low and high density plasmas were modelled for circular T-10 and elongated DIII-D tokamaks [76].

- A **mixed ray tracing/full wave** ICRH mode conversion model [77]: The adopted 1D full wave model gives a realistic description of the mode conversion in the ion-ion hybrid region as it accounts for temperature oblique incidence poloidal magnetic field and finite parallel electric effects. Each ray entering the confluence region is stopped and a full wave computation is subsequently made.

- **Coupled full-wave and ray-tracing** numerical treatment of mode conversion in a tokamak plasma [78]: a new approach for the numerical description of tokamak plasma waves in the ion cyclotron range of frequencies. It implies coupling of the full-wave and ray-tracing codes and is capable of unified treatment of waves of completely different scale and behavior. The method is applied for simulations of the electron heating scenario, based on fast wave (FW)-ion Bernstein wave (IBW) mode conversion near the ionion hybrid resonance in Tore Supra. The two-dimensional full-wave ALCYON code is used to describe the global FW field pattern in the plasma volume. A small-scale-waves filter, introduced into the code, artificially damps the mode-converted power, which is further prescribed to IBW rays. Remnant small-scale fields are extracted from the global pattern to provide information necessary for IBW rays to start. Three-dimensional evolution of IBW rays is simulated by the RAYS ray-tracing code being unrestricted by finite mesh size and finite Larmor radius effects.

- **FULL-WAVE CODE IPF-FDMC** (Institut fur Plasmaforschung-Finite Difference code for Mode Conversion). It is a time-dependent code which solves Maxwell's equations and the fluid equation of motion for the electrons by replacing the derivatives with finite differences. A numerical damping is introduced. The code takes into account all three dimensions of the calculated quantities in a cylindrical geometry but allows only for 2D variations of the background parameters. Therefore, propagations in the poloidal and toroidal cross-sections are calculated separately. Details concerning the code can be found in [79].

- **MCBC,GEM and IonEx** are ECRIS-plasma codes simulation: in particular 1D simulations use the hot plasma dielectric tensor; in 3D by using an equivalent dielectric constant proportional to the cold plasma index of refraction for R-waves

[80], [81]. FAR-TECH, Inc. has been building a suite of comprehensive numerical tools for end-to-end Electron Cyclotron Resonance (ECR) charge breeding (CB) modeling . They consist of the Monte Carlo Beam Capture (MCBC) code, the Generalized ECRIS Modeling (GEM) code, and the Ion Extraction (IonEx) code. GEM uses the quasi-linear diffusion model for rf heating. The effect of cavity mode to ECR heating has not been implemented in GEM.

- **1-D Electron distribution function (EDF)** code to solve the time-dependent equation for the behavior of electron-cyclotron-resonance-heated plasmas [82].

- [83]**ECR heating code** that implements damping of the microwave power in the vicinity of the resonance zone, assumes electron density profiles and uses right hand circularly polarized (RHCP) electromagnetic waves to simulate electron heating in ECRIS plasma.

4.2 Full Wave Simulation of Waves in ECRIS Plasmas based on Finite Element Method (FEM)

This section presents a new full wave simulation model in which Maxwell's equations are solved using the COMSOL Multiphysics FEM solver in presence of a plasma described by input parameters are provided by a dedicated routine running in MATLAB. We exploit COMSOL's ability to accept 3D space-varying dielectric tensor (computed in Matlab) and to solve wave equation in the inhomogeneous, anisotropic and lossy plasma produced in the multi-mode ECRIS cavity, taking into account a realistic electron density and the so called B-min magnetic field confining the plasma. The simulations include energy absorption by the plasma and the presence of lossy cavity walls.

A proper mesh generation, exploiting FEM based COMSOL versatility, allowed us to optimally model ECRIS cavity and microwave waveguide launching structure, with a good computational efficiency and high resolution of the solution especially around the resonance regions. Numerical simulations have been performed in the frequency domain: in the resonance regions especially, the material properties exhibit a spatial variation that leads to a large sparse ill–conditioned matrix which is solved by MUltifrontal Massively Parallel Solver (MUMPS) direct method. We implement a method to perform full wave simulations considering a cold plasma model for the constitutive relations; the obtained results show that the ECR layer presence, along with the cavity walls, strongly influences the shape and strength of the electromagnetic field distribution, featuring a strong non-uniformity of the main electromagnetic parameters.

All the relevant details have been considered in the model including the nonuniform external magnetostatic field used for plasma confinement, the local electron density profile and the full-3D nonuniform magnetized plasma complex dielectric tensor. The results of the simulations are compared to experimental measurements. This represents a new approach to solve wave propagation in an inhomogeneous anisotropic cold plasma considering a position dependent non-axial magnetic field - in order to explore in more detail the problem of RF energy deposition in microwave generated linear plasmas confined by non-axisymmetric magnetostatic fields, under unfavourable conditions of small vessel-size-over-wavelength ratio. *In these small devices, where the typical dimension are often comparable with wavelength of the injected RF wave, the effects of the vessel walls cannot be neglected (i.e. the waves cannot be assumed as plane waves propagating in free space) and a full-wave calculation including multireflections and "cavity scrambling" effects must be invoked. This represents a significant step forward with respect to other approaches already attempted in the past [83].*

4.2.1 Electromagnetic formulation of wave equation in plasma

As we extensively explained in chapter 2, under the influence of a magnetic field, a plasma exhibits an anisotropic electric behaviour and can be modeled introducing anisotropic constitutive relations where the permittivity is a second order tensor. In order to have a more compact and focused treatment, we resume in this section only the most important equation implemented and solved by our code. Considering the plasma a dispersive medium modeled as a cold magnetofluid with collisions, Maxwell's equations and constituive relation for source-free, anisotropic media, using harmonic time dependence $e^{j\omega t}$, can be written as:

$$\nabla \times \mathbf{E}(\mathbf{r}) = \mathrm{i}\omega \mathbf{B}(\mathbf{r}) \tag{4.1a}$$

$$\nabla \times \mathbf{H}(\mathbf{r}) = -\mathrm{i}\omega\epsilon_0 \mathbf{E}(\mathbf{r}) + \mathbf{J}(\mathbf{r}) = -\mathrm{i}\omega\bar{\bar{\epsilon}} \cdot \mathbf{E} \tag{4.1b}$$

where

$$\mathbf{J} = \bar{\bar{\sigma}}\mathbf{E} \tag{4.2a}$$

and

$$\bar{\bar{\epsilon}} \cdot \mathbf{E} = \epsilon_0 \mathbf{E} + \frac{\mathbf{J}}{-\mathrm{i}\omega} = \left(\epsilon_0 + \frac{\bar{\bar{\sigma}}}{-\mathrm{i}\omega}\right) \cdot \mathbf{E} \tag{4.2b}$$

Displacement $\mathrm{i}\omega\epsilon_0\mathbf{E}(\mathbf{r})$, and conduction $\mathbf{J}(\mathbf{r})$ currents are collected in a tensorial term describing the field-plasma interaction introducing the dielectric tensor:

$$\bar{\bar{\epsilon}} = \epsilon_0 \left(\bar{\bar{I}} + \frac{\mathrm{i}\bar{\bar{\sigma}}}{\omega\epsilon_0}\right) \tag{4.3}$$

Eliminating the magnetic field between (4.1a) and (4.1b) and using constitutive relations, we obtain the wave equation:

$$\nabla \times \nabla \times \mathbf{E} - \frac{\omega^2}{c^2}\overline{\overline{\epsilon_r}} \cdot \mathbf{E} = 0 \tag{4.4}$$

The above equation (4.4) can be solved as a driven problem by a FEM solver that supports a non homogeneous tensorial constitutive relation.

Dielectric tensor formulation

In [36], the wave equation (4.4) is analyzed in free space for plane waves and the dielectric tensor $\overline{\overline{\epsilon}}$ is derived by assuming the applied magnetic field as being aligned to one of the coordinate axes (tipically, z-axis)[80]. This assumption does not cause only loss of generality in most of cases where B_{0_x}, $B_{0_y} \ll B_{0_z}$, but not in ECRIS because the magnetic field structure is obtained by a superimposition of solenoidal and hexapolar coils creating a "quasi-axisymmetric" nonuniform magnetostatic field, called "B-min" structure (Fig. 4.1).
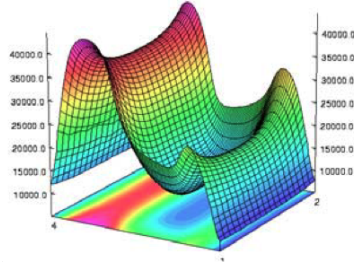
Fig. 4.1. Minimum-B Magnetic field structure

Therefore, in order to obtain a generally valid solution, it is essential that constitutive parameters are formulated in a general orthogonal cartesian coordinate system.

In cold plasma approximation [36], the determination of $\overline{\overline{\epsilon}}$ is based on the equation of motion for single particle:

$$(-\mathrm{i}\omega + \omega_{\mathrm{eff}})\mathbf{v} + \frac{e}{m_e}\mathbf{B}_0 \times \mathbf{v} = \frac{e}{m_e}\mathbf{E} \tag{4.5}$$

Solving (4.5) in $\mathbf{v}$ and using the constitutive relation:

$$\mathbf{J} = N_0 q \mathbf{v} = \overline{\overline{\sigma}} \cdot \mathbf{E} \tag{4.6}$$

we can obtain $\overline{\overline{\sigma}}$ that is related to $\overline{\overline{\epsilon}}$ as we can see in (4.1b) and (4.2b).

Finally $\overline{\overline{\epsilon}}$ is:

$$\bar{\bar{\epsilon}} = \epsilon_0 \bar{\bar{\epsilon}}_r = \epsilon_0 \left(\bar{\bar{\epsilon'}} + i\bar{\bar{\epsilon''}} \right) = \epsilon_0 \left(\bar{\bar{I}} + \frac{i\bar{\bar{\sigma}}}{\omega\epsilon_0} \right) =$$

$$= \epsilon_0 \begin{bmatrix} 1 + i\dfrac{\omega_p^2}{\omega}\dfrac{a_x}{\Delta} & i\dfrac{\omega_p^2}{\omega}\dfrac{c_z + d_{xy}}{\Delta} & i\dfrac{\omega_p^2}{\omega}\dfrac{-c_y + d_{xz}}{\Delta} \\ i\dfrac{\omega_p^2}{\omega}\dfrac{-c_z + d_{xy}}{\Delta} & 1 + \dfrac{j\omega_p^2}{\omega}\dfrac{a_y}{\Delta} & i\dfrac{\omega_p^2}{\omega}\dfrac{c_x + d_{yz}}{\Delta} \\ i\dfrac{\omega_p^2}{\omega}\dfrac{c_y + d_{xz}}{\Delta} & i\dfrac{\omega_p^2}{\omega}\dfrac{-c_x + d_{zy}}{\Delta} & 1 + i\dfrac{\omega_p^2}{\omega}\dfrac{a_z}{\Delta} \end{bmatrix} \tag{4.7}$$

where $a_m = (-i\omega + \omega_{\text{eff}})^2 + B_{0_m}^2 \left(\frac{e}{m_e} \right)^2$, $c_m = B_{0_m} \left(\frac{e}{m_e} \right) (-i\omega + \omega_{\text{eff}})$,

$d_{mn} = B_{0_m} B_{0_n} \left(\frac{e}{m_e} \right)^2$ with $m = x, y, z$, $n = x, y, z$ and

$$\Delta = (-i\omega + \omega_{\text{eff}})a_x + B_{0_z} \left(\frac{e}{m_e} \right)(c_z - d_{xy}) + B_{0_y} \left(\frac{e}{m_e} \right)(c_y + d_{xz}).$$

$\bar{\bar{\epsilon'}}$ is the real part of relative permettivity $\bar{\bar{\epsilon}}_r$, $\bar{\bar{\epsilon''}}$ is the imaginary part, ω the angular frequency of the microwave, $\omega_p = \sqrt{\frac{n_e e^2}{m_e \epsilon_0}}$ the plasma oscillation angular frequency, n_e the electron density, m_e the electron mass, e the electron charge, j the imaginary unit and ω_{eff} the collision frequency; the latter accounts for the collision friction (thus modeling wave damping) and resolves the singularity of some elements of (4.7).

At the electron cyclotron resonance (ECR) layer, where $|B_0(x, y, z)| = B_{ECR}$ and $\omega_c = \frac{eB_0}{m_e} = \omega$, Δ becomes very small, resulting in an strong variation of $\bar{\bar{\epsilon}}_r$. Depending on the values of ω, ω_p and ω_{eff}, $\bar{\bar{\epsilon}}$ and the correlated wave vector $k = k_{real} - jk_{im}$ can have real or imaginary part, therefore different wave propagation or attenuation scenarios are possible.

In [83], authors investigate only some specific scenarios, since the anisotropic plasma is approximated by an isotropic dielectric with the refractive index of R-wave [84]. This can be done only for plane wave with a precise polarization and a fixed angle between **k** and **B**$_0$ that allows to replace the tensor (4.7) with a scalar quantity, i. e. the refraction index of either ordinary or extraordinary waves that can be analitically computed.

Our generalized formulation, that considers the cold plasma electromagnetic modes, allows us to consider in 3D simulations the full tensorial properties of the magnetized plasma we are dealing with, evaluating the plasma response on electromagnetic wave propagating inside ECRIS cavity. In the following we do not consider any particular propagation mode or a specific angle between **k** and **B**$_0$, taking into account any multiple scattering of the waves at chamber walls and considering arbitrary propagation angle at whatever point into the plasma.

The plasma density profile and background magnetic field, included via ω_p and ω_c, respectively, can be of arbitrary shape on the simulation domain.

4.2.2 3D RF Numerical Simulations

Model definition

The cylindrical cavity representing the plasma chamber is a metallic box connected to a microwave source via a rectangular waveguide operating in the TE_{10} mode. Figure 4.4 shows the geometry and in Table 4.1 all the important simulation input parameters are listed. Many geometrical details of ECRIS assembly can be removed in order to reduce the computational costs without any loss in the approach validity.
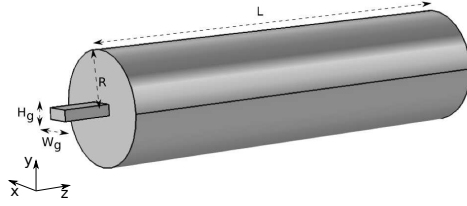
Fig. 4.2. Simulated Geometry: Cavity and waveguide.

Table 4.1. Simulation input parameters.

Parameter	Value	Description
L	480 [mm]	Cavity length
R	65 [mm]	Cavity radius
ν_{RF}	8 [GHz]	Frequency
ω_{RF}	$2\pi\nu_{RF}$ [rad/s]	Angular frequency
ω_{eff}	$\omega_{RF}/10^3$ [rad/s]	Collision frequency
W_g	28.5 [mm]	Waveguide width
H_g	12.6 [mm]	Waveguide height
P_{RF}	100 [W]	RF Power

High computational costs of the FEM simulations for large problems with high frequency, lead us to consider a slighty lower frequency (8 GHz however), as a first step, with respect to the typical operational frequencies ($\nu_{RF} > 10$ GHz) of second generation ECRIS. We chose this frequency value, much higher than the fundamental resonant frequency of the empty cavity, to be sure that we have enough degree of freedoms to excite an electromagnetic field distribution pattern with a large azimuthal and longitudinal mode number.

The inner cavity volume is filled by lossy plasma characterized by dielectric tensor (4.7). The lossy cavity walls are modeled via the appropriate 'impedance boundary

condition' [85]. The magnetostatic field can be modelled in a 3D environment according to the following equations: $B_{0_x} = x(-B_1 z + 2S_{ex}y)$, $B_{0_y} = -B_1 yz + S_{ex}(x^2 - y^2)$, $B_z = B_1 z^2 + B_2$, where S_{ex} is a constant related to the hexapole field, and B_1 and B_2 are related to the solenoid ones. Fig. 4.3 displays the electron density n_e and magnetostatic profile $\mathbf{B}_0$ along the line $(x = 0, y = 0, z)$, used as simulation input parameters, in the normalized form:

$$X = \frac{\omega_p^2}{\omega^2} = \frac{n_e e^2}{m_e \epsilon_0} \frac{1}{\omega^2}$$

,

$$Y = \frac{\omega_c}{\omega} = \frac{e|B_0|}{m_e} \frac{1}{\omega}$$

Absolute values of n_e profile are shown in the right-hand vertical axis of Fig. 4.4. The density profile comes from modeling on plasma dynamics and heating in [86]: the plasma density distribution into an ECRIS splits into two different regions: *i)* a dense volume enclosed by the iso-magnetic surface corresponding to ECR condition (and called 'plasmoid') and *ii)* a rarefied halo made of particles escaping or flowing out from the plasmoid. Then we used an electron density "gaussian" profile showing a flat top shape into the plasmoid and a rapid decrease from ECR layers towards the plasma chamber walls.

We started by setting as maximum density, located at the center of the chamber $(z = 0)$, $n_{max} = 0.1n_c$ where $n_c = \frac{\omega^2 \epsilon_0 m_e}{e^2}$ is the cutoff density of the ordinary wave [36]. These data allow to compute in MatLab environment, the full anisotropic tensor $\bar{\bar{\epsilon}}(x, y, z)$, whose $\bar{\bar{\epsilon}}_{11}$ element is plotted as example along z-axis in Fig. 4.5. The problem is finally solved in two stages: first we compute in Matlab environment the full anisotropic tensor (4.7), then the wave equation is solved by using the direct linear system solver MUMPS [87] of COMSOL.

Mesh generation

Mesh creation procedure is a critical issue for a FEM simulation: it significantly impacts on rate of convergence, solution accuracy and CPU time required. An unstructured tetrahedral mesh is needed, with a mesh density high enough to capture all relevant electromagnetic features, especially in ECR zone where $|B_0(x, y, z)| = B_{ECR}$ where, in a very thin layer, dielectric permittivity changes very rapidly (see Fig. 4.5). This implies a non-uniform mesh density that has to strongly increase around the ECR layer. In our case this was done by individuating the iso-surface $|B_0(x, y, z)| = B_{ECR}$ (that can be computed and reproduced in COMSOL) working as a reference surface for starting mesh construction and growth. The mesh size is kept very small close to this surface, and grows with a controllable rate to keep as low as possible the computational costs. COMSOL mesh generation flexibility allowed to obtain a very high
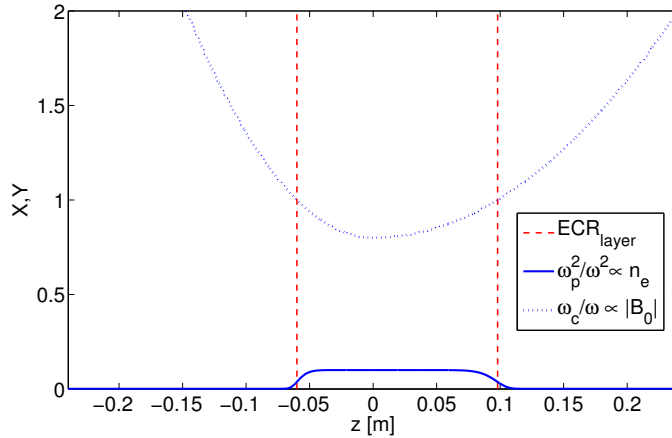
Fig. 4.3. Profiles of X= ω_p^2/ω^2 (proportional to n_e) and Y= ω_c/ω (proportional to B_0) along the longitudinal z-axis, used as input parameters to compute the permettivity tensor for 3D simulation. The dash vertical lines highlight the ECR layer positions.
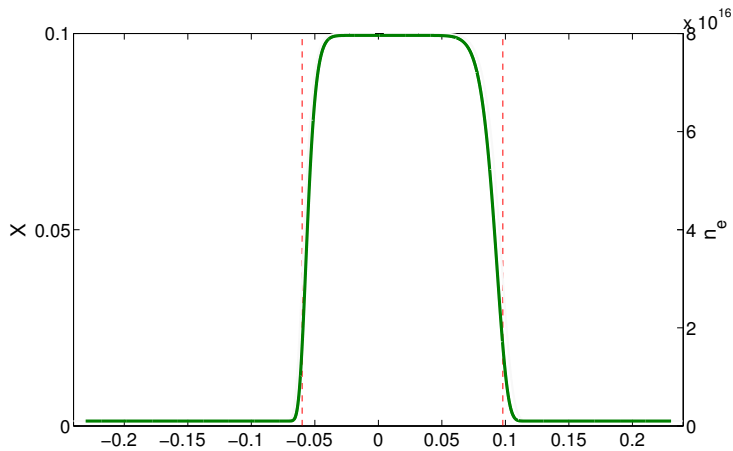
Fig. 4.4. Zoom of the profiles of X= ω_p^2/ω^2 (proportional to n_e) and (on the right) n_e along the longitudinal z-axis, used as input parameters to compute the permettivity tensor for 3D simulation. The dash vertical lines highlight the ECR layer positions.

mesh quality even though we addressed a critical problem with non smooth surfaces potentially leading to tetrahedrons with poor aspect ratio. Figure 4.6(a) shows spatial distribution of the mesh size, which becomes very small around the ECR closed surface where the refractive index is subjected to very large oscillations. Figure 4.6(b) shows the absolute size of the tetrahedrons along the longitudial z-axis.

Computational issues

We put several efforts to check computational accuracy and the convergence of the chosen mesh refinement strategy. FEM solution of the electromagnetic problem of
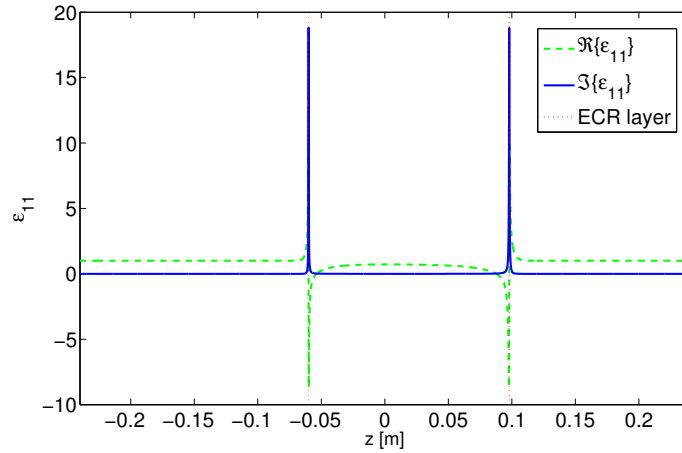
Fig. 4.5. Real and Imaginary part of ϵ_{11}: they are peaked at ECR layer
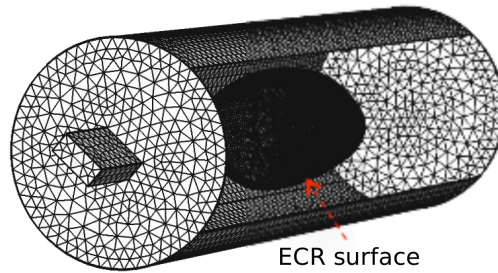
(a) Non-uniform mesh density accounting for ECR layer.
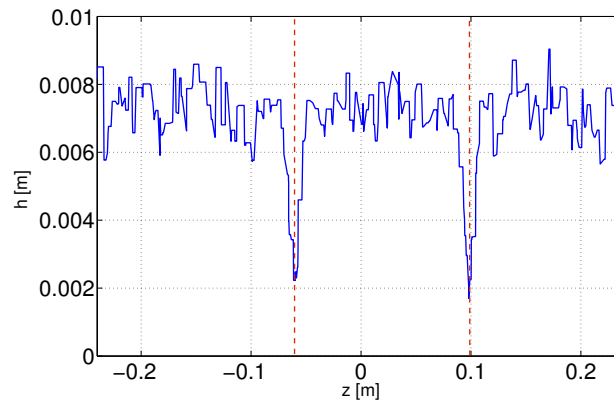
(b) Mesh element size h along longitudinal z-axis. The dash vertical lines highlight the ECR layer positions.

Fig. 4.6. Mesh generated in COMSOL.

waves propagating into an anisotropic medium (the magnetized plasma) is a very difficult computational effort especially because of the strong fluctuation in the refractive index. Despite the mesh strategy discussed above, the setup leads to very ill–conditioned linear, sparse, complex, non-symmetric systems. To avoid convergence

problems and slow convergence rate, we used Direct COMSOL Sparse linear system solver MUMPS [87], solving models with more than 4 million of unknowns with the aid of a computer equipped of four 2.70 GHz eight-core Intel® Xeon® E5-4650 Processors, with 256 GB of RAM[1]. Usually the standard convergence criterion adopted by commercially available simulators, implements an adaptive mesh refinement, that is based on the evaluation of the solution's error between two consecutive passes. This philosophy is not applicable in a direct resolution scenario which does not require iterations and does not include convergence criteria (only round-off error checks). We were therefore forced to individuate a proper mesh refinement criterion; the **electromagnetic power loss density P_{loss} was individuated as a physically most significant parameter** that, as shown in the previous pages, critically depends on the wave dynamics in near resonance zones where k, $\bar{\bar{\epsilon}}$ and **E** strongly fluctuate and the mesh size accuracy is of particular relevance. This parameter was evaluated for simulations with different mesh densities in order to make sure that results are mesh independent. In Table 4.5 different mesh setup are shown: five mesh elements per wavelength [2] are sufficient to obtain a convergent P_{loss}, whose value varies less than 0.4 %.

Table 4.2. Summary of results: simulations performed on 4 eight-core Intel® Xeon® 2.70 GHz E5-4650 Processors, 256 GB RAM.

maximum element size	# of tetrahedra	DoF	CPU time	RAM [GB]	**Power loss [Watt]**
$\lambda/4$	407473	$2.58E^6$	51 min, 24 s	129	73.43 W
$\lambda/5$	430200	$2.73E^6$	1h, 6 min	133	72.94 W
$\lambda/7$	520031	$3.31E^6$	1h, 12 min	158	72.80 W
$\lambda/8$	597284	$3.80E^6$	2h, 2 min	193	72.51 W

Simulation Results

Hereinafter we show the most important simulation results. We formerly investigated the overall impact of the plasma contained into the chamber on the cavity-electromagnetic field distribution. It is noticeable how the typical standing wave pattern of a vacuum resonating cavity, (Fig. 4.7), is strongly perturbed when the plasma filled cavity is considered (Fig. 4.8). Moreover, we can clearly see in Fig. 4.8 and Fig. 4.9 that, when electromagnetic wave approaches the resonance zones, the electric field increases up to almost one order of magnitude. On the other hand, an attenuation of electric field on z-axis (Fig. 4.10) is evident, as already seen in [86] for electron

---

[1] upgraded now to 512 GB.

[2] this number refers to the minimum mesh density outside the ECR critical surface.

density distribution that shows a 'hole' in near axis zone, due to electromagnetic field distribution pattern.
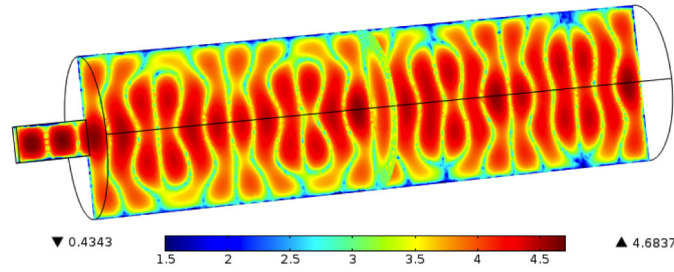
Fig. 4.7. $\log_{10}(|E|+1)$ in vacuum chamber (false color representation)
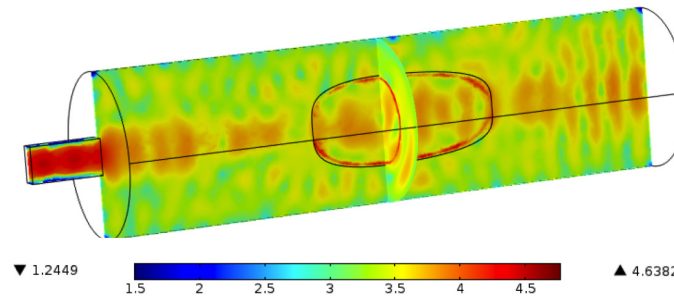
Fig. 4.8. $\log_{10}(|E|+1)$ in plasma filled chamber (false color representation)

In addition, on the resonance surface the imaginary part of wave vector k_{im}, (see Fig. 4.11), is peaked and the microwave power is damped because the electric field decreases as $e^{k_{im}r}$; in these zones the dissipated power density, shown in Fig. 4.11, achieves its maximum value. In Fig. 4.12 we show the dissipated power density by multislice representation (3D): it is evident that the most part of the power is absorbed at the ECR layer. ***At the frequency of 8 GHz, the 95% of input RF Power is absorbed from lossy plasma and only the 0.3% is dissipated from copper cavity walls***. The other relevant result is that the electromagnetic field is not uniformly distributed on ECR surface and it produces a non uniform power loss density distribution on ECR surface as it can be seen in Fig. 4.13. This result is consistent with the experimental data and the plasma modeling [88], suggesting that the RF energy is not uniformly deposited inside the plasma core, being affected by quasi-modal structures established in the plasma filled cavity. As a general comment the above presented results are in agreement with theory and represent an important step forward in ECRIS plasma comprehension with respect to older studies [80].
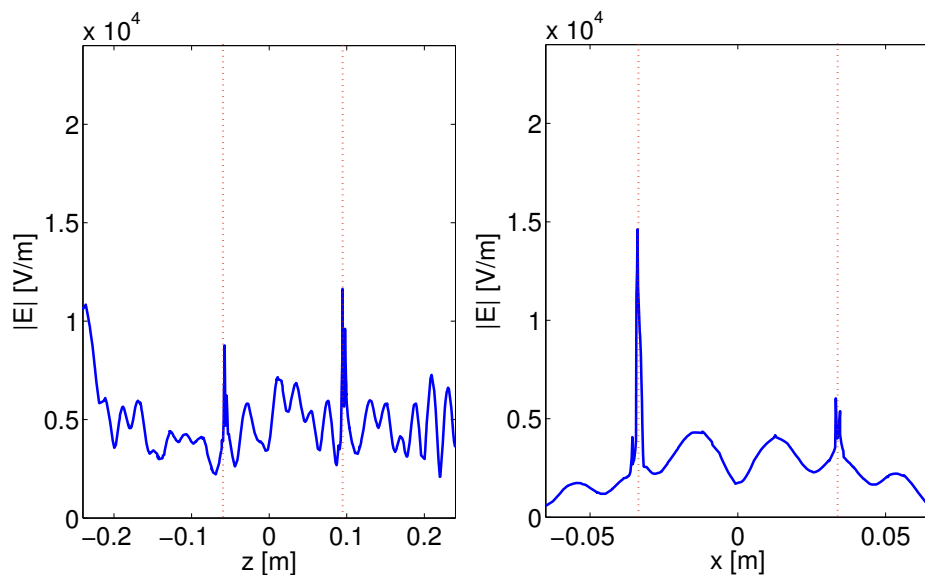
Fig. 4.9. Electric field on a off-axis longitudinal line (x=0.01, y=0, z), parallel to z-axis, and along the transversal direction x (x, 0, 0) . The red dotted lines highlight the ECR layer positions.
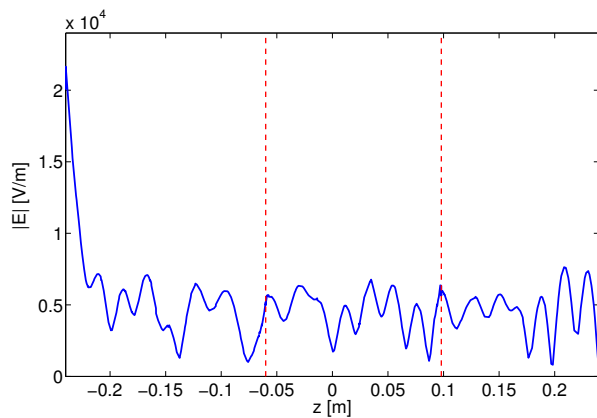
Fig. 4.10. Electric field along z-axis (x=0, y=0, z). The red dot lines highlight the ECR layer positions

The model versatility allows to solve and evaluate the effects on electromagnetic field propagation and absorption by using different ion source operating parameters, as different electron density n_e profiles (see Fig. 4.14), while keeping a Gaussian profile in all simulations. This parametric study has been done for an ECRIS cavity operating at 5 GHz, in order to further decrease the computational time.
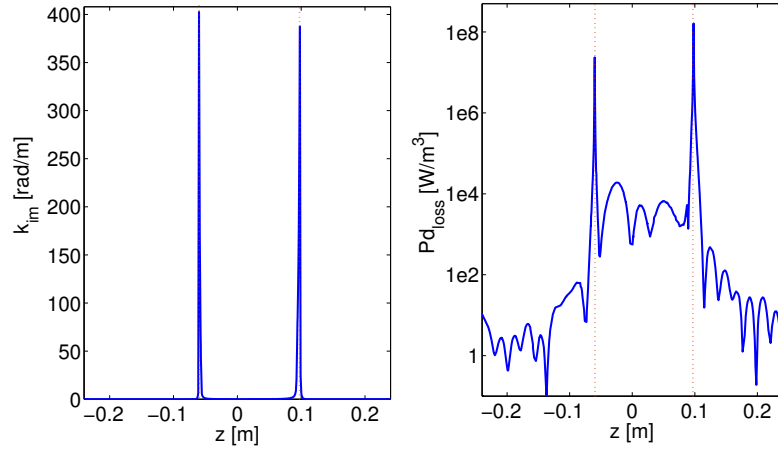
Fig. 4.11. k_{im} and power loss density Pd_{loss} along z-axis. At ECR layers(red dot lines) k_{im} and Pd_{loss} show a maximum.
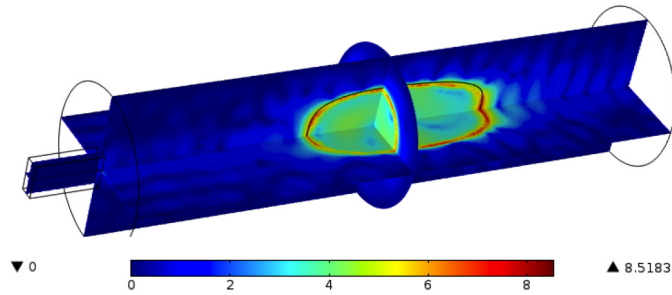
Fig. 4.12. Electromagnetic power loss density $[W/m^3]$ (logarithmic scale)

In Figure 4.15, it is shown the electric field on the z-axis when simulating the different n_e profiles. Thereinafter they will be labeled then as #1-#4 (for respectively, $\frac{max(n_e)}{n_c}$=0.1, 0.5, 0.9 and 1.2).

Two results should be highlighted in Fig. 4.15: *a)* for the **#3** profile there is a sort of "cavity effect" and a field amplification in the inner plasmoid region (plasma resonant effect) occurs, ascribable to the discontinuity at ECR layers, that is very similar to what has been observed in [80] in a simpler configuration; *b)* when $n_e > n_c$ (**#4 profile**)[3], the wave still propagates into the plasmoid without appreciable attenuation. In the case #3, inside the plasmoid k_{real} (Fig. 4.16) becomes very small, producing a greater discontinuity of the propagation constant from inside to outside the plasmoid.

---

[3] that is traditionally called "overdense" plasma condition in which, the upper limit of density n_c, allowing field propagation in ECRIS plasmas, is overcome
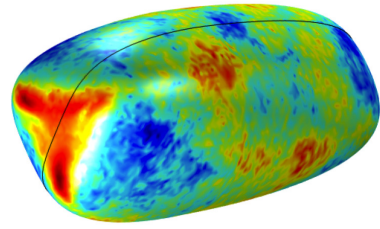
(a) Electromagnetic power loss density (W/m^3) on

ECR surface (left side view)
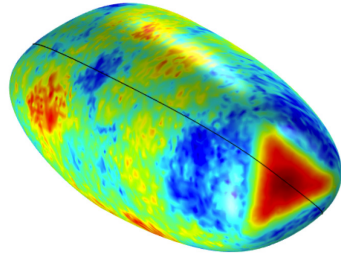
(b) Electromagnetic power loss density (W/m^3) on

ECR surface (right side view)

Fig. 4.13. Non uniform distribution of electromagnetic power loss density on ECR surface.
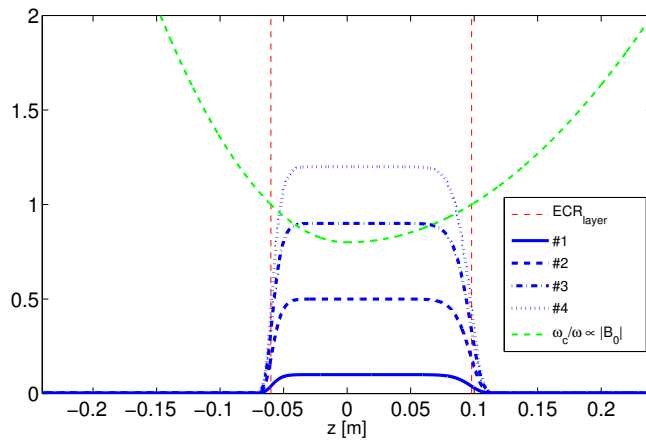
Fig. 4.14. Different n$_e$ profiles used for simulations.
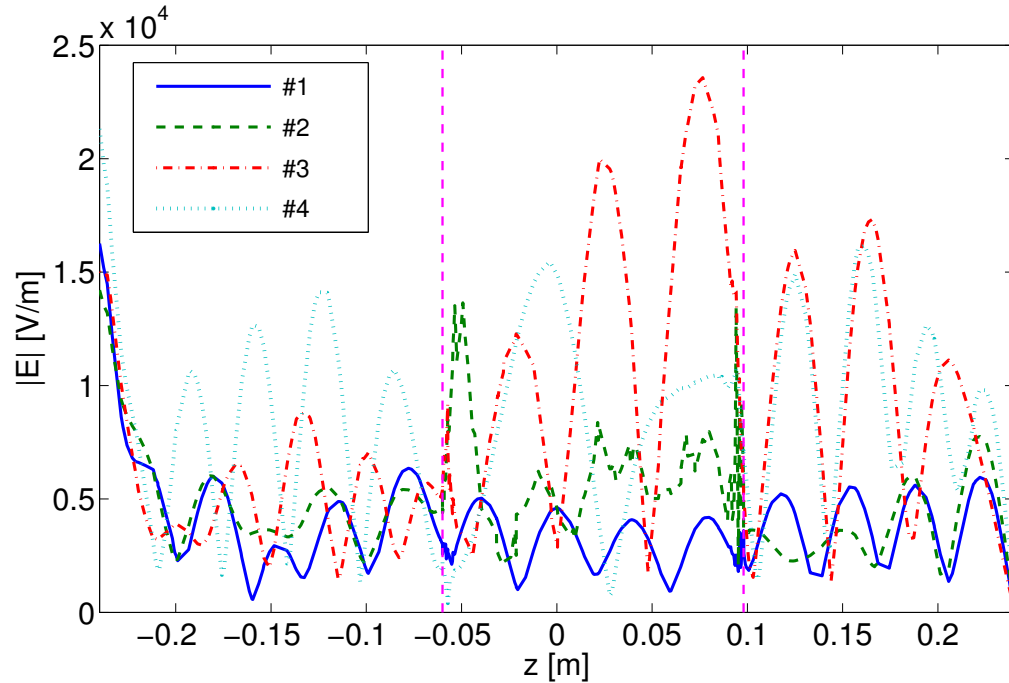
Fig. 4.15. Electric field along z-axis for different density profiles

The cavity effect provided by the plasma, producing the mentioned inner resonance field amplification, is more evident by looking Fig. 4.17: it compares 3D electric field distribution for low density (#1) and quasi-critical plasma density (#3) condition. Increasing the plasma density both Fig. 4.18 and Fig. 4.19 show that the inner plasmoid electromagnetic loss power increases (Fig. 4.20). The case #4, showing a propagating mode also inside the plasmoid, supports our claim that a restrictive plane wave analysis, as done in [80] is not feasible in ECRIS-like configuration where a full-wave approach becomes mandatory. To verify that the proposed model is capable to capture new physics, we carried ut a test simulation with a oversimplified model a pure scalar refraction index is considered. As a benchmark Fig. 4.21 shows the damping effect inside an overdense plasmoid considering – in a simplified model – only an equivalent O-wave refractive index.

In contrast to predictions of plane waves dispersion theory, summarized by Clemow-Mullaly-Allis CMA diagram, in a bounded plasma a finite propagation occurs even through the plasma regions where $X > 1$. The classical wave screening, as predicted by the plane wave model, fails due to phase mixing and superposition of reflected waves from the conducting boundaries, leading to the formation of electromagnetic standing wave modes.
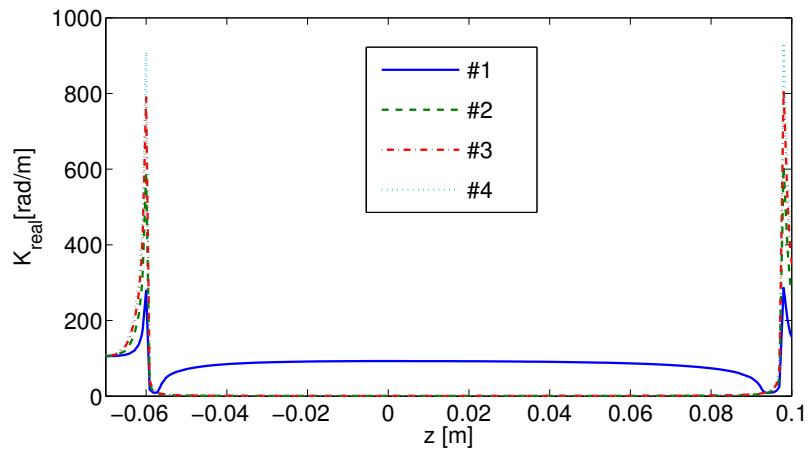
Fig. 4.16. Propagation constant k_{real} (rad/m) along longitudinal z-axis
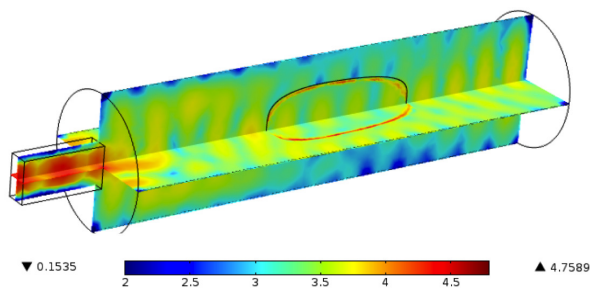
(a) $\log_{10}(|E|+1)$: Electric fied on multislice with # 1 density profile
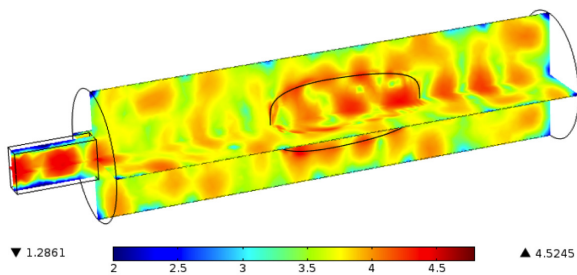
(b) $\log_{10}(|E|+1)$: Electric fied on multislice with # 3 density profile

Fig. 4.17. Electric fied at two different density profile
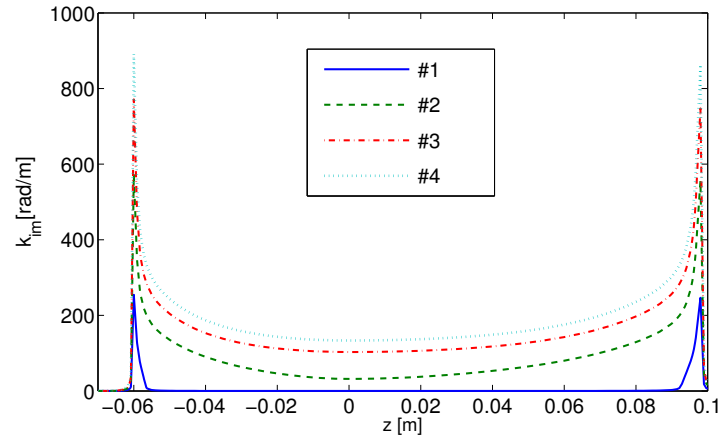
Fig. 4.18. Attenuation constant along longitudinal z-axis
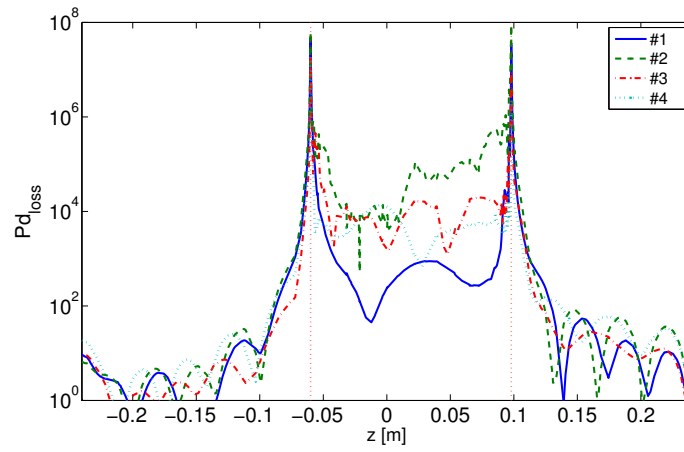
Fig. 4.19. Power loss density Pd_{loss} over z-axis. At ECR layers(red dot lines) Pd_{loss} show a maximum.

Table 4.3. Summary of simulation results at 8 GHz

Simulation Setup	P_{loss} [W]	E_{max} [V/m]
#1	72,9	6.3e5
#2	79	2.9e5
#3	39.3	4e5
#4	35.5	2.5e4

(a) Power loss density with # 1 density profile

(b) Power loss density with # 3 density profile
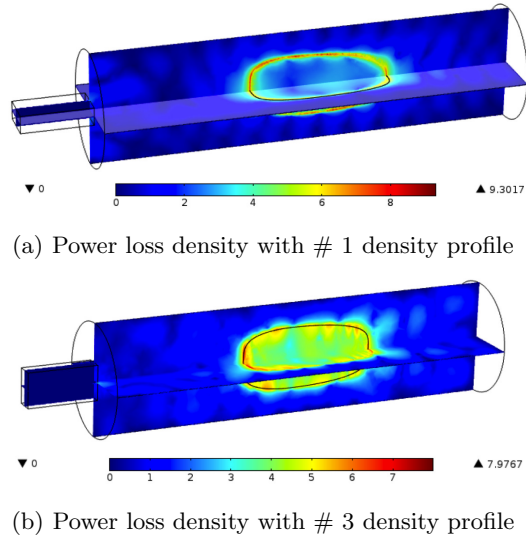
Fig. 4.20. Electromagnetic power loss density $[\text{W/m}^3]$ (logarithmic scale)
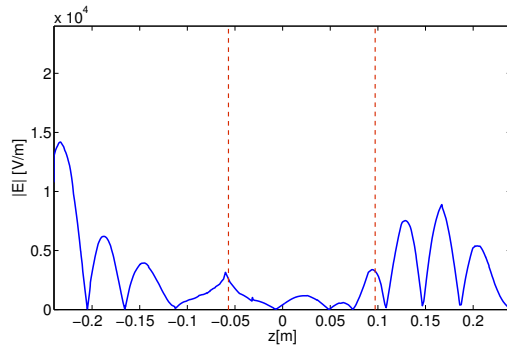
Fig. 4.21. Oversimplified model: Electric field along z-axis. The red dash lines highlight the ECR layer positions.

In Table 4.3 some important simulation results are listed as a summary of the analysis described. It demonstrates how strong is the effect of the plasma load on coupling properties.

4.3 Full-wave plus kinetic calculations: a "stationary" Particle in cell (PIC) code

In the above model, we assumed a n_e profile as a given. Numerical solution of Vlasov equation via kinetic codes coupled to FEM solvers is described in this section, based on a Particle In Cell (PIC) strategy, that we have termed "stationary" PIC for its pecurialities presented hereinfater .

4.3.1 Particle method

Our approach is based on a numerical particles-in-cell or "particle" method to approximate the distribution as a probability distribution function, according to the Klimontovich formalism [38]. The Vlasov theory for studies of plasma waves and wave-particle interactions starts from the mean-field Vlasov equation as kinetic model of a collisionless plasma with distribution function f_α:

$$\frac{\partial f_\alpha}{\partial t} + \mathbf{v} \cdot \frac{\partial f_\alpha}{\partial \mathbf{r}} + \frac{q_\alpha}{m_\alpha}(\mathbf{E} + \mathbf{v} \times \mathbf{B}) \cdot \frac{\partial f_\alpha}{\partial \mathbf{v}} = 0 \tag{4.8}$$

with m_α and q_α mass and charge of the α species. We consider here a plasma consisting of a single species only (electrons), so that m_e and e denote electron mass and charge respectively. We retrieved the electromagnetic field found through the 3D numerical simulations described in the previous section. Plasma self-generated electrostatic potentials are not included into the simulation model, since their implementation would result in additional computational costs. Being relevant in the sheath region especially (i. e. in proximity of the source extraction) their effect can be excluded at this stage.

In the PIC approach to Vlasov equation we can consider a plasma as a collection of N macro-particles (being N much smaller than real plasma particles), with corresponding spatial coordinates and momenta described by the functions $\mathbf{r}_i(t)$ and $\mathbf{p}_i(t)$. These functions can be viewed as trajectories in the six-dimensional single-particle phase space. The phase space density is thereby described by the Klimontovich distribution function:

$$f_\alpha(\mathbf{r}, \mathbf{v}, t) = \sum_{i=1}^{N} \delta(\mathbf{r} - \mathbf{r}_i(t))\delta(\mathbf{p} - \mathbf{p}_i(t)) \tag{4.9}$$

The trajectories obey the equations:

$$\frac{d\mathbf{r}_i}{dt} = \mathbf{v}_i(t) \tag{4.10a}$$

$$\frac{d\mathbf{p}_i}{dt} = q\left[\mathbf{E}(\mathbf{r}_i(t), t) + \mathbf{v}_i(t) \times \mathbf{B}(\mathbf{r}_i(t), t)\right] \tag{4.10b}$$

since according to the Vlasov equation the particle distribution function is constant following the particle motion.

Our Particle method simulates a plasma system by following a number of particle trajectories that obey the single particle equations of motion (4.10), including external RF field (electric and magnetic) and the superimposed magnetostatic field ensuring plasma confinement. By the point of view of RF energy absorption and electron density response to cavity mode structures, in fact, ions can be ignored considering their high inertia relatively to the high frequency domain. A specific routine of the developed computer code has been dedicated to particle motion (hereinafter called "particle mover routine", or simply "Particle Mover"): we used the Boris' scheme including relativistic electron mass variation [89].

Mean field definition

In this perspective, equation (4.8) can be linearised, splitting the distribution function into a stationary (or equilibrium) f_{e0} and an oscillating f_{e1} part:

$$\left[\frac{\partial}{\partial t} + \mathbf{v} \cdot \frac{\partial}{\partial \mathbf{r}} + \frac{e}{m_e} (\mathbf{v} \times \mathbf{B}_0) \cdot \frac{\partial}{\partial \mathbf{v}} \right] f_{e1} =$$
$$= -\frac{e}{m_e} (\mathbf{E}_1 + \mathbf{v} \times \mathbf{B}_1) \cdot \frac{f_{e0}}{\partial \mathbf{v}} \tag{4.11}$$

As an approximation of f_{e0}, we will initialize the particles position by a random sampling weighted on a presetted initial background density, while the velocities can be taken from a Maxwellian velocity distribution given by Gaussian distribution in the three axes with standard deviation $\sigma = \sqrt{\left(\frac{kT_e}{m_e} \right)}$, assuming initial electron temperature $T_e = 1$ eV. Then, the particles phase space evolves according to deterministic equations of motion (4.10). The 3D PIC code is coupled to Maxwell's equations (4.1)

The overall simulation strategy is depicted in figure 4.22. The method is based on a strict interplay between COMSOL solver and the particle mover implemented in MATLAB. Several loops are expected to be needed in order to get convergence. Due to huge time-consuming calculations needed at each loop-step k, hereby we show results up to step 2, i.e. after evaluation of RF action on electrons and vice-versa, for two times.
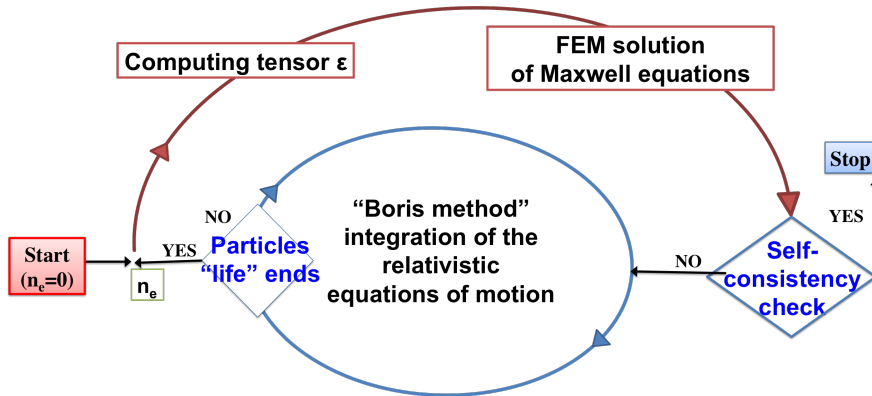
Fig. 4.22. Diagram showing the simulation strategy.

Our code does not assume any rotational symmetry for the magnetostatic field, so that the real 3D external B field (B-minimum) is taken into account, thus retrieving the permittivity tensor (4.7) [55]:

The numerical code uses a numerical artifice to consider a well defined statistical sample and accumulate statistical information (positions and velocities) for all the life of the sample itself: in other terms, the "Particle Mover" code solves the equation of

motion (4.10) of each single macro-particle for its entire life, accumulating the electron density in 3D grid. In this sense, our approach can be defined as a "stationary" PIC. In a classical PIC scheme, field calculation is done at each (very small) time step, then particles are let to evolve for very short times in the kinetic part of the code assuming a "frozen" RF field.

Particles move inside a 3D frame entering different cells: the plasma chamber domain is subdivided into $200 \times 200 \times 600 = 24 \cdot 10^6$ cells (so obtaining a sub-mm^3 precision) thanks to a uniform spatial grid spacing $\Delta x = \Delta y = \Delta z = 0.5$ mm. In a time-integration view, the fields are calculated from an initial charge and current density, then the particles move for a small distance over a short Δt, finally the fields are recalculated according to the new phase space configuration, by repeating this procedure for N time steps. Conversely, we assume the stationary case where a sample of macroparticles followed for their entire life (i.e. until they impinge on the chamber walls, meaning they have been lost by plasma confinement system) describes the stationary structure of the plasma in the phase space, through the "trick" of density accumulation in a 3D grid; the density accumulation is made as single particles paths evolve in the volume contained into the plasma chamber. Indeed, we assume a stationary electromagnetic field as well.

With the simulation parameters listed in Table 5.2, we can follow 300000 electrons/5h, with a average electron life time T_{life}=27 μs. We also consider electrostatic (Spitzer) collisions at 90° between electrons as a stochastic Poisson process, so that the time-dependent probability between each pair of consecutive events (electron collisions) has an exponential distribution with parameter $1/\tau_{90°}$. Evaluating the position (therefore the density) inside the chamber, we can extract a collision probability $P(t) = 1 - e^{-\left(\frac{t}{\tau_{90°}}\right)}$ at time t and density n_e that depends on $\tau_{90°} = \dfrac{m_e^2 2\pi\epsilon_0^2 v_e^3}{n_e e^4 ln\Lambda}$, i.e. the mean time between two collisions. At each fixed integration time, we compare the collision probability with a randomly extracted number and if a collision occurs a new direction is assigned to the electron by rotating its velocity vector of 90°.

4.4 Simulation results

In ECRIS, electrons are resonantly heated by hundred of watts (or even few kW) of microwave power in the GHz range. RF is normally coupled to the plasma chamber through a rectangular waveguide. As already done for full-wave only calculations, the electromagnetic model can be simplified without loosing information assuming a simplified cylindrical chamber geometry, with a single on-axis microwave injection rectangular waveguide. Ii is is shown Fig. 4.23 as it was modelled for calculating RF field in our simulation.
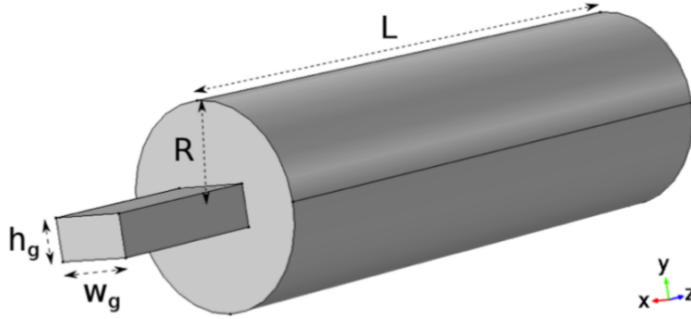
Fig. 4.23. Simulated Geometry: Cavity and waveguide.

Table 4.4. Simulation input parameters.

Parameter	Value	Description
L	300 [mm]	Cavity length
R	50 [mm]	Cavity radius
ν_{RF}	5 [GHz]	Frequency
λ_{RF}	60 [mm]	Frequency
ω_{RF}	$2\pi\nu_{RF}$ [rad/s]	Angular frequency
w_g	40.386 [mm]	Waveguide width
h_g	20.193 [mm]	Waveguide height
P_{RF}	1000 [W]	RF Power
T_{step}	2 [ps]	Integration Time step
h	$\frac{\lambda_{RF}}{5}$	Mesh maximum element size
h_{ECR}	1 [mm]	h close to ECR layer
r	2.5	Mesh growth rate
r_{ECR}	1.2	r close to ECR layer

Table 4.5. Details on computation in Comsol and Matlab

Description	Value
COMSOL Version	4.3b
MATLAB Version	R2011b ("Trivial multithreading[4]")
COMSOL Solution Time	44 min. 40 sec
COMSOL memory occupation	92.68 GB
MATLAB Solution Time	45 min (N=1000 particles)
Interpolation Time	50 min

As a first step $k = 1$ the electromagnetic field is solved in a vacuum chamber: the dimensions of the rectangular waveguide are 40.386 mm x 20.193 mm in order to allow a single TE_{10} mode propagation at frequency of 5 GHz; the radius and length of the cylindrical plasma chamber are 50 mm and 300 mm, respectively: both geometrical dimension and frequency (lower than values normally used in last generation ECRIS) reduce computational costs without loss of generality in the approach validity, maintaining all the significant physical properties of a conventional ECRIS. The meshing sequence is controlled, setting a very low mesh size h_{ECR}=1 mm on the ECR layer and increasing it up to h=$\frac{\lambda_{RF}}{5}$ in the remaining computational domain, following the FEM "rule–of–thumb" of **five nodes per wavelength**, that represents an optimal compromise between RAM requirement and accuracy.

The figure 4.24 shows the electric field distribution inside the cylindrical cavity excited by the rectangular waveguide. The presence of the cavity walls, modeled via the perfect electric conductor boundary condition, makes the electromagnetic field pattern to configure in a cavity mode like structure.

▼ 0.8672   0.5   1   1.5 $\times 10^5$ ▲ 1.6497×10^5
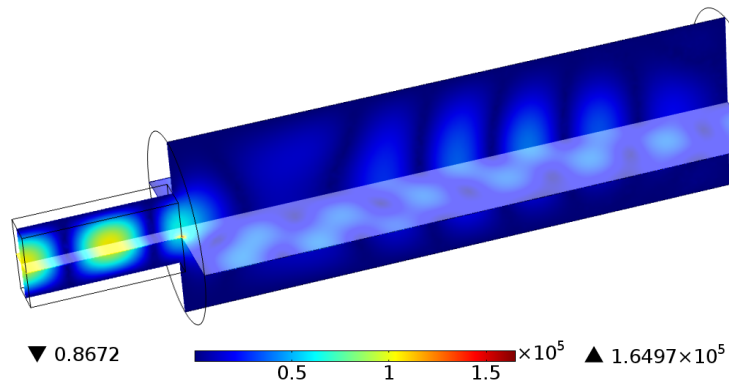
Fig. 4.24. Norm of the Electric field in vacuum chamber [V/m].

Now the RF field should be introduced into the Particle Mover code, in order to obtain the phase-space stationary electron distribution. This first step $k = 1$, in which particles move in presence of the RF field in "vacuum" cavity, has been obtained elsewhere [59]. These former results highlighted that electrons mostly concentrate into the iso-magnetic closed surface corresponding to the ECR condition. This high density region was called "plasmoid", while the surrounding volume was named "halo". In [59] results about 2D time-dependence PIC model were also mentioned, confirming this separation between inner/outer ECR surface plasma regions: a dense plasmoid surrounded by a rarefied halo. The result - although not self-consistently obtained by

---

[4] We run the kinetic code on different MATLAB istances to compute the motion of many set of particles samples

evaluating plasma effect on RF- was however in qualitative agreement with experimental results of Bibinov and Tuske [47, 90], they being among the few ones having performed space-resolved measurements of plasma density through optical emission spectroscopy techniques [47],[90]. Therefore, in the perspectives on the present thesis - where we want to calculate plasma influence on RF and vice-versa - we can reasonably assume that the starting condition of the step $k = 1$ is given by a "plasmoid-halo" model. We then proceeded to calculate RF field once defined a plasmoid region with a maximum density located at the center of the chamber $(z = 0)$, a "quasi-gaussian" profile showing a flat-top shape into the plasmoid and a rapid decrease from ECR layers towards the plasma chamber walls, according to the following equation:

$$n_e(x, y, z) = n_{halo} + n_{max} e^{-\left(\frac{B - 0.8 B_{ECR}}{0.2 B_{ECR}}\right)^6} \tag{4.12}$$

where $n_c = \dfrac{\omega^2 \epsilon_0 m_e}{e^2}$ is the cutoff density of the ordinary wave, $n_{max} = 0.7 n_c$ is the maximum electron density and n_{halo} is the minimum density $(n_{halo} = 10^{15})$, two order of magnitude lower than the $n_{max} = 10^{17}$ outside the plasmoid.
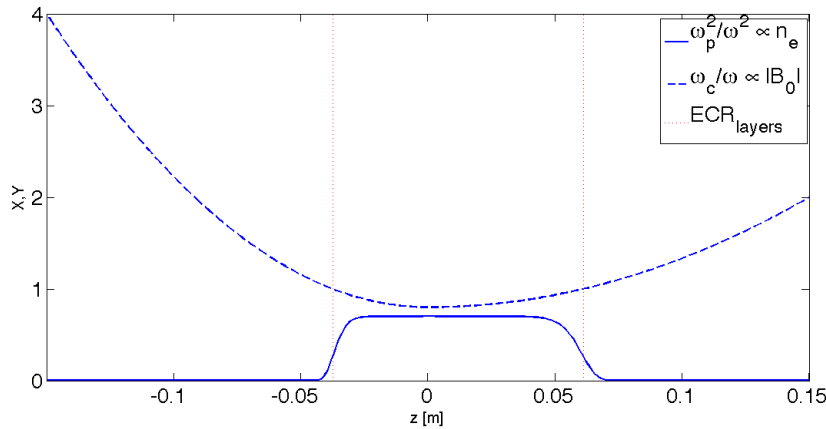
Fig. 4.25. 1D profile along the z (longitudinal) axis of the electron density and magnetostatic field assumed as input for step $k = 2$ RF field calculation.

In figure 4.25 the 1D density profile is shown along with the corresponding magnetic field profile. According to the derived 3D spatial distribution of either n_e and B, the tensor (4.7) can be evaluated at each mesh point. Figures 4.26 and 4.27 illustrate the COMSOL outputs for either electric field distribution and power dissipation $(P_{diss} = (\overline{\sigma} \cdot \mathbf{E}) \cdot \mathbf{E})$ into the cavity (and the plasma in particular). The profile of the ECR region has been put in evidence. It can be noted that the electric field distribution [91] is partially perturbed by the plasma, while keeping a disuniformity that still puts in evidence a standing wave nature of the inner-cavity radiation. The absolute strength of the electric field inside the plasma chamber is even increased, (the maximum value of the electric field inside the chamber is increased from 1.2×10^5 to

1.41×10^5), when the plasma is considered, meaning that in the specific case (i.e. for the considered frequency) the waveguide-to-cavity coupling has been improved by the plasma itself. Power deposition plot (figure 4.27), in addition, shows areas where the best coupling between the wave and the particles takes place (note that the figure is given in logarithmic colormap scale): the largest fraction of energy is obviously absorbed at the ECR (as expected), moderate energy exchange occurs in the inner plasmoid volume, while becoming several orders of magnitudes less efficient the halo part of the chamber. The total input RF power was 1 kW, the 45% of which was reflected.

Once determined how does the simplified step $k = 1$ model of the plasma density profile affect the RF field, we can go back using the computed RF field as mean field (input field) of the Particle Mover. The electromagnetic field coming out from COM-SOL mesh-node points is imported in Matlab, interpolated using the *"mphinterp" function* (built in "COMSOL with Matlab" library) that evaluates the electromagnetic field at the coordinates specified (we specified those of the space domain of the Particle Mover). Starting positions of the electrons are chosen according to a weighted sampling following from the density profile of figure 4.25.
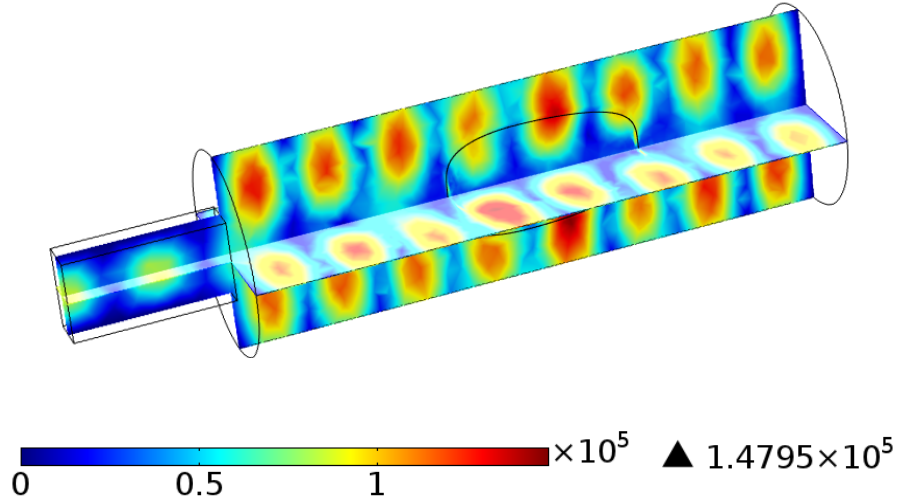
Fig. 4.26. Electric field distribution [V/m] considering plasma effects at simulation step $k = 1$.

In fig. 4.28 the 3D distribution of the electron density is shown (on the left), along with the density distribution projection over the plasmoid surface (i.e. ECR iso-magnetic surface) and the projected 2D density distribution in the transversal direction. The non-homogeneous distribution of the density in the plasmoid-halo scheme is preserved even in step $k = 2$, meaning that it is a characteristic feature of this

▼ -7.232×10^{-9} [color scale: 0 to 5]   ▲ 9.7336
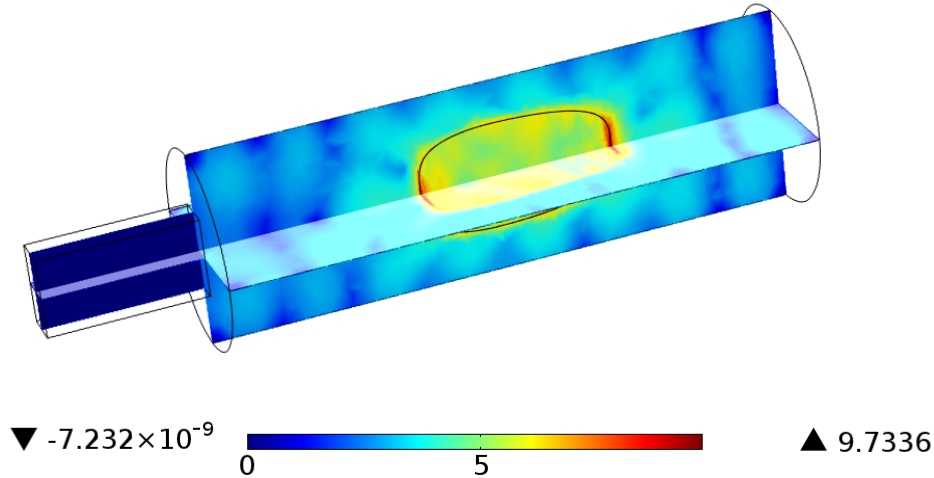
Fig. 4.27. RF power dissipation [W/m$_2$] into the plasma at simulation step $k = 1$.
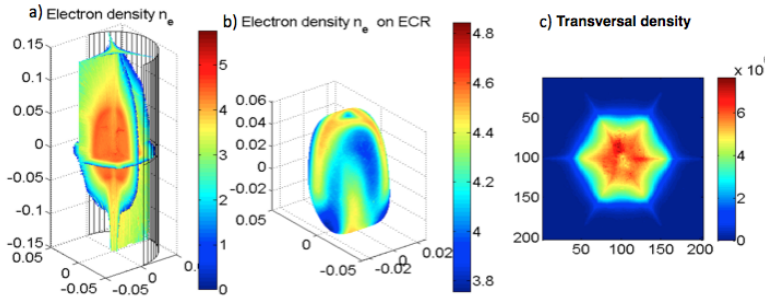
Fig. 4.28. From left to right: a) total electron density distribution [a.u] in a 3D view (log colormap scale); b) density distribution [a.u] over the plasmoid surface (i.e. ECR iso-magnetic surface)(log colormap scale); c) 2D transversal density distribution [a.u] integrated over the z (longitudinal) axis (linear colormap scale)

kind of plasmas. In [86] this structure was explained considering the plugging effect provided by the RF acceleration of electrons passing for the first time through the ECR, which are expelled at large rates from magnetic loss cones and whose turning points coincide with the ECR layer itself. An additional effect is probably given by *pseudo-ponderomotive potential*, as formerly supposed by Dimonte et al. [92], even though more detailed analysis are needed to evaluate its relative weight. Other non-homogeneities are due to the magnetostatic field structure (the "arms" on the plamoid surface). Another characteristic feature is given by the "hole" in the near axis region, due to a density depletion. In order to go more in detail in understanding plasma structure coming out from the simulations, we splitted the above pictures according to different electron energy ranges [93]. We followed a commonly used convention in the ECRIS field, selecting five different **energy ranges**:

- I$_1$: $E < 2eV$,

- I_2: $2 < E < 100 eV$,

- I_3: $100 < E < 1000 eV$,

- I_4: $1 < E < 50 keV$,

- I_5: $E > 50 keVs$,

corresponding to the so called "bulk-plasma" electrons (I_1), to the electrons producing low charged ions (I_2), the ones generating ions at mean charge states (I_3), at high charge states (I_4) and, finally, to the so-called "suprathermal" electrons (I_5) whose role and formation mechanism is still controversial [94–96] but useless for ionization and highly charged ions build-up. Density distributions in 3D views and in 2D plots integrated over the axial coordinate are shown in figure 4.29.

No electrons populate the I_1 domain, meaning that interaction with RF heats the totality of the electrons bringing them in the higher energy domains. A large amount of electrons have few eV of energy and populate the I_2 interval: electrons in this range reach the highest relative density ($> 10^5$ in a.u.) among all the selected intervals, but only in some localized regions. Their concentration assumes the maximum value in the near axis region.The distribution of the particles in the I_3 interval is smother than in the second one, but once again concentrated in the quasi-axial zone. Different is the situation of I_4 and I_5 domains: in these cases, the density concentrates mainly in off-axial regions, leaving a depletion hole all around the axis. Figures in the lower row allow to compare relative densities among the various energetic domains, then comparing them with experimental data. Densities of electrons in I_4 and I_5 domains in near-axis region are about 10% and 1% of the I_2 and I_3 domains. Since we assumed an absolute plasmoid density value of $0.7n_c$, these numbers are in good agreement with the results collected and discussed in [86]: in that paper, authors performed an experiment measuring X-rays energies coming from near axis plasma in the 2-30 keV domain and in the >60 keV domain, that are roughly comparable with the simulated ones. A good agreement also comes out if simulated data are compared to the experiments performed by Biri et al. [93, 97], which showed an off-axis concentration of highly charged ions and hot electrons. As already argued in [86], the hole formation could explain hollow beams generation often observed in ECRIS working below 18 GHz of pumping wave frequency [98, 99]. In reference [86], however, calculations were stopped to step $k = 1$, and still controversial was the effect of the plasma on the RF field, also deemed eventually causing standing wave structure to disappear. Step $k = 2$ calculations now confirm hollow density distribution into the plasma. **The reason why standing wave structure distribution is invoked to explain hollow density/hollow beam formation can be understood by looking to figures 4.30 and 4.31**.
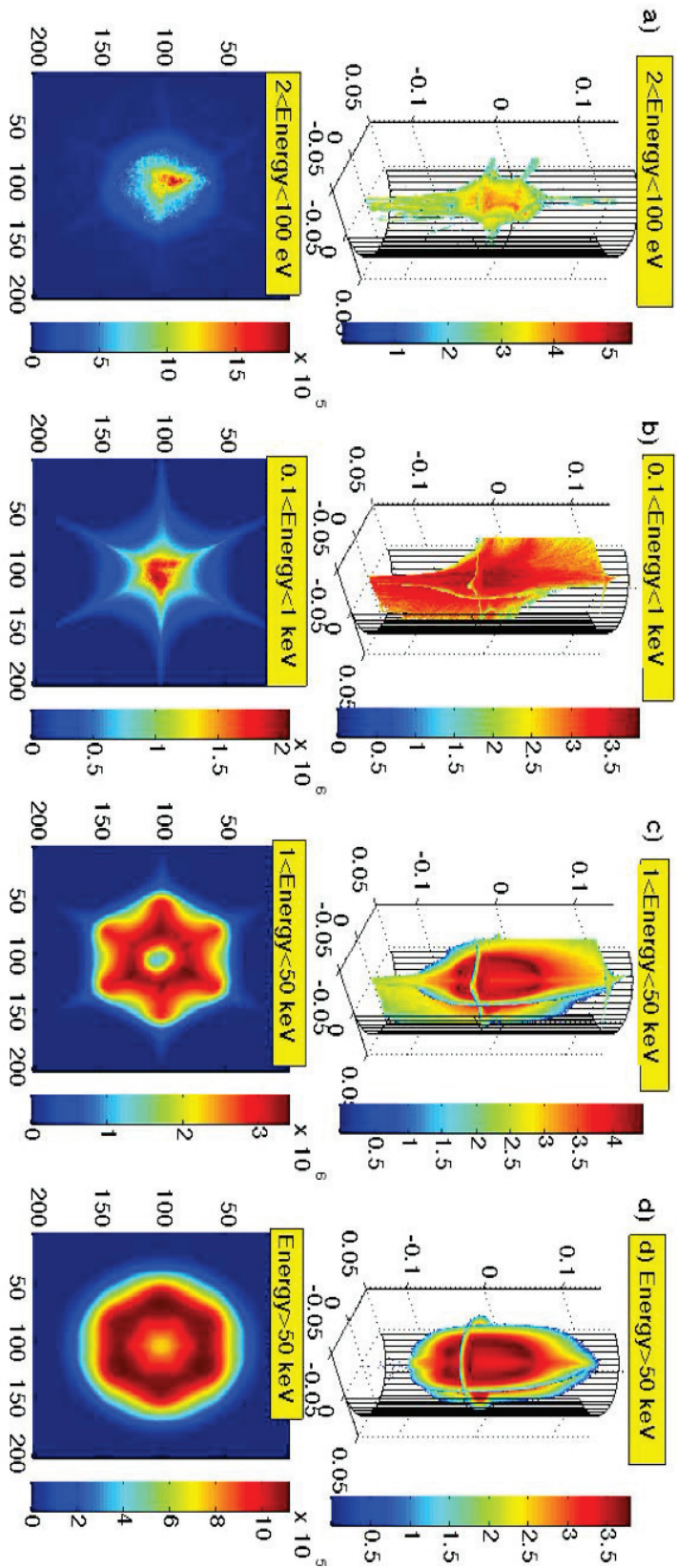
Fig. 4.29. Upper row: 3D density distribution [a.u] at different energy ranges (a.u. in log scale); Lower row: integrated density distribution in a 2D transversal view (a.u. in linear scale).
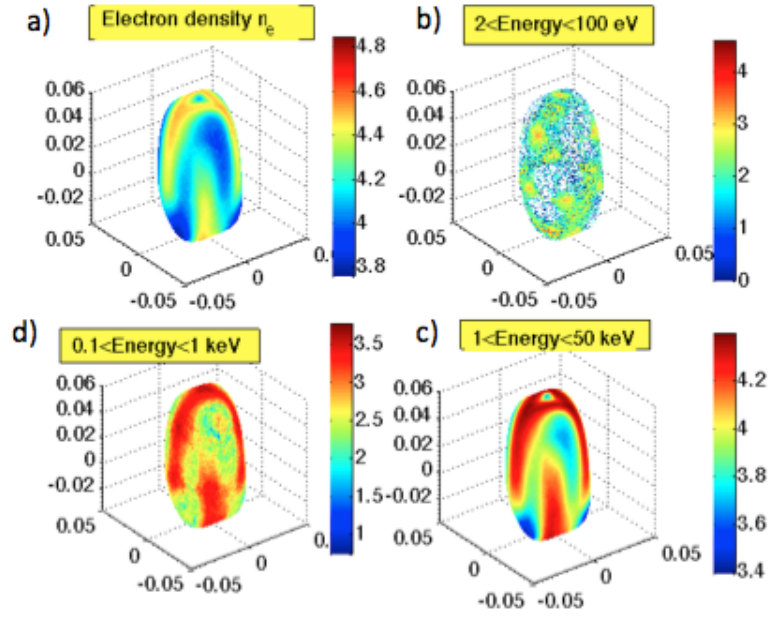
Fig. 4.30. From up-left, clockwise (all plots in log colormap scale): a) total electron density distribution [a.u] over the plasmoid surface; b) electron density over the plasmoid concerning I_2 energy domain; c) electron density [a.u] over the plasmoid concerning I_4 energy domain; d) electron density [a.u] over the plasmoid concerning I_3 energy domain.
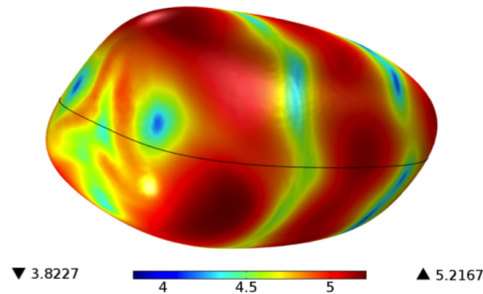
Fig. 4.31. Electric field strength [V/m] over the plasmoid surface (logarithmic colormap scale);

It can be seen that the density distribution in the I_2 interval is affected by local "bunches" of particles roughly corresponding to regions of higher electromagnetic field (providing electron plugging). Less evident is the effect on the I_3 and I_4 domains (more energetic electrons are more affected by magnetic drifts which partially smooth the density distribution), but a near axis density depletion is evident in I_4, i.e. in a rather high energetic domain. Figure 4.31 shows that on the top of plasmoid surface, corresponding to axial region, the RF field is one order of magnitude weaker than in off-axis zones. This may explain a lower plugging efficiency of electrons and the following axial density depletion. An even more clear picture of density distribution

concerning the different energetic intervals is given by the 1D profiles shown in in the sequence of figure 4.32-4.36. In particular, figure 4.32 displays the density distribution along a transversal axis and it shows that the higher is the energy, the far the density distributes from near axis regions. These outputs are in agreement with the results shown in [86], confirming that the self-consistent solution is not so far. Concentration of the plasma inside the plasmoid is evident also along the longitudinal direction (see figure 4.33). Peaks are also placed in proximity of the ECR layers, where the electrons spend a relevant fraction of their "life" since mirrored by the combined effect of magnetic field force plus RF plugging. Figure 4.34 illustrates the azimuthal distribution (on the midplane of the plasma chamber) of the electrons (once again, displaced according to the different energetic intervals). It is clear that the plasma distribution is modulated by the multi-mirror magnetic structure: electrons concentrate in pole regions, while being more rarefied in the gaps zones. This effect is less evident on the cold population (strong collisionality causes the density to spread out regardless of magnetic structure) and on the ultra-hot population (> 50 keV), where the electrons are subjected to strong drifts across the magnetic field lines. It comes out that the electrons between 1 and 50 keV are the most affected by the magnetic field. Figures 4.35 and 4.36 highlight in more details the difference between poles and gaps. In near pole positions, the density is increased showing a peak in near resonance zone.
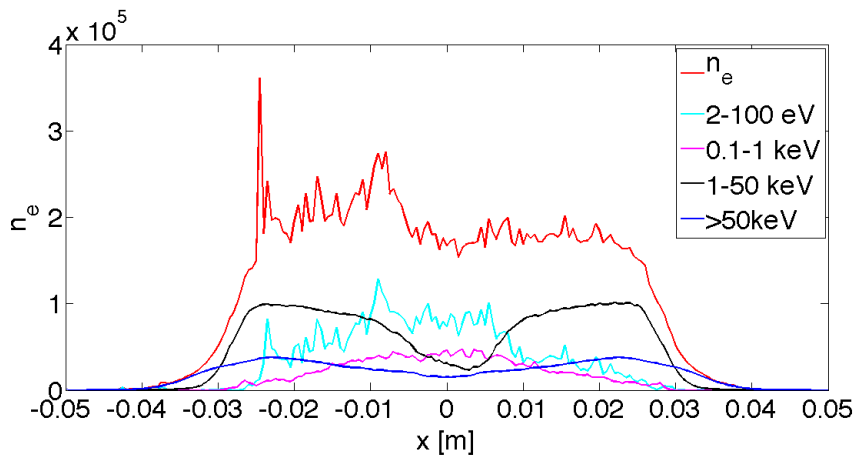
Fig. 4.32. 1D profiles of the electron density [a.u] along x-axis according to the different energetic domains (including n_{tot}), in a.u.
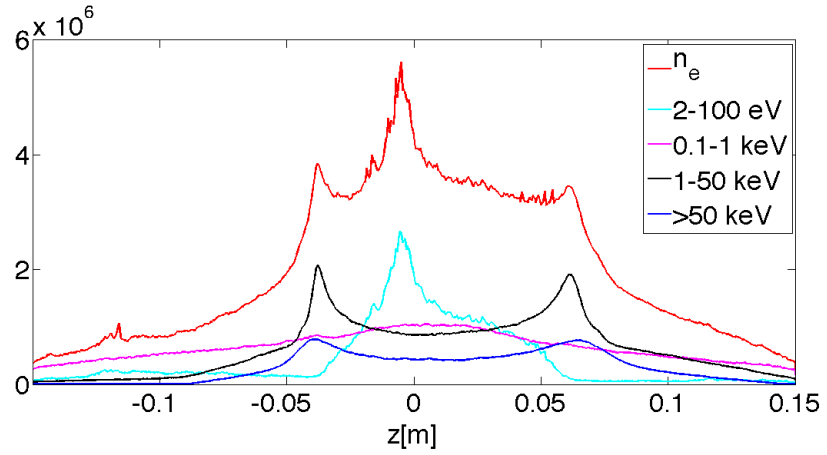
Fig. 4.33. 1D profiles of the electron density [a.u] along z-axis according to the different energetic domains (including n_{tot}), in a.u.
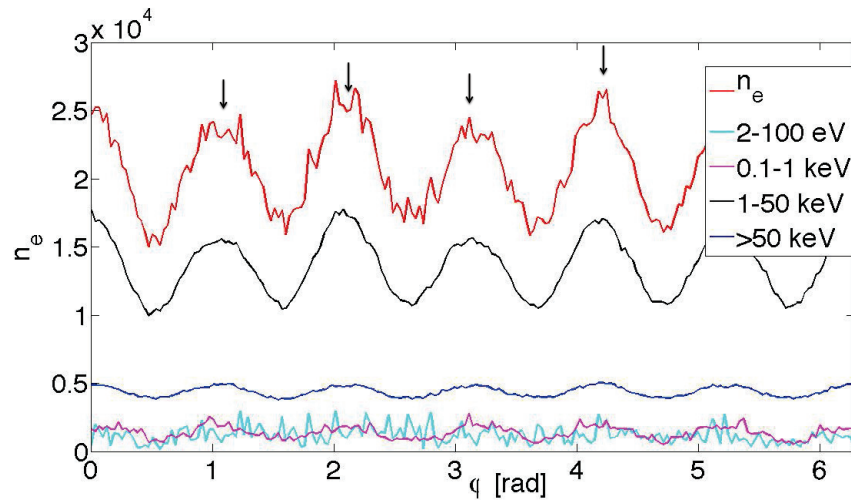
Fig. 4.34. 1D profiles of the electron density [a.u] along ϕ according to the different energetic domains (including n_{tot}), in a.u. Arrows highlight the angles of multi-mirrors.

4.5 Experimental validation of the full-wave code

4.5.1 Consistency and with experimental observation in ECRIS

One of the most significant outputs of the modeling up to now described concerns in the evaluation of wave-to-plasma interaction in a full-wave tensorial scenario. The tensor-based simulations differ considerably from outputs based on single-mode propagation, shown, meaning that modal conversion and cavity wall effects cannot be neglected. It is expected that a predictive approach can be based on these results, helping in the design of future machines (especially the plasma chamber) optimized for high wave damping at ECR layer, low reflected power, efficient electron heating producing a dense plasma and high current beam of multicharged ions. The approach, however, is general and can be easily extended to similar plasma devices fed by mi-
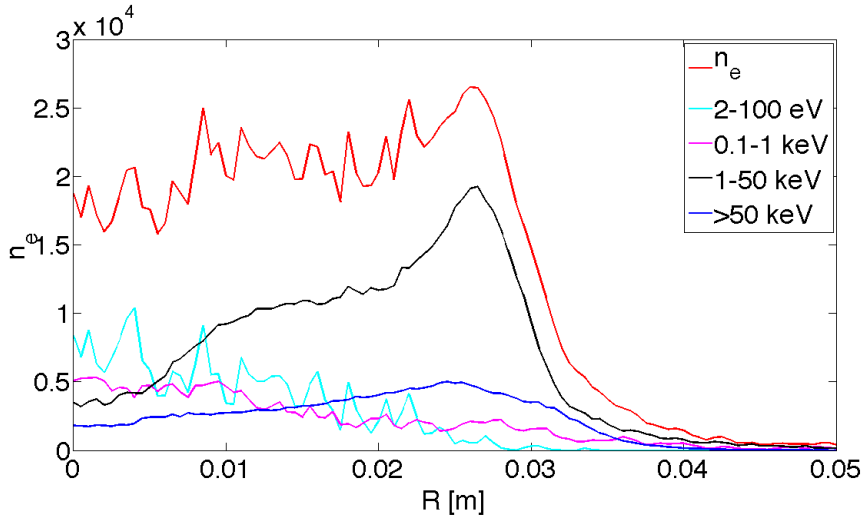
Fig. 4.35. 1D profiles of the electron density [a.u] along a magnetic pole according to the different energetic domains (including n_{tot}), in a.u.
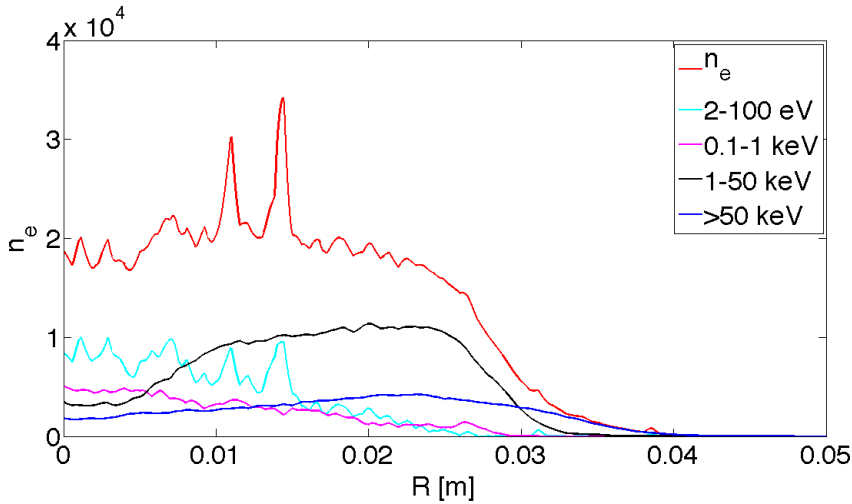
Fig. 4.36. 1D profiles of the electron density [a.u] along a magnetic gap according to the different energetic domains (including n_{tot}), in a.u.

crowave in the GHz range. The next step will be the implementation of the *warm* plasma dielectric tensor effects that play an important role in ECRIS plasma dynamics. The numerical approach to solve the spatial dispersion of the medium in this approximation, it is proposed in section 4.6.2. The most important clues coming out from the simulations are that although vacuum field RF field distribution (that is a cavity, modal field distribution) is perturbed by the plasma medium, the non uniformity in the electric field amplitude still persists in the plasma filled cavity. This non-uniformity can be correlated with non-uniform plasma distribution, explaining a number of experimental observations. A first attempt toward self-consistent, 3D simulation of an ECRIS plasma has been done, including the resonant behaviour of

the plasma vessel. Although we are still far from strict convergence, **some plasma features are now clear**:

- *the plasma concentrate mostly in near resonance region: a dense plasmoid is surrounded by a rarefied halo;*
- *the resonant cavity effects cannot be neglected: resonant mode structures modify plasma density distribution;*
- *electrons at different energies distribute differently in the space: cold electrons in the core, hot ones in near ECR regions*
- *Simulation results explain quite well the experimental observations;*

  Effects on the **ion beam formation** and beam properties can be argued:

- *ions are formed were hot electrons are placed;*
- *this implies the ion beam shape depends on electron/ion distribution on the plasmoid surface;*
- *optimization of the ion beam formation [100] and transport must begin well inside the plasma.*

4.5.2 Electromagnetic Analysis of the Plasma Chamber of an ECR-based Charge Breeder

As an additional benchmark, the full-wave code has been used to investigate in details the microwaves propagation and absorption inside the plasma chamber of the PHOENIX charge breeder [101], designed in the framework of the Selective Production of Exotic Species (SPES) project [102, 103] (SPES-CB). SPES is now under construction at Legnaro National Laboratories (LNL). The aim of PHOENIX is to be adopted as charge breeder with an ECR-based technique [104] (ECR-CB), which transforms the charge state of a radioactive beam from 1+ to q+; this allows post-acceleration. The capture probability, which fixes the effectiveness of the CB, strongly depends on the plasma properties, namely ion/electron density and temperature. Since the years of pionering experiments, charge breeding efficiency has been progressively increased. However a number of experimental results show that room for improvement still exist [27], and it would be of crucial importance for forthcoming facilities like SPES at INFN-LNS. In this perspectives the numerical modelling can play a decisive role. Several still unknown mechanisms, in fact, are involved in the beam-target (plasma) interaction. The results of [27], for example, seem to demonstrate that the Frequency Tuning effect plays also a role even during the breeding process. The numerical approach described here can be fruitfully used to investigate the role of plasma chamber modes, and especially plasma energy absorption, when tuning the pumping wave frequency. The already available experimental data offered also the opportunity

of a direct cross-check and validation The implemented plasma models of increasing complexity, in order to understand what level of accuracy is requested to capture all the relevant physical informations are deeply described in [105]. Then, the actual geometry was taken into account to study the propagation of two precise frequencies, implementing the full-3D non uniform magnetized plasma complex dielectric tensor [55].

Simulation domain

The geometry employed in the presented numerical simulations is the stainless steel plasma chamber of the SPES-CB [102]: it is a cylinder 353 mm long and 36 mm in radius. Its boundaries are an aluminum plate at injection side, with a $r_{1+}=14$ mm hole to allow the 1+ beam injection, and the $r_{ext}=4$ mm extraction electrode. The cut-off frequency of this last aperture, i. e. 22 GHz, is higher than the ones used for plasma ignition (around 14.5 GHz): hence, this boundary was replaced and modeled as a conducting plate. The plasma chamber allows the radial injection of two frequencies through rectangular WR-62 waveguides, located 10 mm from the boundary at injection. Figure 4.37 shows the mesh subdivision of the simulated geometry. The maximum element size was set to 2.7 mm ($\sim$1/4 of the wavelength), a good compromise between accuracy of the calculations and computational costs.
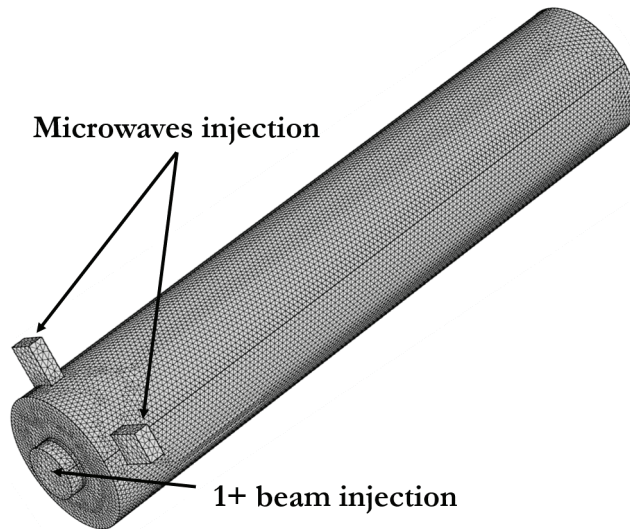

Fig. 4.37. 3D view of the 2.7 mm mesh generated for the simulated geometry. Geometrical details that impact on electromagnetic propagation, as apertures and ports, are taken into consideration.

Analysis of two selected frequencies

We proceded studying the propagation of two fixed frequencies: 14.521 GHz and 14.324 GHz. The first one corresponds to the routine operating frequency; the second one was chosen because an improvement of the performances having was experimentally observed if compared to the previous one, [103]. In all the presented cases an **input power of 100 W** was used, while as boundary conditions an **Impedance Boundary Condition** was applied on each metallic surface, and a **Perfectly Matched Layer** on the surface of the beam injection hole, so as to absorb all the outgoing wave energy without any impedance mismatch [85]. The first simulations were performed considering an empty chamber: the results showed that for both frequencies a consistent part of the power is reflected at the waveguide input, while the most of the rest went out through the 1+ beam injection hole (except for some losses on the conducting walls). The values of the reflected power at the waveguide (43.8% at 14.521 GHz, 38.2% at 14.324 GHz) suggest that the lowest frequency is better matched to the chamber. After the merely electromagnetic study, the plasma was modeled and inserted into the simulation domain. The plasma was modeled through the complete 3D dielectric tensor, computed by MATLAB for each mesh point assigned by COMSOL. In this case the results revealed a huge difference in the electromagnetic behaviour between the two frequencies, as table 4.6 shows: other than much better matched with the chamber, **the 14.324 GHz frequency is three times more efficiently absorbed by the plasma than 14.521 GHz**, simulations say. In the latter case, most of the power flows away through the 1+ ions injection hole. These results are in very good agreement with the experimentally observed frequency tuning effect (see fig. 4.38) at exactly the simulated frequencies, [103]. During the experiments in fact, by feeding microwaves at 14.324 GHz with a Travelling Wave Tube Amplifier (TWTA), instead of the commonly used Klystron at 14.521 GHz, it was observed an increase of the efficiency of Cs^{26+} production and a decrease in its charge breeding time, both of 15%, while the global capture stayed almost constant. This can be considered an indication that, by tuning the frequency, the ionization process can be speeded up without modifyng the capability of the plasma to capture the injected ions. The simulations suggest this should be due to an improved power deposition efficiency. The results shown in figure 4.39 revealed also that the waves propagate inside the resonant surface: as it can be seen by the 3D electric field distribution for both frequencies (in logarithmic scale). Its highest value is found now on a thin layer around the resonance, showing the well known electric field densification mechanism due to the wavelength shortening near the resonance layer, while it is lower elsewhere (except for the near waveguide input region). The effect is clearer

from the 1D plot of the electric field on axis at 14.324 GHz in figure 4.40, where the local increase at the resonance is visible, especially at the extraction side.
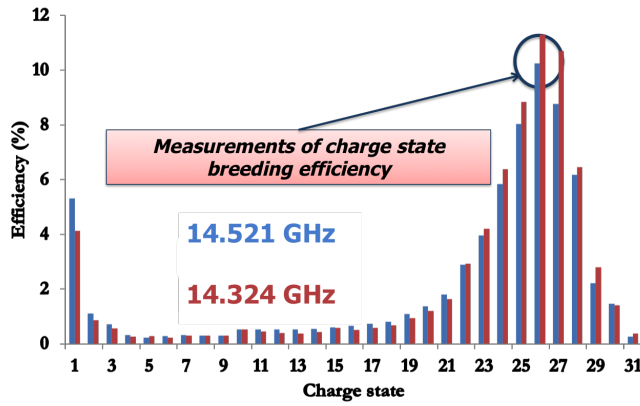
Fig. 4.38. Measurements of charge state breeding efficiency

Table 4.6. Comparison of the power distribution for the two simulated frequencies cosnidering the complete anisotropic picture of the plasma. The matched power is the simulated power minus the power reflected at the waveguide input.

	14.521	14.324
Frequency [GHz]		
Simulated power [W]	100	100
Matched power [W]	68.4	92.6
Power out from the HF-blocker [%]	60.5	15.7
Power absorbed in the plasma volume [%]	24.4	80.4

Conclusions

The presented numerical simulations gave us the possibility to evaluate the importance of properly modeling the plasma, and including the real geometry of the plasma chamber cavity. The comparison between 14.521 GHz and 14.324 GHz supports the frequency tuning effect experimentally observed [99, 103, 106]. *The presented model can be considered such as almost predictive if one aims at comparing two or more different frequencies, for a given geometry and plasma structure.* A complete predictability will be reached after implementing a more realistic plasma-target model, by coupling the presented work to other approaches describing the particle dynamics [107], in order to obtain a self consistent picture of the plasma. A joint effort of INFN-LNS and INFN-LNL groups goes in this direction, continuously developing a multipurpose simulation tool [108].
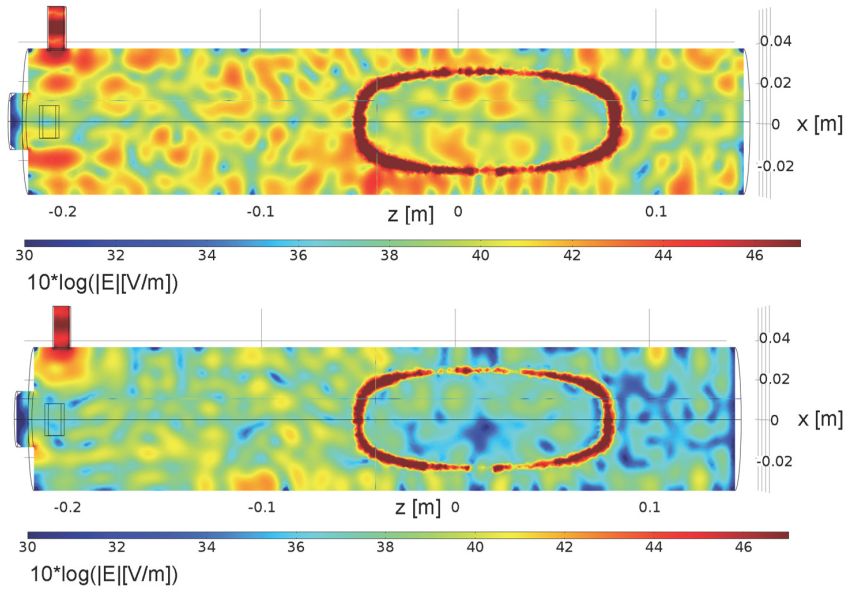
Fig. 4.39. 3D simulated electric field distribution, in logarithmic scale, for 14.521 GHz (upper part) and 14.324 GHz (lower part), obtained implementing the anisotropic plasma model. The maximum of the electric field is located on a thin layer around the resonance; for the sake of clearness, the y axis ticks and labels are omitted.
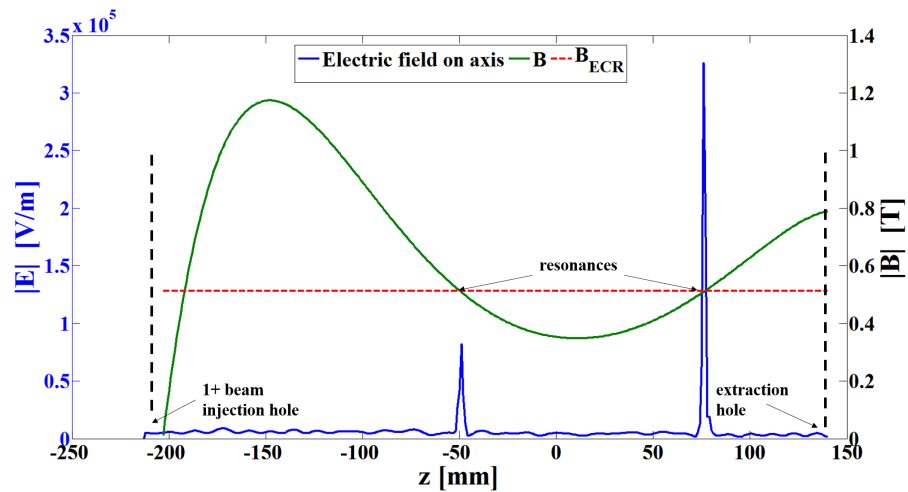
Fig. 4.40. 1D plot of the electric field at 14.324 GHz (left axis) and the magnetic field (right axis) along the plasma chamber axis for the anisotropic plasma model. The absorption at the location of the resonances is clearly visible.

4.5.3 Cross–check with data coming from X-ray diagnostics

An experimental campaign aiming to investigate ECR plasma X-ray emission has been recently carried out at the ECRIS laboratory of Atomki based on a collaboration between the Debrecen and Catania ECR teams. The measurements were carried out in two steps:

In a first series, the X-ray spectroscopy was performed through SDD and HpGe detectors, characterizing the volumetric plasma emission. The on-purpose developed collimation system was suitable for direct plasma density evaluation, performed on-line during beam extraction and CSD characterization. A campaign for correlating the plasma density and temperature with the output charge states and the beam intensity for different pumping wave frequencies, different magnetic field profiles and single-gas/gas-mixing configurations was carried out. Then, in the second stage, a CCD camera was placed beyond a lead pin-hole in order to perform space resolved X-ray measurements (both imaging and spectroscopy)

The results [] revealed a surprisingly very good agreement between the X-ray detections counts density fluctuations, output beam currents and the calculated electromagnetic modal density of the plasma chamber as the comparison between fig. (4.41) and (4.42) shows. A CCD camera coupled to a small pin-hole allowing X-ray imaging was installed. The numerous X-ray photos were taken in order to study the peculiarities of the ECRIS plasma structure and to compare them with single particle and self-consistent numerical simulations.
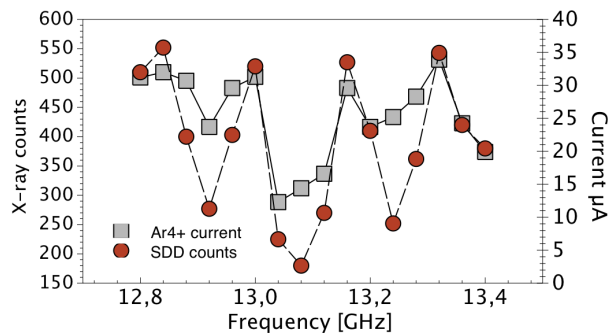
Fig. 4.41. Trend of Ar^{4+} current compared to total flux of X-rays vs. the pumping wave frequency.

The impact of the pumping wave frequency was investigated by looking to the response of the average charge state and Ar^{4+} output current, trying to correlate these data to the X-ray emission in the 2–30 keV energy domain. The total number of X-rays per second (detected rate) is somehow correlated to the so called "energy-content" of the plasma, roughly interpreted as the product rate, i. e. the electron
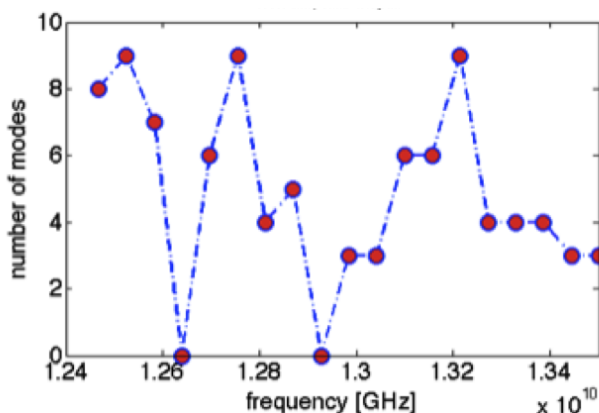
Fig. 4.42. Trend of the e.m. modal density vs. the pumping wave frequency(simulations)

density times the electron temperature. More sophysticated analysis allows extracting the separate n_e and T_e parameters, but for the scopes of the present section the rate vs frequency trend is, by itself, a very meaningful comparison. The Figure 4.41 shows how strongly Ar^{4+} currents and X-ray rates are correlated each other. The idea was then to exploree the modal spectrum of the ATOMKI–ECRIS plasma chamber, trying to plot the modal density (i. e. the number of modes in a given frequency intervals) in the same frequency range as the one used during the experiment.

It resulted that the trends of fig. 4.41 and 4.42 were very similar, meaning that the current trend is extremely correlated to electromagnetic modes density. The impact of the pumping wave frequency was investigated This evidence was considered a clear proof of modes impact on electron heating dynamics. Hence, eventual effects on the spatial displacement of the plasma were investigated.

This was possible by implementing the X-ray-PHC described before. First, the X-ray images were collected without energy resolution, for some selected frequencies. Figure 4.43 show the impact of the frequency on the general shape of the plasma. Then, an energy filtering method (named "photon counting mode") was applied.

Implementing the energy filter to the images, it was possible to discriminate the various electrons populations energy (cold, warm, hot). Fluorescence argon lines were also selected (around the energy of 3 keV): this way, the regions where Ar ions concentrated were displayed.

It came out that Argon ions occupy far-from-poles positions; from comparison with simulations, it seems the same occurs also for warm electrons (i. e. the ones having enough energy for ionisation and excitation of Ar ions).

Moreover, we performed numerical simulations at two operating frequencies 12.84 GHz, 12.92 GHz, trying to understand the greater intensity of X-rays and the larger current of Ar^{4+} obtained at 12.84 GHz with respect to 12.92 GHz : fig. 4.45 shows
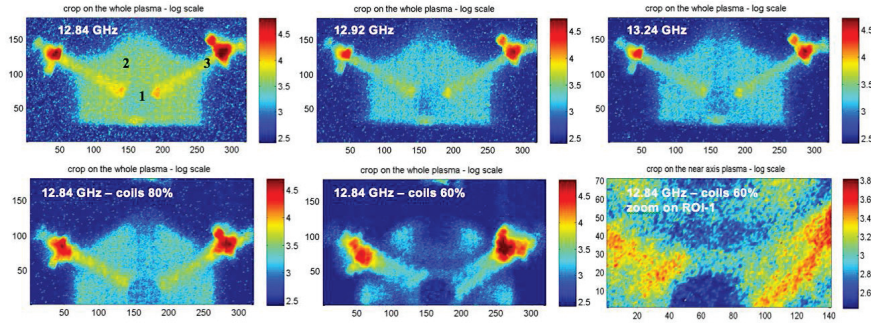
Fig. 4.43. From up-left, clockwise direction: a) 2D-imaging of the plasma at 12.84 GHz; b) 2D-imaging of the plasma at 12.92 GHz; c) 2D-imaging of the plasma at 13.24 GHz; d) 2D-imaging of the plasma at 12.84 GHz, coils at 80% of the maximum strength; e) 2D-imaging of the plasma at 12.84 GHz, coils at 60% of the maximum strength; f) zoom around the plasma chamber axis, the same as configuration e).
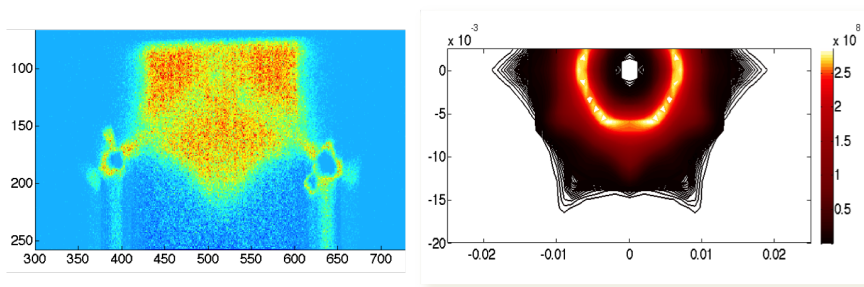
Fig. 4.44. on the left, Experimental result concerning the spatial displacement of ions; on the right, Simulations results: simulated displacement of warm electrons at $2 < E < 30$ keV

that, for 12.84 GHz, the region populated by warm electrons is wider than for 12.92 GHz, meaning that a larger number of Ar ions, even a bigger volume, can be generated at this frequency. This result is in qualitative agreement with X-ray emission area and the output Ar current. This was the first time 3D simulation were directly compared to X-ray measurements.

4.6 Warm plasma approximation

4.6.1 The dielectric tensor at ECR regime

Up to now we have considered the effects of a cold plasma only on waves propagation. A more advanced picture can be given by including, for example, "finite Larmor radius" effects.

So we formerly study plasma heating at ω_c but not at the harmonics of this frequency, so that the limit of zero Larmor radius ρ_{ω_g} is considered.
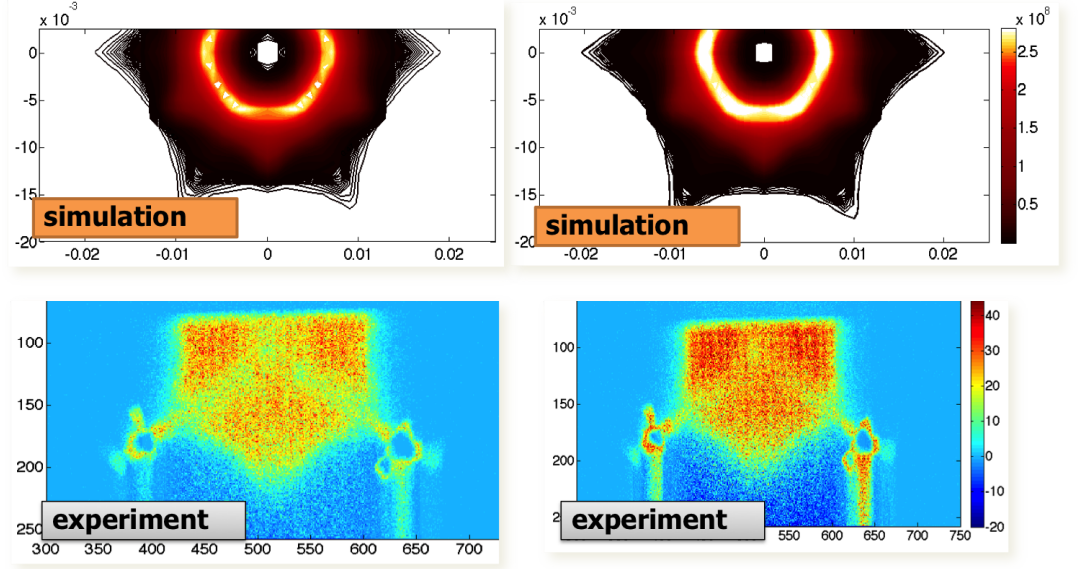
Fig. 4.45. on top, from left to right: 12.92 GHz and 12.84 GHz simulated warm-electrons 2D spatial distribution. on bottom, from left to right:12.92 GHz 12.84 GHz X-ray coming from Ar fluorescence lines displacement.

In the case of taking first order in the temperature from hot plasma Dispersion Relation $b = (k_\perp \rho_{\omega_g})^2 \ll 1$, $(\rho_{\omega_g} = \frac{v_{T_\perp}}{\omega_g}$ is Larmor radius), it is possible to expand $e^{-b}\overline{\overline{\mathbf{X}}}_l$ by b and including only terms up to the first harmonic.

The dielectric tensor ϵ_{ij} components for $\omega_{RF} \gg \omega_{pi}, \omega_{g_i}$ (considering only electrons), $\omega_{RF} \sim \omega_g$ and for large argument expansion of $Z(\xi_l)$ for $l \neq -1$ finally we obtain are:

$$\epsilon_{xx} = \epsilon_{yy} = 1 + \frac{\omega_p^2}{\omega_{RF}^2}\left(\frac{\omega_{RF}}{\sqrt{2}k_z v_{T_z}}\right)\frac{1}{2}Z\left(\frac{\omega_{RF} - \omega_g}{\sqrt{2}k_z v_{T_z}}\right) - \frac{\omega_p^2}{2\omega_{RF}(\omega_{RF} + \omega_g)}$$

$$\epsilon_{zz} = 1 - \frac{\omega_p^2}{\omega_{RF}^2} + \left(\frac{k_\perp c}{\omega_{RF}}\right)^2\left(\frac{\omega_p}{\omega_g}\right)^2\left(\frac{v_T}{c}\right)^2\left(\frac{\omega_{RF}}{\sqrt{2}k_z v_{T_z}}\right)\left(\frac{\omega_{RF} - \omega_g}{\sqrt{2}k_z v_{T_z}}\right)\left[1 + \left(\frac{\omega_{RF} - \omega_g}{\sqrt{2}k_z v_{T_z}}\right)Z\left(\frac{\omega_{RF} - \omega_g}{\sqrt{2}k_z v_{T_z}}\right)\right]$$

$$\epsilon_{xy} = -\epsilon_{yx} = -\mathrm{i}\frac{\omega_p^2}{\omega_{RF}^2}\left(\frac{\omega_{RF}}{\sqrt{2}k_z v_{T_z}}\right)\frac{1}{2}Z\left(\frac{\omega_{RF} - \omega_g}{\sqrt{2}k_z v_{T_z}}\right) - \mathrm{i}\frac{\omega_p^2}{2\omega_{RF}(\omega_{RF} + \omega_g)}$$

$$\epsilon_{xz} = \epsilon_{zx} = \left(\frac{k_\perp c}{\omega_{RF}}\right)\frac{1}{\sqrt{2}}\frac{\omega_p^2}{\omega_{RF}^2}\left(\frac{\omega_p}{\omega_g}\right)\left(\frac{v_T}{c}\right)\left(\frac{\omega_{RF}}{\sqrt{2}k_z v_{T_z}}\right)\left[1 + \left(\frac{\omega_{RF} - \omega_g}{\sqrt{2}k_z v_{T_z}}\right)Z\left(\frac{\omega_{RF} - \omega_g}{\sqrt{2}k_z v_{T_z}}\right)\right]$$

$$\epsilon_{yz} = -\epsilon_{zy} = \mathrm{i}\left(\frac{k_\perp c}{\omega_{RF}}\right)\frac{1}{\sqrt{2}}\frac{\omega_p^2}{\omega_{RF}^2}\left(\frac{\omega_p}{\omega_g}\right)\left(\frac{v_T}{c}\right)\left(\frac{\omega_{RF}}{\sqrt{2}k_z v_{T_z}}\right)\left[1 + \left(\frac{\omega_{RF} - \omega_g}{\sqrt{2}k_z v_{T_z}}\right)Z\left(\frac{\omega_{RF} - \omega_g}{\sqrt{2}k_z v_{T_z}}\right)\right]$$

When T $\rightarrow$ 0, that is, $\xi_{-1} \rightarrow \pm\infty, b \rightarrow 0$, the dielectric tensor of hot plasma is reduced to the dielectric tensor of cold plasma.

At ECR region where $\omega_{RF} = \omega_g$

$$\epsilon_{xx_{ECR}} = \epsilon_{yy_{ECR}} = 1 + \frac{\omega_p^2}{\omega_{RF}} \left(\frac{1}{\sqrt{2}k_z v_{T_z}} \right) \frac{1}{2} i\sqrt{\pi}$$

$$\epsilon_{zz_{ECR}} = 1 - \frac{\omega_p^2}{\omega_{RF}^2}$$

$$\epsilon_{xy_{ECR}} = -\epsilon_{yx_{ECR}} = -\frac{\omega_p^2}{\omega_{RF}} \left(\frac{1}{\sqrt{2}k_z v_{T_z}} \right) \frac{\sqrt{\pi}}{2}$$

$$\epsilon_{xz_{ECR}} = \epsilon_{zx_{ECR}} = \frac{1}{2} \frac{k_\perp}{k_z} \frac{\omega_p^2}{\omega_{RF}^2}$$

$$\epsilon_{yz_{ECR}} = -\epsilon_{zy_{ECR}} = i\frac{1}{2} \frac{k_\perp}{k_z} \frac{\omega_p^2}{\omega_{RF}^2}$$

The so-called *hot dielectric tensor* expresses several new features for the wave propagation in comparison with the cold dielectric tensor. Now, the dielectric tensor is a function of not only ω_c and ω_p but also a the temperature and the wave vector **k**. This leads to a new kind of solutions of the dispersion relation, the electrostatic modes. It is useful to verify if electromagnetic wave resonance mechanism is modified when warm plasma approach is taking into account.

4.6.2 Wavelet analysis

We have seen in the previous section that Finite-temperature plasmas introduce spatial dispersion i. e. the generalized dielectric tensor $\epsilon_{ij}(\omega, \mathbf{k})$ depends on the wave vector **k**. This means that the electric induction **D** at a given spatial point depends not only on the electric field **E** at the same point (**the local medium response**) but also on the electric field in some neighborhood (the nonlocal response).

In this section, we introduce the use of **Continuous-Wavelet-Transform (CWT)** to postprocess full-wave fields which have been generated using the code described in the previous sections. The goal is analysing ECRIS full wave data in the spatial domain to determine the wavenumber spectrum necessary to compute tensor elements derived in section (4.6.1). Indeed, the CWT has the appealing property of yielding information as to the spatial location of spectral modes, compared to the Fourier transform which, conversely, it does not provide any information about their spatial localization. Using a complex-Morlet CWT, the complicated full-wave field pattern is decomposed into its spectral local components $n = ck/\omega$ along a (magnetostatic) field line or a wathever line of Wavelet transformation components. The output of

such an analysis should be the information on the local wavevectors $\mathbf{k}(\mathbf{r})$, for use in subsequent hot plasma tensor calculations derived in the previous section (4.6.1).
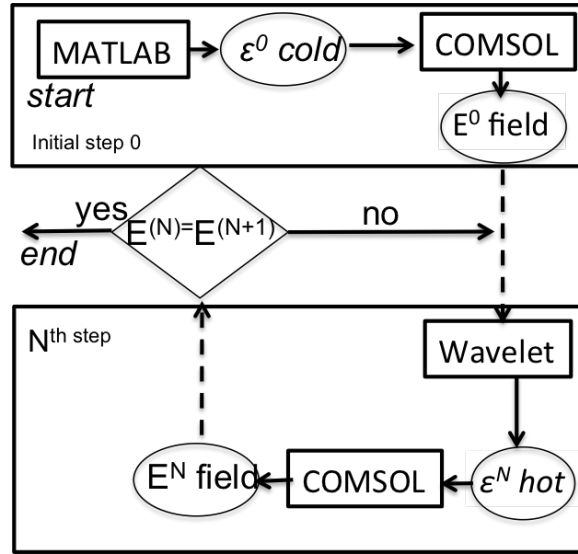
Fig. 4.46. Schematic of the iterative procedure, using COMSOL for the solution of the wave equation and the Wavelet analysis to implement the hot tensor in MATLAB

In general, the CWT of the full-wave fields shows that the local wave $\mathbf{k}$ spectrum broadens as the waves propagate through the plasma and after reflection due to density cutoffs or from the plasma chamber walls, and the components of wavenumber $\mathbf{k}$ greatly increases at the ECR resonances, because of the dramatic shortening of the wavelenght as alrady seen in [109, 110].

Wavelet Analysis Formalism

To first approximation, a Wavelet Transform (WT) can be thought of as technique to extract the spectrogram of a signal. As in *Windowed Fourier Transform (WFT)*, a signal spectrum is Fourier analyzed in segments of size x_w, each small enough for the portions of the signal to be assumed stationary. However, unlike the WFT, which uses a constant x_w for all frequencies, the WT analyzes each frequency component with a x_w matched to its scale. In other words, the WT is designed to have good spatial but poor spectral resolution for high frequency components, and viceversa for low frequency components. This approach minimizes two conflicting types of errors:

- *the Heisenberg error*:

$$\Delta k_H \propto \frac{1}{x_w}$$

- *the gradients error*

$$\Delta k_{\boldsymbol{\nabla}} = \frac{\partial k}{\partial x} x_w$$

over a wide range of frequency components, under the assumption that long wavelength variations occur on a scale length which is longer than the one of short wavelength variations, as it is often the case in physical systems. The use of 1D CWT is applicable for data obtained along a linear path and the resulting spectrum will contain only the component of wavenumber in the direction of the linear path.

In contrast to the STFT() sh technique where the window size is fixed, the wavelet transform enables variable window sizes in analyzing different frequency components within a signal [111]. This is realized by comparing the signal with a set of template functions obtained from the scaling (i.e., dilation and contraction) and shift (i.e., translation along the time, space in our case, axis) of a base wavelet Ψ and looking for their similarities.

A wavelet [112] function is a "small wave", with finite energy, non-zero frequency component, zero mean, defined as

$$X_{WT}(b,s) = \langle x, \Psi \rangle = \frac{1}{\sqrt{|s|}} \int_{-\infty}^{+\infty} x(z)\Psi^* \left(\frac{z-b}{s} \right) dz$$

using the notation of inner product.

The transformed signal $X_{WT}(b,s)$ is a function of the translation parameter b and the scale s, where the symbol $s > 0$ represents the scaling parameter, which determines the time and frequency resolutions of the scaled base wavelet Ψ. The specific values of s are inversely proportional to the frequency. The symbol b is the shifting parameter, which translates the scaled wavelet along the space axis. The symbol Ψ^* denotes the complex conjugation of the base wavelet Ψ. Through variations of the scale s and time shifts b of the base wavelet function, the wavelet transform is capable of extracting the constituent components within a time series over its entire spectrum, by using small scales (corresponding to higher frequencies) for decomposing high frequency components and large scales (corresponding to lower frequencies) for low frequency components analysis.

The base "mother" wavelet function used in our scenario is the Complex Morlet Wavelet [113]:

$$\Psi(z) = e^{-z^2 + jk_0 z}$$

The complex Morlet wavelet can be seen as a plane wave modulated by a Gaussian envelope, where the parameter k_0 is the wavenumber associated with the Morlet wavelet, roughly corresponding to the number of oscillations of the wavelet.

The Wavelet Spectrogram $W\{Ey\}$ of E_y resulting from simulations and plasma model described in section 4.4, along the x-axis shows a spectral broadening of $\mathbf{k}$, probably caused by cumulative effects of the wave path in the cylindrical cavity geometry, cavity walls and reflections at the plasma density cutoff surfaces. (see Fig. (4.47)).
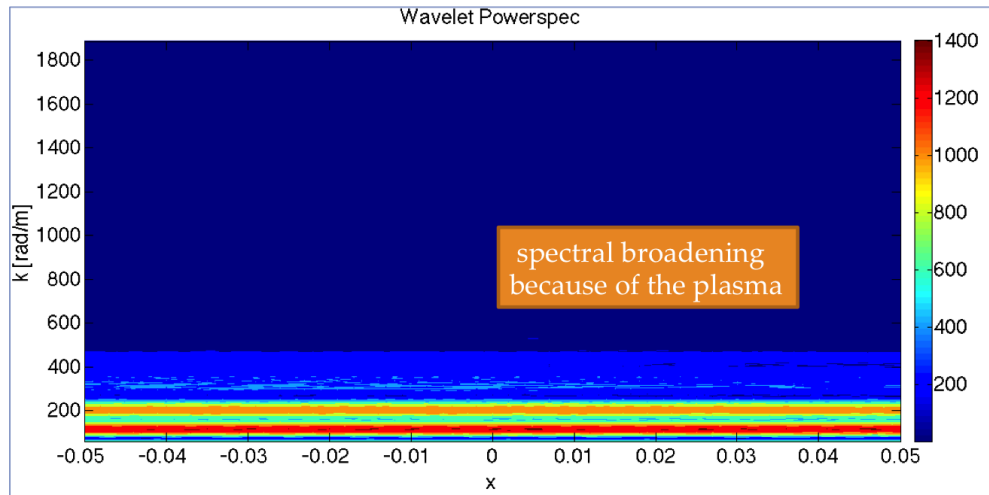
Fig. 4.47. Wavelet Spectrogram: Wavelet of E_y, $W\{Ey\}$ in cavity with plasma along the x-axis

The wavelet Spectrogram of E_z, $W\{E_z\}$ shown in Fig. 4.48, looks as extremely interesting. Two regions of high amplification of the ewave number are visible (i. e. of dramatic λ shortening), corresponding to just the location of the Electron Cyclotron Resonance.
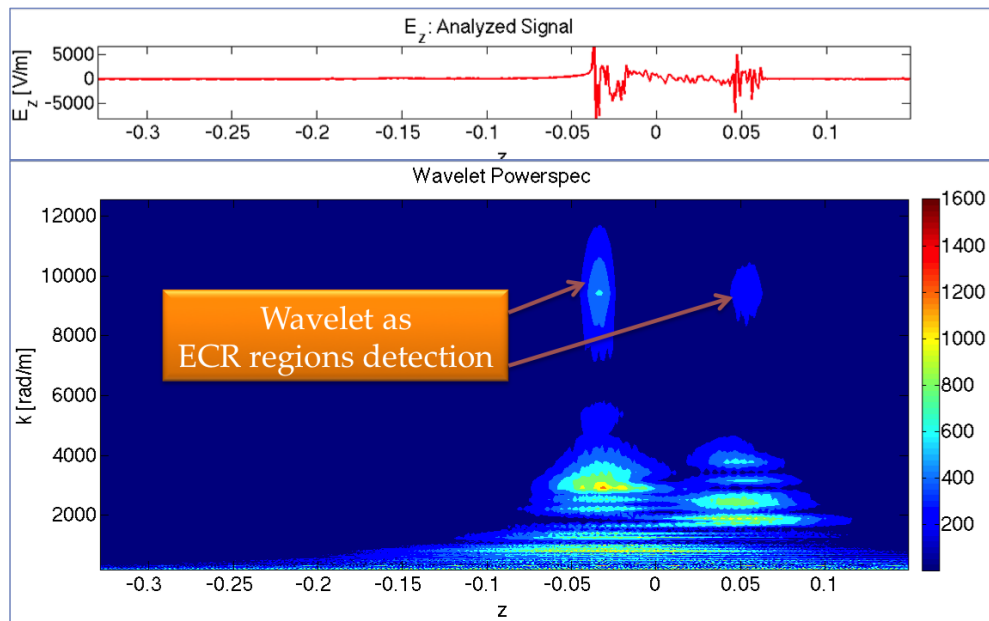

Fig. 4.48. Wavelet Spectrogram: Wavelet of E_z, $W\{E_z\}$ in cavity with plasma along the z-axis. In the upside plot, the amplitude of the electric field is shown, with the clear amplification in near resonance regions.

5

A microwave interferometry at LNS

The aim of any plasma diagnostics tool is to making significant, non perturbing measurements without change the state of the plasma. In the case of microwave diagnostics, the interpretation is often difficult and requires not only the formal theory of electromagnetic interactions with plasma treated in Chapter 1, but also the development of intutitive skills in selecting meaningful semplifications, reinforced from a lot of measurements, performed during the PhD course and described in this chapter. Many of the cases of wave propagation are so much complicated to prevent any exact formulation and solution; a feeling for how things scale from similar, more tractable cases is often essential.

For diagnostics problem applications, only small amplitude probing waves need to be considered. Therefore the reaction of the electrons is treated as linear and the plasma can be modeled in the "cold" plasma approximation described in Chapter 1.

5.1 Introduction and motivation

Microwave-to-plasma coupling optimisation, including new methods of density over-boost provided by plasma waves generation [12, 114–116], as well as magnetostatic field tailoring for generating a proper electron energy distribution function suitable for optimal ion beams formation, will require diagnostics tools spanning across the entire electromagnetic spectrum: from microwave interferometry to X-ray spectroscopy; these methods can be implemented in advanced forms including *high resolution X-ray spectroscopy and spatially-resolved X-ray spectroscopy* made by quasi-optical methods (pin-hole cameras). The optimisation of ion confinement also requires a complete control of cold electrons displacement, that can be performed by **optical emission spectroscopy** (for X-ray and optical spectroscopy see [117]).

As it can be seen in Fig. 5.1, the most suitable tool for measuring the electron density as a whole, i. e. being sensitive to all the energy components, is to implement non–intrusive microwave-based interferometry. Following an approach that is
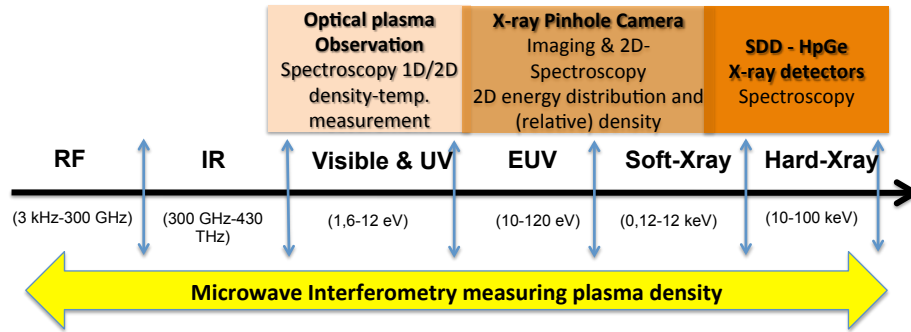
Optical plasma Observation Spectroscopy 1D/2D density-temp. measurement	X-ray Pinhole Camera Imaging & 2D-Spectroscopy 2D energy distribution and (relative) density	SDD - HpGe X-ray detectors Spectroscopy

RF   **IR**   **Visible & UV**   **EUV**   **Soft-Xray**   **Hard-Xray**

(3 kHz-300 GHz)   (300 GHz-430 THz)   (1,6-12 eV)   (10-120 eV)   (0,12-12 keV)   (10-100 keV)

Microwave Interferometry measuring plasma density

Fig. 5.1. Existing plasma diagnostic tools

commonly used in "inverse problems" solutions, like in microwave tomography, the crucial point for the success of the microwave-based techniques will be the knowledge of the plasma dispersion relation.

Other typical diagnostics used for other types of plasma have had a poor application because one side of the plasma chamber of the ion sources, as described in chapter 2, is not accessible because of the extraction system and the magnetic confining trap is an obstacle in other directions. The presence of high voltage makes quite complicate the installation of some diagnostics, too.

The microwave interferometry has been developed mainly for the measurement of plasma density in large reactors for controlled thermonuclear fusion (Tokamaks or Stellarators)[118]. Recently, the R&D on ion Sources group at LNS has, for the first time, proposed the application to the ECR ion sources.

An interferometer is able to measure the difference in path length between a reference beam, which is kept constant in optical length, and a beam transmitted through the plasma. The optical length through the plasma varies because of the change in refractive index, connected with the variation of the electron density. However in ECRIS, it results as impracticable a direct application of conventional techniques such as "phase shift" or "zebra stripes" [119, 120] due to the unfavorable ratio between the wavelength of "probing" and the dimensions of the resonant cavity where the plasma is generated (i. e. the condition $L \sim \lambda_p$ applies) .

The typical density range of ECR plasmas, ranging from 10^{11} to about 10^{12} cm^{-3}, causes the probing beam wavelength to be in the order of few centimetres which is comparable to the plasma chamber radius.

It has been opted therefore for a more sophisticated technique, known as "frequency sweep" [51], by which it is possible to determine the dielectric constant of the plasma - and therefore the density by which such constant depends - on the basis of a measurement of the beating frequency of a signal obtained by the superposition between a traveling wave along a reference arm, and an the other passing through the

plasma, filtering out the unwanted multipath contribution. Analyzing the detected signals in the frequency domain, multipaths contributions due to the microwaves reflection inside the resonant cavity contating the plasma, can thereby be suppressed by isolating and cleaning their contribution to the beating signal spectrum.

5.2 Interferometer Design

The design phase of the interferometer has primarly to take into account the constraints dictated by the electromagnetic properties of the magnetized plasma: the dispersion relation of such anisotropic medium, non-homogeneous and dispersive, highlights the presence of areas of cut-off and resonance conditions, requiring careful design choices, for example with regard to the wavelength probing signal, also in relation to the size of the plasma itself, to the its density gradients and to the effects of refraction and reflection. Other issues to be considered are the geometric constraints imposed by the experimental scenario, in particular the plasma chamber access ports, which considerably limit the available aperture area for the horn antenna used to radiate in cavity.

5.3 Proposal for the interferometry on compact devices

In the classical scheme of a microwave "Mach-Zender" type interferometry, a microwave signal at frequency larger than any cutoff/resonance frequency of the plasma under investigation is splitted into two different branches: the first one is launched into the plasma, the second one is used as reference signal, propagating into a waveguide of calibrated length, as shown in Fig. 5.2.
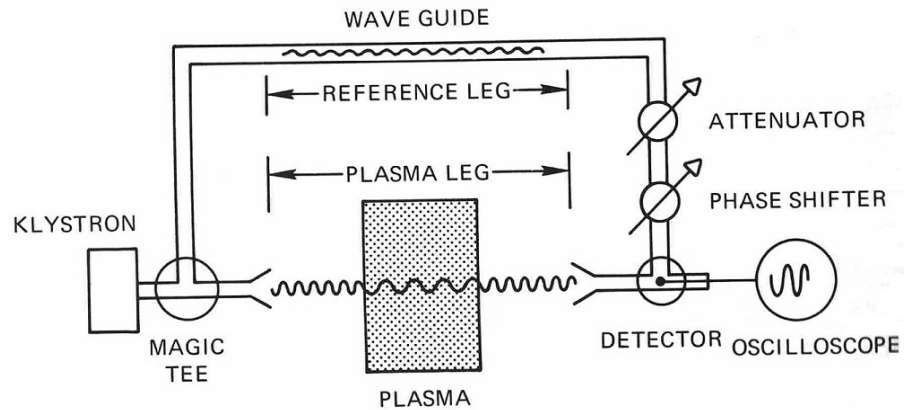

Fig. 5.2. Block scheme of a classical interferometer.

The basic idea [121] is that the density can be determined from phase shift which explicitly depends on the natural plasma oscillation ω_p, i.e. the electron density, as depicted by the mathematical relation below:

$$\Delta\phi = \int_0^L \frac{\omega}{c} \left[1 - \left(1 - \frac{\omega_p^2}{\omega^2} \right)^{1/2} \right] dl \tag{5.1}$$

where $\omega_p^2 = \frac{n_e e^2}{m_e \epsilon_0}$ is the plasma oscillation, L is the plasma length along which the integral is calculated, c the speed of light, ω the probing microwave pulsation, and the other quantities are the standard fundamental physical constants.

In our experimental setup, that is typical of several ECRIS, the direction of the electromagnetic wave vector $\mathbf{k}$ is along the magnetostatic confinement field $\mathbf{B}_0$, then the dispersion relation of the magnetized plasma has two solutions: right-hand (R) and left-hand (L) circularly polarized waves, with the following propagation constants:

$$k_R = \frac{\omega}{c} \sqrt{1 - \frac{\omega_p^2}{\omega(\omega - \omega_g)}} \tag{5.2}$$

$$k_L = \frac{\omega}{c} \sqrt{1 - \frac{\omega_p^2}{\omega(\omega + \omega_g)}} \tag{5.3}$$

where $\omega_g = eB_0/m_e$ is the electron cyclotron frequency and we can assume that the collision frequency is much smaller than the microwave frequency. Without loss of generality we choose a cartesian reference system so that the z axis is parallel to $\mathbf{B}_0$ and to the yz plane containing the propagation constant vector $\mathbf{k}$ directed along $\mathbf{B}_0$. In this configuration the electric field vectors associated to R and L waves can be written as:

$$\mathbf{E}_R = (\hat{x} - i\hat{y})e^{ik_R z} \tag{5.4a}$$

$$\mathbf{E}_L = (\hat{x} + i\hat{y})e^{ik_L z} \tag{5.4b}$$

The sum of the two waves provides the composed wave $\mathbf{E}_t = \mathbf{E}_R + \mathbf{E}_L$ having the following effective constant of propagation:

$$k_{eff} = (k_R + k_L)/2 \tag{5.5}$$

So, the phase shift due to the presence of the plasma is:

$$\Delta\phi = \int_0^L (k_0 - k_{eff})dL \tag{5.6}$$

where $k_0 = \frac{\omega}{c}$ is the free space propagation constant.

Figure 5.3 highlights the conceptual layout of an interferometer setup applied to small-size plasma chambers like in case of ECR ion sources. The main problem consists

in the the multipath given by probing signal reflections at the chamber walls (reflecting surfaces). To be significant, the measurement must be depurated by these spurious components, and this can be done only applying a more sophisticated experimental strategy.
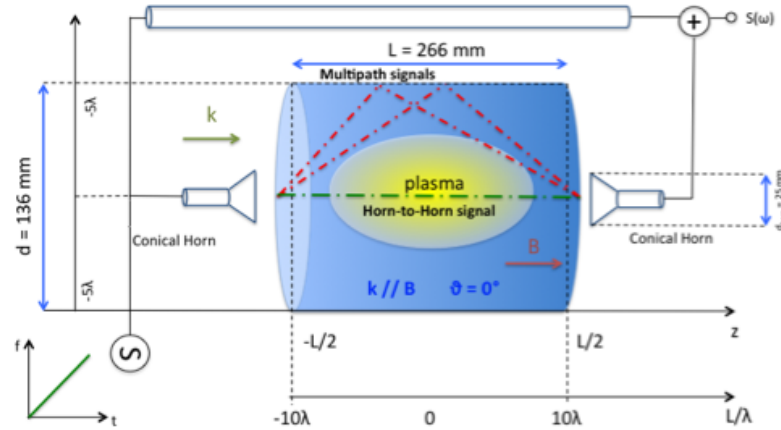

Fig. 5.3. Sketch of the microwave interferometer design, with particular emphasis on the dimensions of the plasma chamber and their relationship with the wavelength. Multipaths (red dashed lines) formation due to the reflection of the probing signal on the walls of the chamber. The green dashed line is the single pass horn-to-horn signal.

The figure 5.3 schematically shows that due to the metallic chamber walls, the detector horn antenna may receive not only the horn-to-horn signal, but also the waves reflected from the chamnber walls. In other words, the simple evaluation of the phase shift of a monochromatic probe signal is not enough to extract a reliable information on plasma density, because the phase shift can be caused also by the multi-path originating from internal reflections.

In order to cope with suppressing the multi-paths two strategies can be adopted (Figure (5.4)) [122]:

- **frequency sweep method** strategy, which will be described in details later on.
- **high-directivity horn antennas** design operating at high frequency and eventually in corrugated configuration.
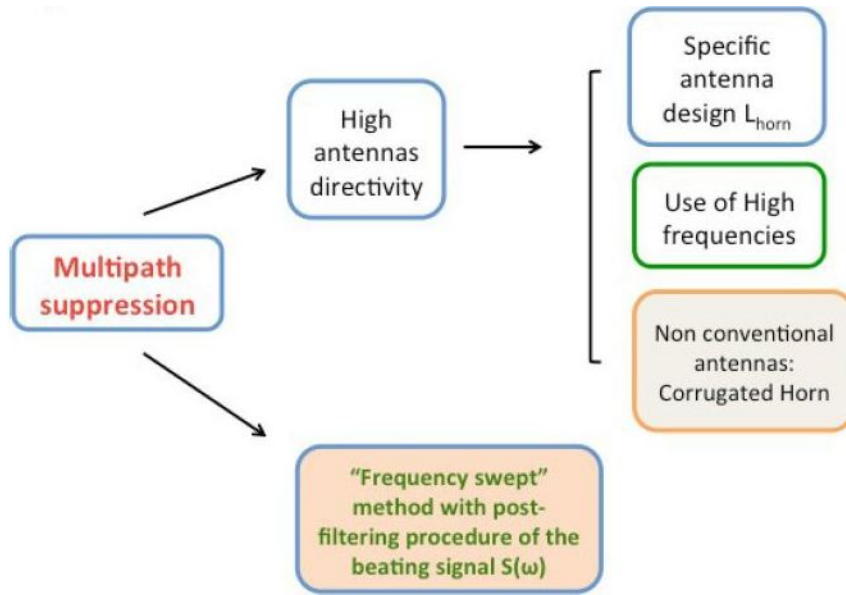
Fig. 5.4. Strategies proposed for the multi-path suppression: the first one is to improve the directivity of horn antenna; the second is to adopt the "frequency sweep" method with a post filtering procedure of the beating signal $S(\omega)$

5.3.1 Sweep-frequency interferometry

The frequency sweep method consists in sending in both the reference and plasma branches a signal characterized by an increasing frequency (this is usually known as *"chirp signal"*); the most simple case is a linear increase signal like depicted in Figure 5.5 and described by the following equation:

$$f(t) = f_0 \pm \frac{\Delta f}{T}t \tag{5.7}$$

where Δf is the frequency range of the sweep and T its time duration.

This approach is typical of the millimetre wave FMCW (frequency modulated continuous wave radar) systems [123], where varactor tuned Gunn oscillators are often used to generate the chirp which is radiated toward a target through an antenna. The echo received T seconds later is mixed with a portion of the transmitted signal to produce a beat signal at a frequency f_b, which is proportional to the round-trip time t.

At a certain time t, the phase of the chirped signal will be given by:

$$\phi(t) = \cos\left(2\pi \int_0^{t'} f(t')dt'\right) = \cos\left(2\pi f_0 t \pm \frac{k}{2}t^2\right) \tag{5.8}$$
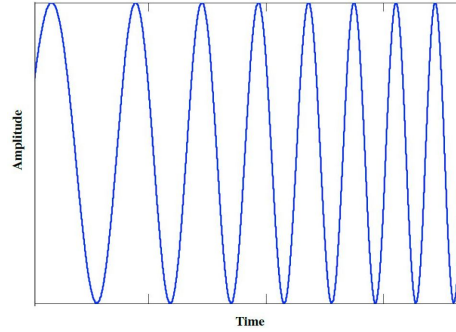
where $k = \frac{2\pi\Delta f}{T}$

Fig. 5.5. Example of a chirped signal

The block scheme of a sweep-frequency interferometer is shown in Fig. 5.6: one signal is sent along the medium we desire to investigate, while another one is sent to a reference leg. The superposition of the two signals will generate a new signal, which is a *beating signal*. The interferometer developed in the framework of this thesis is focused on the possibility to use this beating signal for the detection of the plasma density.
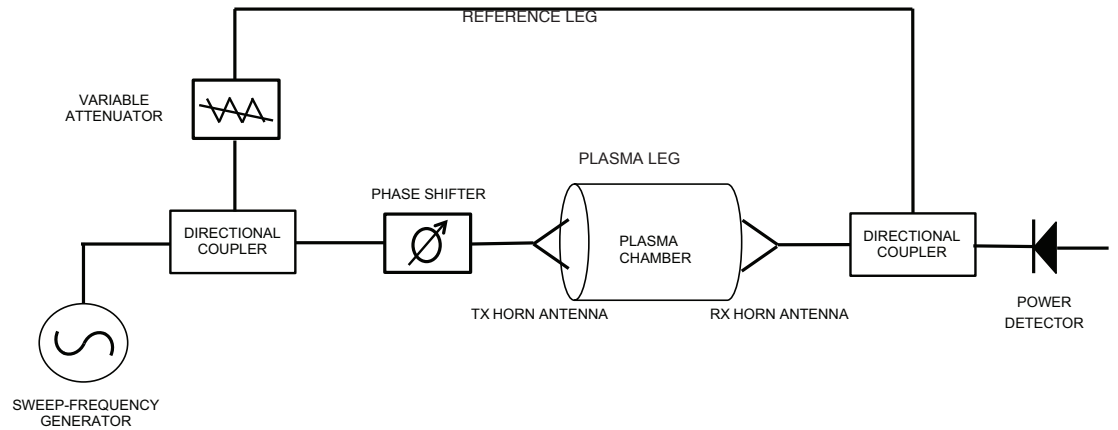

Fig. 5.6. Sweep-frequency interferometer scheme

The addition of the two signals produces a time varying signal $M(t)$ given by:

$$M(t) = A \sin(\omega_{int} + \phi_2 + \phi_p) + B \sin(\omega_{int}t + \phi_1) \tag{5.9}$$

where A and B are respectively the amplitude of the signal traveling through the plasma and through the reference leg, ϕ_1 is the phase shift due to the dispersion in the waveguide of the reference leg, ϕ_2 is the phase shift due to the dispersion in the waveguide of the plasma leg, ϕ_p is the phase shift due to the plasma, ω_{int} is the

operating frequency. Now, since $\sin\alpha + \sin\beta = 2\sin\left(\frac{\alpha+\beta}{2}\right)\cos\left(\frac{\alpha-\beta}{2}\right)$, we can rewrite the (5.9) as:

$$M(t) = 2A\sin\left(\omega_{int}t + \frac{\phi_1 + \phi_2 + \phi_p}{2}\right)\cos\left(\frac{\phi_2 + \phi_p - \phi_1}{2}\right) + 2(A-B)\sin(\omega_{int}t + \phi_1)$$

$$(5.10)$$

Setting $A = B$, which means equal amplitudes, and averaging the previous equation over on a period (since any power detector measures just the period averaged power), we obtain the eq. :

$$P_{M(t)} = \left\langle |M(t)|^2 \right\rangle = S(t) = 2A^2\cos^2\left(\frac{\phi_p + \phi_2 - \phi_1}{2}\right) \tag{5.11}$$

The argument of cosine is the time-dependent phase shift:

$$\Delta\phi(t) = \left(\frac{\phi_p + \phi_2 - \phi_1}{2}\right) \tag{5.12}$$

Hence, equation (5.11) tells us that, if it is possible to design a system such that the net phase difference, as the frequency of the source is varied, is linear in time, the signal $S(t)$ can be simply be described in terms of a constant beat frequency ω_{beat}:

$$S(t) \propto \cos^2(\omega_{beat}\, t) \tag{5.13}$$

where ω_{beat} is the constant beat frequency given by the time variation of phase shift:

$$\omega_{beat} = \frac{\partial \Delta\phi(t)}{\partial t} \tag{5.14}$$

Now let's explain better why a beat frequency arises.

The two waves, arriving with a relative phase difference, interfere each other at the output of the interferometer. When the input frequency is varied, at the output the two waves will arrive with a new different relative phase. The temporal variation of the relative phase, represents the frequency of the beating signal, as expressed by eq. (5.14). The presence of plasma leads to a shift of the beating frequency.

The phase shifts in the reference leg, in the plasma leg and in the plasma are respectively given by:

$$\phi_1(\omega) = \int_{L_{ref}} k_g dl \tag{5.15}$$

$$\phi_2(\omega) = \int_{plasma_{leg}} k_g dl \tag{5.16}$$

$$\phi_{plasma}(\omega) = \int_{plasma} k_{plasma} dl \tag{5.17}$$

where:

- $k_g = (1/c)\sqrt{\omega^2 - \omega_c^2}$ is the wavenumber in the waveguide, where ω_c is the waveguide cut-off frequency.

- $k_{plasma} = (1/c)\sqrt{\omega^2 - \omega_p^2}$ is the wavenumber in the plasma (where ω_p is the plasma frequency).

The temporal variation of the phase difference between the reference leg and the plasma leg, namely the beat frequency, can be written as [124]:

$$\omega_{beat} = \frac{\partial\omega}{\partial t}\frac{\partial\Delta\phi(t)}{\partial\omega} = \frac{\partial\omega}{\partial t}\left(\Delta L\frac{\partial k_g}{\partial\omega} + \int_{plasma}\frac{\partial k_{plasma}}{\partial\omega}dl\right) \tag{5.18}$$

where ΔL is the difference in length between the reference leg and the plasma leg. In absence of plasma $\omega_p = 0$ and then $\frac{\partial k_{plasma}}{\partial\omega} = \frac{1}{c}\frac{\omega}{\sqrt{\omega^2 - \omega_p^2}} = 1/c$, obtaining:

$$\omega_{beat} = \frac{\partial\omega}{\partial t}\left(\Delta L\frac{1}{c}\frac{\omega(t)}{\sqrt{\omega^2(t) - \omega_c^2}} - \frac{L}{c}\right) = const \tag{5.19}$$

In equation (5.18) the beat frequency ω_{beat} contains two parts, that one having ΔL due to the difference in path lengths and the other adding term that is due to the presence of plasma. From eq. (5.19), when solving the differential equation , where ω_{beat} is fixed as constant, we obtain $\omega(t)$, i. e. the temporal trend of the chirp signal

It is immediate to notice that from the equation (5.19), in order to maximize the effect on the beat signal of the plasma leg, ΔL has to be kept as short as possible. We can simplify this just setting $\Delta L = 0$, in this case we would have:

$$\omega_{beat} = \frac{\partial\omega}{\partial t}\left(\frac{L}{c}\right) = const. \tag{5.20}$$

We see that $\omega(t)$ is merely given by $\omega(t) = (const.*(c/L)))*t$, where $const$ is the value of the chosen beat frequency ω_{beat}; now the source frequency has to be simply linear in time.

It is possible to demonstrate that the detected signal $S(\omega)$ can be written as:

$$S(\omega) \propto 2A^2 \cos^2 \left\{ \left[\Delta L \sqrt{\omega^2 - \omega_c^2} + \int_0^L \sqrt{\omega^2 - \omega_p^2(l)} dl \right] / 2c \right\} \qquad (5.21)$$

The effect of the plasma is increased if ΔL is kept small, when ΔL is even neglected, we can write:

$$S(\omega) = 2A^2 \cos^2 \left[\frac{1}{2} \left(\int_L k_{plasma} dl \right) \right] \qquad (5.22)$$

In principle, the method-by virtue of the relation would be able to directly eliminate the "cavity effect" by introducing the proper dispersion relation of the plasma chamber in the given frequency range as an additional term in the equation. The only unknowm term would remain, thereby, the integral on the plasma dispersion relation. Unfortunately, the resonator $\omega(\mathbf{k})$ relation is a well-known collection of modes which result in an expression that is not a mathematical function. It is therefore impossible to prepare a chirp $\omega(t)$ including "a priori" the cavity effects. The experimental technique anyway will allow to do this "a posteriori".

The above mentioned beat signal "cleaning" is a sort of "instrument calibration" to be carried out without the plasma and is possible because we are able to perform spectral analysis of the beating signal: Fast Fourier Transform (FFT) of the receiving horn collecting signal could be done, displaying the quasi-monocromatic beating that it is evident in case of "in-vacuum" propagation as discussed hereiafter in the numerical simulation[122], [124, 125]. Fast Fourier Transform (FFT) will allow to analyze the very noisy spectrum of the beating signal detected in presence of cavity, to filtrate the multipath components with respect to the direct path meaningful signal. This strategy has been numerically tested and finally experimentally validated.

5.3.2 Choice of Microwave Frequency range

The microwave frequency range $\Delta f = f_{min} \div f_{max}$ is determined once known the expected electron densities of the plasma. In addition, its value has important implication on a variety of other issues such as phase sensitivity, system cost, availablity of power sources, etc. We first consider the physics of the microwave propagation and then some practical issues. From the physics standpoint, we need to consider:

- plasma size,
- cutoff and resonance,
- refraction

The first requirement requires a plasma size large compared to the wavelength of the probing beam: typically, it is required that the characteristic transverse plasma size d must satisfy $d \gg \lambda_0$;

Equation shows that appreciable variations of $S(\omega)$ occur only if $\omega_{probe} \geq \omega_p$ Hence, for ω_{min}:

$$\omega^2_{min} \geq \omega^2_{p(max)} = \frac{e^2}{m_e \epsilon_0} n_{e(max)} \tag{5.23}$$

Our test plasma has a typical density range of $10^{17} \div 10^{18}$ m $^{-3}$, therefore the lower value of the frequency range is set by (5.23) expressed in terms of frequency:

$$f_{min} \geq f_{p(max)} = \frac{1}{2\pi} \sqrt{\frac{e^2}{m_e \epsilon_0} n_{e(max)}} \tag{5.24}$$

Replacing the value of the maximum density, we can obtain a **lower limit frequency equal to $f_{min} \simeq$ 18 GHz**.

In order to work in fundamental mode TE_{11} on the circular waveguides and TE_{10} for the rectangular ones, is automatically set the upper limit of the range at 26.5 GHz and our total frequency excursion at [18-26.5] GHz .

An operating frequency f_0=22.5 GHz means 2.5 times f_p at our highest density of 10^{12} cm^3 (being the peak plasma frequency 9 GHz). Inner plasma refractive effects usually suggest a more stringent condition on the minimum microwave frequency: in presence of density gradients, in fact, a microwave beam is refracted according to Snell's law. In particular refraction of the beam by plasma density gradients would occur if $L_n = \frac{n_e}{\nabla n_e} \sim \lambda_0$. In order to obtain a reasonale trade-off between sensitivity ($\omega_0 \sim \omega_p$) and robustness to refraction effect($\omega \gg \omega_p$), we finally fixed the operating range such as $\Delta f = 18 - 26.5$ GHz.

5.4 Antenna design and beating signal simulation with chirped excitation

The design of an high-directivity horn antenna was carried out through CST EM [126] and RF COMSOL [127] simulations. The beating signal with chirped excitation was also investigated by simulations The antenna was design to operate in 20-26 GHz frequency domain as explained in the previous section.

In order to obtain the maximum directivity, that for a conical horn antenna is $D = \left(\frac{\pi d}{\lambda}\right)^2 e_A$, we can only choose an optimum value for the horn length $l_{opt} = \frac{d^2}{3\lambda}$, from Fig. (5.7)[128], because the diameter and the frequency are already fixed from the mechanical constraints.
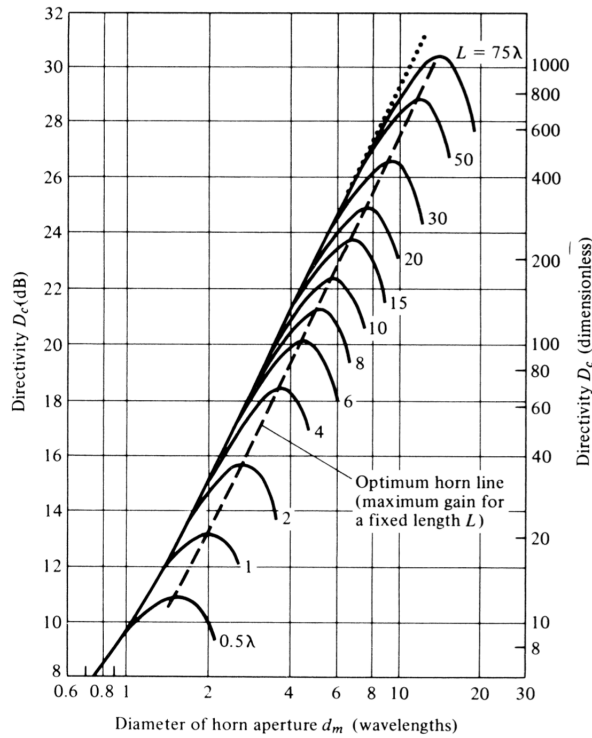
Fig. 5.7. Conical Horn antenna directivity-vs-diameter at varius lengths

Figure 5.8 illustrates the antenna simulation performed by means of a FDTD-FIT method tu optimize the horn length. There are shown the antenna geometry and the electric field inside the horn.

In Fig. 5.9 the radiation diagram in the E and in the H plane are depicted.

In the table in Tab. 5.1 the geometrical parameters of the two antennas are listed.
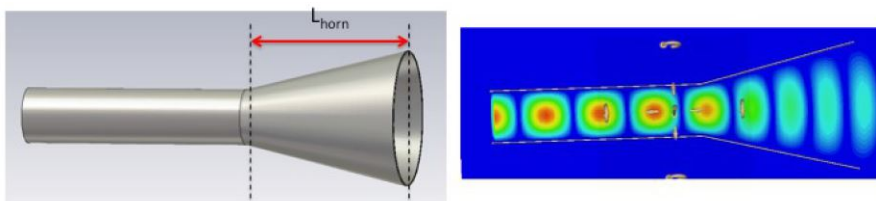

Fig. 5.8. Geometry of the horn antenna and electric field propagation

With the optimum value for $L_{horn} = 50$ mm we can obtain a directivity di $D_{dB} = 14.8$ dB. In fig. 5.10 it is shown the scattering parameter S_{11} that is well-matched for all the frequency range. Finally, fig. 5.11 shows the 3D radiation diagram for the final antenna design.

Parameters		Values
Frequency range	BW	20-26 GHz
Average Wavelength	λ	13.5 mm
Horn aperture radius	R_{horn}	12.5 mm
circular waveguide radius	R_{wg}	5.03 mm
horn length	L_{horn}	50 mm

Table 5.1. Parameters of horn antenna required to fulfill the high directivity transmission.
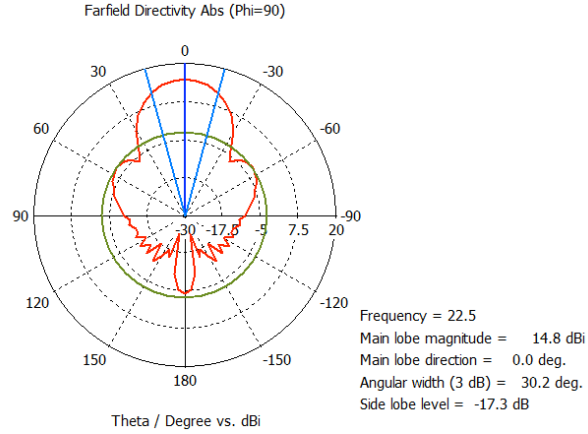
(a) E-plane
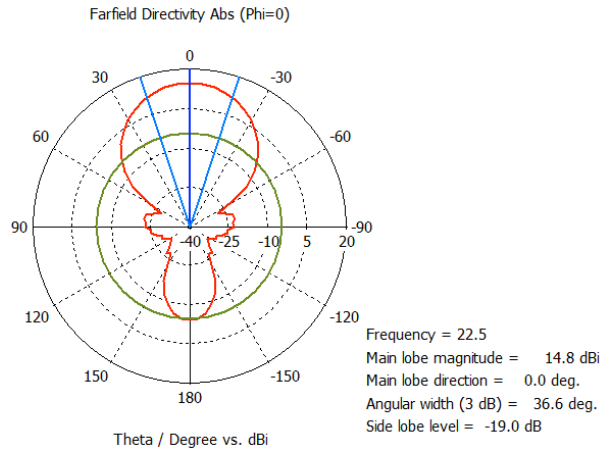
(b) H-plane

Fig. 5.9. Radiation patterns in E and H plane with $L_{horn} = 50$ mm.

Beating signal simulations

Some analytical and numerical calculations have been carried out in order to evaluate the frequency shift in terms of *beating frequency* induced by the plasma and the impact of spurious spectral component introduced by the multipaths. Figure 5.12 shows the beating signal variation due to a plasma of density $n_e = 5 \cdot 10^{17} m^{-3}$ without including any field searching at the plasma chamber walls.
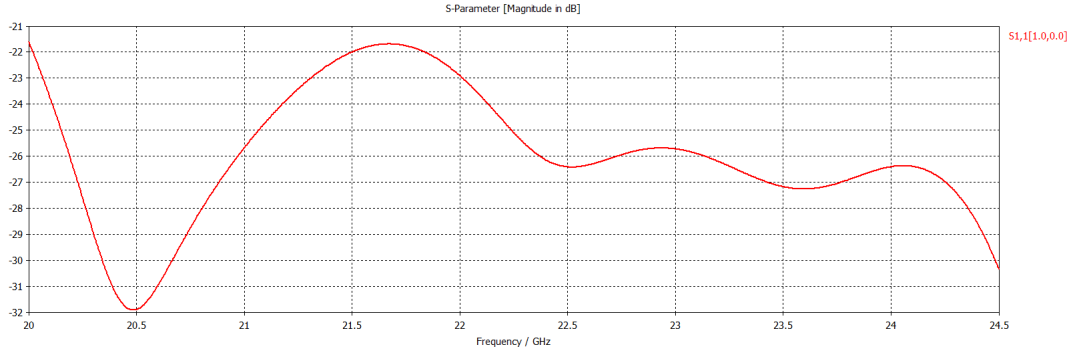
Fig. 5.10. simulation of conical horn antenna: S_{11} parameter vs frequency.
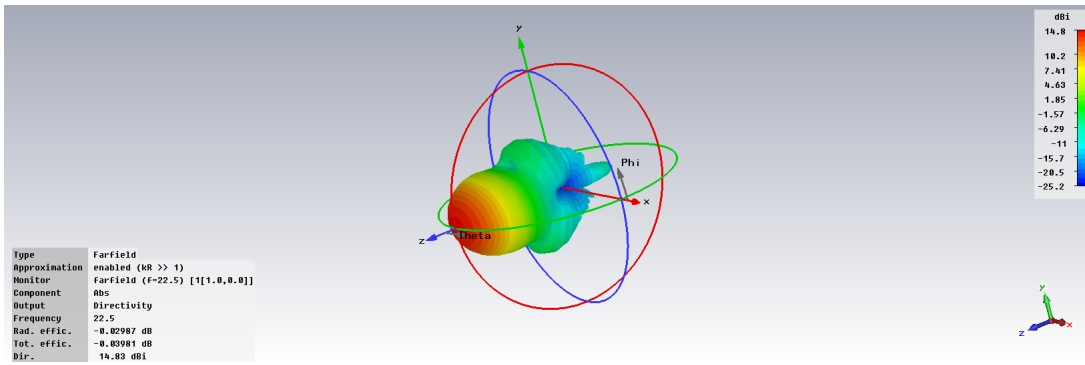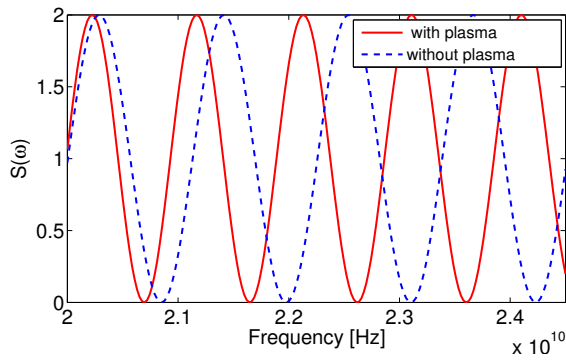

Fig. 5.11. 3D radiation pattern.

Fig. 5.12. Beating signal frequency shift due to the plasma. Plot obtained by considering a plasma of density: $n_e = 5 \cdot 10^{17} m^{-3}$ in eq. (5.22)

The beating frequency shift in the presence of plasma (red curve) compared to the case in the absence of plasma (dotted blue curve). In particular, the beat signal in absence of plasma is given by the relation (5.25), while the beat signal in presence of plasma is given by (5.26):

$$S(\omega) = cos^2(\omega_{b0}t) = \cos^2(\omega(t)\frac{L}{2c}) \tag{5.25}$$

When we consider the presence of plasma, the beating signal becomes:

$$S_{plasma}(\omega) = \cos^2(k_{eff}\frac{L}{2}) \tag{5.26}$$

The frequency sawtooth is:

$$\omega = const\frac{c}{L}t \tag{5.27}$$

$$const = \frac{L}{c}\frac{(\omega_{max} - \omega_{min})}{\Delta t} \tag{5.28}$$

A more realistic picture can be obtained by simulating the beating obtained by the two facing antennas, as depicted by figure 5.14.

Horn-to-horn transmission has been explored by means of CST simulation, including the frequency sweep excitation. Fig. 5.13 and 5.14 illustrate two different situations: Fig. 5.13 illustrates the transmission in free space (single pass wave a at each frequency); in Figure 5.14 we included the cavity (i.e. the plasma chamber of a real ECRIS) and calculated the horn to horn propagation. It is evident that an interference pattern appears (due to walls reflection, i.e. the undesired multi-paths), but, anyway, the most part of the microwave power is concentrated in the near-axis region. This means that the single-pass may be predominant in the received signal.
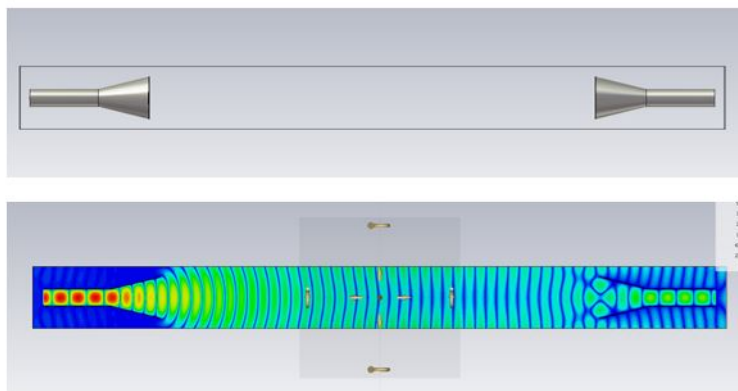

Fig. 5.13. Horn-to-horn propagation in free space

A spectral analysis of the beating signal can be done, as depicted in Fig. 5.15. The FFT of the receiving horn, displays a quasi-monochromatic beating in case of "free-space" propagation: only one peak is evident, corresponding to beating produced by the direct horn-to-horn propagation.

When the scenario is changed, by introducing the cavity between the two horns, the spectrum modifies according to figure 5.16. Now spurious components come out, due to multi-paths effects. In any case, they are well distinguished from the main component given by the single pass signal.
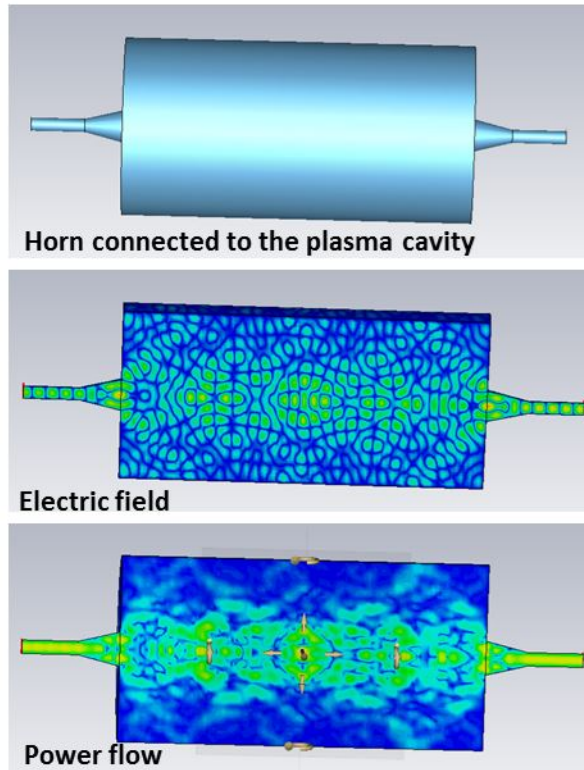
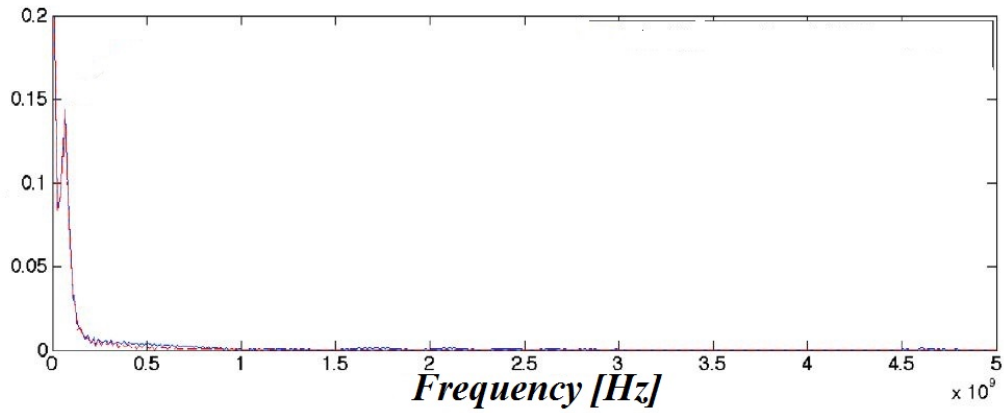**Fig. 5.14.** Horn-to-horn propagation in cavity

Fig. 5.15. Spectrum of the free-space beating signal: only one peak is evident, corresponding to beating produced by the direct horn-to-horn propagation.
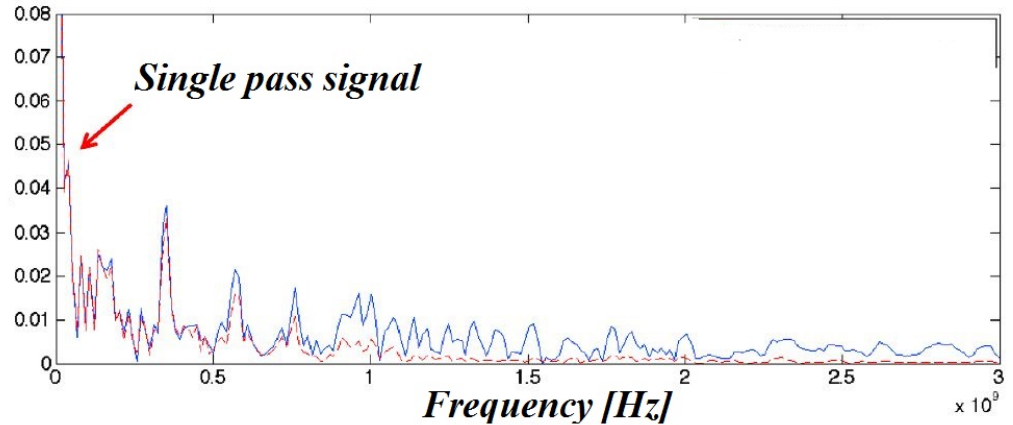
Fig. 5.16. FFT spectrum of the simulated horn-to-horn propagation in "frequency sweep" mode as obtained by numerical simulations: the appearance of many secondary peaks is due to the signal multi-paths caused by the internal reflections in the chamber.

5.5 Interferometer subsystems

In Fig. 5.17 the overall experimental setup is shown. We then need, according to the circled number in Fig. 5.17:

1. A signal generator (YIG Signal oscillator, or a synthesized microwave signal generator) able to produce a frequency sweep in the band of interest (18-26 GHz).
2. Two directional couplers ("3 dB Short Slot Hybrid Divider"'); the first one splits the signal in the two arms. The second one sums the two signals coming from the reference leg and the plasma leg;
3. A 0-360° WR42 Phase Shifter, useful for the calibration of the setup;
4. Two WR42 Rect. to Circ. Transitions transitions in order to couple the waveguides (which have a rectangular cross section) with the basis of the horns (which have circular cross section);
5. 0-30 dB WR42 Variable Attenuator, able to attenuate the intensity of the signal on the reference arm, so that the two signals arrive at the summing directional coupler with the same amplitude (so that the last term of eq. 5.10 vanishes, and the beating signal has a simple expression);
6. Two WR42 90 E or H Bend .
7. 20-25 GHz Conical Horn Antennas, whose features have been already discussed
8. WR42 Straights Sections and WR42 to Coax SMA adapter
9. A power probe detecting the beating signal.

In order to perform RF power measurements along the different branches, and especially the beating signal, a diode power sensor has been used to perform accurate average power measurements.
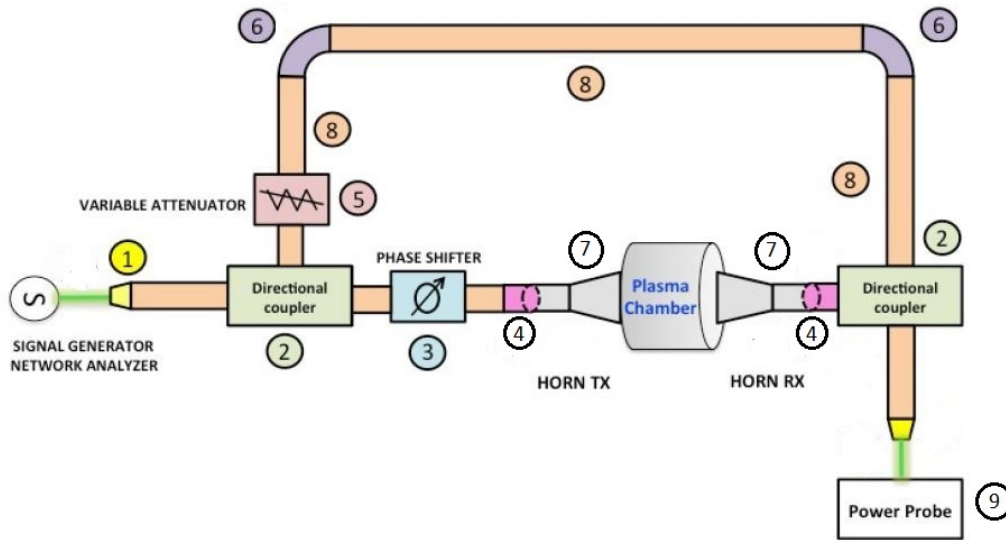
Fig. 5.17. A block scheme of the interferometer with all equipment

This tool is used as a low-passband filter, excluding the higher frequencies, on the order of GHz, and allowing to pass only the lower frequencies, on the order of Hz, which are typical of the beating signal as analitically shown in equation (5.11).

The plasma testbench

Despite the setup has been designed in order to be as versatile as possible, the first implementation was ad-hoc arranged for the MDIS prototype named "Plasma Reactor", a test-bench dedicated to the R&D of new diagnostic tools. This device had been previously used for many research activities including environmental applications aimed to dissociate complex toxic molecules [129] and to study the propagation and absorption of microwaves in cold and weakly ionized plasmas; more recently it has been used to study the mechanism of modal conversion through electrostatic Bernstein waves [130]. It is composed of a cylindrical stainless chamber, whose length is 268 mm, it has an internal diameter of 136 mm and an external diameter of 240 mm.

In the back part, as depicted is Fig. 5.19 there is a rectangular port hosting the waveguide coming from the TWT amplifier and used for the plasma microwave heating. An additional flange hosts the pump for the vacuum, and another one a vacuometer. On the front part (Fig. 5.18) a tilted flange permits the Langmuir probe to reach the center of the chamber. The horn antennas will be installed on two opposite flanges in line of sight as it can be seen in Fig. 5.20. In Fig 5.20 the general mechanical layout is illustrated.

Concerning the magnetic system, it is composed by two permanent magnets (Fig. 5.21) separated by a soft iron spacer; they surround the plasma chamber coaxially and
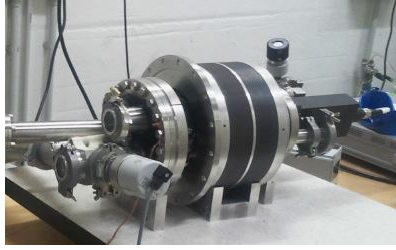
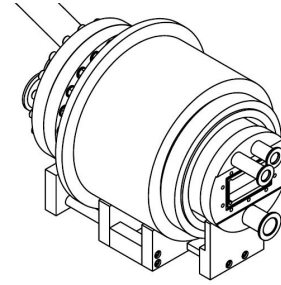**Fig. 5.18.** Front part of the Plasma
Reactor

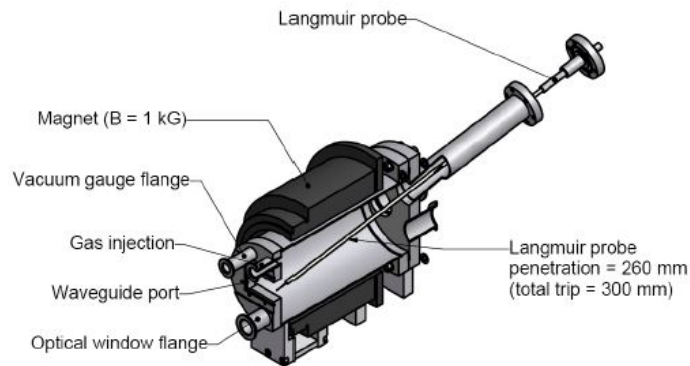**Fig. 5.19.** Back part of the Plasma
Reactor

Fig. 5.20. Components of the Plasma Reactor

can be longitudinally shifted, indeed, the exact positioning of the magnet is sometimes
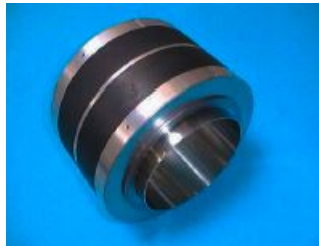crucial.

Fig. 5.21. Permanent magnet of the Plasma Reactor

The magnet is 180 mm length and has an internal radius of 75 mm, and produces
a magnetic field of about 0.1 T along the axis of the chamber

5.6 Experimental strategy

The assembly on the interferometer required a preliminary stage of "tool-by-tool"
tests in order to evaluate, step by step, the response of every device composing the
overall system.

At the beginning, the horn antennas have been characterized. Thereafter, some calibration measurements by means of two different techniques.

Concerning the first approach, the phase of the microwave in free space was measured in order to evaluate the refractive index of air, used as an absolute reference point for checking the proper working conditions of the several sub-systems. Also, the same set up has been used to measure the refractive index of a dielectric material and a calibration curve has been obtained.

Concerning the second approach, it was verified the validity of the frequency-sweep approach by measuring the beating signal in meaningful scenarios.

The tests which we carried out can be summarized in the following list:

- Horn antennas assembly and characterization;
- Calibration of Measurement Devices: Free space refraction index measurement of vacuum and dielectric material through phase shift method;
- Free space refraction index measurement of vacuum and dielectric material through beating signal detection based on frequency-sweep approach;
- In cavity refraction index measurement of vacuum and plasma through beating signal detection based on frequency-sweep approach.

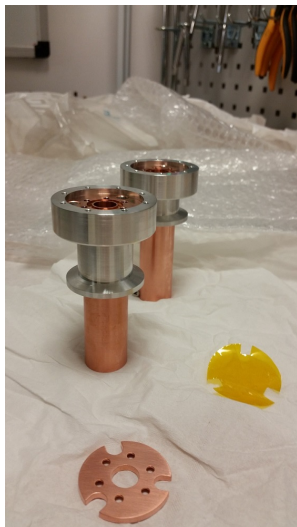### 5.6.1 Horn antennas assembly and characterization

Fig. 5.22. Assembly of the horn antennas

Fig. 5.23. Antennas connection to the transition "in waveguide"

The two circular horn antennas have been manufactured in copper (see Fig. (5.22-5.24): vacuum brek is ensured by a 8 μm layer of Kapton and a proper matching has

Fig. 5.24. The final assembly of the horn antennas

been realized in order to fit them to the standard DN25 flanges of the plasma reactor (Fig .5.25). This considerably increases the versatility of the experimental setup since it can be easily installed on another plasma device. Our setup is operated with a uniform axial magnetic field and the shape of the produced plasma is approximately cylindric.
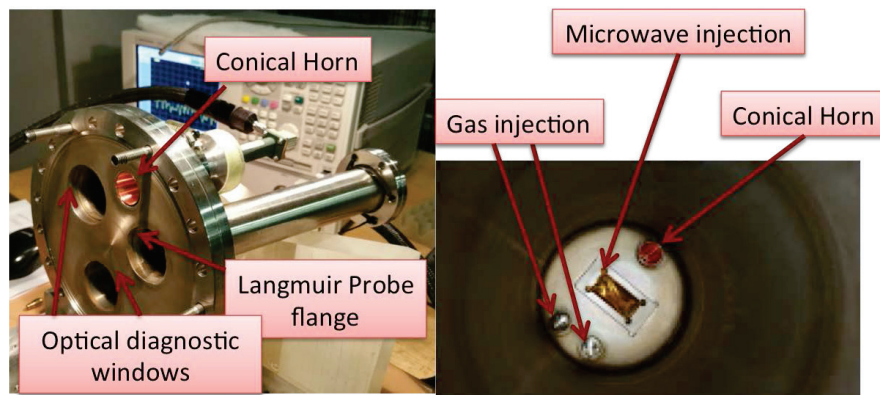

Fig. 5.25. Conical Horn antennas mounted on injection flange

The conical horn antennas are coupled whith a rectangular WR42 to circular WG20 waveguide transition that provides also a Right-Hand Circular polarisation. The use of circularly polarized antennas is desiderable since, in this case, the horn to horn transmission does not suffer signal loss due to polarization mismatch that should be considered for two linearly polarized antennas where the Polarization Loss Factor (PLF) is $\cos^2 \alpha$ (with α the angle between the two horn-linearly-polarized electric fields).

The horn antennas have been experimentally characterized in terms of impedance matching and they are well matched in the band of interest since the coupling horn reflection coefficient $|S_{11}|$, shown in Fig. 5.26, is lower than -17 dB. A larger aperture would improve the antenna directivity and reduce the multipath in cavity but we are limited by mechanical costraints. In Fig. 5.26 we show the free-space $|S_{11}|$ but the antennas remain well matched also when mounted on cavity, as we will show later.
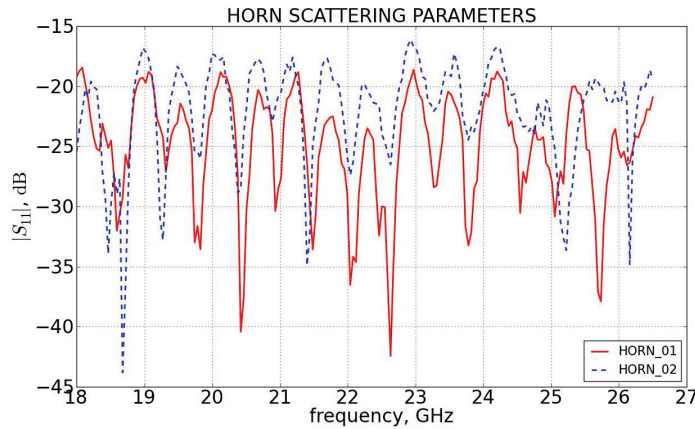
Fig. 5.26. Measured S_{11} for the two the proposed antennas

The horn radiation pattern has been measured experimentally (see Figure 5.27) on a laboratory apparatus in which the transmitting horn was mounted on a stationary pole located 266 mm (length of the plasma chamber) from the receiving antenna that was rotated at steps of 3.2° in the horizontal plane.

The measured radiation diagram of Fig. 5.27 is in agreement with the numerical calculations[122] in terms of shape of the main lobe.

However, measured radiation pattern shows a worsening of the level of sidelobe with respect to the simulation (−11 dB vs −19 dB). This lack of agreement is partly due to the ideal farfield approximation of the simulated radiation patterns, conversely to the closer distance at which the two antennas were experimentally tested (being this closer distance the same then occuring in the plasma reactor).
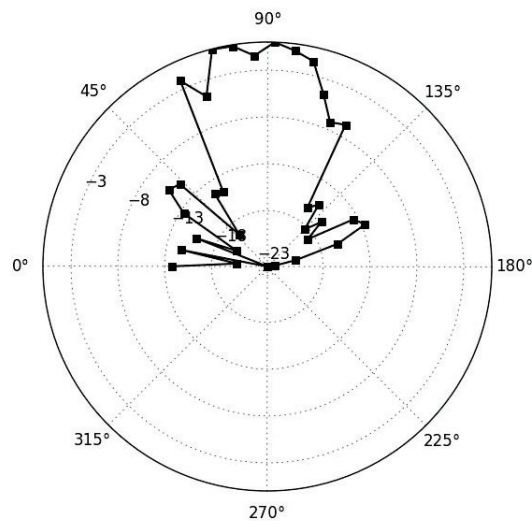

Fig. 5.27. Measured Radiation Diagram at 22.5 GHz

5.7 Free space refraction index measurement by phase shift method

The use of the interferometry in free space, as a first step, allows using a Network Analyzer in place of the reference leg plus couplers and RF probes. In this case the reference arm is internal to the Network Analyzer. We used the Agilent 2-Port PNA-L Microwave N5230A, 10 MHz to 50 GHz Network Analyzer to measure the dielectric constant of materials (Fig. 5.28). The precise knowledge of the material slab thickness
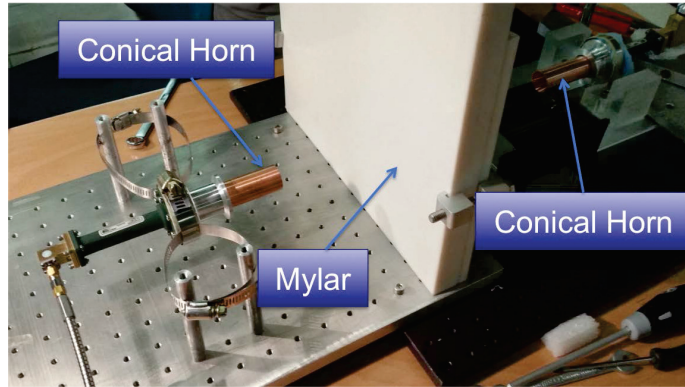

Fig. 5.28. Dielectric constant measurement

provides the information to characterize the frequency dependence of the permittivity from 18 GHz to 26.5 GHz: the measured transmission produces the phase data at that frequencies. The material under test is assumed large, flat and homogeneous. It is easily demonstrated that the plane wave solutions associated with an electromagnetic wave propagating through a uniform dielectric medium with thickness d and dielectric constant ϵ_r satisfy the following relation for the phase shift $\Delta\phi$

$$\Delta\phi = \frac{2\pi}{\lambda_0}\sqrt{\epsilon_r}d = \beta d \tag{5.29}$$

where β is the phase constant. The horn antennas were mounted on an optical bench, fixed to fine (micrometric) stages. First of all the phase-measuring bridge was adjusted to a null, by a waveguide phase shifter. After phase shift in vacuum was measured varying the horn to horn distance ΔL (see Fig. 5.29)

From the antenna theory, we notice that the far field region approximately starts at a distance d when the following conditions are satisfied:

$$d > \frac{2D^2}{\lambda} \tag{5.30}$$

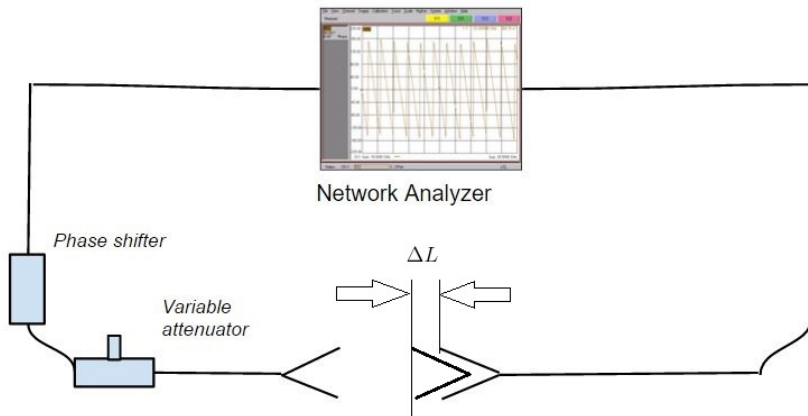$$d \gg D \tag{5.31}$$

$$d \gg \lambda \tag{5.32}$$

Fig. 5.29. setup scheme for the measurement of the refractive index in free space: when the right horn is shifted of ΔL, a phase variation $\Delta\phi$ is observed and measured with network analyzer

where D is the diameter of the antenna and λ the wavelength of the emitted radiation. For our operating conditions we have a λ which is about 1.3 cm and $D = 2.5\,cm$, which gives $d \approx 10\,cm$. The operative distance (i. e. the horn-to-horn distance in the plasma reactor assembly) is 26.6 cm, that should ensure the fulfillment of far-field condition. In any case, we started to check the "near field" effects by formerly placing the antennas at 10 cm from each other.The trend of fig. 5.30 shows the waves cannot be assumed as exactly plane waves and then, the dispersion constant k of the wave is not simply ω/c as theoretically predicted (see fig. 5.30) as it is evident from simulation of fig. 5.31 (note the wavefront for near-field is circular, and it is plane only after some cm)

We thereafter did the other measurements in the far field condition at frequencies of 18, 20, 22.5, 24 and 26 GHz and, from the slope of the fitting curve, we found a very good agreement with the expected value for the refractive index of air. In Fig. 5.32, 5.33, 5.34, 5.35 and 5.36 the fits on experimental values at different frequencies are shown.

The estimated error bar for each point is around 0.5° which is smaller than the dimension of the data point. In the 18 GHz plot we noticed a slight disagreement with the analytical trend: this might be due, once again, to the violation of the far field condition, whose weight is larger for lower frequencies
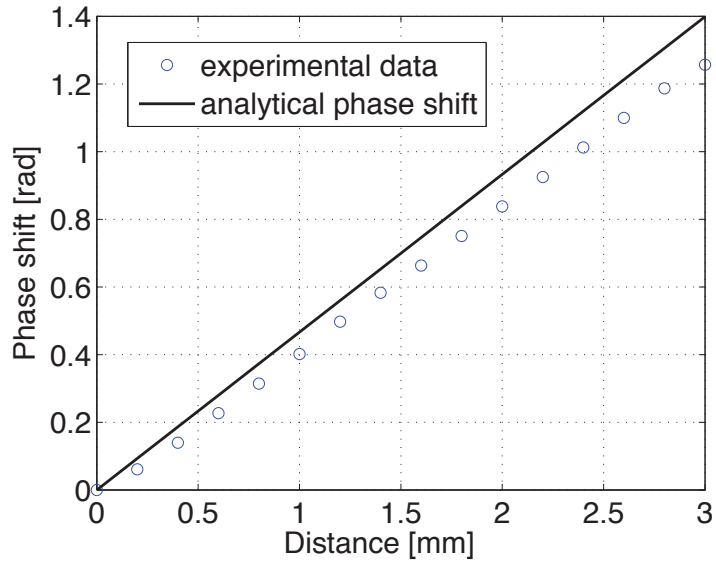
Fig. 5.30. Phase shift measured (circles) and predicted (straight line) for horn antennas placed at $\sim 5\,cm$ of distance
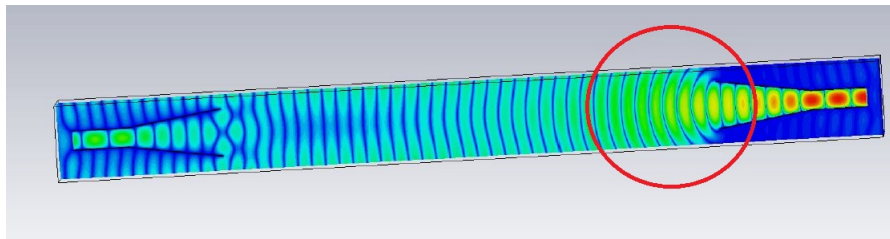

Fig. 5.31. Wavefront between horns, the circled area is approximately the near field region
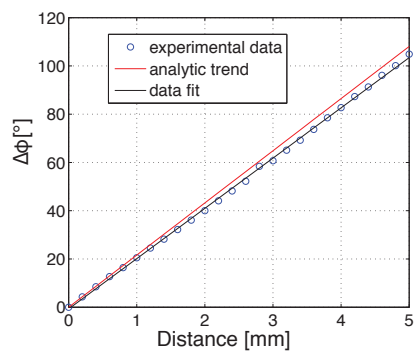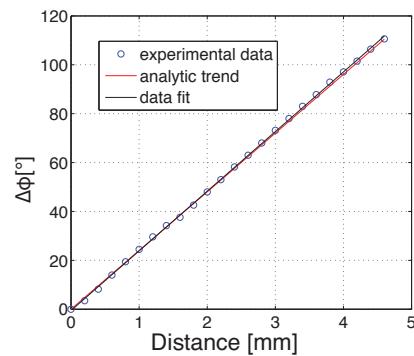

Fig. 5.32. Phase shift vs. distance at 18GHz

Fig. 5.33. Phase shift vs. distance at 20GHz

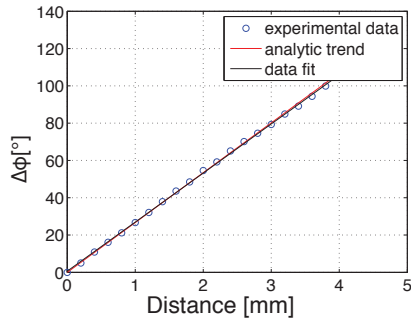| Frequency [GHz]	Refractive Index
18	0.9637
20	1.0159
22.5	0.9884
24	0.9886
26	0.9865

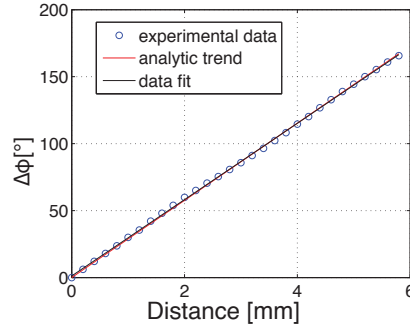**Fig. 5.34.** Phase shift vs. distance at 22.5 GHz
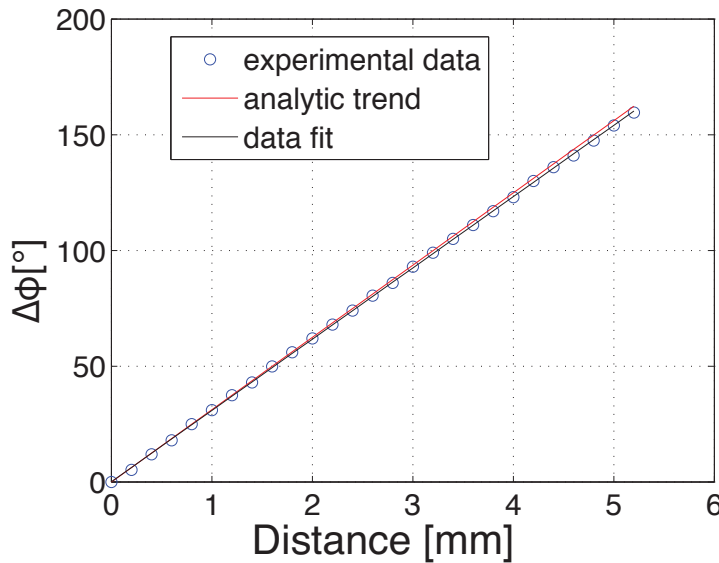
Fig. 5.35. Phase shift vs. distance at 24 GHz

Fig. 5.36. Phase shift vs. distance at 26 GHz

The averaged value for the refractive index of air (vacuum) obtained from the fits is 0.988 ± 0.026, so we have about a 2.6 % of uncertainty. This is a good starting point for trying to estimate the sensitivity and the error sources of the instrument.

After the free space "calibration", the phase shift was measured also in presence of Polyethylene terephthalate (PETP) , to compute its dielectric constant. We used sheets of various thickness t. A block scheme of the setup for this kind of measurements is shown in Fig. 5.37. In Fig. 5.38 and 5.39 are shown a mylar sheet and a mylar slab placed between the horns.

The measured phase shifts (black curve and square marker in Fig. 5.40) very well agree with the expected linear fit, providing a very low error in the derivation of the electrical permettivities ϵ_r, as shown in Table 5.2, that are in very good agreement with the literature data [131].
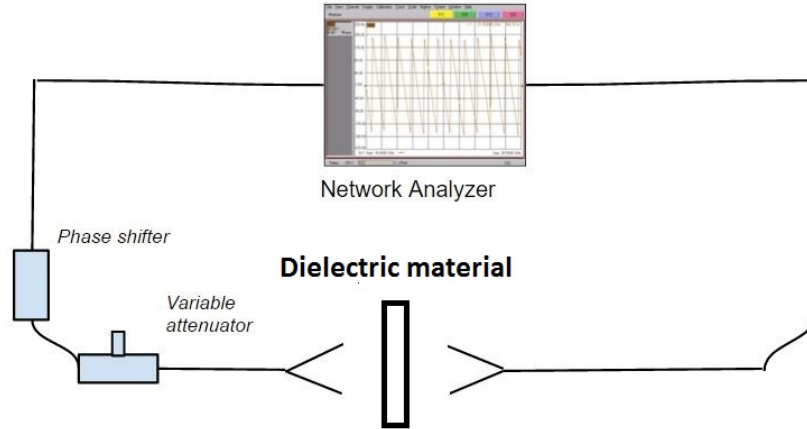
Fig. 5.37. A scheme of the setup for the measurement of the refractive index of a dielectric material: When a layer of dielectric material with thickness ΔL is placed between the horns, a phase variation $\Delta\phi$ is measured by the network analyzer.

Fig. 5.38. A mylar sheet between horns

Fig. 5.39. A mylar slab between horns

As expected, starting form the minimum horn to horn distance of 266 mm, where $\Delta L = 0$, we find a linear relationship between the displacement with respect to the

starting position (zeroing it through the phase shifter) and phase shift (red curve and black circle marker in Fig. 5.40).
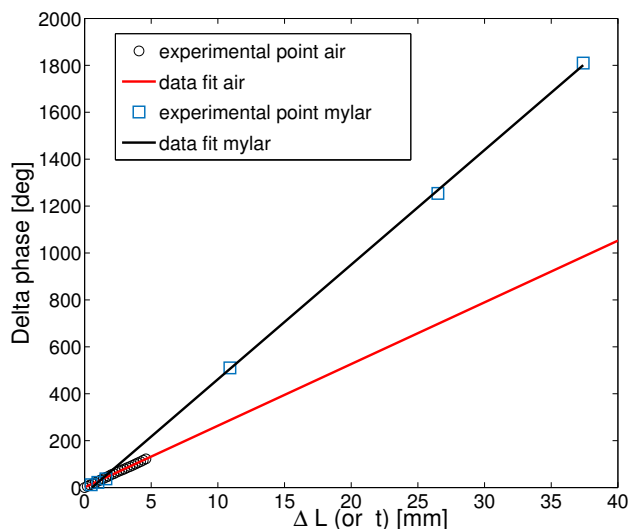
Fig. 5.40. Phase shift as a function of distance between the horn antennas ΔL in presence of vacuum and of various thickness t of PETP (Mylar)

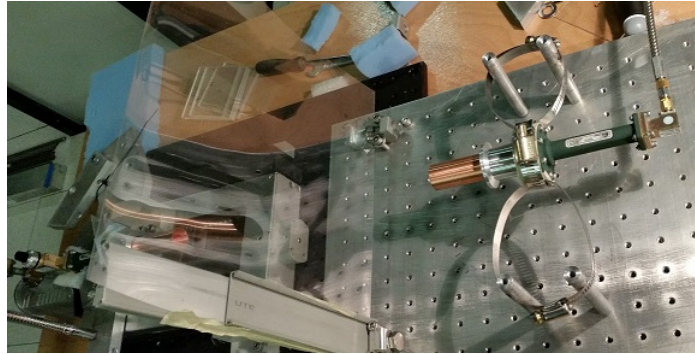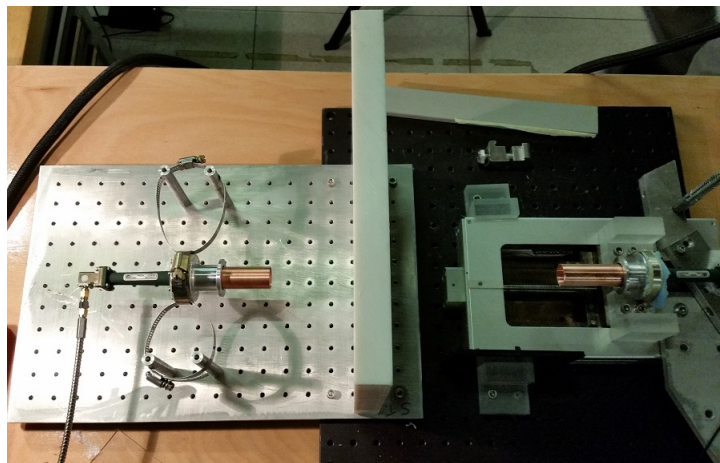The refractive index is calculated from the slope of the curve. It is immediate to see, even only qualitatively, that the two curves have different slopes and points belonging to the same material show a very nice linear tendency.

Table 5.2. Measured and expected refractive indices

Material	Measured index of refraction	Error	Expected Value
Air	0.98	0.9%	1
Mylar	1.82	2.18%	1.6−1.8

The interpretation of such microwave phase-shift measurements is crucial for ensuring the properand reliable interpretation of the observed phase shifts when probing our small cylindrical plasma columns.

5.7.1 The beating signal method in free space

In order to experimentally validate the sweep-frequency strategy, we installed the setup (see Fig. 5.41), performing a series of measurements in free space: as introduced in section 5.3.1, the superposition of the two signals will produce a *beating signal* with at the frequency:

$$\omega_{beat} = \frac{\partial(\Delta\phi)}{\partial t} = \frac{\partial\omega}{\partial t}\left(\Delta L \frac{\partial k_g}{\partial\omega} - \frac{L}{c}N\right) \tag{5.33}$$

where L is the length of the air spacing and N is the refraction index that we want fixed from this first free-space measurement.
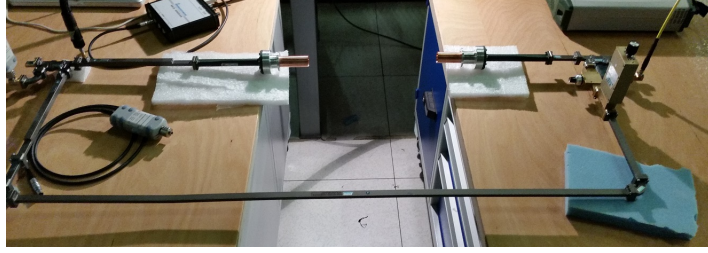
Fig. 5.41. Experimental setup for frequency sweep measurement in free space

Rewriting the 5.33 in terms of frequency and considering a linear sweep, we have:

$$f_{beat} = 2\pi \frac{\Delta f}{\Delta t}\left(\frac{\omega}{c\sqrt{\omega^2 - \omega_c^2}}\Delta L - \frac{L}{c}N\right) \tag{5.34}$$

The measured beating signal is plotted in Fig. 5.42 and, from its FFT (Fig. 5.43), we see that there is only one clearly peaked frequency at 0.4 Hz as we expected because no reflections and/or multipaths are present.
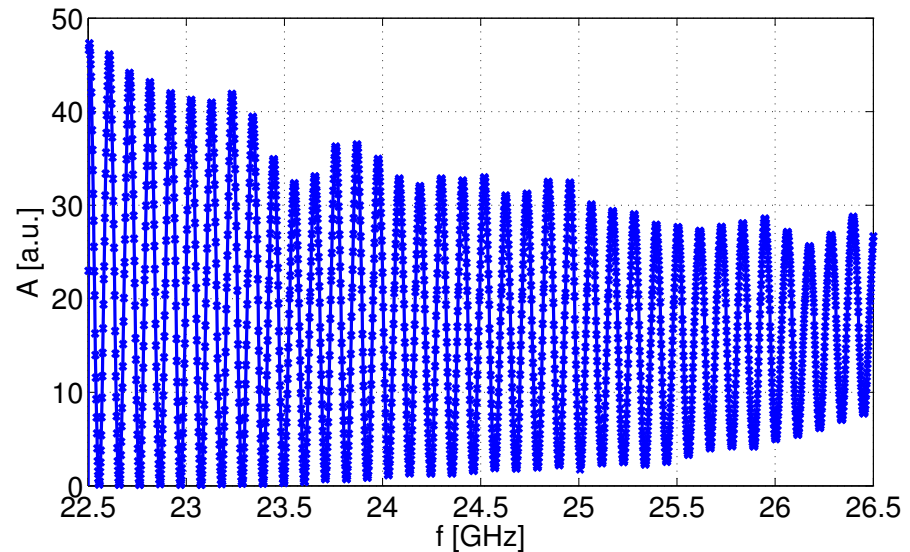
Fig. 5.42. Measured beating signal with horns in free-space
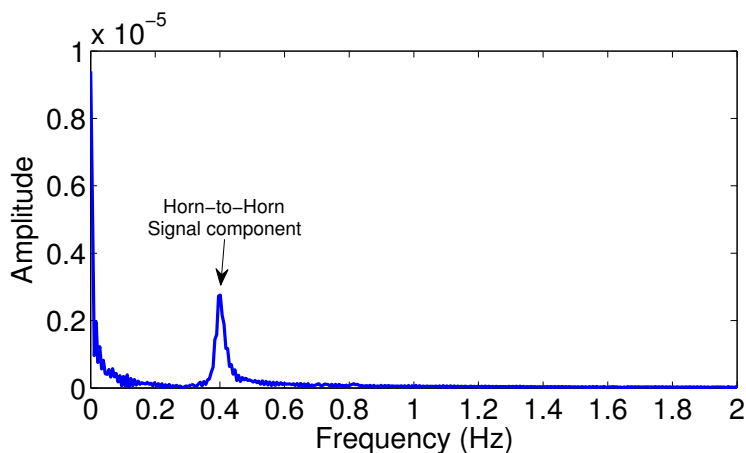
Fig. 5.43. FFT spectrum of the beat signal in free space horns

These free-space measurements are important to derive a **calibration factor** C_F that will allow the evaluation of the refraction index when adding a medium between the horns. In fact, from the following equation:

$$\omega_{beat_V} = \frac{\Delta\omega}{\Delta t}\left(C_F - \frac{L}{c}N\right)$$ (5.35)

,

if we impose $N = 1$ as required for the vacuum refraction index, it is possible to find the calibration factor C_F to be applied in the following paraffin bulk experiment:

$$C_F = \omega_{beat_V}\frac{\Delta t}{\Delta\omega} + \frac{L}{c}$$ (5.36)

This calibration procedure allows to be robust with respect to eventual sources of errors such as the ones in the evaluation of ΔL in eq. (5.33), which can be affected by a non-predictible dispersion relation in all the components of the microwave layout, especially the conical horns, the phase shifter, the WG bends and the directional couplers. On the other hand it includes, corrects and avoids any eventual cavity effect and errors on the direct path dispersion relation that above, for sake of simplicity, we use the "simple" free space $k_0 = \frac{\omega}{c}$ expression.

The validitation of equation (5.33) can be checked adding a quantity L' that we know with very good precision. This way we can verify that the response in terms of ω_{beat} is consistent with the equations. Two waveguides of length 838 mm and 841 mm were added, so to have a total exceeding guided path of $L' = 1681$ mm (see Fig. 5.44)

The expected, new beat frequency is:

$$\omega'_{beat} - \omega_{beat} = \frac{\Delta\omega}{\Delta t}\frac{\omega}{c\sqrt{\omega^2 - \omega_c^2}}\Delta l$$ (5.37)
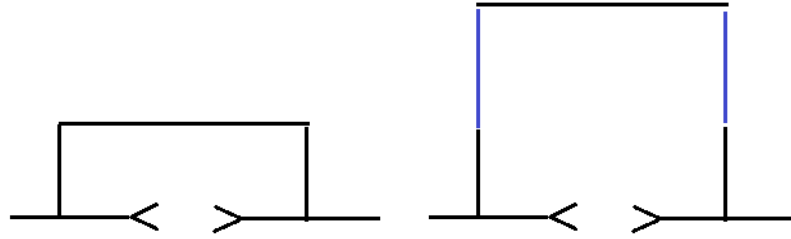
Fig. 5.44. Adding of a guided path L' to verify the model, the length of the blue waveguides is known

The FFT of the measured beating signal with the additional of a guided path allowed to verify that our experiment is in perfect agreement with equation (5.37).

5.7.2 The beating signal method: measurement with paraffin

Thanks to the calibration factor C_F obtained in the free-space measurement, in the next step, the refractive index of a cylinder of paraffin wax has been measured. The paraffin wax cylinder has the same length of the plasma reactor horn-to-horn distance and it has been placed between the horns as shown in Fig. (5.45).

Fig. 5.45. Setup with paraffin wax cylinder between horns

The measured beating signal is shown in Fig. 5.46.

The FFT of the measured signal (Fig. (5.47) shows a peak at 0.38 Hz which is slightly down-shifted with respect to free space. With this value and the C_F obtained in the free-space measurement we can found the paraffin refractive index N_{par} being equal to 1.48 by eq. 5.38.

$$f_{beatparaffin} = 2\pi \, \frac{\Delta f}{\Delta t} \left(C_F - N_{par} \frac{c}{L} \right) \tag{5.38}$$
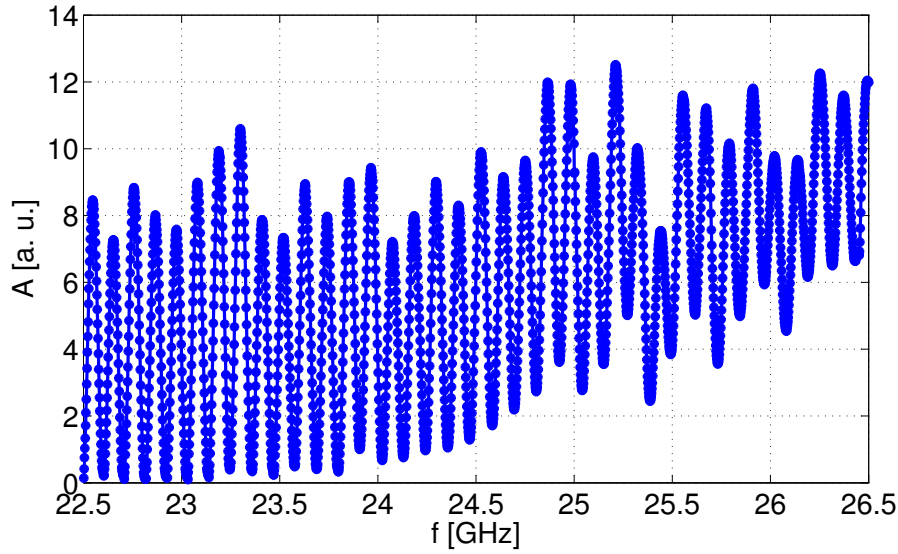
Fig. 5.46. Measured beating signal with paraffin in free-space
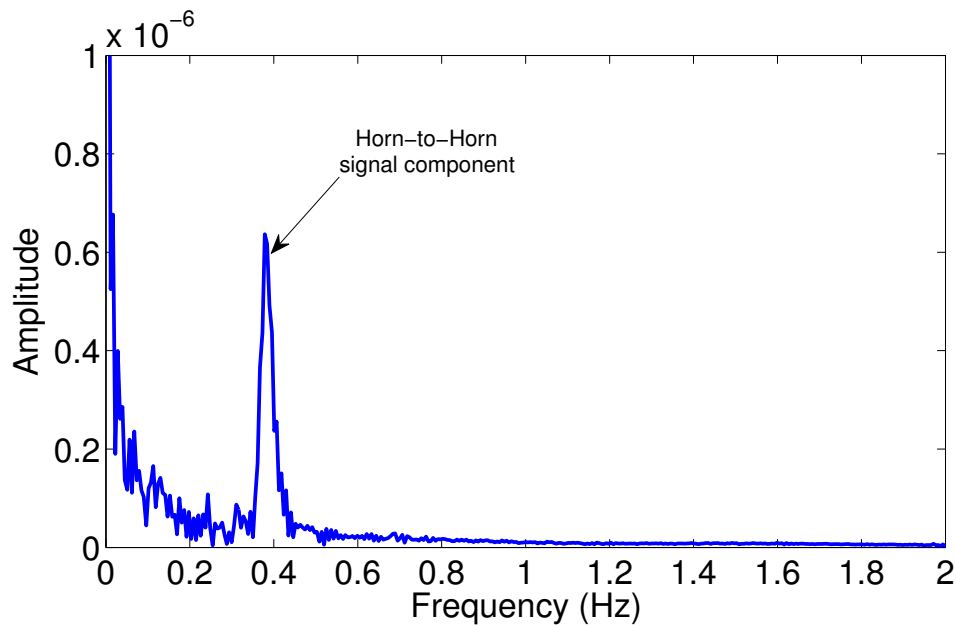
Fig. 5.47. FFT spectrum of the measured signal with paraffin wax

The results of the measurement of the refractive index of the material tested is in accordance with literature [131].

5.8 Interferometric measurements on Plasma Reactor

We finally assembled the complete layout (sketched in Fig. 5.48) for the interferometric measurement (Fig. (5.49)), to test the plasma chamber effects on the measured

pattern. The presence of a resonant cavity will give the need to filter out the multipath and noise contribution as we will show.
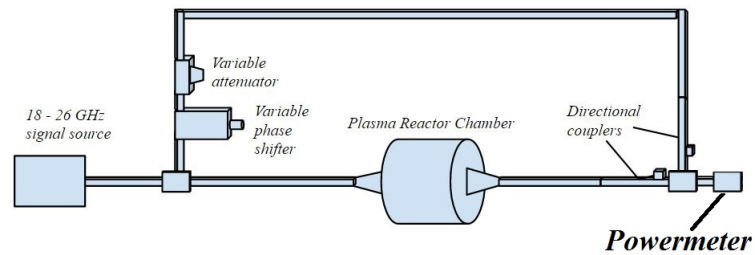
Fig. 5.48. A sketch of the experimental setup for the measurement of the beating signal in cavity with short arms
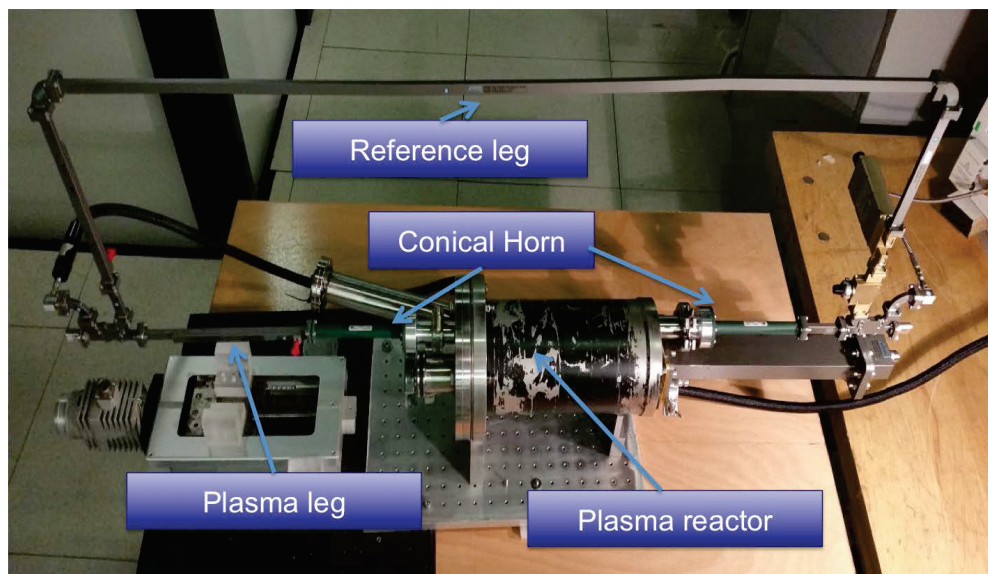
Fig. 5.49. K-band (18-26.5 GHz) microwave interferometer mounted on a plasma reactor operating at 2.45 GHz.

First of all we tested the behavior of the horns when they are installed on the Plasma Reactor. The basic idea is that if we understand the effect of the environment, namely, the internal walls causing the multiple-reflections, when there is no plasma, another calibration factor – let's say C'_F – will be derived before turning on the plasma inside the resonator.

After the horn antennas were mounted on the flanges of the plasma reactor chamber, (Fig. 5.50), we measured the S_{11} (as shown in Fig. 5.51). S_{11} shows that the antennas is well matched also when mounted on cavity.
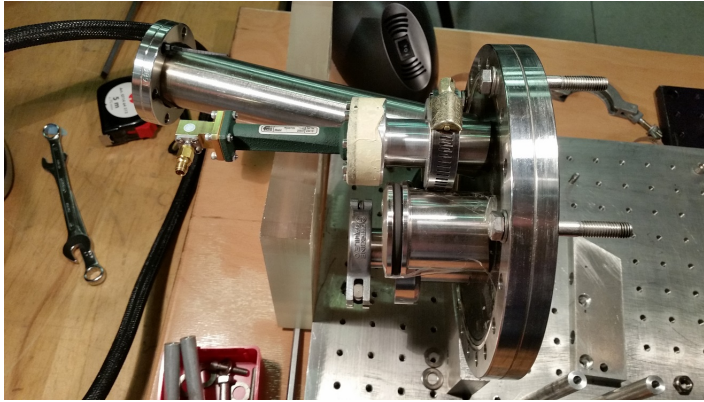
Fig. 5.50. Horn mounted on Plasma Reactor flange
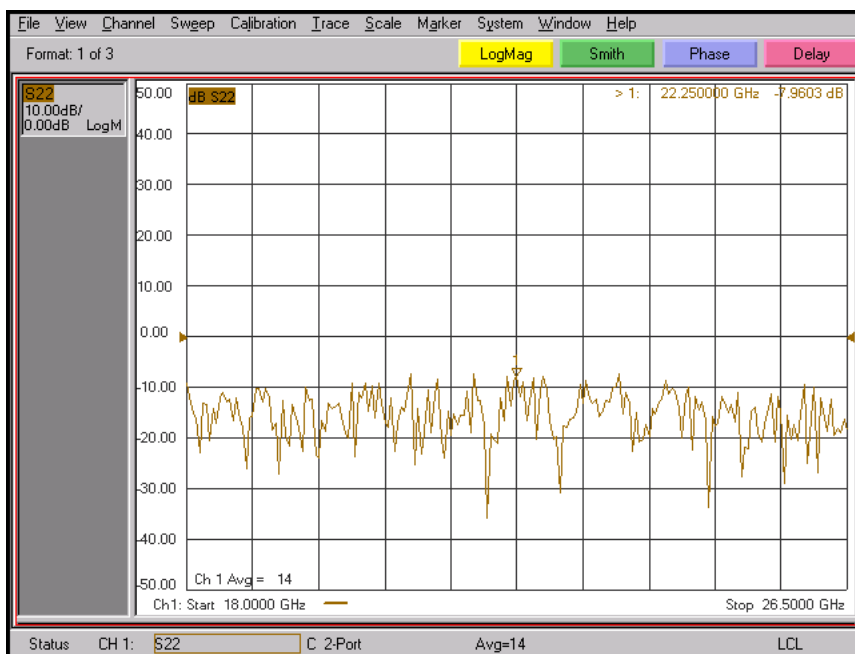
Fig. 5.51. Measure of $|S_{11}|$ [dB] when tha horn antenna is installed on the closed plasma chamber cavity

As it is possible to see in Fig. 5.52 and in Fig. 5.53, three diagnostic tools are installed at the same time: the horns for the microwave interferometry, the Langmuir probe for a point-by-point measurement of the plasma density and a collimator used for the installation of a X-ray detector.

In Fig. (5.54), the measured beating signal in the under–vacuum cavity is shown, which is characterized by a more relevant noise with respect to the free-space case, originating by the aforementioned multipaths.

The FFT of the beating signal (Fig. 5.55) shows the presence of the peak due to the direct path, at 0.3957 Hz and other spurius components due to the multipaths. The direct path component is at larger frequency than the multipath, due to its lowest optical path.
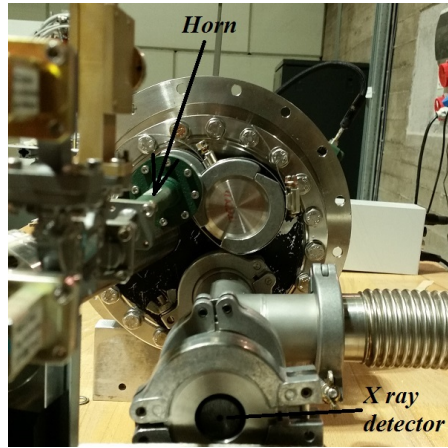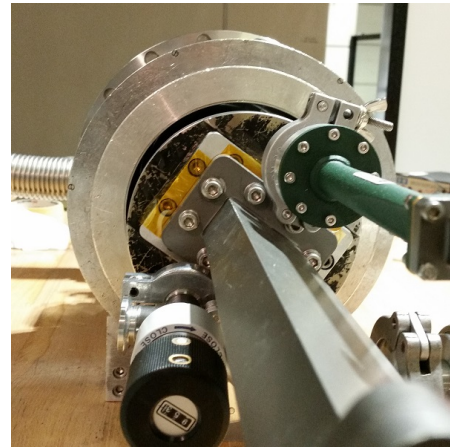
Fig. 5.52. Front part   **Fig. 5.53.** Back part
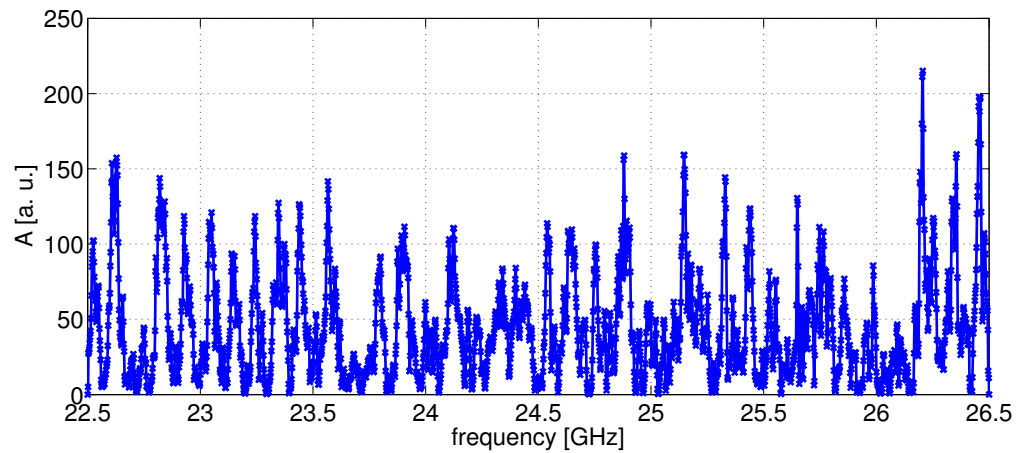
Fig. 5.54. Measured beating signal in vacuum cavity

Then we studied the response of the system when changing the frequency sweep time ΔT. The results are shown in the FFT plots in fig. 5.56 for sweep times of 10, 50, 70, 90 and 100 seconds. The results of these measurements are summarized in the table 5.3 with the correspondent expected values.

Sweep Time (sec)	Experimental ω_b (Hz)	Expected ω_b (Hz)
10	3.6200	3.6234
50	0.7113	0.7247
70	0.5082	0.5176
90	0.3957	0.4026
100	0.3614	0.3623

Table 5.3. Experimental and theoretical beating frequency as a function of the sweep time
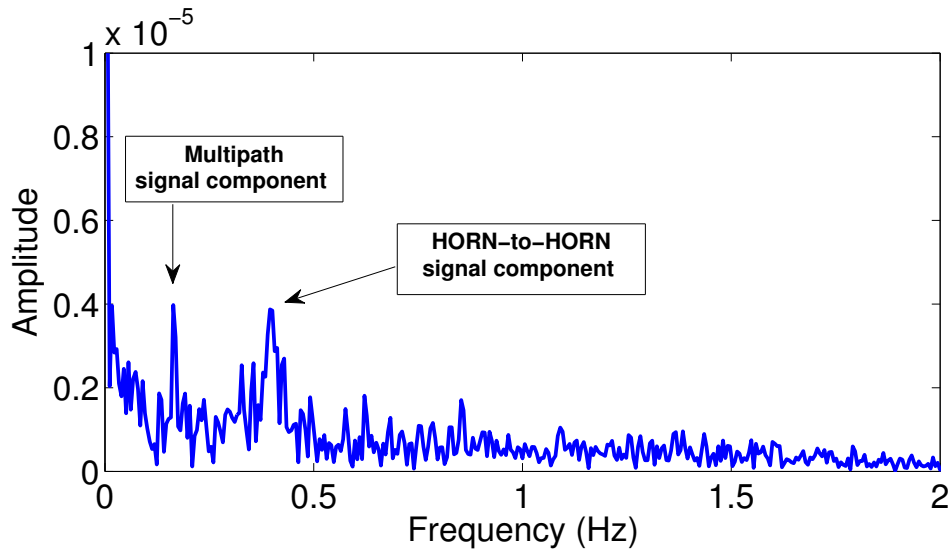
Fig. 5.55. FFT spectrum of the measured signal in vacuum cavity

It is possible to notice that the experimental data show a very good agreement with the theoretical predictions and a very nice linear trend (Fig. 5.57).
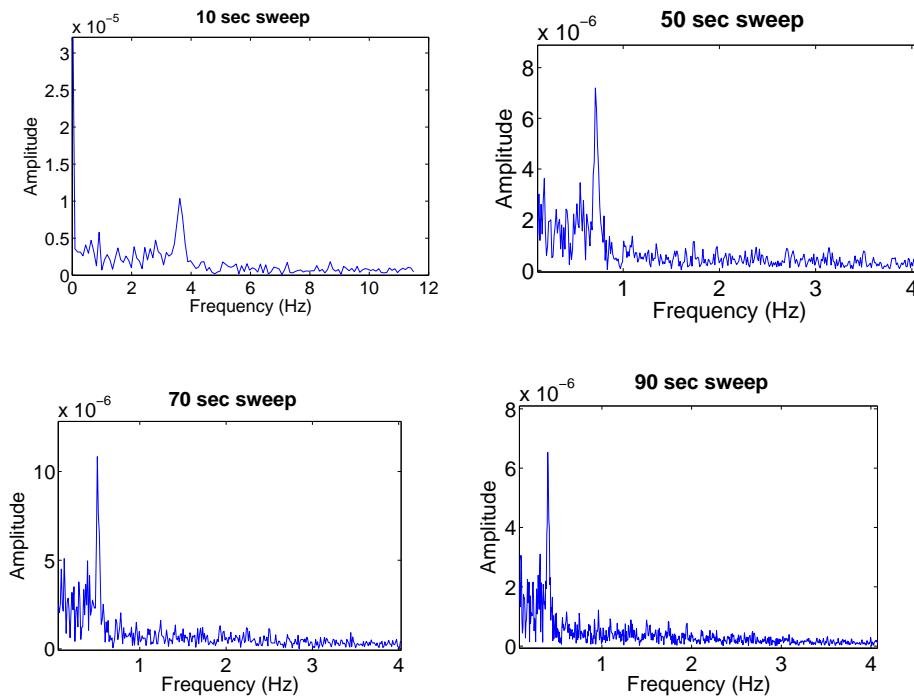
Fig. 5.56. FFT spectra of the beating signals for different sweep times

In summary, these measurements show that, in spite of the presence of the cavity, we are anyway able to distinguish the single pass component. Indeed, the peak corresponding to the horn-to-horn signal can be individuated.
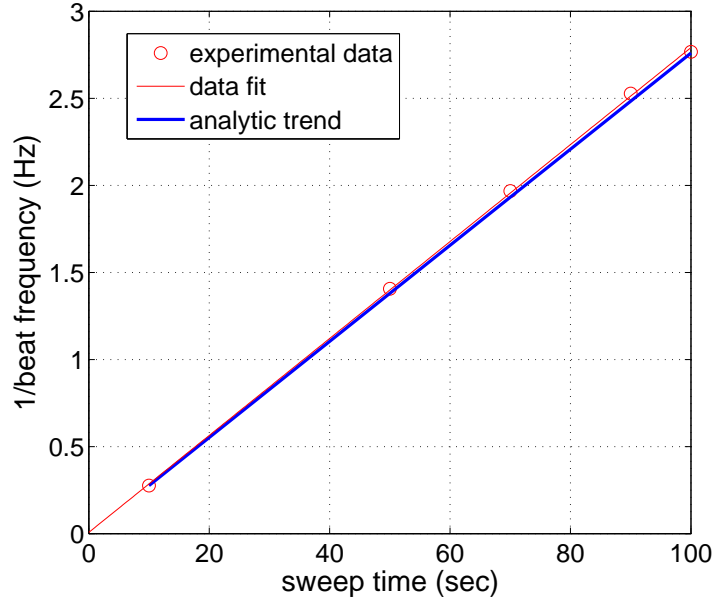
Fig. 5.57. beating frequency vs sweep time in cavity

5.9 Measurement in plasma

We report here the first measurements obtained in presence of plasma. In this experiment a plasma has been heated by 150 W microwave power coming out from a TWT-Amplifier at the frequency of 3.7476 GHz. This radiation interacts with a rarefied gas of nitrogen-oxygen mixture mainained at 10^{-4} mbar inside a metallic resonator surrounded by a 0.1 T permanent magnet. This way, the microwave field is coupled to the free electrons of the gas through the Electron Cyclotron Resonance or other off-resonance interactions which boost the plasma density up to $10^{17} \div 10^{18}$ particles per cubic meter.

In Figure 5.58, it is shown the measured beating signal in the plasma filled cavity and in Figure 5.59, the corresponding FFT spectrum.

$$\omega_{beat} = \frac{\partial \omega}{\partial t} \frac{\partial \Delta \phi(t)}{\partial \omega} = \frac{\partial \omega}{\partial t} \left(\Delta L \frac{\partial k_g}{\partial \omega} + \int_{plasma} \frac{\partial k_{plasma}}{\partial \omega} dl \right) \tag{5.39}$$

Figure (5.60) shows the FFT spectrum of the measured signal compared with the vacuum case.

The measured beat frequency is $\omega_{beat_P} = 2\pi(0.406) \pm 3.6589 \cdot 10^{-4}$ rad/s,

From the following equation:

$$N_P = C_F \frac{c}{L} - \omega_{beat_P} \frac{\Delta t}{\Delta \omega} \frac{c}{L} \tag{5.40}$$
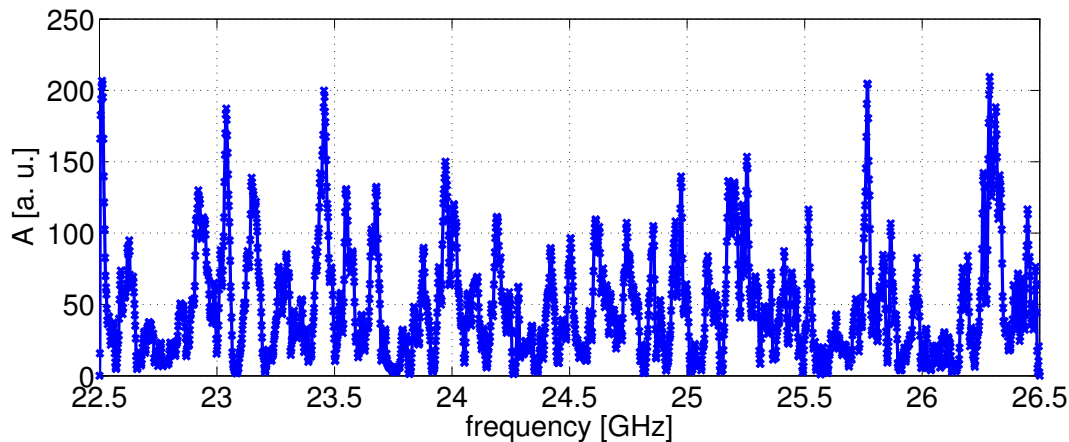
Fig. 5.58. Measured beating signal in plasma filled cavity
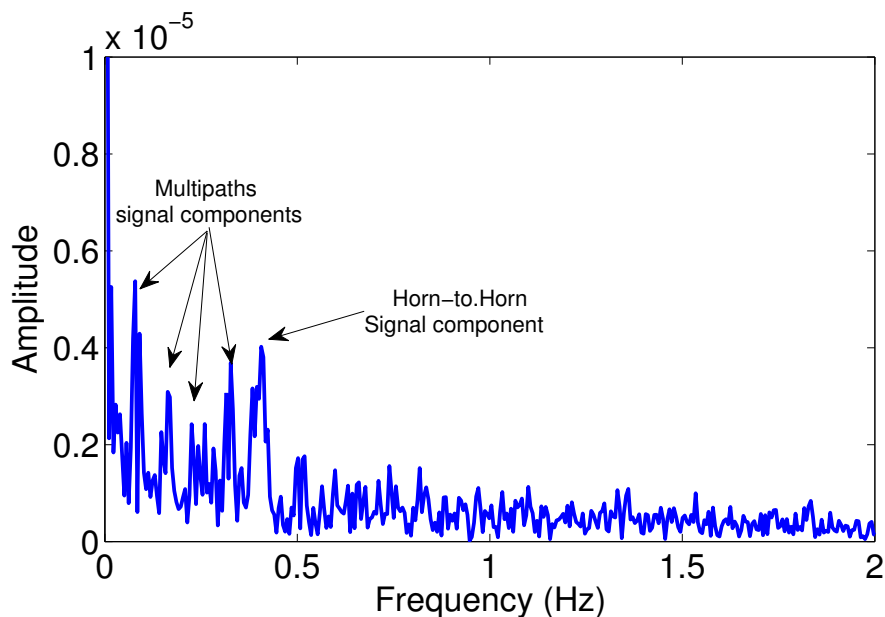
Fig. 5.59. FFT spectrum of the measured signal in plasma filled cavity

we can obtain a plasma refraction index of $N_p = 0.7905 \pm 0.111$. The density was evaluated considering, in equation (5.5) both the minimum and the maximum frequency (the two curves of Fig. 5.61). However, since the effect of the plasma is relatively more relevant at the lower frequencies, we opted to extrapolate the density from the lower curve. The only drawback eventually consists in a underestimation of the density value.

This represents the first microwave interferometric plasma measurement on a ion source (ECRIS) device. A summary of the experimental results is reported in table 5.4. The estimated density lies in the interval $1 \div 3 \cdot 10^{18} \mathrm{m}^{-3}$.
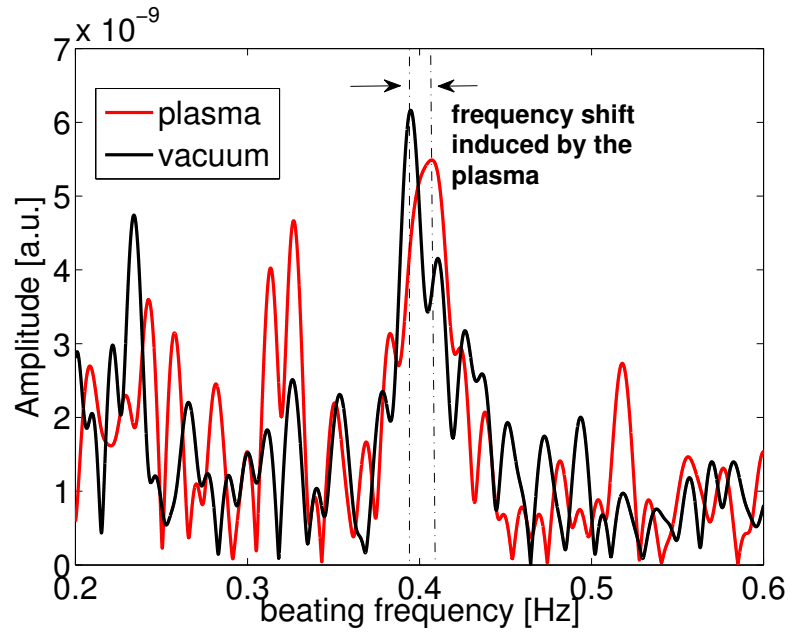
Fig. 5.60. Beating frequency shift between vacuum and plasma FFT
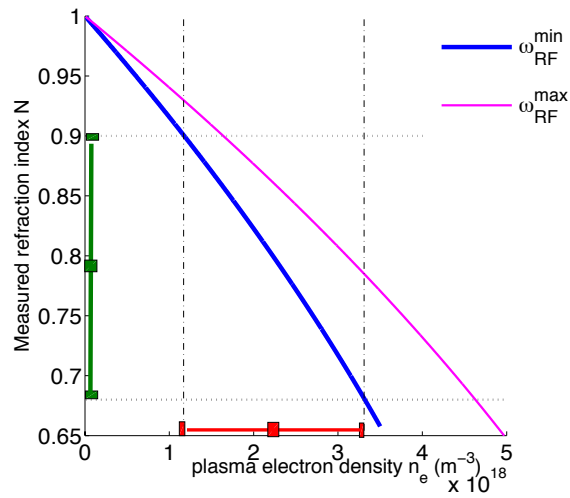
Fig. 5.61. Error bars on N_p versus n_e plot

Table 5.4. Index of refraction results

Medium	$P_{RF[W]}$	$\omega_{beat}[rad/s]$	N
vacuum	0	$2\pi(0.3974)$	1^1
Bulk paraffin wax	-	$2\pi(0.3802)$	1.43
plasma	150	$2\pi(0.407)$	0.790 ± 0.111
Holed paraffin^2	-	$2\pi(0.3794)$	0.59

[1] assumed as an absolute well-know given value

[2] modeling a less than one plasma refraction index

New launching schemes: the experiment on the Flexible Plasma Trap at LNS

With the aim to study and design alternative plasma heating mechanisms for ECRIS, this chapter describes numerical simulations and experimental tests, carried out on an innovative ECRIS-like device, called Flexible Plasma Trap (FPT) installed at LNS. In particular a microwave launcher has been electromagnetically characterized to excite Electrostatic Bernstein Waves (EBW) inside the FPT.

The microwave launcher represents the matching element between plasma and the transmission components, exactly in the same way a more usual antenna represents, for radiation, the transition between lines and propagating media. As we will show, the difficulties firstly arises for the compactness of the plasma chamber in which the waves should be irradiated. The mechanical constraints also complicate the positioning of the overall launching system. The solution proposed consists of a phased waveguide "array" of two elements: using a relative phase shift between them, a steering of the radiated beam can be produced, in order to obtain an optimum incidence angle. Actually the EBW generation may be optimized in terms of O-mode insertion angle with respect to the external magnetic field direction.The proposed launcher represents an alternative to the fixed radiation lobe of the classical rectangular waveguide currently feeding ECR ion sources plasmas. The electric field inside the plasma chamber cavity excited by the designed antenna has been measured by using ad-hoc designed and constructed microwave probes.

6.1 Motivation for a new microwave launcher

As we explained in chapter 1, an important topic of the research on axisymmetric magnetized plasmas of ion source is the heating of so-called overdense plasmas through the excitation of electron Bernstein waves (EBW) [12]. For these waves there exists no density cutoff. Furthermore, they are very well absorbed at the cyclotron resonance and its harmonics [132].

The EB waves are, however, electrostatic modes and need to be excited via a inner plasma mode-conversion process, starting from eletromagnetic waves (the X mode) at the upper hybrid resonance (UHR) layer, where $\omega_{UH} = \sqrt{\omega_p^2 + \omega_g^2}$. Their generation may involve one (XB) or two mode conversion scenarios (OXB) that are efficient only in a narrow window of the following parameters: **frequency, polarization and angle of incidence**.
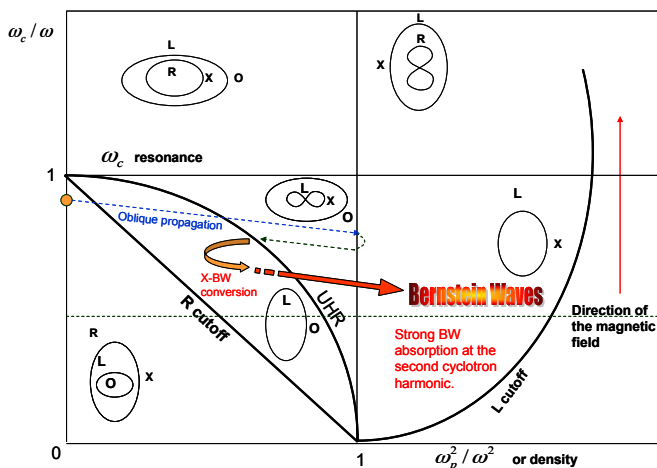
Fig. 6.1. Representation on the CMA diagram of the generation mechanism and of the allowed region of propagation for EBW.

The problem is, therefore, how to lead the incident waves efficiently to the UHR layer and couple them to B waves according to the scheme depicted in Fig. 6.1.

When the scale length of the density gradient near the UHR layer, $L_n = \left| \dfrac{n_e}{\boldsymbol{\nabla} n_e} \right|$, is equal or larger than the free space wavelength, $\lambda_0 = 2\pi c/\omega$, oblique injection of O wave at an optimal angle can be adjusted such that the wave has the parallel refractive index at the plasma cutoff layer suitable for a complete mode conversion into an X mode [133]. This method is referred to as the OXB method, since the wave power reaches the UHR layer after conversion from an O wave to an X wave at the plasma O-cutoff layer. The mode conversion rate of this method deteriorates as L_n decreases below λ_0, while for the extremely steep density gradient case, such as $L_n \sim 0.1\lambda_0$, the perpendicular injection of X waves is effective.

Numerous experiments were performed in fusion plasma [13], toroidal devices where ray tracing approximation allows to compute the electromagnetic waves traveling inside the plasma. In these very large (L≫ λ) scenarios some well-established optical techniques (e. g. grooved miirrors, lenses and grating polycromator), were

adopted to optimize the O-X-B conversion, in terms of wave polarization and incidence angle.

On the contrary, as ir was mentioned during the previous chapters, in ECRIS , the wavelength is comparable not only with the L_n but even with the plasma minor radius. Therefore, optical approximation is not applicable, and the full-wave calculations must be applied to simulate the wave behaviour in the plasma. The presence of resonant cavity additionally causes the polarization scrambling thus strongly complicating the OXB modeling; the above issues make unpractical some straightforward solutions already adopted for fusion plasma applications. When the condition $\lambda_0 \sim L_p \sim L_c$ holds, other researchers [134] have demonstrated that even the CMA diagram starts to fail in describing waves propagation properties.

We hereinfater describe the followed approach:

- *Preparatory virtual experiment*: a standard selfconsistent approach followed by stellarator or tokamak scientists which is based on the assumption of a given n_e/B profile, then verifying the consistency of the assumed scenario with modal conversion constraints;
  Numerical simulations, useful to identify the location in the FPT plasma chamber of cut-offs and resonances; moreover, the full-wave code developed in the frame of this thesis and described in chapter 4 has been applied to solve waves propagation in the magnetized plasma of FPT, taking into account also the mode conversion mechanism of OX-conversion for the generation of EBW;
- Proper *coupling of the microwave power to the ECRIS* plasma to obtain mode conversion and EBW heating: a launcher antenna will be described, and results of these investigations in terms of antenna pattern and behaviour in cavity will be presented;
- *Microwave measurements* of the wave amplitude irradiated by the microwave launcher in FPT plasma chamber cavity were performed through a "special"microwave probe: we measured the electromagnetic field profiles radiated field in cavity by the launcher and it will help to argue if the mode conversion occurs and where the resonance absorption zones are placed.

6.2 Flexible Plasma Trap (FPT) assembly

The installation at LNS of a source designed for the possible excitation of EBW will allow to study their properties in still unexplored physical context. The availability of a compact plasma trap with flexible magnetic field, able to excite either the ECR and off-resonance plasmas, is absolutely necessary to understand the ability to obtain a high density plasma.

The investigation of EBW-heating under different magnetic field configurations will be carried out by means of a plasma trap made of three solenoids (fig. 6.2 and 6.3) which allow the tuning of the magnetic field profile.
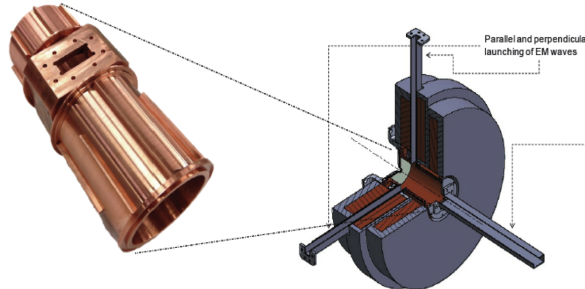
Fig. 6.2. A sketch of the microwave input in the plasma chamber with respect to the magnets.
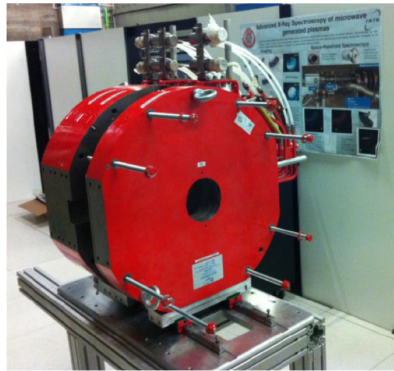
Fig. 6.3. FPT magnetic coils system

In particular we can considered three magnetic field profiles (fig. 6.4):

1. "Off-Resonance configuration" will permit the studies on plasma dynamics in case of parrallel/perpendicular launching in a B field configuration like that of MDIS;

2. "Simple mirror" for multiply charged ions production;

3. "Magnetic Beach" for exploiting mode conversion at UHR and EBW absorption in higher harmonics; to be converted into a BW, the X mode requires a rapidly dropping magnetic field which makes possible either UHR and second harmonic absorption.

The FPT plasma chamber can be coupled to three different waveguide inputs, including the possibility to have contemporary input of microwaves in three directions
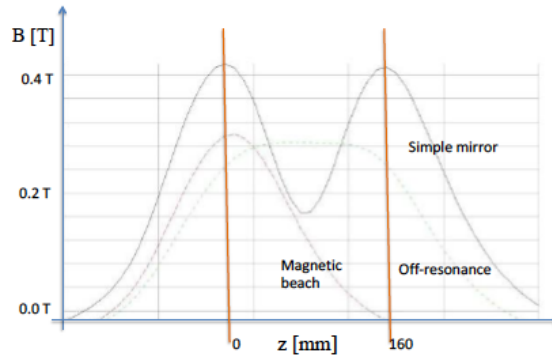
Fig. 6.4. Off-resonance, simple mirror and magnetic beach field profiles.

one perpendicular to the other, to have an adequate water cooling in the microwave windows location, and to permit at the same time to host different type of diagnostics, optical, X-ray and microwave probes diagnostics, then, in the next future,also microwave interferometry.

The plasma chamber is shown in fig. 6.5(a) and 6.5(b) . Its dimensions are 82.0 mm in diameter and 260.1 mm in length. It is made of oxygen free high conductivity copper The plasma chamber has been equipped by a stainlesssteel made pre-chamber in order to host the vacuum system and the diagnostics tools.
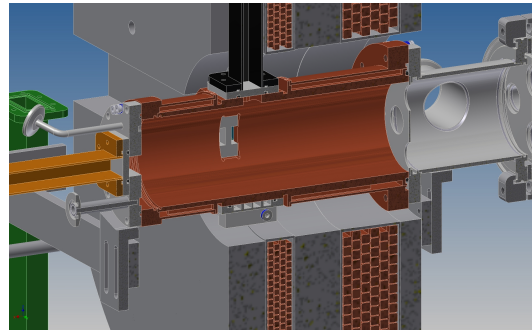
(a) FPT pre-chamber, plasma chamber, and solenoid rendering

(b) Oxygen free high conductivity copper FPT plasma chamber

Fig. 6.5. FPT plasma chamber

Waves-launching inside the FPT

The FPT plasma will be generated using two different microwave systems, through parallel and perpendicular microwave injections: one operates at a central frequency of 5 GHz and the other around 14 GHz, to explore also the aspects of resonant absorption of waves' energy by electrons at the second-harmonic. Furthermore, it will be possible to operate with a double mode ECRIS: a fraction of power provided to the plasma by means of the usual ECR-heating process, and the remaining amount of power injected along the perpendicular direction with respect to the axis-symmetric magnetic field, in order to excite EB-waves through OXB.

The general ensamble of the FPT setup is shown in figure 6.6; it can be seen that the design is very compact but versatile. The TWT providing frequency-variable electromagnetic waves, the waveguides for parallel and perpendicular launching, the magnetic system and the support for diagnostics hosting are illustrated in the picture
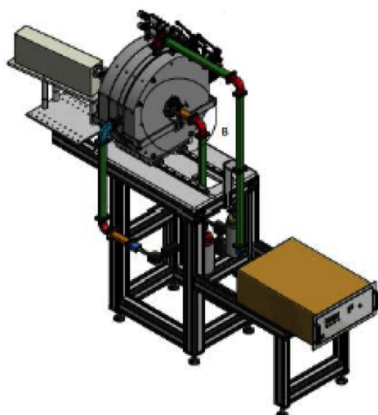
Fig. 6.6. A view of the general ensemble of the FPT setup, including the RF system.

6.3 Numerical modeling

The virtual experiment consists in assuming the desired density profile, then self-consistently checking that the resonance/cutoff layers displacements are compatible with the assumed profile. If the desired profile is a single peaked gaussian with maximum in the central part of the plasma chamber (because of energy transport issues, center-peaked profile is greatly preferable in order to have a hot plasma core), the compatibility check consists in verifying - that the energy deposition that occurs at the ECR harmonics - is placed in proximity of the assumed density peak. The cutoff layers where the conversion may happen, as well as the resonance layers for absorption of the electromagnetic waves, can be predict thanks to our full-wave code and

could be controlled by proper adjustment of the magnetic induction inside the plasma during the experimental phase.

The OXB mode conversion scenario on FPT plasma chamber has been obtained by numerical simulations. These latter simulations represent an example of the application of the full-wave code for the OXB process modeling. Fig. 6.7 and 6.8 display the electron density n_e and magnetostatic field $\mathbf{B}_0$, used as simulation input parameters.
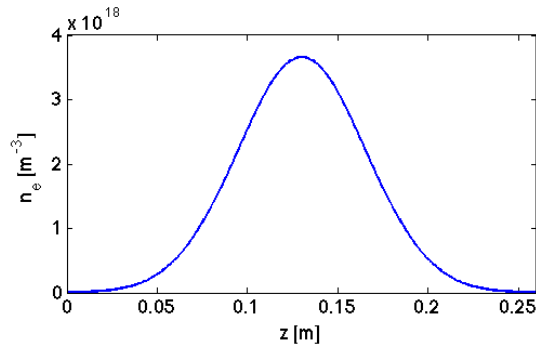
(a) Gaussian electron density profile along z-axis used in the simulation
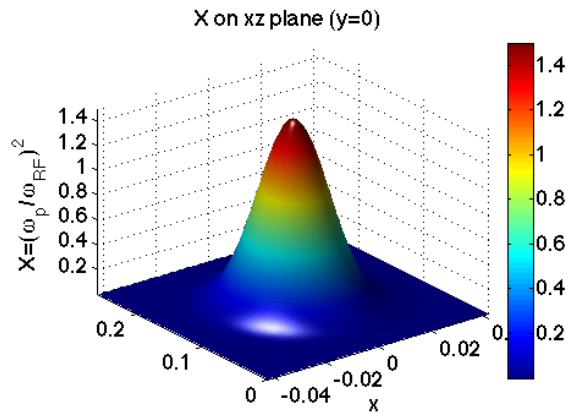
(b) Dimensionless electron density X=ω_p^2/ω^2 on xz plane $(y=0)$

Fig. 6.7. Profile of electron density n_e along the longitudinal z-axis along the line ($x = 0$, $y = 0$, z) on the upper plot, and X= ω_p^2/ω^2 (proportional to n_e) on xz plane on the lower plot, used as input parameters to compute the cutoff and resonance zones.

We used a gaussian electron density profile for the simulation with a maximum density of $n_{max} = 1.5 n_{cutoff}$ in order to simulate an overdense plasma. The numerical results are obtained for the configuration of "simple mirror" magnetic field (see fig. 6.8(a) and 6.8(b)) and a microwave injection frequency $f_{RF} = 14$ GHz.

In Fig. 6.9 and 6.10 the situation for FPT plasma is shown. Density is normalized to n_{cutoff} and magnetic field to a B_{res}. The vertical lines show the positions of the cutoffs and resonances defined by the equations described in Chapter 2.
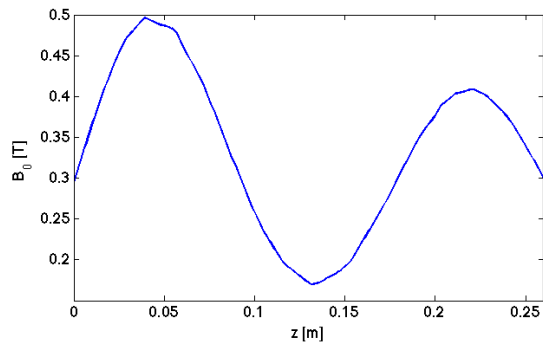
(a) 'Simple mirror" magnetic field B on z-axis, used in the simulation
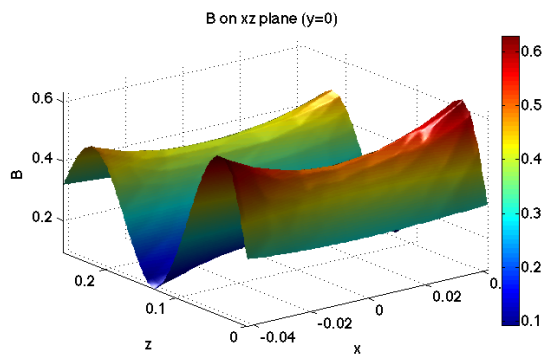
(b) Magnetic field B on xz (y=0) plane

Fig. 6.8. Profile of magnetic field B along the longitudinal z-axis along the line ($x = 0$, $y = 0$, z) on the upper plot, and a magnetic B-isosurface on xz plane on the lower plot, used as input parameters to compute the cutoff and resonance zones.

The self-consistency check has been performed by virtue of such plots. It seems the reciprocal displacement of cutoffs and resonances is suitable for RF power conversion through OXB mechanism, with a following deposition of energy at the second harmonic of the 14 GHz cyclotron resonance. Therefore, we proceed to the following step, consisting in the full-wave simulation of the field structure into the plasma chamber.

Indeed, it is needed to know the O-cutoff layer position, if there are way to access the inner side of the plasma without reflection of the electromagnetic mode by the cutoff layers (R or L-cutoff), and find the possible way to obtain the EB-mode via the OXB mode conversion process. In our case, the microwave power will be launched from the lateral side of the FPT plasma chamber.

Therefore, the full system of Maxwells equations, including the cold magnetized plasma already described in chapter 4, has been solved in the geometry of the FPT plasma chamber (see figure 6.12).

We performed a mesh refinement study, exploiting the adaptive mesh refinement, based on an error estimate during the solution stage. As it is possible to see in figure
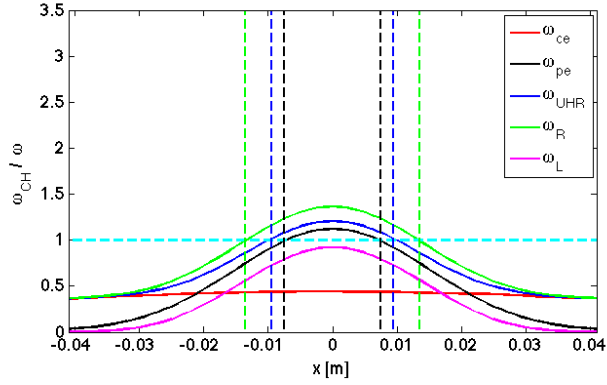
(a) Cutoffs and resonances along x-axis
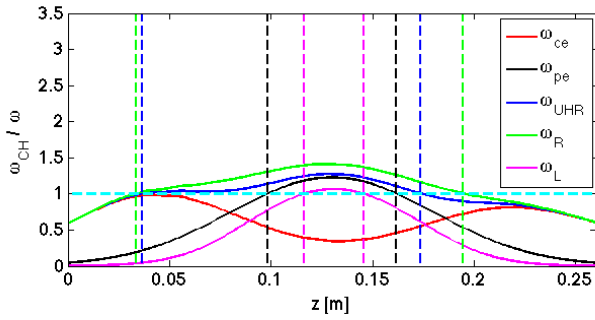
(b) Cutoffs and resonances along z-axis

Fig. 6.9. Cutoffs and resonances in FPT linear plasma along 1D directions, assuming the density and B-field profiles of fig. 6.8 for frequencies normalized to heating wave angular frequency 14 GHz

6.13, an extremely fine mesh on the ECR and UHR surface has been obtained, thanks to "functional evaluation based" on the electric field gradient.

In figure 6.14, it is shown the electric field distribution in the chamber: effectively, the electric field has a strong gradient near the UHR layer that corresponds to a X-mode wavelength shortening near the UHR layer itself. Moreover we can clearly see the peaks in UHR region where X-wave is absorbed after OX conversion in the O-cutoff layer.

These simulations represent a very important example to show how the developed full-wave code can be fundamental to investigate EBW generation schemes in the overdense plasma FPT.

(a) Cutoffs and resonances on xy-plane

(b) Cutoffs and resonances on xz-plane
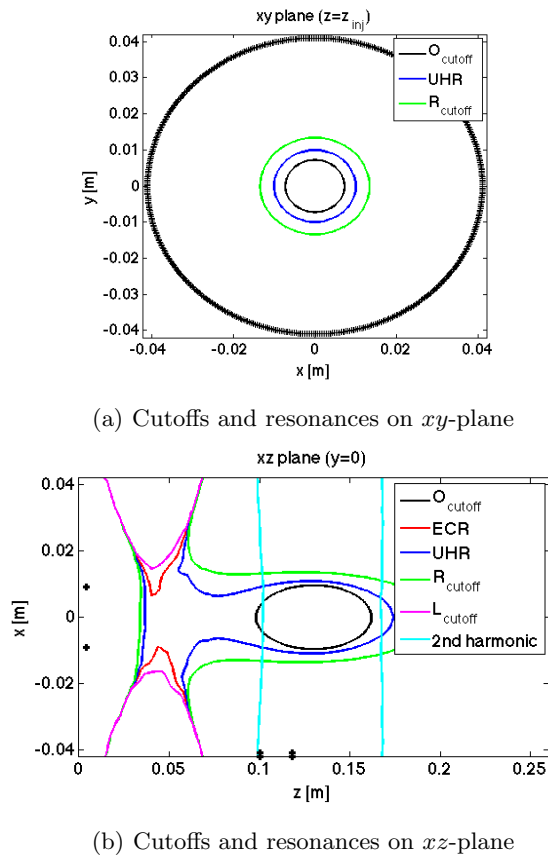
Fig. 6.10. Cutoffs and resonances in FPT linear plasma along 1D directions, assuming the density and B-field profiles of fig. 6.8 for frequencies normalized to heating wave angular frequency 14 GHz
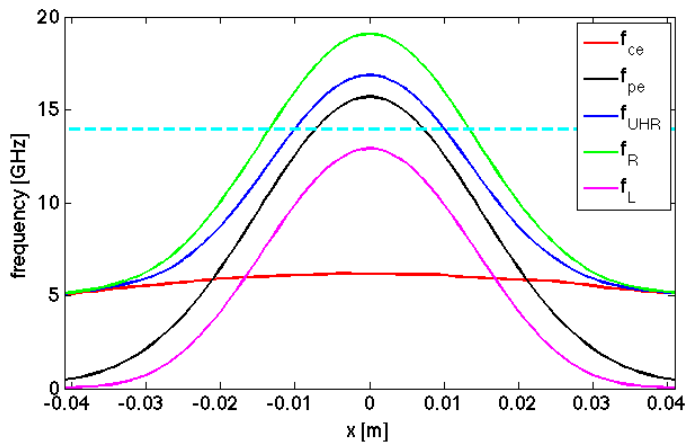
Fig. 6.11. Cutoffs and resonances in FPT linear plasma along 1D directions, assuming the density and B-field profiles of fig. 6.8 for frequencies normalized to heating wave angular frequency 14 GHz
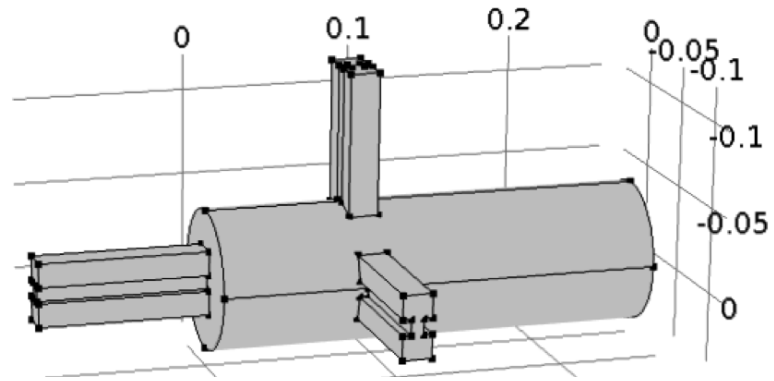
Fig. 6.12. Simulated Geometry: Cavity and microwave WRD350 waveguide injections (axial and radial ports) on FPT.
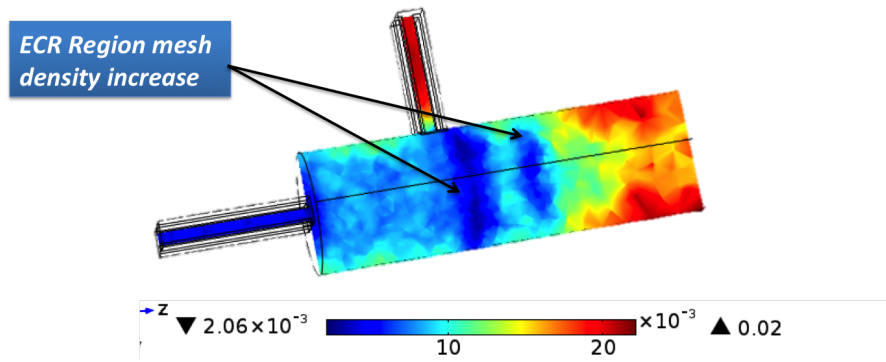
Fig. 6.13. Mesh size [m] generated using adaptive mesh refinement
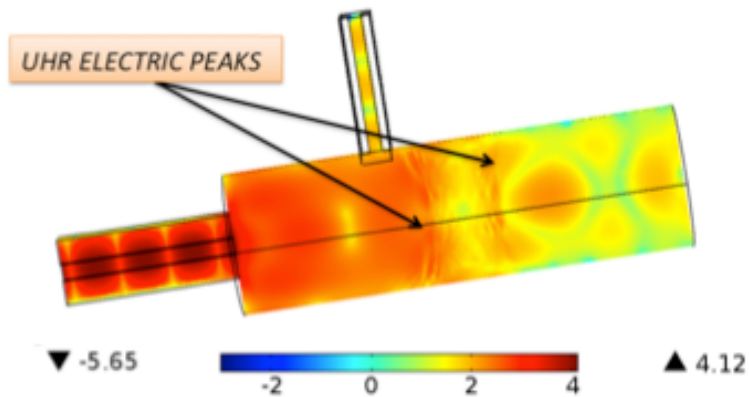
Fig. 6.14. Simulated distribution of electric field amplitude $|E|$ in log scale to emphasize the strong gradient near the resonance layer

6.4 The new microwave launcher based on a two-waveguides-array

This section is devoted to the microwave transmission line of the heating antenna. Simulations showed O-X-B-like scenarios are possibile by properly launching the pumping O-wave from the radial port. As mentioned in the previous section, the antenna should be optimized in order to emit the heating power with an optimal $\mathbf{k(r)}$ angle with respect to the external magnetic field $\mathbf{B_0}$. The absorption of the waves in the vicinity of the resonance layer should be almost complete in a single "pass", if the proper mode of irradiation is chosen. If the single pass absorption is not fully exploited, the multiple reflections, from cavity walls may be helpful to increase the overall conversion efficiency.

Since the mechanical tilt of the antenna is impossible due to the several constraints, the antenna optimization must be done in order to ensure tilting of the emission lobe without any physical movement.

In addition, the launcher handling of high power radiation (hundreds of Watts), with a proper transmission line system, is needed.

Taking inspiration from phased multi-waveguide structures (nicknamed waveguide "grill") [135],[136] designed to launch microwaves at the lower hybrid resonance to heat large toroidal plasmas, a double-waveguide antenna system has been proposed hereinafter for the FPT. It consists of an array of two properly phased rectangular WR62 with their small side parallel to the magnetic field direction of the linear plasma chamber. The microwave transmission line is schematically shown in fig. 6.15
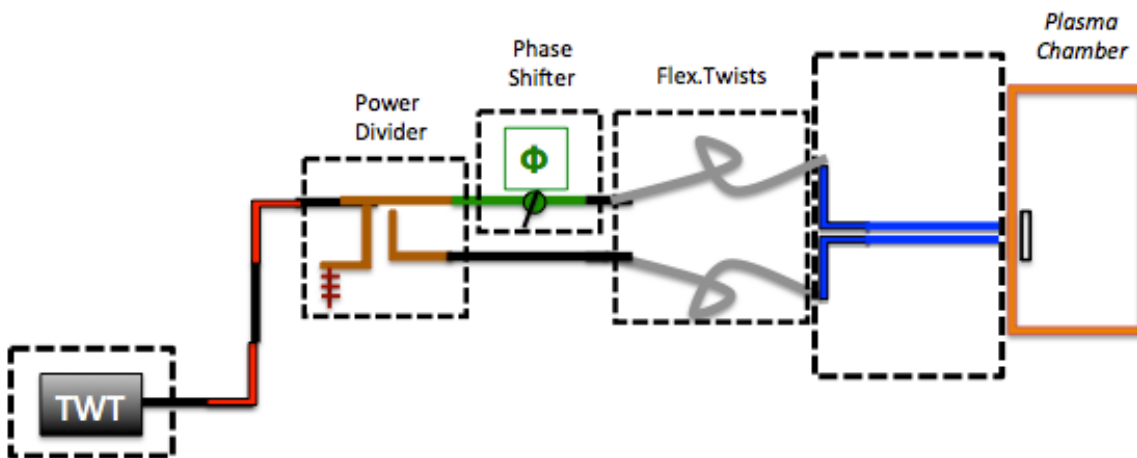
Fig. 6.15. Schematic diagram of the microwave circuit which energizes the double-waveguide array

The two waveguide driven in TE_{10} mode with relative phase controlled by a calibrate phase shifter, a loaded four-port power divider and two flexible and twistable WR62 waveguide compose the launcher layout, are shown in Figure 6.15.

The table 6.1 lists in detail the microwave components used for the layout arrangement.

WR62 Straight sections
WR62 bends
WR62 custom E-plane Miter Bends
WR62 hybrid coupler (3 dB power splitter)
WR62 termination 250 Avg. Power (Watts)
WR62 high power waveguide phase shifters
WR62 Flex-Twist Waveguide Assemblies
WR62 Dual Crossguide Directional Couplers
TWT amplifier 13.75 - 14.5 GHz Max O/Pr: 675 W

Table 6.1. Launcher transmission line microwave components

The phase shifter that allow to have a minimum phase adjustment from 0-360 degrees with low insertion loss and low VSWR for waveguide WR62 (see figure 6.16(a) and 6.16(b)). The double-waveguide antenna systems could give a fundamental improvement in the control of the power spectrum obtained, by using a properly phase between waveguides and should produce a more effective coupling than a single guide.

A photograph of the double-waveguide arrays is shown in fig. 6.16.
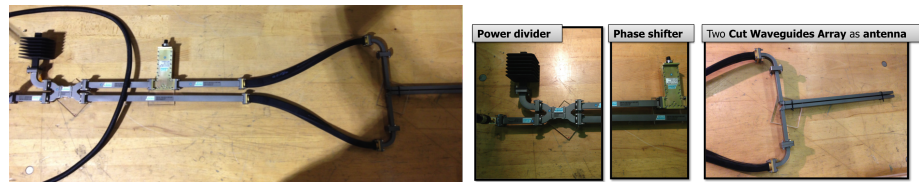
(a) A photograph of the double-waveguide arrays

(b) A photograph of the power divider, phase shifter and double-waveguide arrays

Fig. 6.16. photographs of the power divider, phase shifter

The antenna will be fixed inside the transversal microwave injection camera port. At first, the antenna design was investigated numerically, and then the antenna pattern was investigated in the lab. At first, the antenna design was designed on the bases of numerical simulation, then the antenna pattern was measured in free-space and fi-

nally, the electric field was measured in cavity thank to "homemade" high frequency probes.

6.4.1 Antenna design

CST microwave studio was used for the free-space antenna characteristics investigation. The k direction for different phase shift can be simulates as well. Fig. 6.17 shows that, for example, with a 45° of phase shift, a clear tilt of the radiated wave in the near-field region can be produced with respect to the 0° case. A series of simulations were then performed for different phase-shifts (see the next section for a direct comparison with experimental measurements).
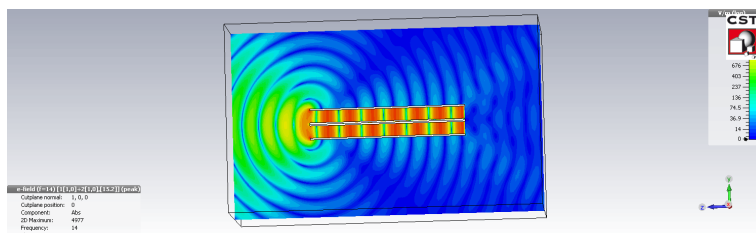
(a) E-field for 0° of phase shift
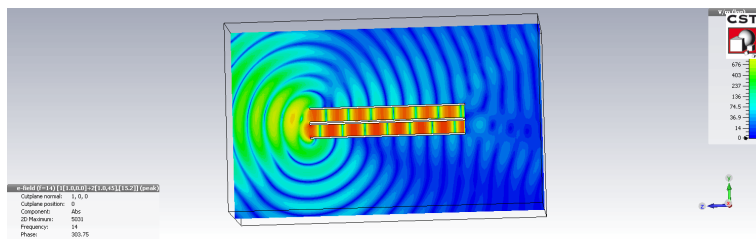
(b) E-field in vacuum for 45° of phase shift

Fig. 6.17. Simulated E-field distribution in the near field region in vacuum for 0° and 45° of phase shift between the two TE_{01} rectangular WR62 waveguides

6.4.2 Antenna measurements

We use the Agilent 2-Port PNA-L Microwave Network Analyzer to characterize the phased array. From Figure 6.18 it is possible to see that the antenna is well matched from 13.75 GHz and above 14.5 GHz for a over 5% impedance bandwidth.

The behavior of the double waveguide radiating into a vacuum can be simply described in terms of partial waves that are reflected at each aperture, cross-coupled to the neighboring guide, or radiated. The two return waves in each guide interfere destructively when $\Delta\Phi = 0°$ producing a total reflection minimum, and constructively for $\Delta\Phi = 180°$ producing a total reflection maximum.
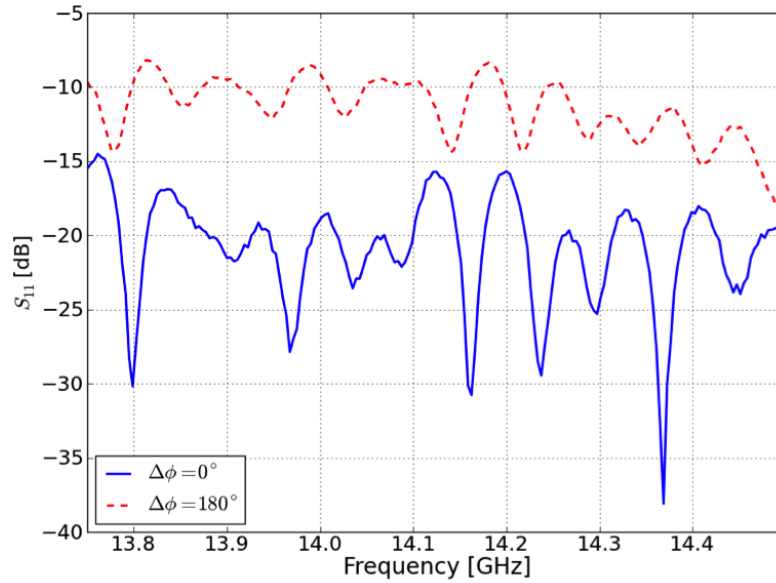
Fig. 6.18. Reflection coefficient versus frequency for the double waveguide antenna when the phase difference between guides is $\Delta\phi = 0°$ and $\Delta\phi = 180°$.

To experimentally evaluate the radiation pattern, the phased array was illuminated by a pyramidal horn antenna tuned on the same bandwidth. The horn antenna was placed at steps of $10°$ along a circle of radius 12 mm, corresponding to the maximum distance between the mouth of the launcher and the chamber walls. This system allows to measure the EM field amplitude distribution along the arc of the fixed radius equals to 12 cm, with the centre of the arc at the antenna end. The Anritsu MG3693C 2-31.8 GHz synthesized signal generator was attached to the antenna through a coaxial-to-waveguide transition. The antenna emits the HF in free space and a horn antenna measures the EM field amplitude in the region near the antenna. The amplitude signal from the horn was picked up by Rohnde&Schwarz power meter NZP22.

In Figure 6.19, both measured and simulated radiation pattern for different $\Delta\Phi$ are shown. The most significant tilt-angles measured experimentally are shown in Figure 6.20 (a). The maximum tilt-angle achieved is $\theta_0 = 40°$ for a phase difference equal to $\Delta\Phi = 120°$; the power difference with the secondary lobe is about 7.5 dB. By set-up a phase difference $\Delta\Phi = 48°$ it is possible to rotate the radiation up to $20°$ with a power of secondary lobe negligible. As it can be seen, the experimental characterization are in very good agreement with the CST simulation results.

The $0°$ shift case has a radiation pattern which is mostly directed along the axis of the waveguide. It means that the wave is emitted into the plasma perpendicularly

to the external magnetostatic field vector. At $\Delta\Phi = 48°$ a maximum of emitted power along the direction $\theta_0 = 13°$ is visible.

The $\Delta\Phi = 180°$ case has two lobes along the the direction $\theta_0 = 57°$.
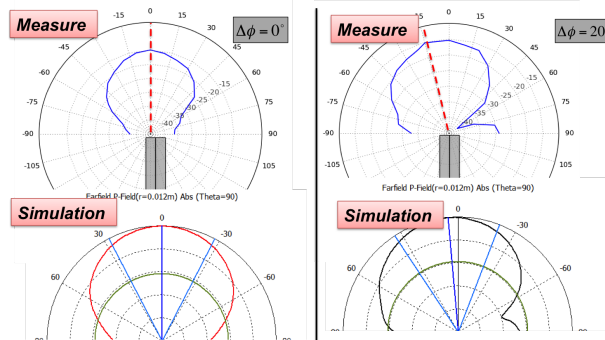
(a) Simulated vs measured radiation patterns at $\Delta\Phi = 0°$ and $\Delta\Phi = 20°$
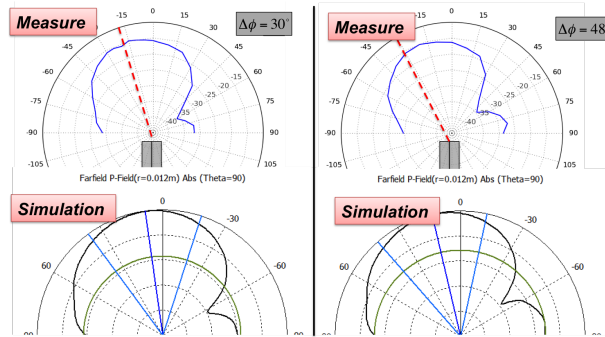
(b) Simulated vs measured radiation patterns at $\Delta\Phi = 30°$ and $\Delta\Phi = 48°$
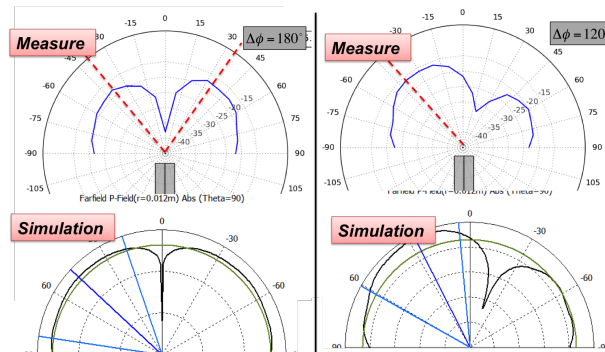
(c) Simulated vs measured radiation patterns at $\Delta\Phi = 180°$ and $\Delta\Phi = 120°$

Fig. 6.19. Comparison between simulated and measured radiation patterns
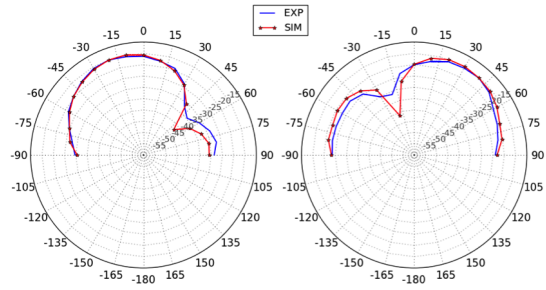
(a) Simulated vs measured radiation patterns at $\Delta\Phi = 48°$ and $\Delta\Phi = 120°$
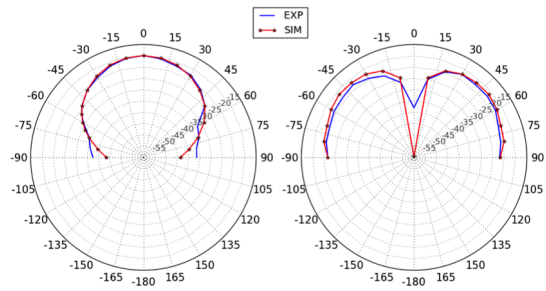
(b) Simulated vs measured radiation patterns at $\Delta\Phi = 0°$ and $\Delta\Phi = 180°$

Fig. 6.20. Comparison between simulated and measured radiation patterns

6.5 Antenna measurements inside the FPT plasma chamber

To improve the mechanical matching of the phased array with the plasma chamber, a new "customized" adaptor has been designed and realized at INFN-LNS. It allows to adapt a WRD350 standard flange into two standard WR62 waveguides by a H-shaped septum. The Figures 6.21 and 6.22 show renderings of the new perpendicular microwave injection on FPT system ion source .
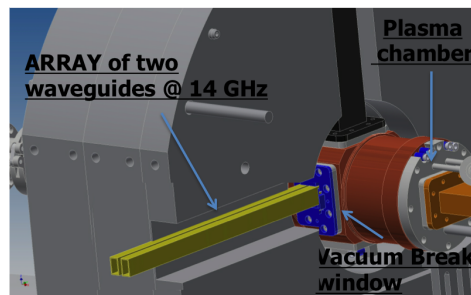
Fig. 6.21. Laucher arrangement in FPT: two-waveguide array, vacuum plasma chamber

(a)
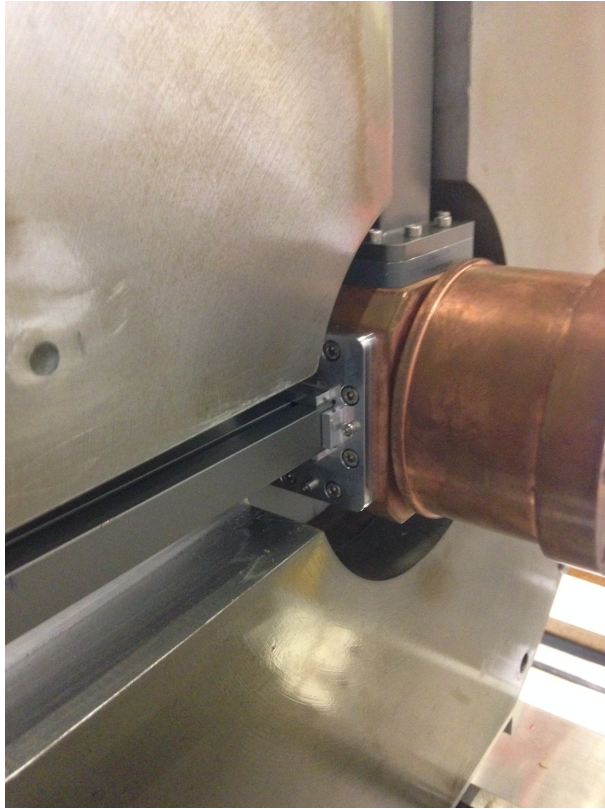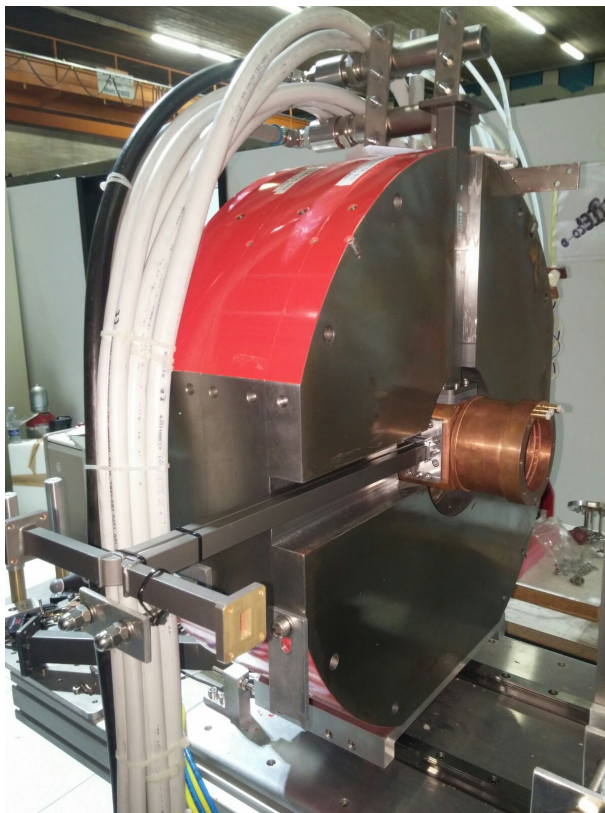
(b) Laucher arrangement in FPT: two-waveguide array,
vacuum plasma chamber

Fig. 6.22. Laucher arrangement in FPT: two-waveguide array, vacuum plasma chamber.

The measurements of the power irradiated by the antenna inside the plasma chamber have been performed by means of ad-hoc designed probes mounted on the chamber endplate. The detailed description of the probes is given in the following section.

6.5.1 High frequency Electromagnetic Probes

This section describes the measurement system developed to investigate the wave field distribution in FPT plasma chamber.

To measure the field amplitude radiated by the launcher inside the plasma chamber cavity, a movable microwave probe, sensitive to the short wavelengths and small enough to achieve the desired spatial resolution has been designed. The measurement setup is shown in figures 6.23 and 6.24

A 2-pin probe shown in fig. 6.25 is used to measure the wave field. The 2-pin probe has one pin grounded and another connected to the inner wire of a coaxial transmission line. The length of both pins is 3.5 mm. This enables measurement of the potential difference in the radial direction and so the E-field component perpendicular to the pins.
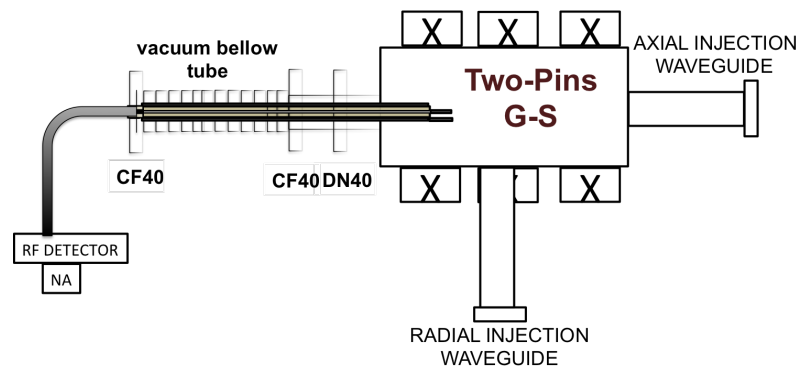
Fig. 6.23.

Sketch of the microwave probes introduced axially inside the plasma chamber of the FPT. A bellow is used for ensuring step-by-step movements of the probe under vacuum conditions. A motorized stage is able to place the probes at the desired position, while a feedthrough operated over a standard DN-40 (CF) flange allows to collect the detected signal.

A computer controlled step motor provides the 0.1 mm precision positioning of the probe set. The HF probes are connected to vacuum feedthrough that was mounted on a CF-40 flange. A bellow allows movements under vacuum conditions. In the current setup, the probes penetrate into the plasma chamber along a line parallel to the chamber axis.

The results of the amplitude measurements with 2-pin probe are shown in fig. 6.26 for different phase shift.
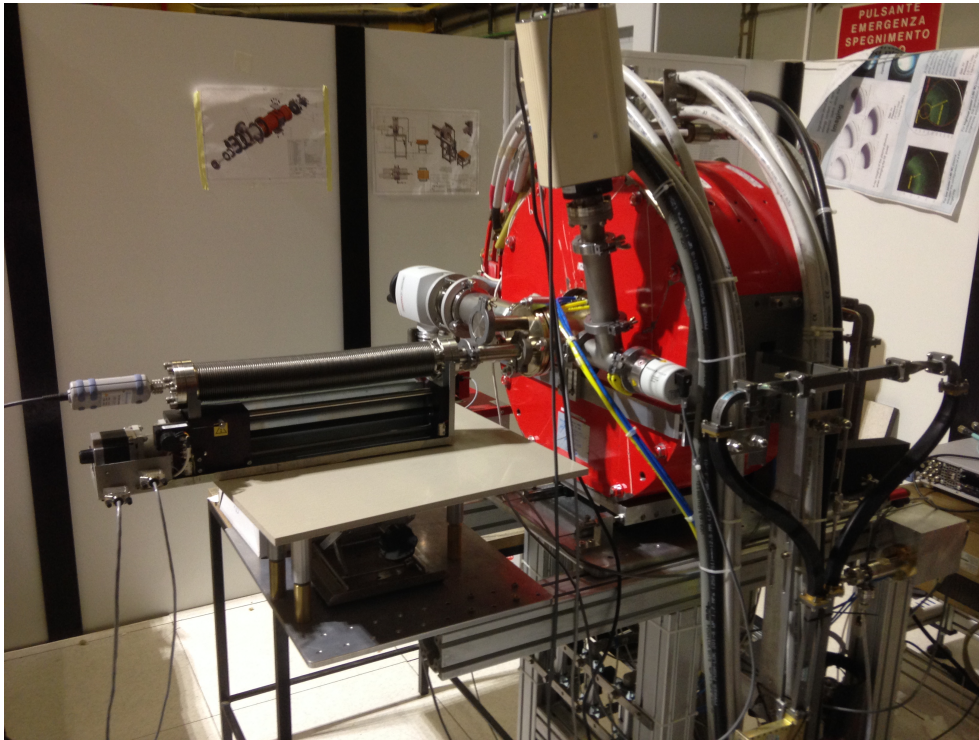
Fig. 6.24. A picture of the complete FPT assembly, showing the system used to hold and move the HF probes inside the plasma chamber.

6.5.2 Measured electric field

After introduced inside the plasma chamber, the probes were axially moved over a total excursion of 220 mm (i.e. covering almost the entire plasma chamber length). The phase-shift of the double-waveguide array was arranged to 0-60-120-180 degrees, i.e. at the most meaningful shift values according to the numerical simulations and free-space measurements.

The results of the measurements are shown in figure 6.26

The picture shows that at 60 and 120 degrees clear peaks arise in the peripheral part of the chamber, while for $\Delta\Phi = 180°$ a well-pronounced maximum appears at $z = 130mm$. Despite the high-control lobe direction evidenced by the simulation and by the free-space measurements, the reflections caused by the plasma chamber metallic walls complicate the waves patterns and introduce a strong scattering. It is worth mentioning in case of plasma contained into the chamber most of the launched

(a) 2-pin microwave probe view 1

(b) 2-pin microwave probe view 2

(c) 2-pin microwave view 3: detail on the "sensitive" part
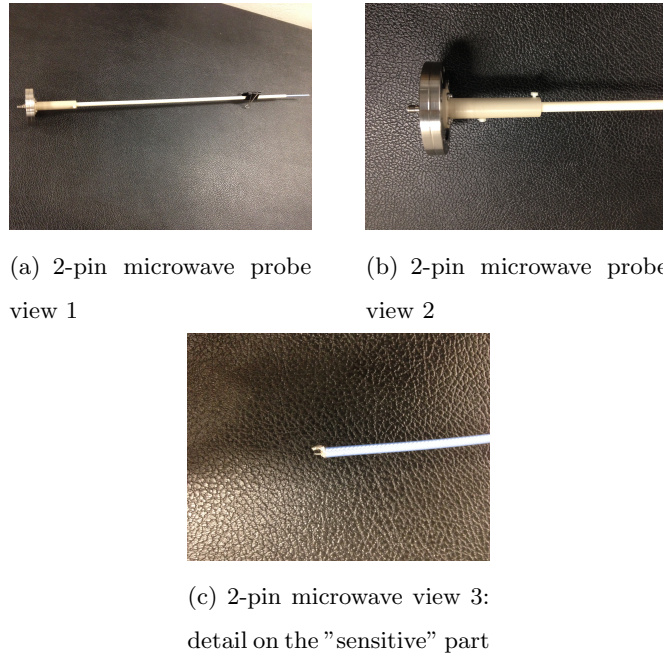
Fig. 6.25. Different views of the assembly of the 2-pin microwave probes
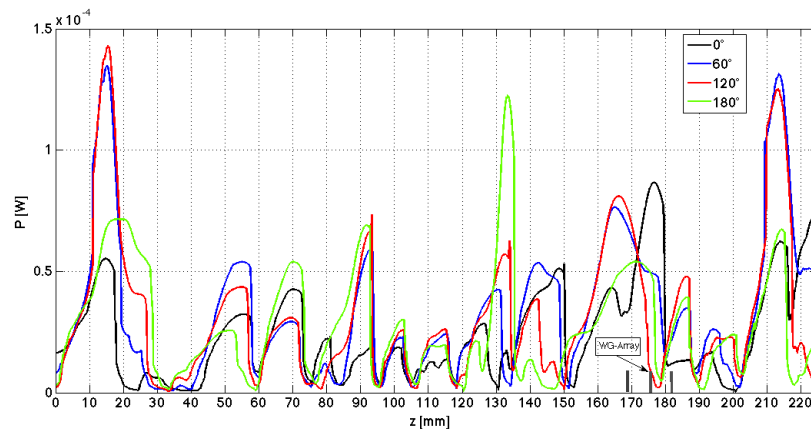
Fig. 6.26. Measured amplitude and phase of HF with different phase shift types

radiation will be hopefully converted/absorbed after a single-pass through the O-cutoff/UHR layer, thus restoring a situation more similar to the free space case. In any case, these preliminary results already demonstrate that the way-to-launch microwave radiations can be externally controlled even in case of irradiation into the compact-size plasma chamber of an ECRIS.

The next step will consist in the measurements of the irradiated pattern in presence of the plasma load, and then, finally, in the optimization of the launching for exciting EBWs into the plasma. The generation of the EBWs, according to what done in the past, will be monitored by using the X-ray diagnostics for highlighting the plasma

heating boost, as well as the interferometer developed in the frame of the present thesis for measuring the jump of the plasma density above the value imposed by the electromagnetic cutoff.

7

Conclusion and Perspectives

The modeling of waves in magnetized anisotropic plasma for microwave heating and diagnostic has been the main argument developed in this PhD thesis.

The relation $L_p \sim L_c \sim \lambda_0$ (where L_p and L_c are the plasma and plasma chamber lengths, and λ_0 is the RF vacuum wavelength) has required a "3D full-wave approach" based on a "finite element method". The RF modeling was matched to a kinetic code for solving the electron motion thus obtaining for the first time a quasi-self-consistent solution for electron density and energy distribution. The collected results explain a number of experimental observations. These results have also addressed the design of an innovative microwave launcher – consisting of a two-phased-waveguides array – as an alternative to the classical solutions. The launcher has been characterized by measuring the impedance matching and radiation patterns, in very good agreement with simulations. Theory and numerical models of microwave propagation in this kind of plasmas have been additionally valuable for the design of the novel microwave interferometer, able to probe plasmas contained inside compact chambers. The interferometer has permitted to measure the plasma refractive index with a precision around 10%. It will be also very useful for checking the effectiveness of the designed new launching scheme.

The present work may relevantly contribute to consolidate the leading role of INFN (and of the LNS group working on ion source development) in the field of ion source science and technology.

The results obtained in the framework of the thesis activities have permitted to shade additional light on the complexity of wave–to–plasma interaction in the resonant plasma chamber of ECRIS machines.

The actual picture of power transfer rising to the plasma that occurs in a real ECRIS is much more complex than the pure absorption of energy from right hand circularly polarized (RHCP), because this transfer can occur under conditions that deviate significantly from a pure ECR heating view (upper hybrid resonance (UHR), higher harmonic resonances, non liner power absorption). Such an approach is based

on semiempirical and general scalings, summarized by the *Geller's scaling laws* based on the increasing of frequency and of magnetic field. Although this has given valuable results in the last two-three decades ensuring a constant rise of performances, on the other hand, this "brute force" approach is nowadays showing its many limitations. For istance, it is now clear that currently the microwave launching systems in ECRIS devices are affected by a lack of optimization processes, still evidencing a scientific and technological gap with respect to large-size fusion devices.

For these reasons, this PhD thesis has been carried out with the aim to investigate the microwave coupling to the plasma, to analyze and design new techniques to improve the performances of the ECRISs and new microwave diagnostic techniques putting us on a road that takes beyond what achieved so far, i. e. towards a **"microwave-absorption oriented"** design of future ion sources.

Acknowledgments

Concluding my PhD course, there are many people that I would like to thank for giving me, in different ways, the support and the guidance necessary to complete this work. I would like to start by thanking my coadvisor, Dott. David Mascali. Working together day by day, he taught me how to scientifically face any problem. The experimental activities and results here reported have been mainly generated by his intuitions, vision and a lot of very exciting scientific discussions about rewarding scientific challenges that have made me grow not only professionally. I would like to express my gratitude to Prof. Gino Sorbello, who formerly supported my work for the master thesis and then followed my PhD activities as tutor and Prof. Tommaso Isernia for his fruitful advices while still giving me the freedom to work in my own way at LNS. The work described in this thesis has been carried out at the Laboratori Nazionali del Sud of INFN Catania: I wish to express my gratitude to Dr. Santo Gammino and Ing. Luigi Celona. They gave me the opportunity to work on the ion source R&D team and they have been always available when I need any suggestion especially for a better comprehension of the microwave-plasma interaction in the ECRIS. I would like to thank also the others components of my research group Dr. Giuseppe Castro, Ing. Ornella Leonardi, Dr. Lorenzo Neri for the pleasant time spent working together. More in general, I felt honored to work with the INFN-LNS staff: they are real experts people in their fields and I have learned something from each one of them. I would especially mention the valuable contribution of INFN-LNS technicians, mechanical designers and mechanical workshop which has realized many "customized" items needed for the different experimental setups.

Finally, my deepest gratitude goes to my love Roberta, my parents and my brothers Filippo and Gabriele for their infinite love and support. Special thanks go to my grand parents, to whom I want dedicate this thesis. They are my life.

Special thanks also to my friends Beppe and Mario, who are always close to me.

References

[1] R. Geller. *Electron Cyclotron Resonance Ion Sources and ECR Plasmas.* Inst. of Phys. Pub. Philadelphia, 1996.

[2] F. F. Chen. *Introduction to the Plasma Physics and Controlled Fusion: Plasma Physics.* U.K.London Press, 1986.

[3] http://www.frib.msu.edu.

[4] http://europeanspallationsource.se.

[5] http://myrrha.sckcen.be.

[6] http://www.cnao.it/index.php/it/.

[7] R. Geller. Electron cyclotron resonance multiply charged ion sources. *Nuclear Science, IEEE Transactions on Volume:23 , Issue: 2*, 1976.

[8] Yurij Podoba. *Radio frequency heating on the WEGA stellarator.* PhD thesis, Greifswald, 2006.

[9] Alf Khön. *Investigation of microwave heating scenarios in the magnetically confined low-temperature plasma of the stellarator TJ-K.* PhD thesis, Universität Stuttgart, 2010.

[10] Bin William. *Evaluations of high density plasma heating through O-X-B double mode conversion of EC-Waves in FTU Tokamak.* PhD thesis, Universitá degli studi di Milano, 2009.

[11] Ira B.Bernstein. Bernstein modes. *Phys. Rev. 109, 10*, 1958.

[12] H. P. Laqua, the W7-AS Teamdag, and the ECRH Groupddag. Electron bernstein wave heating and emission via OXB process at W7-AS. *Plasma Phys. Control. Fusion 41 A273-A284*, 1999.

[13] Francesco Volpe. *Electron Bernstein emission diagnostic of electron temperature prole at W7-AS Stellarator.* PhD thesis, Ernst-Moritz-Arndt-Universitat Greifswald, 2003.

[14] J. Preinhaelter J. and V. Kopeckỳ. Penetration of high-frequency waves into a weakly inhomogeneous magnetized plasma at oblique incidence and their transformation to bernstein mode. *J. Plasma Phys. 10 1*, 1973.

[15] D. Mascali. *A new approach to the study of the ECR Heating and Particle Dynamics in the plasma of Electron Cyclotron Resonance Ion Surces.* PhD thesis, INFN-LNS, 2007-2008.

[16] S. Gammino. 3rd and 4th generation ECRIS: Some possible scenarios. *High Energy Phys. Nucl. Phys, 31, 137*, 2007.

[17] A. G. Drentje. Techniques and mechanisms applied in electron cyclotron resonance sources for highly charged ions. *Rev. Sci. Instrum. 74, 2631*, 2003.

[18] Y. Kawai, G. D. Alton, O. Tarvainen, P. Suominen, and H. Koivisto. Effect of broadband microwave radiation on the performance of a conventional B-minimum geometry ecr ion source. *Rev. Sci. Instrum. 77, 03A331*, 2006.

[19] G. D Alton ad F. W. Meyer, Y. Liu, J. R. Beene, and D. Tucker. Enhancing the performances of traditional electron cyclotron resonance ion sources with multiple-discrete-frequency microwave radiation. *Rev. Sci. Instrum. 69, 2305 (1998)*, 1998.

[20] L. Celona, S. Gammino, G. Ciavola, F. Consoli, and A. Galatà. Analysis of the SERSE ion output by using klystron-based or TWT-based microwave generators. *AIP Conf. Proc. 749*, 2005.

[21] R. Geller. Proc. 1 int. conf. ion sources, Saclay, 537, (1969). *Proc. 1 int. conf. Ion sources, Saclay, 537, (1969)*, 1969.

[22] D. Mascali, L. Neri, S. Gammino, L. Celona, G. Ciavola, N. Gambino, R. Miracoli, and S. Chikin. Plasma ion dynamics and beam formation in electron cyclotron resonance ion sources. *Rev. Sci, Instrum. 81, 02A334 (2010)*, 2010.

[23] N. Sakudo. Microwave ion sources for industrial applications (invited). *Review of Scientific Instruments*, 2010.

[24] S. Gammino and G. Ciavola. ECR ion sources and scaling laws. *Proc. 14th Int. Conf. Cycl. Capetown, South Africa, 1995. p. 377*, 1995.

[25] D. Hitz et al. The comparison of 18 and 28 ghz behavior of SERSE: Some conclusions. *Proc. 15th Int. Workshop ECR Ion Sources. Jyvaskyla, Finland, 2002. p. 100*, 2002.

[26] S. Gammino, G. Ciavola, and L. Celona. Difference in the performances of ECR ion sources when they are fed by klystron-based generator or travelling-wave-tube-based generator. *Nucl. Instr. Meth. 491,342.*, 2005.

[27] R. Vondrasek, R. Scott, R. Pardo, H. Koivisto, O. Tarvainen, P. Suominen, and D. H. Edgell. ECRIS operation with multiple frequencies. *AIP Conf. Proc., 2005. 749, 31.*, 2005.

[28] Z Q Xie and C M Lyneis. Rev. sci. instrum. 66, 4218 (1995). *Rev. Sci. Instrum. 66, 4218 (1995)*, 1995.

[29] R. Vondrasek, R. Scott, R. Pardo, and H. Koivisto. Operational improvements of the argonne ECR sources. *Proc. 15th Int. Workshop on ECR Ion Sources, Jyvaskyla, Finland, 2002, p. 174.*

[30] S. Gammino, G. Ciavola, and L. Celona. Difference in the performances of ECR ion sources when they are fed by klystron-based generator or travelling-wave-tube-based generator. *Nucl. Instrum. Methods Phys. Res. A491 (2002) 342–345.*

[31] Krall N. A. and Trivelpiece A. W. Principles of plasma physics. *San Francisco Press,San Francisco, CA) 1986.*

[32] Podoba Y. Y., Laqua H. P., Warr G. B., Schubert M., Otte M., Marsen S., Wagner F., and Holzhauer. Phys. rev. lett., 98 (2007) 255003. *Phys. Rev. Lett., 98 (2007) 255003.*

[33] G. Castro, D. Mascali, F. P. Romano, L. Celona, and S. Gammino. Comparison between off-resonance and electron Bernstein waves heating regime in a microwave discharge ion source. *Rev. Sci. Instrum. 83, 02B501 (2012).*

[34] D. Mascali, L. Celona, S. Gammino, R. Miracoli, G. Castro, N. Gambino, and G. Ciavola. Electrostatic wave heating and possible formation of self-generated high electric fields in a magnetized plasma. *Nuclear Instruments and Methods in Physics Research A.*

[35] Weston M. Stacey. *Fusion Plasma Physics, 2nd Edition.* Wiley, 2012.

[36] T.H. Stix. *Waves in Plasmas.* American Inst. of Physics, 1992.

[37] D. G. Swanson. *Plasma Waves, 2nd Edition.* CRC Press, 2003.

[38] M. Brambilla. *Kinetic Theory of Plasma Waves: Homogeneous Plasmas.* International series of monographs on physics. Clarendon Press, 1998.

[39] S. Barbarino. Appunti di campi elettromagnetici.

[40] V. Erckmann and U. Gasparino. Electron cyclotron resonance heating and current drive in toroidal fusion plasmas. *Plasma Phys. Control. Fusion 36 (1994) 1869-1962, printed in the UK*, 1994.

[41] D. Bohm and E. P. Gross. Theory of plasma oscillations. a. origin of medium-like behavior. *Phys. Rev. 75, 1851*, 1949.

[42] Solomon J. Buchsbaum William P. Allis and Abraham Bers. *Waves in Anisotropic Plasmas.* The MIT Press, 2003.

[43] Hans-Jurgen Hartfuss and Thomas Geist. *Fusion Plasma Diagnostics with mm-Waves: An Introduction.* Wiley, 2013.

[44] Orso Meneghini. *Full-wave modeling ot the lower hybrid waves on Alcator C-Mod.* PhD thesis, MIT, 2012.

[45] K T McDonald. An electrostatic wave, arxiv:physics/0312025.

[46] H Igami, M Uchida, H Tanaka, and T Maekawa. Polarization adjustment of incident electromagnetic waves for optimal mode-conversion to electron bernstein waves. *Plasma Physics and Controlled Fusion, Volume 46, Number 1.*

[47] N. K. Bibinov, V. F. Bratsev, D. B. Kokh, V. I. Ochkur, and K. Wiesemann. Spectroscopic determination of the cold electron population in very low pressure ECR discharges in N_2/He mixtures. *Plasma Sources Sci. Technol.*, 14:109, 2005.

[48] C Lyneis, P Ferracin, S. Caspi, A. Hodgkinson, and G L Sabbi. Concept for a fourth generation electron cyclotron resonance ion source. *Rev. Sci. Instrum. 83, 02A301*, 2012.

[49] Francesco Paolo Romano, Claudia Caliri, Luigi Cosentino, Santo Gammino, Lorenzo Giuntini, David Mascali, Lorenzo Neri, Lighea Pappalardo, Francesca Rizzo, and Francesco Taccetti. Macro and micro full field xray fluorescence with an xray pinhole camera presenting high energy and high spatial resolution. *Analytical Chemistry.*

[50] S. Biri, E. Takacs, R. Racz, L.T. Hudson, and J. Palinkas. Pinhole x-ray camera photographs of an ecr ion source plasma. *Plasma Science, IEEE Transactions on Plasma Sciences*, 39(11):2494–2495, Nov 2011.

[51] M. A. Heald and C. B. Wharton. *Plasma diagnostic with microwaves.* Robert E. Krieger, 1996.

[52] Segre Sergio E. A review of plasma polarimetry - theory and methods. *Plasma Phys. Control. Fusion*, 41, 1999.

[53] C. H. Ma, D. P. Hutchinson, P. A. Staats, and K. L. Sluis. Measurements of electron density and plasma current distributions in tokamak plasma. *International Journal of Infrared and Millimeter Waves*, 3(2):263–277.

[54] G. Torrisi, D. Mascali, L. Neri, G. Castro, G. Patti, L. Di Donato, L. Celona, G. Sorbello, T. Isernia, S. Gammino, and G. Ciavola. Full wave simulation of waves in ECRIS plasmas based on the finite element method. *AIP Conf. Proc. 1580, 530*, 2014.

[55] G. Torrisi, D. Mascali, G. Sorbello, L. Neri, L. Celona, G. Castro, T. Isernia, and S. Gammino. Full-wave FEM simulations of electromagnetic waves in strongly magnetized non-homogeneous plasma. *Journal of Electromagnetic Waves and Applications, Volume 28, Number 9, 2014, pp. 1085-1099(15)*, 2014.

[56] D. Mascali, G. Torrisi, L. Neri, G. Sorbello, G. Castro, L. Celona, and S. Gammino. 3D-full wave and kinetics numerical modelling of electron cyclotron resonance ion sources plasma: steps towards self-consistency. *The European Physical Journal D, Volume 69, Issue 1*, 2015.

[57] Torrisi G., Mascali D., Neri L. andSorbello G., Celona L., Castro G., Di Donato L., Isernia T., and Gammino S. Modeling the electromagnetic field in anisotropic

inhomogeneous magnetized plasma of ECR ion sources. *Atti della XX Riunione Nazionale di Elettromagnetismo, Padova, 15-18 settembre 2014.*

[58] L. Celona et al. Microwave to plasma coupling in electron cyclotron resonance and microwave ion sources. *Rev. Sci. Instrum. 81*, 2010.

[59] Mascali D, Neri L, Gammino S, Celona L, Ciavola G, Gambino N, Miracoli R, and Chikin S. Plasma ion dynamics and beam formation in electron cyclotron resonance ion sources. *Rev. Sci Instrum.81(2):02A334*, 2010.

[60] L. Celona et al. Observations of the frequency tuning effect in the 14 GHz caprice ion source.,. *Rev. Sci. Instrum. 79:023305*, 2008.

[61] K. Crombe et al. Aip conf proc. 97: 1406. 2011.

[62] M. El Khaldi et al. Aip conf proc. 27: 31187. 2009.

[63] E. G. Evstatiev, V. A. Svidzinsky, J. A. Spencer, and J. S. Kim. Analytical and numerical modeling of radio frequency electron cyclotron resonance power absorption within the cold plasma picture. *Rev. Instr. Sci. 85, 02A503*, 2014.

[64] T. Thuillier, T. Lamy, L. Latrasse, Iv. Izotov, Av. Sidorov, Va. Skalyga, Vg. Zorin, and M. Marie-Jeanne. Study of pulsed electron cyclotron resonance ion source plasma near breakdown: The preglow. *Rev. Sci. Instrum. Issue 2, 79 02A314*, 2008.

[65] J. Vamosi and S. Biri. Trapcad a program to model magnetic traps of charged particles. *Computer physics communications, 98(1-2), pp. 215-223*, 1996.

[66] G. D. Shirkov and andG. Zschornack C. Mühle andG. Musiol. Ionization and charge dispersion in electron cyclotron resonance ion sources. *Nucl. Inst. and Meth. A: 302, 1, pp. 15*, 1991.

[67] C. Pernot A. Girard, G. Melin, and Phys C. Lecot. Modeling of electron-cyclotron-resonance-heated plasmas. *Phys. Rev. E 62, 1182*, 2000.

[68] A.P. Smirnov and R.W. Harvey. Calculations of the current drive in DIII-D with the GENRAY ray tracing code. *Bull. Amer. Phys. Soc. Vol. 40, No. 11, p. 1837, Abstract 8P35 (1995); CompX report CompX-2000-01*, 2001.

[69] M Brambilla. Numerical simulation of ion cyclotron waves in tokamak plasmas. *Plasma Physics and Controlled Fusion, 41, 1*, 1998.

[70] http://www.csm.ornl.gov/ shelton/fusion.html.

[71] J. Hillairet, D. Voyer, A. Ekedahl, M. Goniche, M. Kazda, O. Meneghini, D. Milanesio, and M. Preynas. ALOHA: an Advanced LOwer Hybrid Antenna coupling code. *Nuclear Fusion, Volume 50, Number 12*, 2010.

[72] S. Ceccuzzi, R. Maggiora, Milanesio D, F. Mirizzi, and L. Panaccione. Benchmark of Lower Hybrid coupling codes (brambilla, GRILL3DU, TOPLHA) with the FTU conventional grill experimental data. *AIP Conf. Proc. 1406, 153 (2011); http://dx.doi.org/10.1063/1.3664951*, 2011.

[73] R. Bilato and M. Brambilla. FELHS code for lowerhybrid launcher coupling and near fields. *35th EPS Conference on Plasma Phys. Hersonissos, ECA Vol.32D, P-5.094*, 2008.

[74] Lancellotti V., Milanesio D., Maggiora R., Vecchi G., and Kyrytsya V. TOPICA: an accurate and efficient numerical tool for analysis and design of ICRH antennas. *Nucl. Fusion 46 S47699*, 2006.

[75] M.Brambilla. Evaluation of the surface admittance matrix of a plasma in the finite larmor radius approximation. *Nuclear Fusion, 35 , 1265-1280*, 1995.

[76] Vdovin V.L. 3d full wave code modelling of ECRF plasma heating in tokamaks and ITER at fundamental and second harmonics. *Proceedings of the 23rd IAEA Fusion Energy Conference Daejeon*, 2010.

[77] D Van Eester. A mixed ray tracing/full wave ICRH mode conversion model. *Plasma Phys. Controlled Fusion, Vol. 34:1539-1562*, 1992.

[78] Yu. V. Petrov, Becoulet, and I A. Monakhov. Coupled Full-Wave and Ray-Tracing Numerical Treatment of Mode Conversion in a Tokamak Plasma. *American Physical Society, 41st Annual Meeting of the Division of Plasma Physics*, 1999.

[79] A Khn, Cappa, E Holzhauer, F Castejn, Fernndez, and U Stroth. Full-wave calculation of the OXB mode conversion of Gaussian beams in a cylindrical plasma. *Plasma Physics and Controlled Fusion 50 8*, 2008.

[80] Brian P. Cluggish andJin Soo Kim. Modeling of wave propagation and absorption in electron cyclotron resonance ion source plasmas. *Nucl, Inst. and Meth. Section A: 664, 1, ppp. 8497*, 2012.

[81] J.S. Kim, L. Zhao, B. P. Cluggish, I. N. Bogatu, S. Galkin, and L. Grubert. Status of far-tech's electron-cyclotron-resonance charge-breeder simulation toolset; MCBC GEM and IONEX. *TUCO-C04 Proceedings of ECRIS08*.

[82] A. Girard, C. Perret, G. Melin, and C. Lcot. Modeling of electron-cyclotron-resonance ion source and scaling laws. *Review of Scientific Instruments*, 69(2):1100–1102, 1998.

[83] T. Ropponen, P. Suominen O. Tarvainen and, T.K. Koponen, T. Kalvas, and H. Koivisto. Hybrid simulation of electron cyclotron resonance heating. *Nuclear Instruments and Methods in Physics Research pp. 115-124*, 2008.

[84] D. G. Swanson. *Plasma waves*. Academic press san diego, 1989.

[85] RF Module. Users Guide COMSOL Multiphysics.

[86] D. Mascali, S. Gammino, L. Celona, and G. Ciavola. Towards a better comprehension of plasma formation and heating in high performances electron cyclotron resonance ion sources. *Rev. Sci. Instrum.*, 83:02A336, 2012.

[87] http://mumps.enseeiht.fr.

[88] Toivanen el al. Effect of electron cyclotron resonance ion source frequency tuning on ion beam intensity and quality. *Review of Scientific Instruments, 81: 02A319.*

[89] C. K. Birdsall and A. B. Langdon. in. *Plasma physics via computer simulation*, pages 356–357, 2005.

[90] O. Tuske, L. Maunoury, J. Y. Pacquet, C. Barue, M. Dubois, G. Gaubert, P. Jardin, N. Lecesne, P. Leherissier, F. Lemagnen, R. Leroy, and Antonio C. C. Villari M. G. Saint-Laurent. Visible light spectrometry measurements for studying an ECRIS plasma and especially applied to the MONO1001 ion source. *Rev. Sci. Instrum. 75, 1529 (2004); http://dx.doi.org/10.1063/1.1691528*, 75, 1529, 2004.

[91] Fabio Maimone. *Investigation on the Microwave-based techniques to improve the performances of the Electron Cyclotron Resonance Ion Sources.* PhD thesis, Universitá di Catania, 2012.

[92] G. Dimonte, B. M. Lamb, and G. J. Morales. Effects of nonadiabaticity on applications of the ponderomotive force near gyroresonance. *Plasma Physics, Volume 25, Number 7.*

[93] S. Biri, A. Valek, T. Suta, E. Takcs, Cs. Szab, L. T. Hudson, B. Radics, J. Imrek, B. Juhsz, and J. Plinks. Imaging of ecr plasmas with a pinhole x-ray camera. *Review of Scientific Instruments*, 75(5):1420–1422, 2004.

[94] D. Leitner, J. Y. Benitez, C. M. Lyneis, D. S. Todd, T. Ropponen, J. Ropponen, H. Koivisto, and S. Gammino. Measurement of the high energy component of the x-ray spectra in the VENUS electron cyclotron resonance ion source. *Rev. Sci. Instrum.*, 79(3):033302. doi: 10.1063/1.2821137, 2008.

[95] S. Gammino, D. Mascali, L. Celona, F. Maimone, and G. Ciavola. Considerations on the role of the magnetic field gradient in ecr ion sources and build-up of hot electron component. *Plasma Sources Sci Technol*, 18, 4, 2009.

[96] D. Mascali, L. Celona, S. Gammino, G. Castro, R. Miracoli, L. Malferrari, F. Odorici, G. P. Veronese, R. Rizzoli, and T. Serafino. Generation mechanism and new damping of method of suprathermal electrons in a multi-mirror ECR machine. *Plasma Sources Sci Technol*, 22, 2013.

[97] R. Rácz, S. Biri, and J. Pálinkás. Plasma sources sci. *Technol.*, 5002:7, 2011.

[98] V. Toivanen, H. Koivisto, O. Steczkiewicz, L. Celona, O. Tarvainen, T. Ropponen, S. Gammino, D. Mascali, and G. Ciavola. *Rev Sci. Instrum.*, 81: 02A319, 2010.

[99] L. Celona, G. Ciavola, F. Consoli, S. Gammino, F. Maimone, P. Spädtke, K. Tinschert, R. Lang, J. Mäder, J. Roßbach, S. Barbarino, R. S. Catalano,

and D. Mascali. Observations of the frequency tuning effect in the 14 GHz CAPRICE ion source. *Rev Sci. Instrum.*, 79:023305, 2008.

[100] P. Spädtke, R. Lang, J. Mäder, F. Maimone, J. Roßbach, and K. Tinschert. Ion Beam Extraction from Magnetized Plasma. *20th International Workshop on ECR.*

[101] J. Angot, T. Lamy, M. M. Jeanne, P. Sortais, and T. Thuillier. LPSC PHOENIX ECR charge breeder beam optics and efficiencies. *ECRIS-Proceedings of the 20th International Workshop on Electron Cyclotron Resonance Ion Sources, Sydney, Australia*, 2012.

[102] A. Galatà, M. Comunian, L. Bellan, M. Maggiore, G. Patti, C. Roncolato, G. Bisoffi, A. D. Russo, L. Calabretta, J. Angot, and T. Lamy. The SPES-Charge Breeder and its beam line at INFN-LNL. *International Conference on Electromagnetic Isotope Separators and Related Topics (EMIS), Grand Rapids, MI.*, 11-15 May 2015.

[103] A. Galatà, G. Patti, C. Roncolato, J. Angot, and T. Lamy. The new ECR charge breeder for the Selective Production of Exotic Species project at INFN-Laboratori Nazionali di Legnaro. *Review of Scientific Instruments*, 87(2), 2016.

[104] P. Delahaye, O. Kester, C. Barton, T. Lamy, M. Marie-Jeanne, and F. Wenander. Evaluation of charge breeding options for EURISOL. *European physical journal*, 46:421–433, 2010.

[105] A. Galatà, D. Mascali, L. Neri, G. Torrisi, and L. Celona. A three-dimensional numerical modelling of the PHOENIX-SPES charge breeder based on the Langevin formalism. *Review of Scientific Instruments*, 87(2), 2016.

[106] D. Mascali, L. Celona, F. Maimone, J. Mäder, G. Castro, F. P. Romano, A. Musumarra, C. Altana, C. Caliri, G. Torrisi, L. Neri, S. Gammino, K. Tinschert, K. P. Spädtke, J. Roßbach, R. Lang, and G. Ciavola. X-ray spectroscopy of warm and hot electron components in the CAPRICE source plasma at EIS testbench at GSI. *Rev. Sci. Instrum.*, 85:02A956, 2014.

[107] A. Galatà, D. Mascali, L. Neri, G. Torrisi, and L. Celona. A three-dimensional numerical modelling of the PHOENIX-SPES charge breeder based on the Langevin formalism. *Review of Scientific Instruments*, 87(2), 2016.

[108] L. Neri, G. Castro, G. Torrisi, A. Galatà, D. Mascali, L. Celona, and S. Gammino. Recent progress in plasma modelling at infn-lns. *Review of Scientific Instruments*, 87(2), 2016.

[109] O. Meneghini, S. Shiraiwa, and R. Parker. Wavelet-based analysis of Lower Hybrid Full-Wave Fields. *Plasma and Fusion Research 240311*, 7, 2012.

[110] D.A. D' Ippolito, J.R. Myra, E.F. Jaeger, L.A. Berry, and D.B. Batchelor. Local Mode Analysis of 2D ICRF Wave Solutions. *AIP Conference Proc. 694, 463,*

2003.

[111] Stephane G Mallat. A theory for multiresolution signal decomposition: the wavelet representation. *Pattern Analysis and Machine Intelligence, IEEE Transactions on*, 11(7):674–693, 1989.

[112] A. Grossmann and J. Morlet. Decomposition of hardy functions into square integrable wavelets of constant shape. *SIAM J. Math. Anal., 15, pp. 723-736*, 1984.

[113] J. Morlet. *Sampling Theory and Wave Propagation, ssues in Acoustic Signal Image Processing and Recognition Volume 1 of the series NATO ASI Series pp 233-261*.

[114] Castro G., Mascali D., Romano F. P., Celona L., Gammino S., Lanaia D., Di Giugno R., Miracoli R., Serafino T., Di Bartolo F., Gambino N., and Ciavola G. Comparison between off-resonance and electron bernstein waves heating regime in a microwave discharge ion sourcea). *Review of Scientific Instruments*, 83(2), 2012.

[115] D. Mascali, L. Celona, S. Gammino, R. Miracoli, G. Castro, N. Gambino, and G. Ciavola. Electrostatic wave heating and possible formation of self-generated high electric fields in a magnetized plasma. *Nuclear Instruments and Methods in Physics Research Section A: Accelerators, Spectrometers, Detectors and Associated Equipment*, 653(1):11 – 16, 2011. Superstrong 2010.

[116] Golovanivsky Konstantin S., Dougar-Jabon Valery D., and Reznikov Dmitry V. Proposed physical model for very hot electron shell structures in electron cyclotron resonance˘driven plasmas. *Phys. Rev. E*, 52:2969–2973, Sep 1995.

[117] S. Biri, A. Valek, T. Suta, E. Takcs, Cs Szabó, L. T. Hudson, B. Radics, J. Imrek, B. Juhász, and J. Pálinkás. Imaging of ECR plasmas with a pinhole x-ray camera. *Review of Scientific Instruments, 75, pp. 1420-1422*, 2004.

[118] Orlinskij DV and Magyar G. Plasma diagnostics on large tokamaks. *Nuclear Fusion*, 28(4):611, 1988.

[119] Yoshihiko Mizumachi. Improved Zebra-Stripe Method of a Microwave Interferometer. *Japanese Journal of Applied Physics*, 11(2):272, 1972.

[120] Gibson A and Reid GW. A zebra-stripe display for an optical interferometer, and its use to measure plasma density in the presence of vibration. *Applied Physics Letters*, 5(10):195–197, 1964.

[121] I.H. Hutchinson. *Principles of Plasma Diagnostics*. Cambridge University Press, 2005.

[122] Giuseppe Torrisi, R. Agnello, G. Castro, L. Celona, V. Finocchiaro, S. Gammino, D. Mascali, L. Neri, S. Passarello, G. Sorbello, and T. Isernia. Design of

a microwave frequency sweep interferometer for plasma density measurements in ecr ion sources. *IPAC15 conference proceedings at the JACoW*, 2015.

[123] M. Skolnik. *Radar Handbook*. McGraw Hill, 1970.

[124] Earl E. Scime, Robert F. Boivin, John L. Kline, and Matthew M. Balkey. Microwave interferometer for steady-state plasmas. *Review of Scientific Instruments 72, 1672*, 2000.

[125] John Howard and David Oliver. *Appl. Opt., Vol. 45, Issue 34, pp. 8613-8620*, 2006.

[126] CST INC. *CST MICROWAVE STUDIO*, 2013.

[127] Multiphysics COMSOL. v. 4.3 a, Users' Guide, RF Module. 2012.

[128] Balanis Constantine A. *Antenna theory: analysis and design*. John Wiley Sons, 2012.

[129] Gammino S. et al. Diagnostics and preliminary operations of a microwave discharge plasma reactor for complex molecules dissociation. *34th EPS Conference on Plasma Physics 2007, EPS 2007 - Europhysics Conference Abstracts 01/2007; 31(2)*.

[130] G. Castro, D. Mascali, R. Agnello, L. Celona, O. Leonardi, L. Neri, D. Nicolosi, G. Torrisi, and S. Gammino. Experimental investigation of non-linear wave to plasma interaction in a quasi-flat magnetostatic field. *Rev. Sci. Instrum. 87, 02A507 (2016)*.

[131] A. Elhawil, L. Zhan, J. Stiens, C. De Tandt, N. A. Gotzen, G. V. Assche, and R. Vounckx. Quasi-optical free-space method for dielectric constant characterization of polymer materials in mm-wave band. *Proceedings Symposium IEEE/LEOS Benelux Chapter, 2007, Brussels*, 2007.

[132] M. Bornatici, R. Cano, O De Barbieri, and F. Engelmann. Electron cyclotron emission and absorption in fusion plasmas. *Nucl. Fusion 23, 1113-1276 (1983)*.

[133] A K Ram and S D Schultz. Excitation, propagation, and damping of electron Bernstein waves in tokamaks. *Physics of Plasmas*, 7(10):4084–4094, 2000.

[134] DeyIndranuj and Bhattacharjee Sudeep. Penetration and screening of perpendicularly launched electromagnetic waves through bounded supercritical plasma confined in multicusp magnetic field. *Physics of Plasmas*, 18(2), 2011.

[135] M. Brambilla. Slow-wave launching at the lower hybrid frequency using a phased waveguide array. *NUCLEAR FUSION 16 1 (1976)*, 1976.

[136] S. Bernabei, M A Heald, W M Hooke, R W Motley, F J Paoloni, M. Brambilla, and W D Getty. Plasma-wave coupling and propagation using phased waveguide arrays. *NUCLEAR FUSION 17 5 (1977)*, 1977.